

Plasticity of Metal Matrix Composites Reinforced With Continuous Alumina Fibers

by

Pavel Bystrický

Ingénieur de l'Ecole Nationale Supérieure d'Electrochimie et d'Electrometallurgie
de Grenoble, 1988

D.E.A., Institut National Polytechnique de Grenoble, 1988

Submitted to the
Department of Materials Science and Engineering
on January 10, 1997
in Partial Fulfillment of the Requirements for the Degree of

DOCTOR OF PHILOSOPHY



at the

MASSACHUSETTS INSTITUTE OF TECHNOLOGY

FEBRUARY 1997

© 1997 MASSACHUSETTS INSTITUTE OF TECHNOLOGY.

Signature of Author: _____
Department of Materials Science and Engineering
January 10, 1997

Certified by:  _____ 
Andreas Mortensen
Professor of Metallurgy

Accepted by: _____
Linn W. Hobbs
John F. Elliott Professor of Materials
Chairman, Department Committee on Graduate Students

MASSACHUSETTS INSTITUTE
OF TECHNOLOGY

JUN 16 1997 Science

Plasticity of Metal Matrix Composites Reinforced With Continuous Alumina Fibers

by

Pavel Bystrický

Submitted to the
Department of Materials Science and Engineering
on January 10, 1997
in Partial Fulfillment of the Requirements for the Degree of

DOCTOR OF PHILOSOPHY IN MATERIALS SCIENCE

Abstract

Continuous parallel alumina fiber reinforced composites are produced by pressure-infiltration, and tested in tension/compression along the fiber axis with a goal of measuring the influence exerted by the reinforcement on the flow stress of aluminum and copper based matrices. In this configuration, the longitudinal matrix strain is uniform in the composite, and the equistrain rule of mixtures, modified to take into account stresses due to differential lateral contraction, can be used to back-calculate the matrix flow stress from that of the composite.

Derived matrix *in-situ* stress-strain curves are presented for cast Dupont FP™ and 3M Nextel 610™ alumina fiber reinforced pure aluminum, Al-0.9wt%Mg, Al-4.5wt%Cu, pure copper, Cu-7wt%Al, Cu-1wt%Ti at room temperature, and pure aluminum at 77 K. Precision in the measurement of matrix *in-situ* stress-strain curves is analyzed, and it is found that, within experimental uncertainty, no enhanced matrix work hardening rates similar to those found in the Cu/W system can be conclusively detected. It is found that the fibers alter the matrix plastic flow behavior by increasing the flow stress amplitude of the matrix, and by rendering yield in compression more progressive than in initial tension. Essentially, all features of matrix/fiber interaction can be rationalized as being due to dislocation emission in the matrix caused by thermal mismatch strains within the material during composite cooldown from processing temperatures.

Thesis Supervisor: Andreas Mortensen
Title: Professor of Metallurgy

Table of Contents

ABSTRACT	2
TABLE OF CONTENTS	3
LIST OF FIGURES	6
LIST OF TABLES	11
ACKNOWLEDGMENTS	13
1. INTRODUCTION	14
2. BACKGROUND / LITERATURE REVIEW	17
2.1 NATURE AND PROCESSING OF METAL MATRIX COMPOSITES	17
2.2 MECHANICS OF FIBER REINFORCED METALS	18
2.3 COMPOSITE STRESS-STRAIN CURVE	21
2.4 PLASTICITY IN REINFORCED METALS	21
2.5 PROPOSED THEORIES OF MATRIX WORK-HARDENING	26
3. MATRIX <i>IN-SITU</i> STRESS-STRAIN DERIVATION	29
3.1 MECHANICAL ANALYSIS: HILL'S BOUNDS	29
3.2 DETERMINATION OF APPARENT <i>IN-SITU</i> MATRIX RATE OF WORK HARDENING AND FLOW CURVES	32
3.3 UNCERTAINTY IN DERIVED MATRIX <i>IN-SITU</i> STRESS-STRAIN CURVES	34
4. EXPERIMENTAL PROCEDURES AND ERROR ANALYSIS	36
4.1 CONSTITUENTS	36
4.1.1 FIBERS	36
4.1.2 MATRICES	37

4.2 FABRICATION OF THE COMPOSITES	37
4.2.1 FIBER PREFORM PREPARATION	37
4.2.2 ALUMINUM-BASED MATRIX COMPOSITES	39
4.2.3 COPPER-BASED MATRIX COMPOSITES	41
4.2.4 SAMPLE DESIGNATION	41
4.3 MECHANICAL TESTING	41
4.3.1 GEOMETRY	41
4.3.2 TREATMENT PRIOR TO TESTING	43
4.3.3 ROOM TEMPERATURE TESTING	45
4.3.4 ERROR ANALYSIS IN ROOM TEMPERATURE TESTING	47
4.3.4.1 Error in Cross-section Measurements	48
4.3.4.2 Error in Load Calibration	50
4.3.4.3 Error in Strain Calibration	50
4.3.4.4 Error Due to Sample Misalignment	50
4.3.4.5 Error Due to Digitization and Signal Noise	51
4.3.4.6 Overall Error on Stress and Strain at Room Temperature	52
4.3.5 LOW TEMPERATURE TESTING	52
4.3.6 ERROR ANALYSIS IN LOW TEMPERATURE TESTING	56
4.4 DETERMINATION OF FIBER VOLUME FRACTION	58
4.4.1 PYCNOMETRY	59
4.4.1.1 Water Pycnometry	59
4.4.1.2 Xylene Pycnometry	60
4.4.2 ERROR ANALYSIS IN PYCNOMETRY	61
4.4.2.1 Composite Constituents	63
4.4.2.2 Experimental Error in the Volume Fraction	64
4.4.3 MATRIX DISSOLUTION	66
4.4.3.1 Experimental Error in Matrix Dissolution	67
4.4.4 VOLUME FRACTION DETERMINATION FROM THE STRESS-STRAIN CURVE	69
4.5 ANALYSIS OF STRESS-STRAIN CURVES	71
4.5.1 DETERMINATION OF COMPOSITE RATE OF WORK HARDENING CURVES	71
4.5.2 UNCERTAINTY ON FIBER MODULUS	74
4.5.3 UNCERTAINTY ON STRESS-STRAIN SLOPE	74
4.6 METALLOGRAPHY	75
5. RESULTS	77
<hr/>	
5.1 COMPOSITE CHARACTERIZATION	77
5.1.1 INFILTRATION	77

5.1.2 MICROSTRUCTURE	85
5.1.3 FIBER VOLUME FRACTION	85
5.2 MECHANICAL TESTS	87
5.2.1 UNREINFORCED MATRIX REFERENCE	87
5.2.2 COMPOSITES	91
5.2.3 FRACTURE	126
6. DISCUSSION	134
<hr/>	
6.1 UNREINFORCED MATRICES	134
6.2 UNCERTAINTY ON MATRIX STRESS, AND BROKEN FIBERS IN PURE COPPER MATRIX COMPOSITES	135
6.3 MATRIX YIELDING	140
6.4 DISLOCATION DENSITIES	145
6.5 FLOW STRESS IN TENSION-COMPRESSION AND HARDENING BEHAVIOR	148
6.6 RESIDUAL STRESSES	149
6.7 MATRIX WORK-HARDENING RATE	154
7. CONCLUSION	156
<hr/>	
SUGGESTIONS FOR FUTURE WORK	157
APPENDIX A: MATERIALS CONSTANTS AND SUMMARY OF TEST RESULTS	159
APPENDIX B: DESCRIPTION OF DATA ACQUISITION PROGRAM	177
APPENDIX C: DESCRIPTION OF DATA PROCESSING PROGRAM	187

List of Figures

Figure 2-1 - Derived stress-strain curves of the copper matrix in composites reinforced with (a) 10 μm and (b) 20 μm tungsten fibers, produced by vacuum infiltration. The volume fraction of fibers is given for each curve. Single crystal and polycrystalline unreinforced copper curves are also shown (Fig. 5 from [4]).	23
Figure 2-2 - Derived stress-strain curves of the copper matrix in composites reinforced with 37% tungsten fibers, produced by electrodeposition and hot-pressing. The numbers shown correspond to fiber diameters, in μm , with as-pressed unreinforced copper plotted for comparison (Fig. 4 from [5]).	24
Figure 4-1 - Schematic of the pressure infiltration apparatus used to produce aluminum-based matrix composites.	38
Figure 4-2 - Schematic of the pressure infiltration apparatus used to produce copper-based matrix composites.	40
Figure 4-3 - Geometry of bars for mechanical testing	45
Figure 4-4 - Schematic of custom grips for tension-compression testing at room temperature and 77 K.	49
Figure 4-5 - Gripping set-up prior to testing, with pure Cu/FP sample in top grip, showing mounted strain gages and connections to strain gage amplifier.	53
Figure 4-6 - Pure Al/FP sample, gripped in top and bottom grips, ready for testing at 77 K. Note porous copper "phase separator" which minimizes turbulence of liquid nitrogen flow during test.	54
Figure 4-7 - Mechanical test in progress in liquid nitrogen. The temperature reading (-195°C) is from a thermocouple placed near the sample's strain gages.	55
Figure 4-8 - Example of determination of yield stress (taken as point at which departure from linearity occurs) after elastic unloading (data from 1-3•CuAl/3M Test1, computed and plotted in Yield! II program).	73
Figure 5-1 - Annealed 99.996%Cu reinforced with 60% Fiber FP, after mechanical testing, showing complete infiltration and uniform fiber distribution (Sample 1-1•Cu/FP).	80
Figure 5-2 - As-cast and annealed 99.996%Cu reinforced with 60% Fiber FP, hydrogen peroxide etch (Table 4-5). Etch pits with identical orientation and shape show large grain size (Sample 0-3•Cu/FP).	81
Figure 5-3 - As-cast Al-4.5wt%Cu reinforced with approximately 42% Fiber FP. Keller's etch shows the presence of θ (CuAl_2) phase at the fiber-matrix interface.	82
Figure 5-4 - As-cast Fiber FP reinforced Al-0.9wt%Mg. Low volume fraction ($V_f = 34\%$) allows large grains, revealed by Barker's etch, to be clearly distinguishable under polarized light, with grain boundaries pinned at fibers (Sample 10•AlMg/FP).	83
Figure 5-5 - As-cast Cu-1wt%Ti reinforced with 53% Fiber FP, etched in potassium dichromate (Table 4-5), showing a grain boundary (Casting number 1•CuTi/FP).	84

Figure 5-6 - Unreinforced matrix reference stress-strain curves of pure aluminum (tested at room temperature and at 77 K) and of Al-4.5wt%Cu and Al-0.9wt%Mg.	89
Figure 5-7 - Unreinforced matrix reference stress-strain curves of pure copper (tested once and eleven times in tension-compression) and of Cu-7wt%Al and Cu-1wt%Ti.	90
Figure 5-8 - (a) Stress-strain curve of pure aluminum composite reinforced with 21.4% Fiber FP, tested at room temperature (Sample 1-1•Al/FP) (top graph). (b) Corresponding Theta curves for each cycle (bottom graph). Horizontal lines represent $E_f V_f$ (dashed line) and $E_f V_f + \theta_{h,pl} \pm \Delta(E_f V_f + \theta_{h,pl})$.	96
Figure 5-8 - (c) Apparent <i>in-situ</i> matrix stress-strain curve of pure aluminum computed from composite reinforced with 21.4% Fiber FP, tested at room temperature (Sample 1-1•Al/FP). Dashed line shows unreinforced matrix tested as reference.	97
Figure 5-8 - (d) Total estimated uncertainty on apparent <i>in-situ</i> matrix stress-strain curve of pure aluminum computed from composite reinforced with 21.4% Fiber FP, tested at room temperature (Sample 1-1•Al/FP).	98
Figure 5-9 - (a) Stress-strain curve of pure aluminum composite reinforced with 48.5% Fiber FP, tested at 77 K (Sample 0-4•Al/FP) (top graph). (b) Corresponding Theta curves for each cycle (bottom graph). Horizontal lines represent $E_f V_f$ (dashed line) and $E_f V_f + \theta_{h,pl} \pm \Delta(E_f V_f + \theta_{h,pl})$.	99
Figure 5-9 - (c) Apparent <i>in-situ</i> matrix stress-strain curve of pure aluminum computed from composite reinforced with 48.5% Fiber FP, tested at 77 K (Sample 0-4•Al/FP). Dashed line shows unreinforced matrix tested as reference.	100
Figure 5-9 - (d) Total estimated uncertainty on apparent <i>in-situ</i> matrix stress-strain curve of pure aluminum computed from composite reinforced with 46.2% Fiber FP, tested at 77 K (Sample 0-6•Al/FP).	101
Figure 5-10 - (a) Stress-strain curve of pure aluminum composite reinforced with 67.2% Nextel 610 fibers (Sample 2-9•Al/3M) (top graph). (b) Corresponding Theta curves for each cycle (bottom graph). Horizontal lines represent $E_f V_f$ (dashed line) and $E_f V_f + \theta_{h,pl} \pm \Delta(E_f V_f + \theta_{h,pl})$.	102
Figure 5-10 - (c) Apparent <i>in-situ</i> matrix stress-strain curve of pure aluminum computed from composite reinforced with 67.2% Nextel 610 fibers (Sample 2-9•Al/3M). Dashed line shows unreinforced matrix tested as reference.	103
Figure 5-10 - (d) Total estimated uncertainty on apparent <i>in-situ</i> matrix stress-strain curve of pure aluminum computed from composite reinforced with 67.2% Nextel 610 fibers (Sample 2-9•Al/3M).	104
Figure 5-11 - (a) Stress-strain curve of Al-4.5wt%Cu composite reinforced with 44.5% Fiber FP (Sample 3-6•AlCu/FP) (top graph). (b) Corresponding Theta curves for each cycle (bottom graph). Horizontal lines represent $E_f V_f$ (dashed line) and $E_f V_f + \theta_{h,pl} \pm \Delta(E_f V_f + \theta_{h,pl})$.	105
Figure 5-11 - (c) Apparent <i>in-situ</i> matrix stress-strain curve of Al-4.5wt%Cu computed from composite reinforced with 44.5% Fiber FP (Sample 3-6•AlCu/FP). Dashed line shows unreinforced matrix tested as reference.	106

Figure 5-11 - (d) Total estimated uncertainty on apparent <i>in-situ</i> matrix stress-strain curve of Al-4.5wt%Cu computed from composite reinforced with 44.5% Fiber FP (Sample 3-6•AlCu/FP).	107
Figure 5-12 - (a) Stress-strain curve of Al-0.9wt%Mg composite reinforced with 33.8% Fiber FP (Sample 10•AlMg/FP) (top graph). (b) Corresponding Theta curves for each cycle (bottom graph). Horizontal lines represent $E_f V_f$ (dashed line) and $E_f V_f + \theta_{h,pl} \pm \Delta(E_f V_f + \theta_{h,pl})$.	108
Figure 5-12 - (c) Apparent <i>in-situ</i> matrix stress-strain curve of Al-0.9wt%Mg computed from composite reinforced with 33.8% Fiber FP (Sample 10•AlMg/FP). Dashed line shows unreinforced matrix tested as reference.	109
Figure 5-12 - (d) Total estimated uncertainty on apparent <i>in-situ</i> matrix stress-strain curve of Al-0.9wt%Mg computed from composite reinforced with 33.8% Fiber FP (Sample 10•AlMg/FP).	110
Figure 5-13 - (a) Stress-strain curve of pure copper composite reinforced with 58.2% Fiber FP (Sample 4-5•Cu/FP) (top graph). (b) Corresponding Theta curves for each cycle (bottom graph). Horizontal lines represent $E_f V_f$ (dashed line) and $E_f V_f + \theta_{h,pl} \pm \Delta(E_f V_f + \theta_{h,pl})$.	111
Figure 5-13 - (c) Apparent <i>in-situ</i> matrix stress-strain curve of pure copper computed from composite reinforced with 58.2% Fiber FP (Sample 4-5•Cu/FP). Dashed line shows unreinforced matrix tested as reference.	112
Figure 5-13 - (d) Total estimated uncertainty on apparent <i>in-situ</i> matrix stress-strain curve of pure copper computed from composite reinforced with 58.2% Fiber FP (Sample 4-5•Cu/FP).	113
Figure 5-14 - (a) Stress-strain curve of Cu-7wt%Al composite reinforced with 52.1% Fiber FP (Sample 1-3•CuAl/FP) (top graph). (b) Corresponding Theta curves for each cycle (bottom graph). Horizontal lines represent $E_f V_f$ (dashed line) and $E_f V_f + \theta_{h,pl} \pm \Delta(E_f V_f + \theta_{h,pl})$.	114
Figure 5-14 - (c) Apparent <i>in-situ</i> matrix stress-strain curve of Cu-7wt%Al computed from composite reinforced with 52.1% Fiber FP (Sample 1-3•CuAl/FP). Dashed line shows unreinforced matrix tested as reference.	115
Figure 5-14 - (d) Total estimated uncertainty on apparent <i>in-situ</i> matrix stress-strain curve of Cu-7wt%Al computed from composite reinforced with 52.1% Fiber FP (Sample 1-3•CuAl/FP).	116
Figure 5-15 - (a) Stress-strain curve of Cu-7wt%Al composite reinforced with 68.6% Nextel 610 fibers (Sample 1-2•CuAl/3M) (top graph). (b) Corresponding Theta curves for each cycle (bottom graph). Horizontal lines represent $E_f V_f$ (dashed line) and $E_f V_f + \theta_{h,pl} \pm \Delta(E_f V_f + \theta_{h,pl})$.	117
Figure 5-15 - (c) Apparent <i>in-situ</i> matrix stress-strain curve of Cu-7wt%Al computed from composite reinforced with 68.6% Nextel 610 fibers (Sample 1-2•CuAl/3M). Tests number 5 and 6 (see preceding figure) were not plotted for greater clarity.	118
Figure 5-15 - (d) Total estimated uncertainty on apparent <i>in-situ</i> matrix stress-strain curve of Cu-7wt%Al computed from composite reinforced with 68.6% Nextel 610 fibers (Sample 1-2•CuAl/3M).	119

- Figure 5-16 - (a) Stress-strain curve of Cu-1wt%Ti composite reinforced with 53.9% Fiber FP (Sample 1-2•CuTi/FP) (top graph).
 (b) Corresponding Theta curves for each cycle (bottom graph). Horizontal lines represent $E_f V_f$ (dashed line) and $E_f V_f + \theta_{h,pl} \pm \Delta(E_f V_f + \theta_{h,pl})$. 120
- Figure 5-16 - (c) Apparent *in-situ* matrix stress-strain curve of Cu-1wt%Ti computed from composite reinforced with 53.9% Fiber FP (Sample 1-2•CuTi/FP). Dashed line shows unreinforced matrix tested as reference. 121
- Figure 5-16 - (d) Total estimated uncertainty on apparent *in-situ* matrix stress-strain curve of Cu-1wt%Ti computed from composite reinforced with 52.2% Fiber FP (Sample 1-3•CuTi/FP). 122
- Figure 5-17 - (a) Stress-strain curve of Cu-1wt%Ti composite reinforced with 72.6% Nextel 610 fibers (Sample 1-1•CuTi/3M) (top graph).
 (b) Corresponding Theta curves for each cycle (bottom graph). Horizontal lines represent $E_f V_f$ (dashed line) and $E_f V_f + \theta_{h,pl} \pm \Delta(E_f V_f + \theta_{h,pl})$. 123
- Figure 5-17 - (c) Apparent *in-situ* matrix stress-strain curve of Cu-1wt%Ti computed from composite reinforced with 72.6% Nextel 610 fibers (Sample 1-1•CuTi/3M). Dashed line shows unreinforced matrix tested as reference. 124
- Figure 5-17 - (d) Total estimated uncertainty on apparent *in-situ* matrix stress-strain curve of Cu-1wt%Ti computed from composite reinforced with 72.6% Nextel 610 fibers (Sample 1-1•CuTi/3M). 125
- Figure 5-18 - Fracture surface of Fiber FP reinforced pure aluminum tested at 77 K (Sample 0-4•Al/FP). 127
- Figure 5-19 - Longitudinally split fiber in Fiber FP reinforced pure aluminum tested at 77 K, showing strong interfacial bonding (Sample 0-4•Al/FP). 128
- Figure 5-20 - Fracture surface of Fiber FP reinforced Cu-7wt%Al, showing intermediate interfacial bond strength (Sample 1-1•CuAl/FP). 129
- Figure 5-21 - Fracture surface of Fiber FP reinforced pure copper, showing fiber-matrix debonding (Sample 0-3•Cu/FP). 130
- Figure 5-22 - Fracture surface of Fiber FP reinforced Al-0.9wt%Mg, showing strong interfacial bonding (Sample 2•AlMg/FP). 131
- Figure 5-23 - Detail of fracture surface of Fiber FP reinforced Al-0.9wt%Mg, showing strong interfacial bonding. Fiber FP grains, of average size 0.5 μm , are clearly visible (Sample 2•AlMg/FP). 132
- Figure 5-24 - Fracture surface of Nextel 610 fiber reinforced Cu-1wt%Ti, showing strong interfacial bonding. Note planar character of fiber fracture (Sample 1-1•CuTi/3M). 133
- Figure 6-2 - Longitudinal cross-section of Sample 4-2•Cu/FP ($V_f = 60\%$). The area shown is approximately one fifth of that used to estimate the proportion of broken fibers. 138
- Figure 6-3 - Example of graphical determination of the residual stress from the center of symmetry of an *in-situ* matrix stress-strain tension-compression test (Cu-1wt%Ti matrix from composite reinforced with 53.9% Fiber FP; Initial cycle; Sample 1-2•CuTi/FP). 152

Figure B-1 - Front panel of data acquisition virtual instrument, used to acquire load and strain data in volts, plot stress (MPa) vs. strain (%), and save data in real time (Instron Configuration program, written using the LabVIEW software package).	178
Figure B-2 - Block diagram of data acquisition virtual instrument (Instron Config. vi).	179
Figure B-3 - Front panel of Calibration vi (Part of Instron Config. vi).	180
Figure B-4 - Block diagram of calibration vi (Part of Instron Config. vi).	181
Figures B-5 to B-9 (pages 182 to 186) - Block diagrams of main sub-vi's of Instron Config. vi .	182
Figure C-1 - Front panel of Yield! II data processing program (written in LabVIEW), showing composite stress-strain curve (upper left; broken lines are least-square fits of linear regions), corresponding θ - ϵ graph (lower left), and apparent <i>in-situ</i> matrix σ - ϵ curves (upper right). The latter were computed with $V_f(pyc)=52.2\%$ using the classical (green line) and corrected (blue line) rule of mixtures.	188
Figure C-2- Block diagram of Yield! II data processing program.	189
Figures C-3 to C-7 (pages 191 to 195) - Block diagrams of main sub-vi's of Yield!II data processing program.	191

List of Tables

Table 3-1 - Properties of composite constituents (assumed isotropic) at room temperature	30
Table 3-2 - Bounds on composite modulus (GPa)	31
Table 4-1 - Test bar heat treatment schedules	44
Table 4-2 - Measured constituent densities and corresponding values from the literature	65
Table 4-3- Estimated experimental errors on measured stress and fiber volume fraction V_f	68
Table 4-4 - Orientation dependence of modulus and resulting error in fiber volume fraction	70
Table 4-5 - Etchants	76
Table 5-1 - Results of chemical analyses	78
Table 5-2 - Qualitative measure of fiber/matrix bond strength in composite systems investigated	79
Table 5-3 - Comparison of fiber volume fraction determined from density ($V_f(\rho_{pyc})$) and from matrix dissolution using fiber density ($V_f(\rho_f)$) and matrix density ($V_f(\rho_m)$)	86
Table 5-4 - Matrix elastic slope $\theta_{m,el}$ in the composite and associated experimental uncertainty	93
Table 5-5 - Matrix slope $\theta_{m,pl}$ in stage II and associated experimental uncertainty for aluminum-based matrices (Averages of all measurements; Shaded values are averages for each system; in GPa)	94
Table 5-6 - Matrix slope $\theta_{m,pl}$ in stage II and associated experimental uncertainty for copper-based matrices (Averages of all measurements; Shaded values are averages for each system; in GPa)	95
Table 6-1 - Average tension-compression stress amplitude, in MPa (for given strain amplitude, in %) and corresponding dislocation density in the matrix (with fiber volume fraction in %), computed from Eq. (6.4-1) , page 144	147
Table 6-2 - Apparent <i>in-situ</i> matrix yield stress and residual stress (computed as described in Section 6.6) from stress-strain curves (MPa)	153
Table A- 1 - Elastic moduli and densities used in this work	159
Table A- 2 - Poisson's ratio, coefficient of thermal expansion, and magnitude of Burger's vector	160
Table A- 3 - Stacking fault energies and constants entering Eq (6.4-1), page 145	161
Table A- 4 (a) - Summary of samples tested, with test sequence (<u>T</u> ension or <u>C</u> ompression), and volume fraction determined by pycnometry: aluminum-based systems	162

Table A- 4 (b) - Summary of samples tested, with test sequence (<u>T</u> ension or <u>C</u> ompression), and volume fraction determined by pycnometry: copper-based systems	163
Table A-5 - Summary of all mechanical test results, by system (see next page through p. 176)	163

Acknowledgments

I wish to thank professor Andreas Mortensen for welcoming me into his research group at MIT, for his advice throughout this work, and especially for his help in the final stages of my thesis. Over the course of my studies, he has been both mentor and friend. His wit, enthusiasm, sincere interest in the advancement of my work, as well as his parties, where he frequently displayed his culinary talents and excellent taste in wines, have contributed to making my thesis an enjoyable experience. I also wish to thank the members of my thesis committee, professors Linn Hobbs and Subra Suresh, for the interest they showed in my work and for their many helpful suggestions and comments.

Mechanical tests in liquid nitrogen and tests on pure copper composites would have been difficult to complete without the much appreciated help of Henrik Bjerregård of the Risø National Laboratory in Denmark. Working with him during his one year stay at MIT was a pleasure and gaining his friendship a privilege.

Thanks go to the many UROP students who helped in the lab, and especially to Dorian Balch for his aid in setting up the initial data acquisition system.

The assistance of Maria Wehrle-Due was invaluable and she was sorely missed after her departure. Members of our group, in particular David Dunand, Véronique Michaud, Chris San Marchi, Robert Calhoun, and Elizabeth Earhart, provided much needed advice and support over the years.

I thank Dr. John F. Breedis and co-workers at Olin Metals Research Laboratories for providing custom-cast ingots of copper-based binary alloys, and the 3M and Du Pont de Nemours Corporations for providing the fibers used in this project. Sponsorship of this work by the Office of Naval Research, under the supervision of Dr. Steven Fishman, is gratefully acknowledged.

Finally, I am very grateful to my whole family for their continued support, and especially to my wife Ivka. She was the driving force in my decision to come to the United States and study at MIT, and I would not have completed this thesis were it not for her encouragement, help, and enthusiasm. I also thank our children, Anna and Filip, for all the joy they have brought us.

1. Introduction

“What makes much of the science of materials challenging and interesting is that these three requirements - hardness, stiffness, crack resistance - are mutually incompatible. It is not difficult to have two of them in the same material, but almost impossible to have all three. For example, you can have hardness and stiffness without crack resistance, in fireclay; hardness and crack resistance, without stiffness in rubber; stiffness and crack resistance, without hardness, in brass” [1]. By combining components with different properties, metal matrix composite materials seek to provide an answer to the problem stated above by A. Cottrell: the addition of a stiff and hard reinforcing phase to a ductile metal matrix can result in an overall improvement of these basic mechanical properties when compared to each phase taken separately.

Metal matrix composites have been used on a laboratory scale for several decades but have only recently started to emerge as viable materials in engineering applications. In particular, continuous, aligned ceramic fiber reinforced aluminum composites possess, at any volume fraction of reinforcement, a specific modulus higher than steel, aluminum, and titanium alloys [2, 3]. The specific strength of continuous alumina fiber reinforced composites at volume fractions near 60%, when tested in the longitudinal (fiber) direction, is twice that of high-strength steel and aluminum and titanium alloys; it exceeds the longitudinal specific strength of glass fiber reinforced epoxy, but is below that of graphite/epoxy [3]. Contrary to epoxy matrix composites, alumina fiber reinforced aluminum composites have adequate transverse properties, with a transverse specific strength comparable to steel and a transverse specific modulus approximately double that of steel, aluminum, and titanium [3]. Continuous fiber reinforced aluminum composites are currently being developed for casting of a variety of structural components [3].

Several approaches have been developed towards the prediction of the mechanical behavior of metal matrix composites. These include mean field methods, finite element calculations, and various mechanical analyses of simple elementary metal/reinforcement geometries. Using these methods, prediction of

the response to applied stress of metal matrix composites can now be made reliably for a variety of microstructure types and configurations, by assimilating each phase to a continuum of known rheological behavior.

The utility of modeling tools, and our general understanding of reinforced metal mechanical behavior, remain nonetheless limited by a lack of knowledge of the *in-situ* mechanical response of each phase present, particularly the elastoplastic matrix. In many metals, whether pure or alloyed, microstructural features which govern plastic flow (such as cells, twins or dislocation tangles) span several micrometers and are, hence, on the same size scale as reinforcements commonly used to produce composites. It is therefore a realistic expectation that a reinforcement could cause the plastic flow mechanisms and *in-situ* rheology to differ between the unreinforced metal and the same metal in the composite. One of the best known examples of such an influence of the reinforcement on matrix plastic flow is found in the copper-tungsten system: tungsten fibers 20 μm or less in diameter have been documented to raise the apparent work hardening rate of pure copper to spectacularly high values, which approach its elastic modulus and depend both on fiber diameter and fiber volume fraction [4-7]. The plastic flow stress of the matrix in a composite can, thus, differ from that of an unreinforced matrix which has the same composition, is processed identically, and experiences the same prior strain history.

The objective of the present work is to address this question experimentally, by measuring the *in-situ* flow stress of metallurgically simple metals, reinforced with a high volume fraction of continuous alumina fibers 10 to 20 μm in diameter. This reinforcement size scale is typical of current reinforcing phases used in the production of aluminum matrix composites. The sample configuration, continuous fiber reinforced composites tested in the direction of the aligned fibers, is such that the rule of mixtures remains valid and can be used, after taking into account Poisson's ratio effects, to compute the matrix contribution to the overall composite stress (see Section 2.2, page 18, and Section 3, page 29). The reinforcing phase, fine-grained polycrystalline alumina fibers, was also chosen for microstructural and mechanical simplicity: these fibers (3M Nextel 610™ and

Dupont Fiber FP™) remain elastic, and feature isotropic elastic properties, being fine-grained and relatively free of texture.

More specifically, matrices explored in this work are pure aluminum, Al-0.9wt%Mg, Al-4.5wt%Cu, pure copper, Cu-1wt%Ti, Cu-7wt%Al at room temperature, and pure aluminum at 77 K. The first matrix, reinforced with alumina fibers, was studied at room temperature by Isaacs [8]. The choice of Al-4.5wt%Cu enabled the continuation of this work and its extension to a material of higher engineering significance, which could be heat treated. While the bond between Cu and alumina was much weaker than in the case of Al or Al-4.5wt%Cu, the study of copper composites allowed a direct comparison with the behavior of tungsten filament reinforced copper. The choice of Al-Mg was motivated by the fact that magnesium reduces the ease of cross-slip in aluminum, bringing it closer to that within copper. It is one of the factors believed to increase the rate of work-hardening. Cu-Al and Cu-Ti were used in an effort to improve the strength of the copper-alumina bond while further decreasing the stacking-fault energy of Cu. The microstructures of Cu-7wt%Al and Cu-1wt%Ti alloys are also well documented in the literature. All binary alloy compositions were chosen in order to be close to the solubility limit of the alloying element while remaining in a single-phase region of the phase diagram. In the case of Al-4.5wt%Cu and Cu-1wt%Ti, the second phase was put into solution by heat treatment.

Previous work on the materials explored here, as well as their mechanical behavior are discussed in Chapter 2, with an accent on theories proposed to explain unexpected rates of work-hardening measured in the matrix of tungsten fiber reinforced copper. The method used to derive the apparent *in-situ* matrix stress-strain curve is then discussed in Chapter 3, while experimental methods and the accompanying sources of uncertainty are presented in detail in Chapter 4. Results, from both monotonic and tension/compression tests at room temperature, as well as cryogenic temperature for Fiber FP reinforced aluminum, are given in Chapter 5 and discussed in Chapter 6. Conclusions are followed by a description of the data acquisition and analysis in the Appendices.

2. Background / Literature Review

2.1 Nature and Processing of Metal Matrix Composites

A metal matrix composite is a combination of at least two chemically distinct phases: a strong, generally brittle reinforcement which can have various geometries, from particles or whiskers to short or continuous fibers, and a soft, ductile metal matrix, which holds together and protects the reinforcement. Composites are man-made materials in the sense that they do not form spontaneously. Their fabrication techniques include solid-state methods, deposition processes, and solidification processes.

In the solid state, composites can be produced by powder consolidation or diffusion bonding, using cold or hot isostatic pressing. These methods are best applied to discontinuously reinforced composites, where high pressures and/or post-processing such as extrusion or rolling can be used to optimize microstructure and mechanical properties, and where the reinforcement volume fraction is relatively low. Solid-state bonding is also used following matrix deposition (*e.g.*, by electrolytic techniques) on the reinforcement. Such a technique can be used, in particular, to produce continuous fiber reinforced composites with very uniform reinforcement distribution [5].

The preferred method for fabrication of most composites is often via liquid-state processing, in which conventional casting techniques can be used to produce composites of net, or near-net, shape [9, 10]. The reinforcement can be incorporated by stirring into the molten metal or by infiltration of a preform. Other liquid-state processes include spray deposition and *in-situ* processes. Wetting of ceramic reinforcements by molten metal is generally difficult and requires application of an external force, *e.g.* squeeze-casting or infiltration under pressure.

Solidification of the matrix is directly influenced by the presence of the reinforcement [9, 11, 12]. Matrix grain size refinement may occur at high applied pressures or when the reinforcement catalyzes matrix nucleation. In multiphase

alloys, the last phase to solidify is often rejected and forms clusters in the vicinity of the reinforcement, notably in matrices of Al-4.5wt%Cu.

Since matrix and fiber generally possess different coefficients of thermal expansion, cooling from liquid-state processing temperatures results in the generation of thermal residual stresses in the matrix. Plastic relaxation of these stresses has been shown to cause a marked increase in the dislocation density of the matrix [13-24]. Mechanisms of dislocation emission from the reinforcement have been shown to include dislocation punching from the reinforcement surface. However, dislocation structures generated by this effect are generally found to be complex, leading to a variety of microstructures, and in some cases featuring inhomogeneous dislocation distributions within the metal. For example, dislocations may be concentrated near the reinforcement or in cell walls. Another feature of the relaxation of thermal strains by dislocation emission is that dislocation densities resulting from the process can be significantly higher than would be expected, based on simple estimates of the geometrically necessary dislocation density required to compensate for the differential shrinkage between matrix and reinforcement [15, 24]. Although some mechanisms which could lead to an increase in the density of punched dislocations have been proposed [24], causes for this phenomenon are still mostly unknown.

2.2 Mechanics of Fiber Reinforced Metals

Several methods have been used to predict the mechanical behavior of reinforced metals, among which are mean field methods, finite element calculations, and diverse analyses of elementary metal/reinforcement geometries.

Mean field calculations use elastic models adapted to treat metal plasticity, generally by considering that plastic strains are equivalent to a uniform transformation strain. Analysis is often based on Eshelby's treatment of the elastic ellipsoidal inclusion having undergone a transformation strain and/or subjected to external stress in an infinite, elastic solid. To include the effects of a high volume fraction of reinforcing phases typically found in metal matrix composites, averaging

assumptions, such as that of self-consistency, have to be made to account for mechanical interaction between reinforcement elements. Many research groups have used this approach to study composite mechanical behavior [6, 15, 25-35].

Compared to the other two model classes, mean field models have the advantages of algebraic neatness, and of avoiding describing the composite microstructure as a repetition of unit cells of varying simplicity; however, these models remain essentially based on an elastic treatment of the matrix, which can produce unrealistic results on a microscopic level.

These shortcomings have been eliminated in a large number of finite element studies of matrix plastic flow in reinforced metals, reviewed in several recent publications [35-38]. In finite element analyses, the matrix is described using conventional assumptions of continuum plasticity: power law hardening or bilinear stress-strain curves, and using in most cases isotropic Von Mises or Tresca yield criteria. This extensive research effort has brought to light the importance of matrix plastic flow inhomogeneity in the deformation of reinforced metals: in composites having a discontinuous reinforcement, and also in continuous fiber reinforced composites stressed other than along their fibers, the matrix stress-strain state varies greatly with location inside the composite. This does not preclude back-calculation of matrix *in-situ* flow curves from composite mechanical data, if it is assumed that the high stress/strain gradients predicted by the calculations do indeed exist in the matrix (*e.g.*, as done in [39]). However, predicted strain gradients become steep when the reinforcement size is on the order of a few micrometers, in which case the use of standard continuum mechanics to analyze plastic flow in the matrix becomes questionable.

Finite element models show that elastoplastic micromechanical analysis is very complex for most composites (see part III of [40]), except when the phases of a composite deform in parallel. Therefore, in the systems considered here, where the external stress is applied in the direction of the continuous aligned fiber reinforcement, the problem of complex analysis is avoided from both mechanical and physical standpoints. The first reason is that at the small strains typically encountered in metal matrix composites, the rule of mixtures can be used without

ambiguity to calculate the *average* matrix flow stress [6, 7, 41, 42]. The second reason is that, with parallel fiber composites tested longitudinally, composite straining does not introduce inhomogeneities in the matrix stress/strain state other than those initially present due to thermal contraction effects [35, 43-45]. Therefore, although internal stresses due to cooling after processing can introduce stress and strain gradients within the matrix of the as-produced composite [46], the build-up of plastic strain gradients near strain concentration sites such as fiber ends is minimized in this configuration during composite deformation. Since the average strain in both phases is necessarily equal, due to little variation of strain within each phase, both the elastic and inelastic behavior of the composite can hence be predicted with reasonable precision by assuming that each phase contributes a stress equal to that which would be required for it to be deformed homogeneously to the composite strain ϵ_c :

$$\epsilon_c = \epsilon_f = \epsilon_m \quad , \quad (2.2-1)$$

with indices c , f , and m denoting respectively composite, fiber, and matrix. From stress equilibrium:

$$\sigma_c = \sigma_f V_f + \sigma_m (1 - V_f) \quad , \quad (2.2-2)$$

where V_f is the fiber volume fraction, and all stresses correspond to $\epsilon = \epsilon_i$ in each phase. Using Hooke's law $\sigma = E\epsilon$ for the individual constituents, it follows from Eqs. (2.2-1) and (2.2-2) that when both phases are elastic:

$$E_c = E_f V_f + E_m (1 - V_f) \quad . \quad (2.2-3)$$

Equations (2.2-2) and (2.2-3) are the equistrain rule of mixtures expressions for the composite's stress and Young's modulus, respectively.

Equation (2.2-3) is strictly valid only when the lateral contraction of all phases is equal, requiring $\nu_f = \nu_m$ in the elastic regime, because it does not account for the influence of transverse stresses in each phase. Hill [41] derived general expressions for E_c as a function of V_f and phase properties and showed that E_c always exceeds Eq. (2.2-3) when $\nu_f \neq \nu_m$. In a related paper [42], Hill also derived bounds for the

instantaneous composite modulus at any stage of deformation. Hill's bounds are used in this work to derive matrix *in-situ* stress-strain curves, and are discussed in detail in Section 3.1.

2.3 Composite Stress-Strain Curve

The stress-strain curve of a continuous fiber metal matrix composite deformed uniaxially along the fiber direction is commonly divided into three consecutive regions which correspond to different stages of deformation: Stage I, where both metal and fiber behave elastically; Stage II, where the matrix deforms plastically while the fibers are still elastic; and Stage III, in which both matrix and fibers deform plastically (see *e.g.*, page 42 of [15]). Most continuous fiber metal matrix composites exhibit at least Stages I and II. Stage III is absent when the fibers do not exhibit plastic behavior, as is the case with alumina fibers in the present study.

If the matrix has a larger coefficient of thermal expansion than the fiber, it is under residual tensile stress at zero applied composite stress as a result of cooling from the composite's processing temperature. The magnitude of this stress depends on the volume fraction of reinforcement and on the cooling rate. In the case of Ref. [24], the matrix of alumina fiber-reinforced pure aluminum composites, annealed and water quenched prior to mechanical testing, was at its yield stress, such that Stage I was essentially absent during tensile composite deformation.

2.4 Plasticity in Reinforced Metals

It has been known for several decades that a metal behaves differently in the presence of a reinforcing phase. This follows first and foremost from the load-bearing role of the reinforcement, and from the generally highly inhomogeneous nature of plastic flow in composites, recently revealed by micromechanical models. Beyond these effects, however, there are clear indications that the *in-situ* flow behavior of the matrix itself is different in the composite.

In a seminal paper [4], Kelly and Lilholt used Eq. (2.2-2) to derive the apparent *in-situ* matrix stress in Stage II of a copper-tungsten composite. Continuous tungsten wires of 10 and 20 μm diameter were used to reinforce a pure single crystal copper matrix, produced by spontaneous infiltration (molten copper wets tungsten) followed by directional solidification. Despite scatter and rather large uncertainties in their experimental data, Kelly and Lilholt measured work-hardening rates which are 10 to 100 times higher in the matrix of the composite than in the matrix tested alone (see Figure 2-1). The values of the slope of the composite stress-strain curves in Stage II for a variety of volume fractions ($4\% \leq V_f \leq 38\%$) exceed Hill's upper bound, *i.e.*, are higher than the highest predicted rates of work-hardening of fiber reinforced composites [47]. The *in-situ* matrix stress-strain curves drop after about 0.4% strain when the fibers start to deform plastically. An additional remarkable feature found in these data is an apparent scale effect of the reinforcement: the derived *in-situ* matrix stress-strain curves depend on the size of the reinforcing fibers. No such size dependence is predicted by continuum mechanical models.

Kelly and Lilholt's observations are not isolated. Lee and Harris [5] showed positive deviations from the rule of mixtures in polycrystalline copper reinforced with continuous tungsten wires of diameter from 11 to 48 μm , with a volume fraction of 37% (see Figure 2-2). Their fabrication procedure (electroplating of copper onto the wires to form sheets which were subsequently vacuum hot-pressed) produced excellent fiber distribution, apparently much more uniform than that of Kelly and Lilholt's samples. In their tensile tests, the matrix rate of work-hardening increased with decreasing fiber diameter, and featured a somewhat less clearly linear Stage II region than in Kelly and Lilholt's composites. In cyclic tests the matrix rate of work hardening was independent of reinforcement size and higher than in the monotonic case. These authors do not observe a drop in matrix stress in stage III, and explain the extended work-hardening in terms of a Hall-Petch relationship using a postulated 0.5 μm cell size substructure in the cyclic tests instead of the (1.5 to 7 μm) observed grain size.

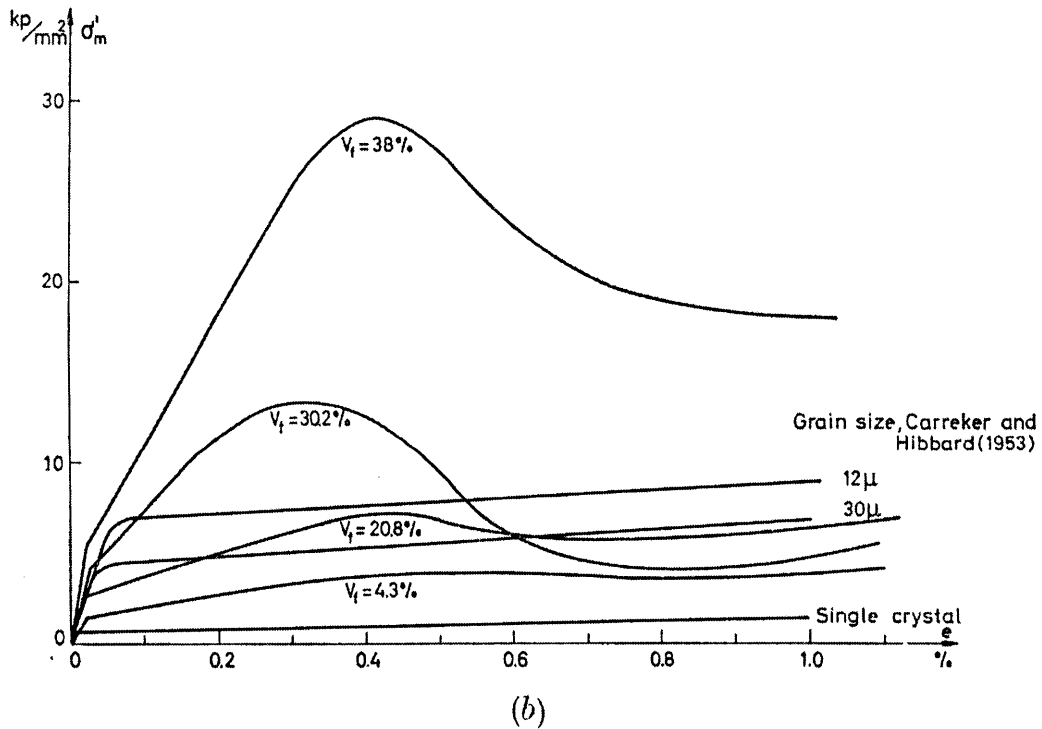
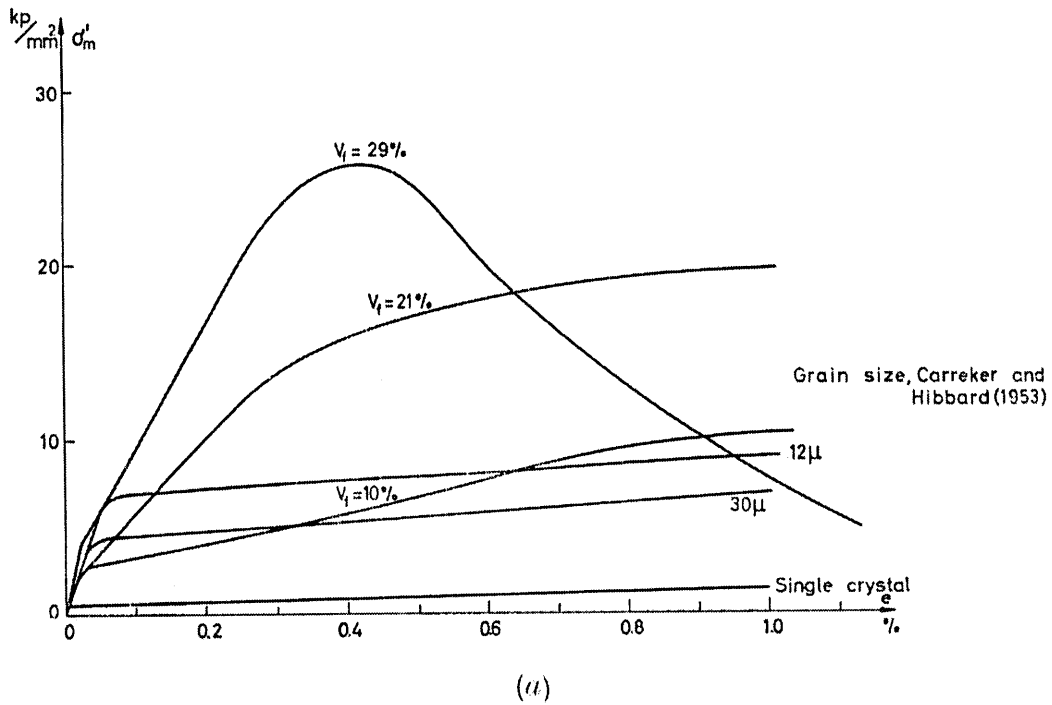


Figure 2-1 - Derived stress-strain curves of the copper matrix in composites reinforced with (a) 10 μm and (b) 20 μm tungsten fibers, produced by vacuum infiltration. The volume fraction of fibers is given for each curve. Single crystal and polycrystalline unreinforced copper curves are also shown (Fig. 5 from [4]).

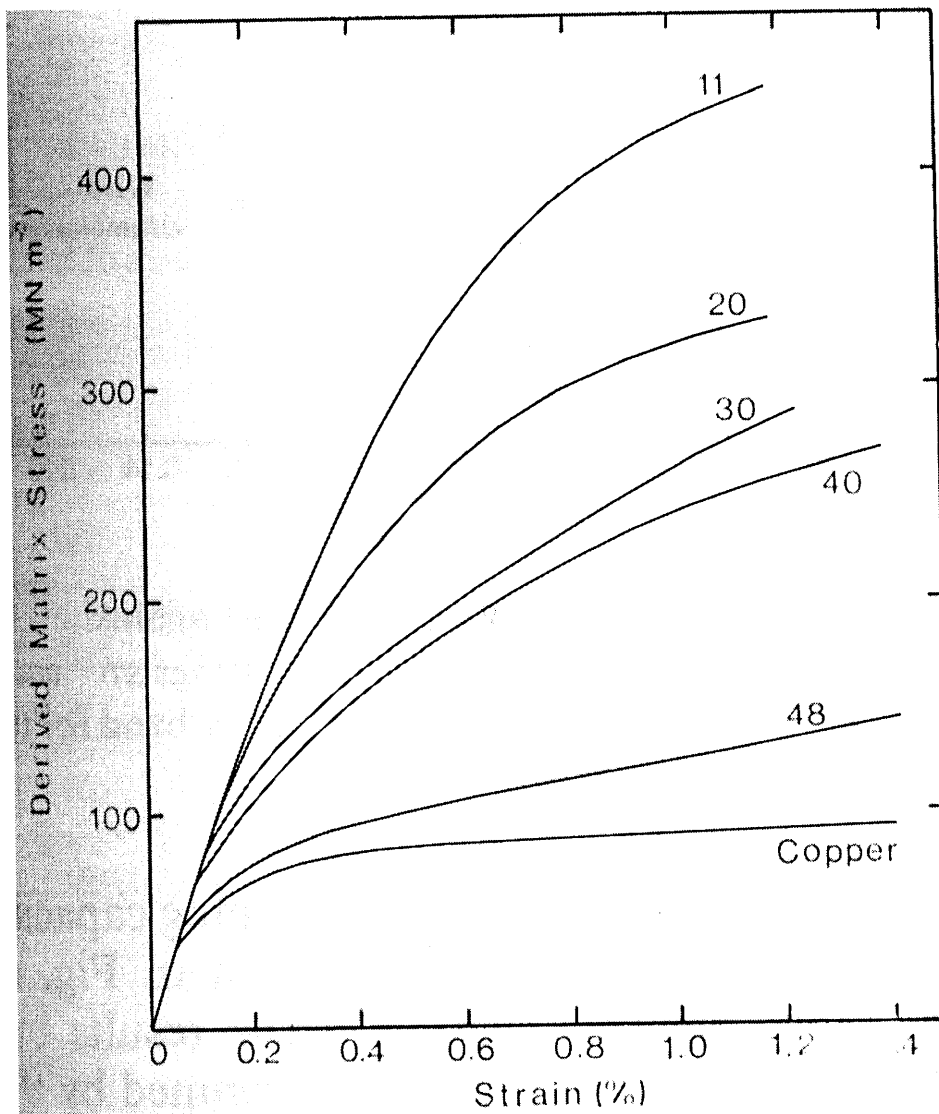


Figure 2-2 - Derived stress-strain curves of the copper matrix in composites reinforced with 37% tungsten fibers, produced by electrodeposition and hot-pressing. The numbers shown correspond to fiber diameters, in μm , with as-pressed unreinforced copper plotted for comparison (Fig. 4 from [5]).

Other examples of dependence on reinforcement size of the composite flow stress in fibrous metal matrix composites are found in pearlitic steel [48], *in-situ* eutectic composites [49, 50], or heavily deformed metal reinforced copper composites [51, 52]; however, these composites feature far finer reinforcements, and are extensively work hardened compared with Kelly and Lillholt's composites, which

resemble current cast fiber reinforced metal composites in their processing history and microstructural scale. Particle reinforced metals [16, 53] also display a dependence of their mechanical behavior on particle size, which is usually attributed to an increase in dislocation punching during cooldown from processing temperature as the reinforcement size decreases.

Although unusually high rates of work-hardening were also reported in copper reinforced with larger fibers (Chawla and Metzger in copper reinforced with 15% tungsten wire of 230 μm diameter [54]; Trybus *et. al.* in copper reinforced with Nb filaments of diameter near 150 μm , $V_f \leq 20\%$ [55]) it seems likely, given the dependence of data on fiber diameter, that the effect reported by Kelly and Lilholt is essentially due to dislocation-fiber interactions which occur when the size of the reinforcement is small enough, typically below 50 μm . Indeed, experiments on large fiber metal matrix composites show no such effect, *e.g.*, Kelly and Tyson [56] (200 and 500 μm diameter tungsten wires and 200 μm molybdenum wires in copper); McDanel *et. al.* [57] (75, 125, and 150 μm diameter tungsten wires in copper); or Cheskis and Heckel [58] (125 and 250 μm tungsten wire and 100 μm boron wire in 2024 aluminum; in this work the *in-situ* deformation behavior of matrix and fiber were measured using X-ray diffraction techniques, to find good agreement with the rule of mixtures). Such an influence of fibers on dislocation creation and motion can be rationalized because metal plastic deformation is a function of microstructural and substructural features (precipitates, cells, ...) which have finite dimensions (typically of a few micrometers) on a par with the spacing between neighboring reinforcement phases and/or their dimensions.

There has been significant research specifically aimed at understanding the influence exerted by the reinforcement on the plastic flow of reinforced metals. Several of these studies are primarily focused on the influence of differential thermal contraction on the initial substructure of the matrix [16, 59-62]. Other efforts, concentrating more generally on the physical metallurgy of reinforced metal plasticity, include studies of highly deformed reinforced copper composites [51, 52], of the copper-tungsten system [6], and of reinforced aluminum composites [39]. This

work, however, has never been applied to explain the observations by Kelly and Lilholt, for which specific and varying theories have been proposed.

2.5 Proposed Theories of Matrix Work-Hardening

Kelly and Lilholt's explanation of their data relies on the constraints arising from the difference in Poisson's ratio of the two phases. They postulate, with no physical explanation, that a certain volume of copper remains elastic in Stage II of their experiments. For the experimental values to agree with Hill's bounds, the amount of copper which would have to remain elastic is equivalent to a 2 μm ring around each fiber in the 10 μm fiber composite and a 3 μm ring in the 20 μm fiber composite.

Other explanations of the "Kelly & Lilholt Effect" have been proposed. Tanaka and Mori [25] used macroscopic laws for plastic flow and an adaptation of the rule of mixtures. Their analysis did yield higher rates of apparent matrix work hardening than is predicted by the rule of mixture or Hill's bounds. However, the disagreement with Hill's bounds was not explained, and the analysis being based on continuum mechanics does not account for the observed influence of fiber diameter on matrix work hardening rate. Neumann and Haasen [63] proposed a model assuming formation within the matrix of a system of parallel dislocation pile-ups between fibers, at a 45° angle to the fibers, with the slip planes spacing as the only adjustable parameter. They claim good agreement with Kelly and Lilholt's results. However, no microscopic evidence appears to exist on the copper-tungsten fiber system to confirm their model. Furthermore, Kelly and Lilholt [4] clearly dismiss an explanation based on dislocation pile-ups as follows: pile-ups at the fiber-matrix interface are not necessary because the longitudinal strains in both phases are equal (*cf.* Eq. (2.2-1)), and furthermore stress concentrations in the fibers arising from pile-ups would weaken the fibers in the composite, which was not observed since a plot of the ultimate tensile strength of the composite versus V_f follows the rule of mixtures.

A frequently encountered explanation is the "Source-Shortening" theory of Brown and coworkers [27, 28, 64-66]. The flow stress of the composite in stage II is written as

$$\sigma_c = \sigma_{for} + \sigma_{Or} + \sigma_{ss} + \langle \sigma \rangle_M , \quad (2.5-1)$$

where σ_{for} is the forest hardening contribution, which depends upon the strain history of the composite and cannot be evaluated from first principles [28]; σ_{Or} is the Orowan stress or initial passage stress of a dislocation through obstacles; σ_{ss} is the source-shortening stress, and $\langle \sigma \rangle_M$ the mean matrix stress.

The Orowan stress

$$\sigma_{Or} \approx \frac{G_m b}{\lambda_0} , \quad (2.5-2)$$

with G_m and b the shear modulus and Burgers vector of the matrix and λ_0 the spacing between fibers in the slip plane, is independent of strain and negligible [28] in the copper-tungsten composites under discussion.

The source-shortening stress is estimated in [28] from a calculation based on Eshelby's inclusion method as

$$\sigma_{ss} \approx \frac{5}{2\pi} V_f K G_f \varepsilon_p , \quad (2.5-3)$$

with ε_p the plastic strain and K a factor dependent on the shear moduli and Poisson's ratios of the composite's phases and on the orientation of the fibers relative to the slip direction. σ_{ss} is the strain dependent analog of the Orowan stress. It is created by the local fluctuating stresses of zero mean value [27], and reflects the fact that as deformation progresses, it becomes more and more difficult for dislocations to bow out between fibers because Orowan loops left behind by previous dislocations act to decrease the effective distance between obstacles.

The mean stress or back stress is the derivative of the elastic energy density in the composite with respect to the plastic strain [28]. It can be determined experimentally

as half of the permanent softening in a Bauschinger test [64, 67-70]. $\langle\sigma\rangle_M$ is the minimum work-hardening which a dispersion-hardened alloy can sustain.

Brown and Clarke calculate that about two thirds of the total work-hardening come from $\langle\sigma\rangle_M$ and about one third from σ_{SS} . The source-shortening contribution is essentially the amount of work-hardening in excess of Hill's upper bound. It is qualitatively comparable to Kelly and Lilholt's postulate of an elastic region around fibers which is impenetrable to dislocations [28].

Brown and Clarke's explanation does not appear to address the scale effect specifically; however, it does consider the obstacle spacing, which is a function of V_f and fiber radius. Furthermore their derivation is restricted to cases where no plastic relaxation occurs around the reinforcement, *i.e.*, to low strains and low temperature of test. Stoltz and Pelloux [70], in their study of the Bauschinger effect in precipitation strengthened aluminum alloys, obtain work-hardening rates below those predicted by the above theory, which they attribute to plastic relaxation around the precipitates and inhomogeneous deformation in their polycrystals. Yet the strain range ($\pm 0.15\%$) is not significantly larger than in Kelly and Lilholt's Cu-W experiments and both were done at room temperature. Hence the theory requires that relaxation be impossible around fibers. This has been rationalized by Kelly [71] for simple Orowan loops around fibers sufficiently fine to cause Orowan strengthening. However, Kelly and Lilholt's W fibers are far larger in diameter (10 to 20 μm) than particles for which Orowan loops and Orowan loop relaxation have been observed.

3. Matrix *in-situ* Stress-Strain Derivation

3.1 Mechanical Analysis: Hill's Bounds

Bounds for the modulus of a longitudinal fiber reinforced composite in which both fiber and matrix are elastic were derived by Hill [41] in the form of limits for the positive deviation of the composite modulus from the rule of mixtures:

$$\frac{4V_f V_m (v_f - v_m)^2}{\left(\frac{V_f}{k_m^p} + \frac{V_m}{k_f^p} + \frac{1}{G_m}\right)} \leq (E_c - E_f V_f - E_m V_m) \leq \frac{4V_f V_m (v_f - v_m)^2}{\left(\frac{V_f}{k_m^p} + \frac{V_m}{k_f^p} + \frac{1}{G_f}\right)}, \quad (3.1-1)$$

where c, f, and m refer to the composite, matrix, and fiber, respectively, V is the volume fraction, v Poisson's ration, k^p the plane strain bulk modulus for lateral dilatation without longitudinal extension, and G the shear modulus. If the composite constituents are assumed isotropic, k^p and G can be computed from E and v as:

$$k^p = \frac{E}{2(1+\nu)(1-2\nu)} \quad \text{and} \quad G = \frac{E}{2(1+\nu)}. \quad (3.1-2)$$

These bounds were each shown to correspond to the modulus of a composite element made of a cylindrical fiber of one phase surrounded by a uniform shell of the other: hence, these bounds are the best possible.

The bounds in Eq. (3.1-1) were also shown to remain valid for the composite instantaneous modulus in the plastic regime of matrix deformation, under the assumption that all phase moduli are constant within each phase and depend only on strain [42]. In the limiting case where the matrix does not harden, i.e. $E_m = 0$ and $v_m = 0.5$, Eq. (3.1-1) reduces to

$$\frac{V_f V_m (1-2v_f)^2}{\left(\frac{V_f}{K_m} + \frac{V_m}{k_f^p} + \frac{1}{G_m}\right)} \leq (E_c - E_f V_f) \leq \frac{V_f V_m (1-2v_f)^2}{\left(\frac{V_f}{K_m} + \frac{V_m}{k_f^p} + \frac{1}{G_f}\right)}, \quad (3.1-3)$$

where the matrix bulk modulus $K_m = \frac{E_m}{3(1-2\nu_m)}$ and all phase moduli (Eq. (3.1-2)) retain their elastic values [42].

Hill's bounds thus state that, in both the elastic and the elastoplastic regimes, there is a finite and bounded positive deviation in the composite stress-strain curve compared with that predicted by the rule of mixtures. The fact that the composite stress-strain curve always deviates above the curve predicted by the equistrain rule of mixtures results from the build-up of additional stresses due to lateral contraction mismatch between the two deforming phases.

The possible range of variation in instantaneous composite modulus therefore depends on the difference between matrix and fiber instantaneous Poisson's ratio, as reflected in Eq. (3.1-1). As plastic deformation appears in the matrix, the apparent Poisson's ratio increases from about 1/3 to 1/2, and the positive deviation in the range of composite stress-strain behavior above the rule of mixtures therefore

Table 3-1 - Properties of composite constituents (assumed isotropic) at room temperature

Material	Poisson ratio ν	Elastic modulus E (GPa)	Shear modulus G (GPa)	Bulk modulus K (GPa)	Bulk modulus in plane strain k^p (GPa)
Alumina	0.23 * 0.25 □	379 ‡	153 ◇	243 ◇	294 ◇
Aluminum	0.345 †	70	26.1 † 26.0 ◇	75 ◇	84 ◇
Copper	0.343 †	115	48.3 † 43 ◇	122 ◇	136 ◇

* Courtney [72, p.48]

† Hertzberg [73, p.7]

‡ see Section 4.1.1, page 36

□ Galasso [74, p.156]

◇ computed using Eqs. (3.1-2) and (3.1-3)

increases. Since the instantaneous value of matrix Poisson's ratio is maximum (and equal to 1/2) when the matrix instantaneous rate of work hardening is zero, the bounds on the difference between the composite rate of work hardening and that predicted by the rule of mixtures both increase to their maximum possible values in that case.

Table 3-2 - Bounds on composite modulus (GPa)

System	Al/Al ₂ O ₃	Cu/Al ₂ O ₃
<u>Elastic Matrix</u>	$v_m=0.345$	$v_m=0.343$
$V_f=30\%$	$0.21 \leq (E_c - E_f V_f - E_m V_m) \leq 0.74$	$0.32 \leq (E_c - E_f V_f - E_m V_m) \leq 0.80$
$V_f=50\%$	$0.24 \leq (E_c - E_f V_f - E_m V_m) \leq 0.78$	$0.37 \leq (E_c - E_f V_f - E_m V_m) \leq 0.89$
$V_f=70\%$	$0.19 \leq (E_c - E_f V_f - E_m V_m) \leq 0.58$	$0.30 \leq (E_c - E_f V_f - E_m V_m) \leq 0.70$
<u>Plastic Matrix</u>	$v_m=0.5$	$v_m=0.5$
$V_f=30\%$	$1.3 \leq (E_c - E_f V_f) \leq 4.4$	$2.0 \leq (E_c - E_f V_f) \leq 5.0$
$V_f=50\%$	$1.4 \leq (E_c - E_f V_f) \leq 4.5$	$2.3 \leq (E_c - E_f V_f) \leq 5.5$
$V_f=70\%$	$1.2 \leq (E_c - E_f V_f) \leq 3.4$	$1.9 \leq (E_c - E_f V_f) \leq 4.3$

Bounds computed from Eq. (3.1-1) and Eq. (3.1-3) for composites investigated in this work are presented in Table 3-2 for both the elastic and perfectly plastic matrix deformation regimes. It is seen that bounds on the positive deviation of the composite modulus in the elastic regime are quite close. Comparatively, in the plastic deformation regime of the matrix, Hill's bounds are both further apart, and higher in value. It is also seen in Table 3-2 that, for systems of present interest, the range of possible deviation between the rule of mixtures and the rigorously

predicted matrix stress-strain curve is relatively independent of fiber volume fraction. Near 50% fiber, this deviation is on the order of 3.0 ± 1.5 GPa for aluminum-based matrix composites, and 4.0 ± 1.5 GPa for copper-based matrix composites.

To derive the matrix *in-situ* stress-strain curve knowing that of the composite, therefore, different bounds and formulae apply in the elastic and in the plastic regimes. In the elastic regime, the rule of mixtures applies with relatively good precision. In the plastic regime, after sufficient plastic elongation has occurred that the elastic strain is negligible, provided the matrix rate of work hardening is not very high, perfectly plastic bounds for deviations of composite instantaneous apparent moduli, given in Table 3-2, are seen to be non-negligible. In other words, lateral contraction stresses create a small, but finite, deviation in composite stress at given strain above the rule of mixtures, which must be taken into account in back-calculating the matrix stress-strain curve from that of the composite.

3.2 Determination of Apparent *in-situ* Matrix Rate of Work Hardening and Flow Curves

Using Hill's formulae, the composite instantaneous stress-strain curve slope θ_c can thus be expressed by rewriting the rule of mixtures as:

$$\theta_c = E_f V_f + \theta_m (1 - V_f) + \theta_h , \quad (3.2-1)$$

where θ_h is the increase in composite slope due to lateral contraction mismatch, bounded by Hill's expressions in (Eqs. (3.1-1) and (3.1-3)). The slope at any point of the matrix curve can therefore be computed from that of the composite as:

$$\theta_m = \frac{\theta_c - E_f V_f - \theta_h}{1 - V_f} . \quad (3.2-2)$$

When matrix deformation is predominantly plastic, for systems of present interest, θ_h is roughly equal to:

$$\theta_{h,pl} \approx \begin{cases} 3.0 \pm 1.5 \text{ GPa} & (\text{Al}/\text{Al}_2\text{O}_3) \\ 4.0 \pm 1.5 \text{ GPa} & (\text{Cu}/\text{Al}_2\text{O}_3) \end{cases} . \quad (3.2-3)$$

On the other hand, when matrix deformation is predominantly elastic, θ_h falls to much smaller values, and the rule of mixtures applies with better precision:

$$\theta_{h,el} \approx \begin{cases} 0.5 \pm 0.3 \text{ GPa} & (\text{Al}/\text{Al}_2\text{O}_3) \\ 0.6 \pm 0.3 \text{ GPa} & (\text{Cu}/\text{Al}_2\text{O}_3) \end{cases} . \quad (3.2-4)$$

If we decompose the total matrix strain into a plastic and an elastic component, by integration of Hill's expressions for the instantaneous composite apparent modulus in each deformation regime, the composite stress can be estimated from that of its components using the formula:

$$\sigma_c = E_f V_f \varepsilon + (1 - V_f) \sigma_m + \theta_{h,el} \varepsilon_{el} + \theta_{h,pl} \varepsilon_{pl} , \quad (3.2-5)$$

where θ_i and ε_i are the positive deviation in composite rate of work hardening and strain, respectively; ε_{el} and ε_{pl} indicate total elastic and plastic strain, respectively. The apparent *in-situ* matrix stress σ_m at given composite total strain ε can then be calculated from the composite stress as:

$$\sigma_m = \frac{\sigma_c - E_f V_f \varepsilon - \theta_{h,el} \varepsilon_{el} - \theta_{h,pl} \varepsilon_{pl}}{1 - V_f} . \quad (3.2-6)$$

In samples tested here, matrix deformation is predominantly plastic. Furthermore, $\theta_{h,el}$ is small compared with $\theta_{h,pl}$ and with experimental error arising from other sources. Hence, $\theta_{h,el} \varepsilon_{el}$ can be neglected in calculating σ_m :

$$\sigma_m = \frac{\sigma_c - (E_f V_f + \theta_{h,pl}) \varepsilon}{1 - V_f} , \quad (3.2-7)$$

which eases computation of *in-situ* curves without introducing significant error.

We thus derive in what follows the matrix *in-situ* stress-strain curve from experimental composite curves using Eq. (3.2-7) and by applying Hill's bounds for the upward deviation in composite stress from the rule of mixtures, evaluated for a

perfectly plastic matrix throughout composite deformation. This, in turn, creates a decrease in the derived value of composite stress compared with that which would have been obtained using the rule of mixtures, as was done by Kelly and Lillholt [4], and other researchers [5]. This deviation is not large, but both θ_{pl} and the uncertainty on the proper value of θ_{pl} , $\Delta\theta_{pl}$, are, in our experiments, on the order of experimental error and, hence, must be taken into account.

3.3 Uncertainty in Derived Matrix *in-situ* Stress-Strain Curves

For all measured quantities x_1, x_2, \dots, x_n , the corresponding uncertainties $\Delta x_1, \Delta x_2, \dots, \Delta x_n$ were estimated as described in Section 4. The uncertainty Δf , on a function $f(x_1, x_2, \dots, x_n)$ computed from these variables was then calculated using:

$$\Delta f = \left| \frac{\partial f}{\partial x_1} \right| \Delta x_1 + \left| \frac{\partial f}{\partial x_2} \right| \Delta x_2 + \dots + \left| \frac{\partial f}{\partial x_n} \right| \Delta x_n, \quad (3.3-1)$$

which gives an upper bound on Δf [75].

Applying this method to Eq. (3.2-2), we obtain the experimental error $\Delta\theta_m$ on the slope at any point of the matrix curve due to error on measurements of V_f and uncertainty in E_f and θ :

$$\Delta\theta_m = \frac{\Delta\theta_c + V_f\Delta E_f + \Delta\theta_h}{1 - V_f} + \frac{|\theta_c - E_f - \theta_h|}{(1 - V_f)^2} \Delta V_f, \quad (3.3-2)$$

where the variation of θ_h with E_f and V_f has been neglected.

Similarly, the experimental error on σ_m is:

$$\Delta\sigma_m = \frac{\Delta\sigma_c + |E_f V_f + \theta_{h,pl}| \Delta\varepsilon + |\varepsilon| (V_f \Delta E_f + \Delta\theta_{h,pl})}{1 - V_f} + \frac{|\sigma_c - \varepsilon (E_f + \theta_{h,pl})|}{(1 - V_f)^2} \Delta V_f. \quad (3.3-3)$$

The most important sources of experimental error in calculating the apparent matrix *in-situ* rate of work hardening or flow stress are the uncertainty in the fiber volume fraction V_f and the fiber modulus E_f .

Experimental errors on σ_c and on V_f are given in Table 4-3, page 68.

4. Experimental Procedures and Error Analysis

4.1 Constituents

4.1.1 Fibers

Fiber FP™ (Type I)[†] continuous polycrystalline 99% pure α -alumina fibers were received from E.I. Du Pont de Nemours & Co. (Wilmington, Delaware). These fibers are produced by textile fiber spinning technology as a yarn containing 210 filaments. The diameter of individual filaments, which have a round cross-section, is 20 μm . The modulus of this fiber is 379 GPa (tensile and compressive) and the average tensile strength 1,380 MPa, which corresponds to a strain to failure of about 0.4% [76, 77]. These fibers are polycrystalline with an average grain size of 0.5 μm (see Figure 5–23, page 132) and no documented texture. Their elastic properties can therefore be considered isotropic. The brittleness of uncoated Fiber FP makes handling difficult and care had to be exercised to minimize fiber breakage during preform preparation.

Nextel 610™ fibers were received from 3M (St Paul, MN). These are over 99% pure polycrystalline continuous α -alumina fibers, with a density of 3.85 g/cm³ and an elastic modulus of 379 GPa^{**}. The grain size of these fibers is in the nm range (see Figure 5–24, page 133), with no known texture; hence, these fibers can also be considered isotropic from the standpoint of their elastic properties. Nextel 610 fibers were delivered in tows of about 400 filaments. Each filament had a round cross-section of diameter 12 μm and a tensile strength (measured at a gage length of 2.5 cm) of 2,300 to 2,600 MPa, with a strain to failure of approximately 0.8%. As for Fiber FP, only pure fibers with no polymer binder were used.

[†] Fibers coated with Si (Fiber FP Type IV) and a polymer binder (Fiber FP Type III) have also been produced by Du Pont. Only the uncoated, pure α -alumina Type I fibers were used here.

^{**} Data provided by 3M. Private communication.

The surface of Nextel 610 fibers is smoother than that of Fiber FP. This, along with their smaller diameter, allows much tighter packing of these fibers in a preform, resulting in fiber volume fractions of the order of 70% for Nextel 610 reinforced composites, compared with about 50% for Fiber FP.

4.1.2 Matrices

Metal matrices chosen for this study were 99.999% pure aluminum, Al-4.5wt%Cu, Al-0.9wt%Mg, 99.996% pure copper, Cu-7wt%Al, and Cu-1wt%Ti. It has been shown that Fiber FP is chemically inert in the presence of Al and Cu [8, 24, 77, 78]. Furthermore, the above mentioned metals were chosen for their mechanical and metallurgical simplicity, and for the extensive literature data related to their properties, heat treatment practice, and characterization.

99.999% pure Al and Al-4.5wt%Cu were provided by ALCOA (Pittsburgh, PA). 99.996% pure copper was purchased from Sambo Copper Alloy Co. (Osaka, Japan). Cu-7wt%Al and Cu-1wt%Ti were cast by Olin Metals Research Laboratories (New Haven, CT). Al-0.9wt%Mg and additional Cu-7wt%Al were cast at MIT expressly for this work from the above-mentioned pure metals and pure Mg. A gas furnace was used for Al-0.9wt%Mg and an induction furnace for Cu-7wt%Al.

4.2 Fabrication of the Composites

4.2.1 Fiber Preform Preparation

Composites were fabricated by pressure casting in apparatus developed and built at MIT. Alumina fibers were typically received wound on bobbins containing 500 grams. The fibers were first aligned and cut to the desired length while being constantly kept wet with distilled water to make the alignment procedure easier and to minimize fiber breakage. The wet fiber bundle was then placed in a metal die and compressed to the desired shape and fiber volume fraction. The latter was about 45

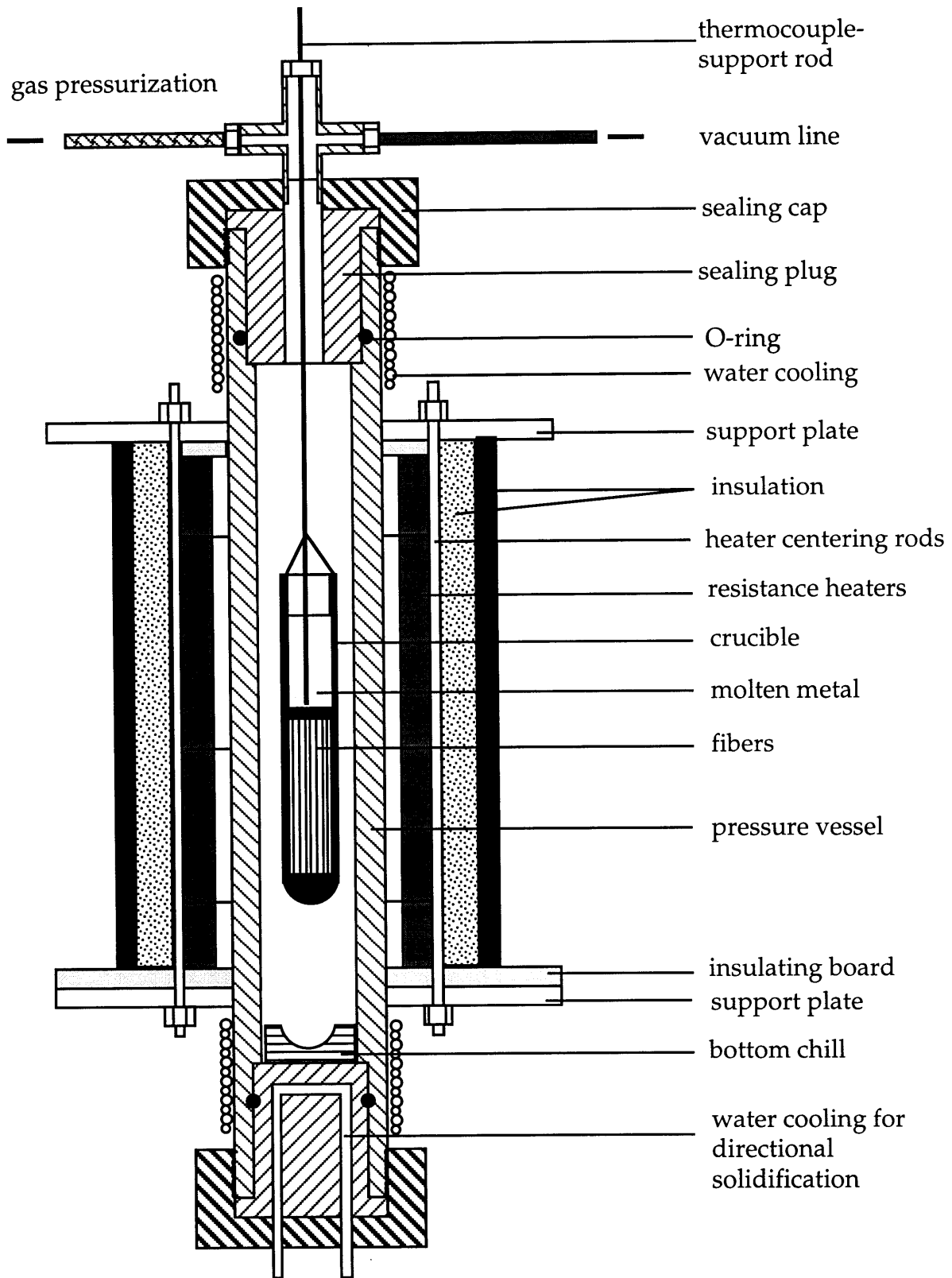


Figure 4-1 - Schematic of the pressure infiltration apparatus used to produce aluminum-based matrix composites.

to 50% for Fiber FP and 65 to 70% for Nextel 610. A higher volume fraction was found to lead to a significant number of fibers breaking below the critical length L_{cr} due to the fiber packing procedure ($L_{cr}=1.4$ mm for fiber FP), while a lower V_f would produce channeling and hence an irregular distribution of fibers in the composite [8]. The wet fiber preform was subsequently frozen solid by immersion into liquid nitrogen. The frozen block of fibers was placed in a graphite die and introduced into an alumina crucible. The graphite die enabled casting of a composite with a square cross-section in a round crucible to minimize subsequent specimen machining. Finally, the crucible was placed in an oven and the fibers dried by heating overnight at 200°C.

4.2.2 Aluminum-based Matrix Composites

Metal was placed in the crucible above the fiber preform, and the assembly, supported by a thermocouple rod, was hung inside the pressure vessel of the casting apparatus (Figure 4-1). The infiltration pressure vessel was a stainless steel tube surrounded by heating resistors described in Ref. [79]. The fibers and metal were heated together under vacuum. When the metal melted, fibers were sealed from the surrounding atmosphere by the matrix wetting the crucible walls above the fibers, which prevented gas bubbles from being trapped between the fibers during infiltration, and eliminated subsequent porosity in the composite.

Infiltration was carried out with argon gas at 6.9 MPa (1000 psi). The pressure was released after about 5 minutes following pressurization. The crucible was then lowered to the water-cooled bottom of the apparatus and the vessel was re-pressurized. This allowed directional solidification under pressure to feed shrinkage. The pressure was maintained until solidification of the metal was complete. The cooling rate of the sample was approximately 2°C/min.

When the temperature dropped to about 300°C below the metal melting point, the crucible was taken out, water quenched and finally broken to remove the

composite. The size of samples produced using this procedure was typically $15 \times 2.8 \times 2.5 \text{ cm}^3$ for Al-based matrix composites.

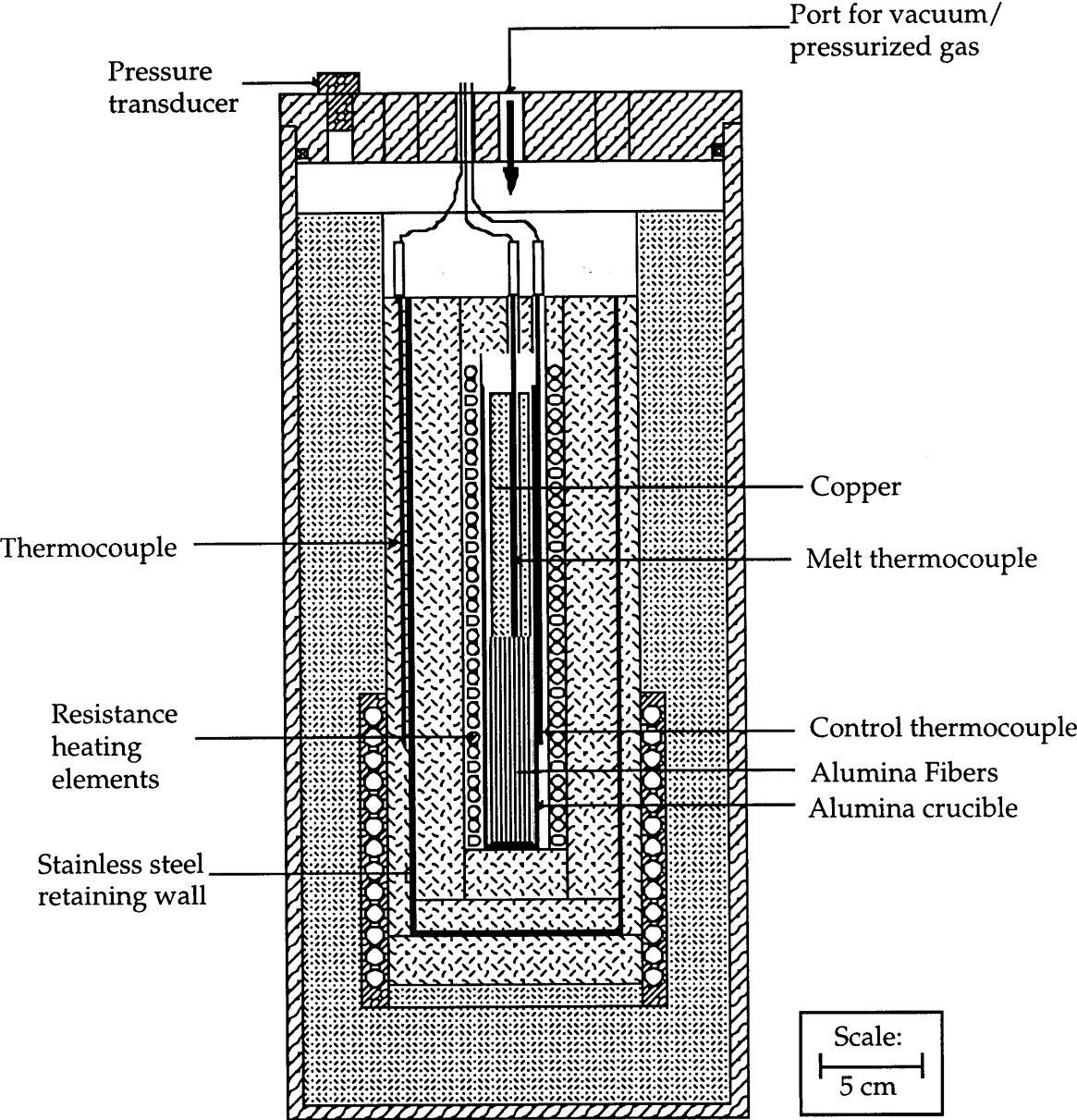


Figure 4-2 - Schematic of the pressure infiltration apparatus used to produce copper-based matrix composites.

4.2.3 Copper-based Matrix Composites

The casting procedure for Cu-based matrix composites was analogous to that of Al-based matrix composites described above, but a different apparatus (see Figure 4-2) was used because of the higher temperature required to melt copper. Due to geometric constraints, the dimensions of the resulting composites were 2/3 of those of Al-based matrix composites produced using the previously described apparatus (see Figure 4-1), typically $10 \times 1.6 \times 1.5 \text{ cm}^3$. Nitrogen gas at 3.5 MPa (500 psi) was used for infiltration. Control of solidification directionality was lessened due to the absence of water-cooling at the base of the apparatus; however, the presence of a temperature difference between the bottom and mid-section of the pressure vessel must have aided in this regard.

4.2.4 Sample Designation

Samples were designated as follows:

x-y•Matrix/Fiber

where

x = infiltration run number (bars with identical run numbers were cast simultaneously and machined from same composite slab)

y = tensile bar number

Matrix = Al (99.999%Al), AlCu (Al-4.5wt%Cu), AlMg (Al-0.9wt%Mg), Cu (99.996%Cu), CuAl (Cu-7wt%Al), or CuTi (Cu-1wt%Ti)

Fiber = FP (Dupont Fiber FP) or 3M (3M Nextel 610)

4.3 Mechanical Testing

4.3.1 Geometry

Bars for mechanical testing were machined from the cast composite using a thin diamond cutting wheel on a high speed surface grinder. Cutting was difficult due to

the presence of ceramic fibers and lowering of the wheel had to be done by very small increments. Even careful cutting and frequent dressing of the wheel did not yield bars with perfectly constant thickness and further machining on a surface grinder using a diamond grinding wheel was required. Final polishing of the bar surfaces was done by hand using fine silicon carbide paper. In the case of Cu/FP, special care had to be exercised in machining because of the weak bond between metal and fibers, particularly to obtain bars with sharp regular edges.

The bar shape complied with standard ASTM D3552-77 (Reapproved 1989), *Tensile Properties of Fiber-Reinforced Metal Matrix Composites*. It was a rectangular parallelepiped of dimensions $12.5 \times 3 \times 147 \text{ mm}^3$ for pure Al and Al-4.5wt%Cu composites and $8.3 \times 2 \times 98 \text{ mm}^3$ for pure Cu, Cu-7wt%Al, Cu-1wt%Ti and Al-0.9wt%Mg composites. The commonly used "dog bone" shape was not adopted because of the more complicated machining required and of the probability of detrimental stress concentration associated with the presence of cut fibers in the curved regions of such a shape.

The Al-0.9wt%Mg/FP composite bars and some Cu/FP bars were cast directly to near net shape using a specially machined graphite die. This procedure saved composite machining time and cost (no cutting was required) and significantly reduced the amount of fibers used. Final surface grinding and polishing, still necessary to ensure uniform sample thickness, was performed identically to all the other bars. Comparable specifications to those of bars machined from a composite block were achieved. Twelve bars of Al-0.9wt%Mg/FP were obtained this way in a single run.

Unreinforced bars of each matrix were pressure cast simultaneously with the corresponding composite systems, with the exception of the Al-4.5wt%Cu unreinforced bar, which was machined directly from the master alloy. It was therefore possible to test both composite and matrix with exactly the same processing conditions and to make direct comparisons between the matrices in the reinforced and the unreinforced states.

4.3.2 Treatment Prior to Testing

To provide a uniform initial stress state and matrices as uniform and reproducible as possible, all test bars were annealed prior to testing. The aluminum composites were water quenched thereafter to ensure consistency with a previous study [24]. In addition, the precipitation-hardenable matrices (Al-4.5wt%Cu, Al-0.9wt%Mg, and Cu-1wt%Ti) required special heat treatments to dissolve the second phase.

Heating was conducted in a Lindberg (General Signal, Watertown, WI) type 55346 tube furnace. All the composites were placed in an alumina boat to prevent direct contact between the composite and quartz. Such contact could result in Si contamination during annealing [80]. Alumina boats containing copper and binary copper alloys were further encapsulated in a quartz tube to prevent matrix oxidation. A titanium (tantalum for Cu-1wt%Ti) getter was placed near the bars. The tube was then evacuated and back-filled with a low pressure (180 mmHg) of UHP Argon before final sealing. The precise heat treatment schedule for each composite system is given in Table 4-1, together with the rationale for selection of this schedule.

Table 4-1 - Test bar heat treatment schedules

Matrix	Heat treatment	Comments
Pure Al/FP and pure Al/3M	500°C for 16 hours in flowing nitrogen, followed by a water quench	Additional heating to 120°C for one hour followed by air cooling to room temperature was required for 3M Nextel 610 reinforced composites to glue tabs on the specimens (see Section 4.3.3).
Al-4.5wt%Cu/FP	solution heat treated at 520°C for 3 days, water quenched, aged at room temperature for 4 to 5 days	T4 treatment
Al-0.9wt%Mg/FP	570°C for 24 hours in flowing Argon, followed by a water quench.	Mechanical tests were conducted within 24 hours of the quench, <i>i.e.</i> before any appreciable precipitation could take place. Natural aging can have varying effects on the microstructure of Al-Mg alloys depending on the Mg and Si content [81].
Pure Cu/FP, Cu-7wt%Al/FP, and Cu-7wt%Al/3M	650°C for 1.5 hours followed by furnace cooling to room temperature.	Thorough anneal for copper, according to Bradfield <i>et al.</i> [82]
Cu-1wt%Ti/FP and Cu-1wt%Ti/3M	900°C for 45 minutes, followed by a quench in ice brine	The solubility of titanium in copper decreases from about 6wt% at 900°C [83] to less than 0.1wt% below 400°C [84]. Spinodal decomposition occurs in supersaturated CuTi solid solutions. In alloys with less than 3wt%Ti, it can be prevented by fast quenching [85-88]. Cu-1wt%Ti samples were therefore quenched as quickly as possible by braking the quartz capsule in ice brine.

4.3.3 Room Temperature Testing

To prevent surface damage by the grips of the tensile testing machine, aluminum tabs were glued to the ends of the test bars. The tabs were tapered to a small (7°) angle to minimize stress concentration near the gage section, Figure 4-3.

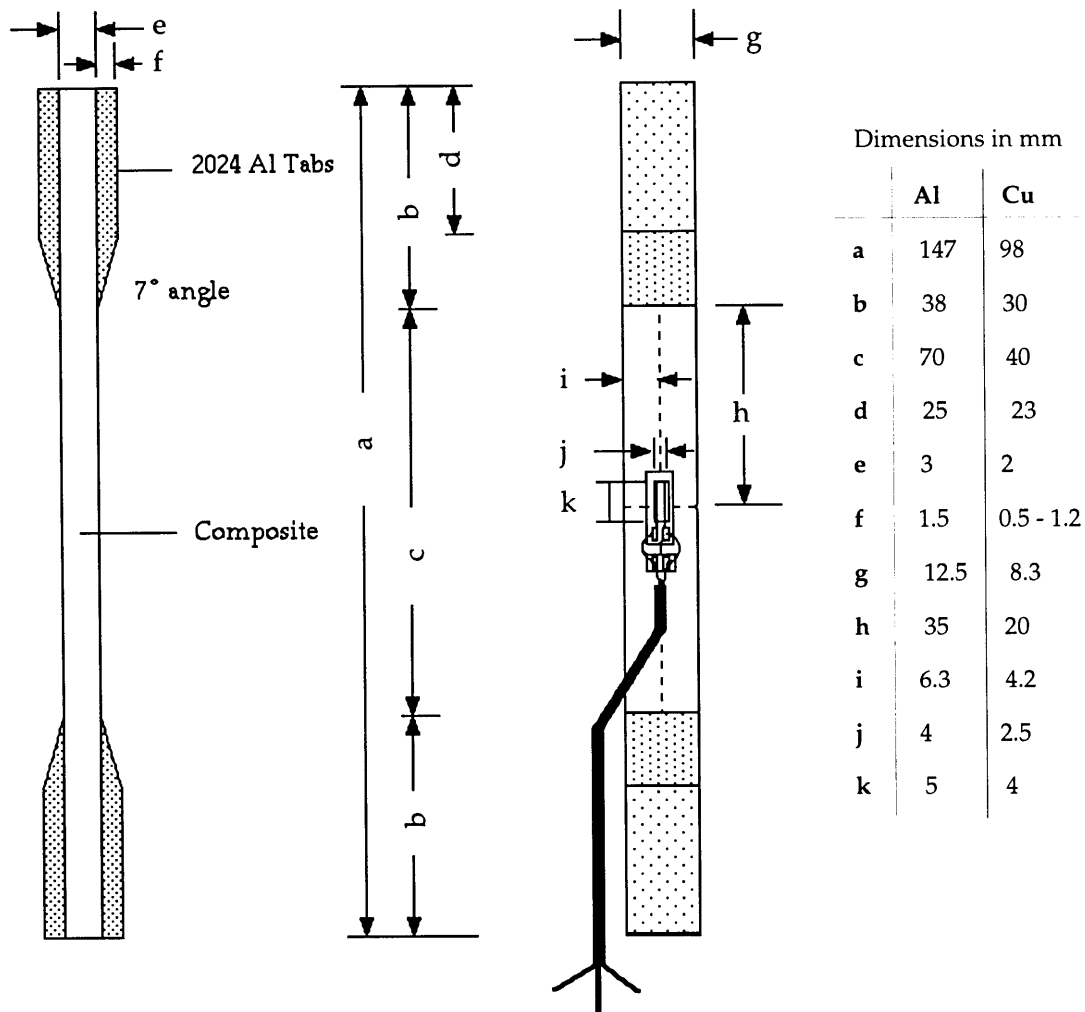


Figure 4-3 - Geometry of bars for mechanical testing

Low temperature curing epoxy (Hysol Epoxi-Patch from Dexter Corp. of Seabrook, NH or the slightly stronger and less brittle 3M Epoxy 2216 B/A from 3M Corp. of St Paul, MN) was used for Dupont FP fiber reinforced composites. The glue was cured at room temperature for 24 hours. A stronger glue was necessary for 3M Nextel 610 fiber reinforced composites; 3M Scotchweld AF-163-2 (0.06 weight) (received from 3M Corp. of St Paul, MN), which required curing above room temperature, was therefore used. With this last glue, glue strips were applied onto the tabs surface, the tabs clamped to the specimen ends, and the whole assembly cured in an oven at 120°C for one hour.

Strain on each sample was measured by two strain gages located in the center of the gage length, one on each side. The gage dimensions were such that they cover an area containing at least 100 fiber diameters. The strain gages used for room temperature testing were type CEA-06-125UW-350 for large bars and CEA-06-125UN-350 for small bars. These were glued using M-Bond 200 brand adhesive (special cyanoacrylate from Measurements Group, Inc., Raleigh, NC). Testing was conducted on an Instron™ model 1125 machine (Instron Corporation, Canton, MA), at a nominal strain rate of 0.01 sec⁻¹. The strain gages were connected using the standard 3-leadwire method to a Wheatstone bridge in quarter bridge mode in a two channel Measurements Group™ model 2120 conditioner (Measurements Group, Inc., Raleigh, NC). Signal calibration was repeated prior to each test. Care was exercised in tests to minimize electrical noise perturbation of the recorded signals (predominantly from the testing apparatus motor). To this end the location of strain recording equipment in relation to the testing apparatus was optimized, and copper mesh Faraday cages were constructed around all wiring and associated equipment.

Load and strain data were acquired directly on a Power Macintosh™ 7100/80 computer (Apple Computer, Inc., Cupertino, CA) using an analog to digital converter in differential mode (NB-MIO-16-H board) and LabVIEW® software from National Instruments Corporation, of Austin, TX. A custom data acquisition program was written in LabVIEW® (see Appendix B). It allowed continuous buffered data acquisition of the load and two strain signals in volts, conversion into

engineering units, on-screen display of the actual stress-strain curves, and data saving to disk in real time. Data were typically acquired at 400 points/s for each channel. Every 100 points were averaged for noise removal, to yield an effective sampling rate of 4 points/s/channel. The average of the two strain signals from each side of the bar was used to plot the final stress-strain curve. In this configuration, the data acquisition set-up yielded very accurate measurements (see Section 4.3.4.5, page 51). All the results presented in this work are from as-acquired data and needed no additional smoothing.

Compression tests were also conducted on bars of the same geometry. Specimens with a different aspect ratio were not considered because of the possibility of progressive yielding, whereby different points of a given cross-section yield at different times. Custom grips were designed and machined, Figure 4–4 to Figure 4–7. The screw driven tightening mechanism allowed for precise alignment of the composite bar. The whole assembly was rigid, which enabled both tensile and compressive tests as well as sequential tension-compression cycling. Compression tests were conducted to strains below that at which the two strain gages indicated the onset of buckling in the samples.

4.3.4 Error Analysis in Room Temperature Testing

Prior to each test, with the sample gripped in the top grip only, calibration was performed as follows. The load signal was acquired for 30 s at zero load (resp. full scale load) and the resulting data were averaged to yield the origin X_0 (resp. full scale X_m). Similarly, the strain origin ϵ_0 and 0.1% strain ϵ_m (simulated by the internal shunt calibration of the strain gage amplifier) were measured for both strain signals. Stress σ (MPa) and strain ϵ_i (%) ($i=1,2$) were then computed using

$$\sigma = \frac{S}{145.0377 \cdot A} \frac{(Ld(V) - X_0)}{(X_m - X_0)} , \quad (4.3-1)$$

$$\varepsilon_i = \varepsilon_{cal} \frac{(\varepsilon_v(V) - \varepsilon_0)}{(\varepsilon_m - \varepsilon_0)} \quad \text{and} \quad \varepsilon = \frac{\varepsilon_1 + \varepsilon_2}{2} , \quad (4.3-2)$$

where S = Load scale (lbs), A = Sample cross-section (in²), and ε_{cal} = Strain (%) simulated by calibration of amplifier. ε_{cal} is always very close to 0.1%, but depends on the value of the resistance necessary to equilibrate the Wheatstone bridge, the gage and leadwire resistances, and the gage factor of the active strain gage. ε_{cal} was calculated for each type of gage used following the method on p.9 of the 2120 conditioner manual (Measurements Group, Inc., Raleigh, NC).

4.3.4.1 Error in Cross-section Measurements

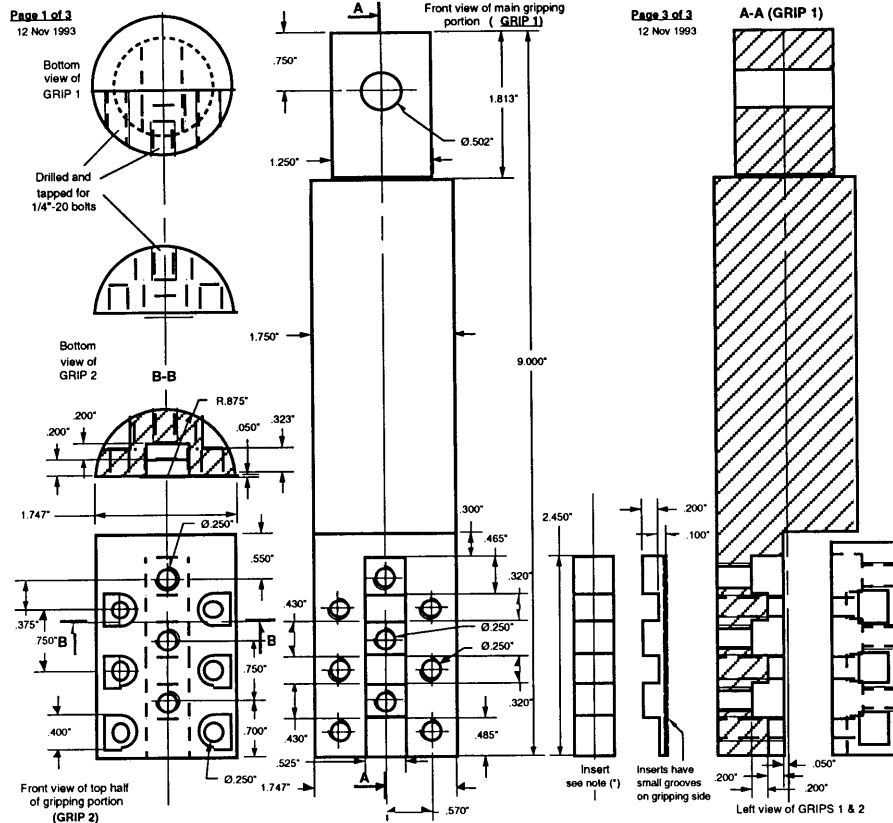
The width and thickness of each sample in the gage section were measured with a micrometer having a precision of 0.001 mm. Evenness of width and thickness varied from excellent for aluminum composites (with a typical deviation of 0.001 mm throughout the gage section) to fair for some copper-based composites (deviations of the order of 0.01 mm and/or bad edges). Departure from a perfectly rectangular cross-section was due to difficulty in machining some of the more brittle composite systems. This resulted in most cases in a slight non-parallelism of the sample's faces, *i.e.* a trapezoidal cross-section. Repeated measurements throughout the cross-section at the strain gage location, followed by averaging of the results, nonetheless yielded good accuracy. Hence, the uncertainty on the cross-section was estimated to vary from:

$$\frac{\Delta A}{A} = \frac{0.001}{3} + \frac{0.001}{12.5} = 0.04\% \quad \text{for aluminum-based composites to}$$

$$\frac{\Delta A}{A} = \frac{0.01}{1.3} + \frac{0.015}{7.5} = 1\% \quad \text{for the worst case of one CuAl/Nextel 610 composite with}$$

bad edges. In general, the uncertainty on the cross-section was of the order of 0.3% for copper-based composites and less than 0.1% for aluminum-based composites (see Table 4-3, page 68).

Page 1 of 3
12 Nov 1993



Page 3 of 3
12 Nov 1993

(*) Inserts should fit tightly into gripping portion but still be allowed to translate in a direction perpendicular to axis of grip when pushed by 1/4"-20 bolts.

GRIPS FOR INSTRON TENSILE TESTING MACHINE		
		12 Nov 1993
SCALE: 1:1 (Except where noted)		
Pavel Bystricky MIT Room 16-501	Tel: (617) 253-3242 Fax: (617) 258-8836	

Part Name	Quantity	Material
GRIP 1 (Main bar)	2	SS 303
GRIP 2	2	SS 303
Insert	4	SS 303
Adapter Ring	1	SS 303

Page 2 of 3
12 Nov 1993

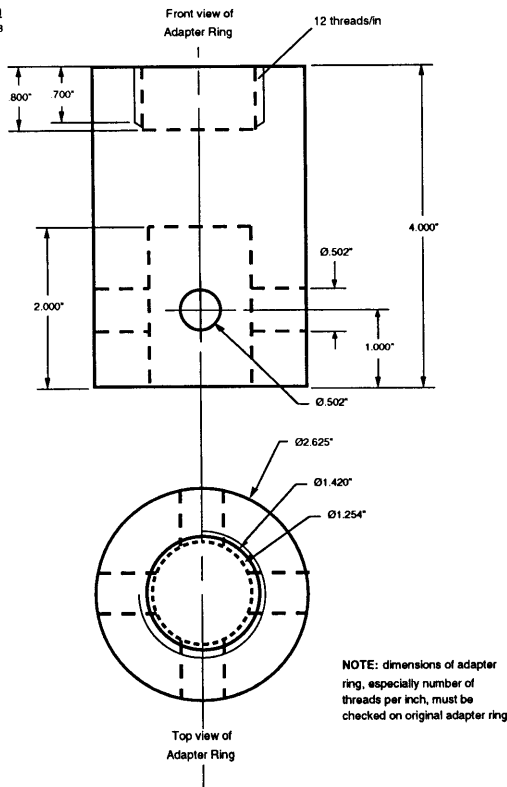


Figure 4-4 - Schematic of custom grips for tension-compression testing at room temperature and 77 K.

4.3.4.2 Error in Load Calibration

The load scale was chosen according to the expected strength of each sample in order to optimize accuracy. It varied from 2,000 lbs for Cu/FP to 10,000 lbs for Al/3M composites. When load is measured with the mechanical pen recorder, the load weighing accuracy of the Instron™ 1125 machine is better than $\pm 0.5\%$ of the indicated load (or $\pm 0.25\%$ of the recorder scale in use, whichever is greater). In the present tests, the mechanical pen recorder was bypassed and the load signal was acquired digitally at a high sampling rate, which significantly increased the readout accuracy (no part of the load weighing system other than the pen recorder exhibits mechanical inertia; for more details, see p. 3-3 of the Instron Model 1125 Manual, Instron corporation, Canton, MA). The error in load ΔS was therefore considered negligible compared to the error on sample cross-section:

$$\frac{\Delta S}{S} \ll \frac{\Delta A}{A} . \quad (4.3-3)$$

4.3.4.3 Error in Strain Calibration

The error due to Wheatstone bridge non-linearity, in %, is approximately equal to the strain in % ([89, Technical Note 507, p.1]). The strain amplitude, and hence the error $\frac{\Delta \epsilon_{cal}}{\epsilon_{cal}}$, was typically 0.2% for FP and 0.3% for most Nextel 610 reinforced composites (up to 0.5% for some Al/Nextel 610 composites).

4.3.4.4 Error Due to Sample Misalignment

In a uniaxial stress field, the error in strain indication due to misalignment of strain gages is given by ([89, Technical Note 511]):

$$\Delta \epsilon_{mis} = \frac{\epsilon_p - \epsilon_q}{2} (\cos 2(\phi \pm \beta) - \cos 2\phi) , \quad (4.3-4)$$

where

ϕ = angle of misalignment of sample in grips

β = angular mounting error of strain gage

ϵ_p = maximum principal strain

ϵ_q = minimum principal strain = $-\nu\epsilon_p \approx -0.3\epsilon_p$

Slight misalignment of the sample in the grips was difficult to avoid but was largely compensated by the fact that strain was measured on both sides of each bar and averaged.

Measurement of ϕ and β yielded $\phi \leq 1^\circ$ and $\beta \leq 0.5^\circ$. The error due to misalignment was thus:

$$\frac{\Delta\epsilon_{mis}}{\epsilon_{mis}} = 0.05\% \quad . \quad (4.3-5)$$

4.3.4.5 Error Due to Digitization and Signal Noise

The resolution of the analog to digital conversion was 4.88 mV for the load signal (using a gain of 1 and ± 10 V input range) and 2.44 mV for the strain signals (gain of 2 and ± 5 V range). The data acquisition apparatus was shielded from external electromagnetic noise (most of which originated from the motor at the base of the Instron machine's frame) by using copper mesh and optimizing the instruments' location. The most effective electromagnetic shield proved to be the console of the Instron machine itself. After averaging the oversampled data for each channel, the noise in the signal (peak to peak deviation when load and strain were held constant) was typically less than 4 mV for load and less than 0.5 mV for strains. Since the peak to peak deviation is approximately equal to four standard deviations in the data [90] and the maximum amplitude of the tests was 10 volts (0 to 10V for load, -5 to +5V for strains), the uncertainty from digitization and signal noise was estimated as:

$$\frac{\Delta Ld}{Ld} = \frac{0.004}{4 \times 10} = 0.01\% \quad \text{for load data, and}$$

$$\frac{\Delta \epsilon}{\epsilon} = \frac{0.0005}{4 \times 10} = 0.001\% \text{ for strain data.}$$

4.3.4.6 Overall Error on Stress and Strain at Room Temperature

Compared to the magnitude of the other sources of error reviewed above, the error arising from noise in the data can safely be ignored. We therefore consider the errors on the measured values of L_d , $X_{0'}$, X_m , $\epsilon_{0'}$, and ϵ_m in Eqs. (4.3-1) and (4.3-2) to be negligible, and take $\Delta \epsilon_v \approx \Delta \epsilon_{mis}$ to obtain

$$\frac{\Delta \sigma}{\sigma} \approx \frac{\Delta A}{A} \quad \text{and} \quad \frac{\Delta \epsilon}{\epsilon} \approx \frac{\Delta \epsilon_{cal}}{\epsilon_{cal}} + \frac{\Delta \epsilon_{mis}}{\epsilon_{mis}} \approx |\epsilon| + 0.05\% . \quad (4.3-6)$$

Resulting estimates of the experimental errors in mechanical data for each composite system considered are given in Table 4-3, page 68.

4.3.5 Low Temperature Testing

A special container for liquid nitrogen was designed and built to fit around our custom grips (see Figure 4-6 and Figure 4-7). An aluminum ring was pressure-fitted around the base of the bottom grip. An aluminum cylinder was placed around the bottom grip and attached to the base with a set of clamps and O-rings. Extension of the enclosure to the gage section and the top grip was provided by a removable Plexiglas cylinder. Liquid nitrogen was supplied into the container *via* a thin rubber tube fitted with a "phase separator" (small porous plug which enables efficient dispensing of liquid nitrogen, provided by BOC Gases, The BOC Group, Inc., DE). Since the container was not insulated, a controlled continuous inflow of liquid nitrogen was allowed to compensate for losses from evaporation. Temperature in the gage section was monitored with a type K thermocouple and shown to be constant and equal to $-196 \pm 1^\circ\text{C}$. Figure 4-6 and Figure 4-7 show a test in progress.

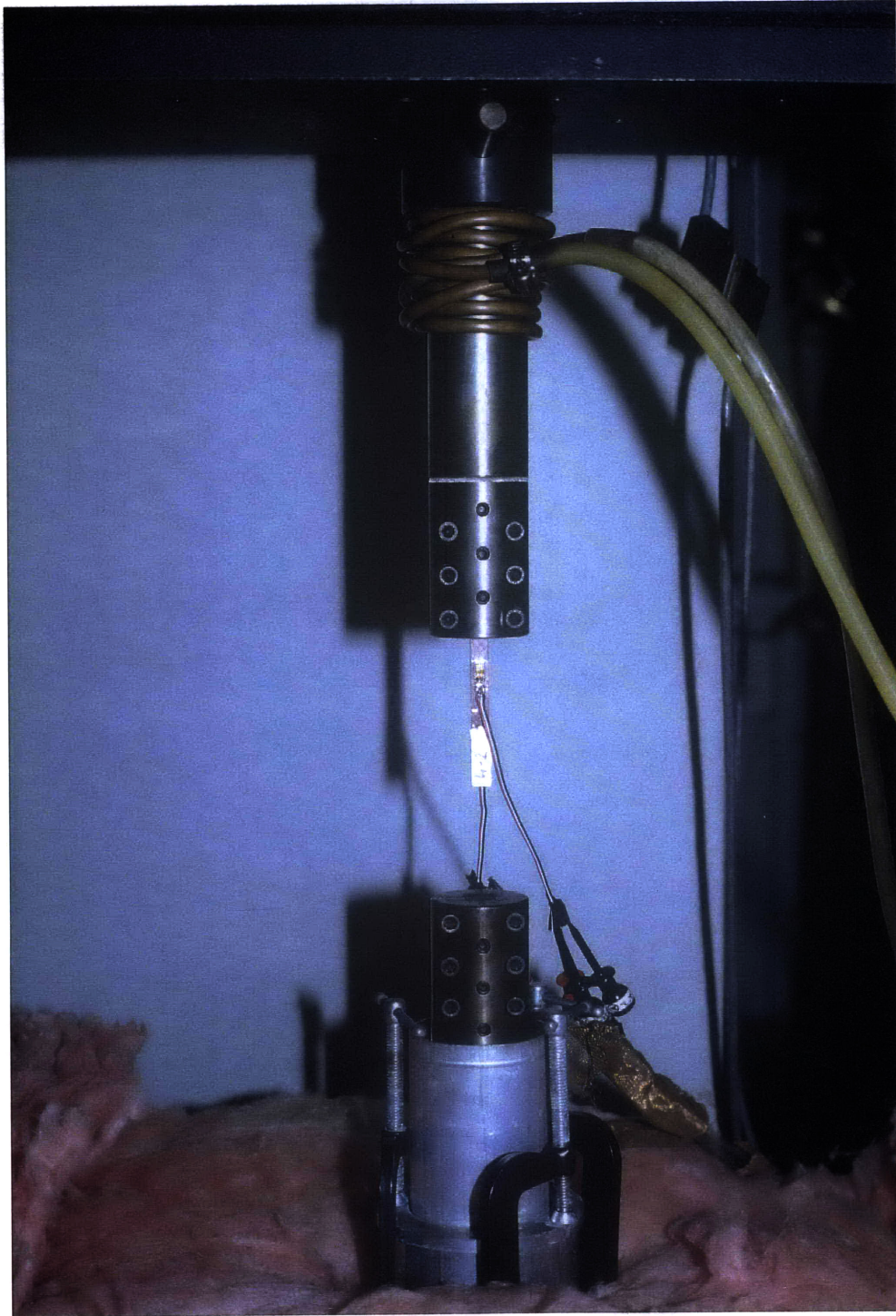


Figure 4-5 - Gripping set-up prior to testing, with pure Cu/FP sample in top grip, showing mounted strain gages and connections to strain gage amplifier.

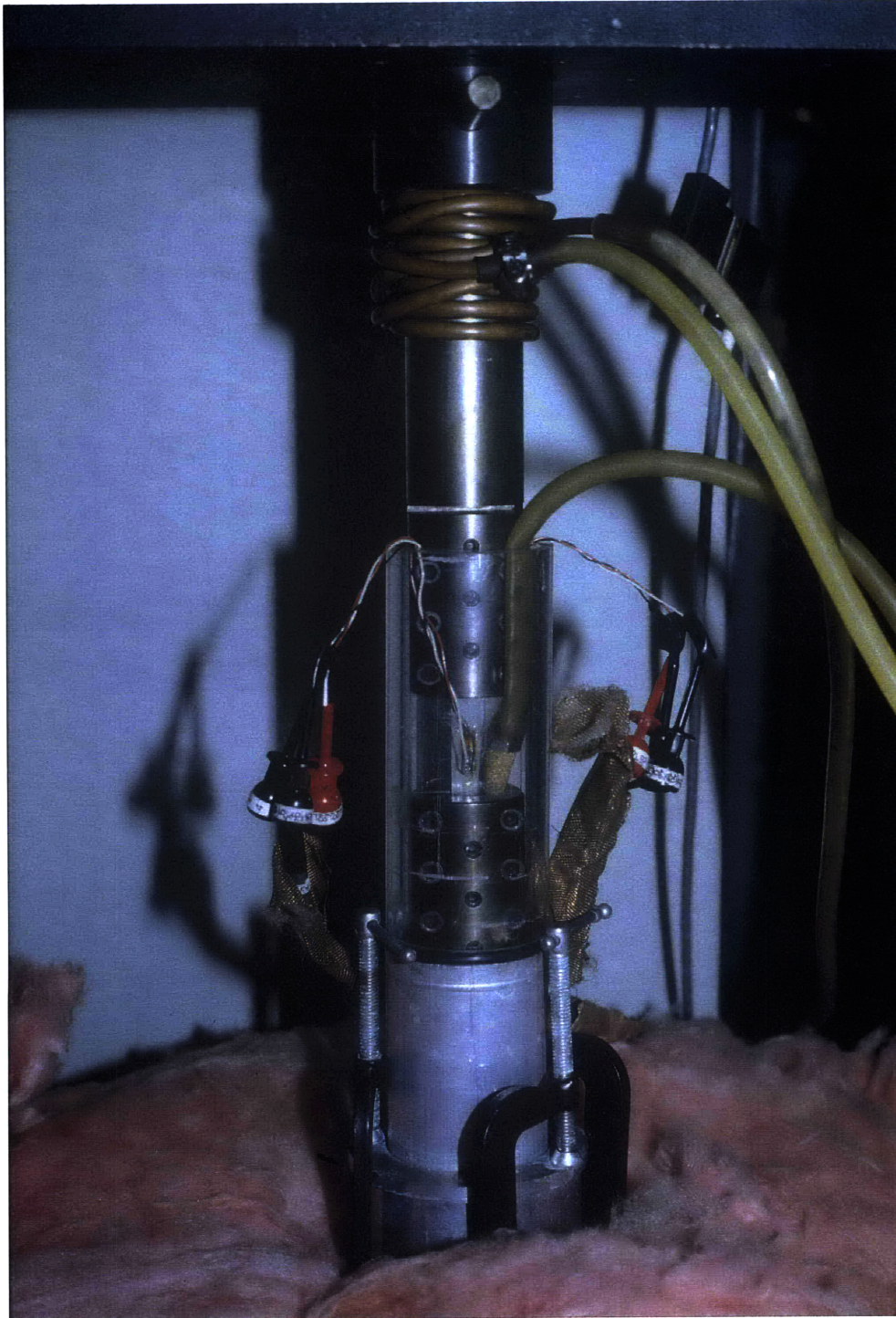


Figure 4-6 - Pure Al/FP sample, gripped in top and bottom grips, ready for testing at 77 K. Note porous copper "phase separator" which minimizes turbulence of liquid nitrogen flow during test.



Figure 4-7 - Mechanical test in progress in liquid nitrogen. The temperature reading (-195°C) is from a thermocouple placed near the sample's strain gages.

The procedure for sample preparation (machining, annealing, tabs) was the same as described above for room temperature, but special strain gages and an elevated temperature curing glue were required. The strain gages used were type WK-06-125AD-350 (from Measurements Group, Inc., Raleigh, NC), with pre-attached leadwires. For unreinforced bars, type WK-13-125AD-350, which provides a thermal expansion compensation better matched to pure aluminum, was used. The strain gages were glued with M-Bond 610 (two-component epoxy-phenolic adhesive from Measurements Group, Inc., Raleigh, NC), clamped in place and cured at 120°C for 3 hours. The same glue was then applied over the strain gages to provide environmental protection and cured at 150°C for 2 hours. This second curing cycle was also designed to relieve stresses in the glue line between strain gage and sample.

Monotonic and tension-compression tests were performed in liquid nitrogen on pure aluminum matrix composites and unreinforced pure aluminum. Samples were gripped in both (top and bottom) grips at room temperature, then immersed in liquid nitrogen. The cross-head was moved carefully during cool-down to compensate for thermal contraction of the sample. The calibration procedure, identical to that for room temperature tests (see Section 4.3.4 above), was done as soon as the temperature had stabilized and immediately prior to testing. As a result, no temperature compensation needed to be applied to the strain reading.

4.3.6 Error Analysis in Low Temperature Testing

The room temperature error analysis exposed above remains valid in this case with the following changes:

- The gage factor is temperature-dependent. The value of ϵ_{cal} was thus adjusted using data from Measurements Group, Inc. (Raleigh, NC): a temperature change $\Delta T=218^\circ\text{C}$ produces a change $\Delta\epsilon_{cal} = 0.0021\% \pm 0.0004\%$ for the strain gages used. Given the small uncertainty in $\Delta\epsilon_{cal}$, the error in strain measurements at low temperature was thus about the same as that at room temperature (see Section 4.3.4.6 page 52), namely:

$$\frac{\Delta\varepsilon}{\varepsilon}(77\text{ K}) \approx |\varepsilon(77\text{ K})| + 0.05\% . \quad (4.3-7)$$

• The sample cross-section was corrected to allow for thermal contraction. The CTE of the composite was therefore calculated using Schapery's model for a unidirectional fiber-reinforced composites [91]; according to Vaidya and Chawla [92], this model's predictions come closest to experimental results for fiber reinforced composites. Schapery gives the CTE transverse to the fiber direction, α_{\perp} as:

$$\alpha_{\perp} = (1 + \nu_m)\alpha_m V_m + (1 + \nu_f)\alpha_f V_f - \alpha_{\parallel} \nu_c , \quad (4.3-8)$$

where

$$\nu_c = \nu_f V_f + \nu_m V_m , \quad (4.3-9)$$

α_{\parallel} is the composite CTE in the longitudinal direction, given by:

$$\alpha_{\parallel} = \frac{\alpha_f V_f E_f + \alpha_m V_m E_m}{V_f E_f + V_m E_m} , \quad (4.3-10)$$

ν is Poisson's ratio, E is Young's modulus, V the volume fraction, and subscripts f and m represent fiber and matrix, respectively. The average coefficient of thermal expansion (CTE) of aluminum when the temperature decreases from room temperature to that of liquid nitrogen (77 K) is $18 \cdot 10^{-6} \text{ K}^{-1}$ (calculated from [93] and [94]). The average CTE of Al_2O_3 in that temperature interval was estimated as $3.4 \cdot 10^{-6} \text{ K}^{-1}$ from [95].

The resulting correction in the sample cross-section is of the order of 0.6%, and was incorporated in the analysis. Since the formulae above have been documented to have good predictive power for α_{\perp} in aligned fiber composites, this correction is deemed precise; hence, thermal contraction is assumed not to affect $\frac{\Delta A}{A}$ or, by implication, the uncertainty on measured stress.

• The fiber modulus E_f at 77K was computed using Wachtman's equation for the temperature dependence of Young's modulus of oxide compounds (proposed by Wachtman *et al.* [96] and derived later by Anderson [97]):

$$E = E_0 - BT \exp\left(-\frac{T_0}{T}\right), \quad (4.3-11)$$

where E_0 (Young's modulus at absolute zero temperature), B , and T_0 are constants for a given compound. For polycrystalline Al_2O_3 , these constants can be obtained using the following data from [96]:

$$\frac{E_0}{E_{25}} = 1.0148 \pm 0.0001, \quad \frac{B}{E_{25}} = 1.399 (\pm 0.006) \cdot 10^{-4} \text{ K}^{-1}, \quad \text{and} \quad T_0 = 311 \pm 4 \text{ K}, \quad (4.3-12)$$

where E_{25} is Young's modulus at room temperature. For Fiber FP, $E_{25} = 379 \pm 3$ GPa (see Section 4.5.2 page 74). Hence, the modulus of Fiber FP at 77 K can be estimated as $E_{\text{FP}}(77 \text{ K}) = 385 \pm 3$ GPa. It may be noted that the precision in the above data is such that applying Eq. (4.3-11) does not increase significantly the estimated uncertainty (of ± 3 GPa) on the computed value of $E_{\text{FP}}(77 \text{ K})$.

4.4 Determination of Fiber Volume Fraction

Prior to mechanical testing, the fiber volume fraction V_f of each composite test bar was determined by measuring the density of each sample by pycnometry. Knowing the density of each component phase from literature data and separate measurements, and assuming there is no significant porosity within the composites, V_f for each sample was then computed from the rule of mixtures as the average value from at least three measurements. After mechanical testing, this measurement was confirmed for several bars by dissolution of the matrix in an acid solution, followed by filtering and weighing of the fibers.

4.4.1 Pycnometry

4.4.1.1 Water Pycnometry

The pycnometric method used here is similar to ASTM standard D2320-87. Essentially, pycnometry uses Archimedes' principle to determine the density of a specimen by comparison of its dry weight with that of an equal volume of water.

A pycnometer, consisting of a glass container closed by a cap fitted with a capillary tube, was filled with reverse osmosis deionized water above the graduation line of the capillary tube and placed in a thermostatic water bath, held between 23°C and 27°C. Care was taken to remove all visible air bubbles before closing the pycnometer. When the water temperature had reached equilibrium, a paper tissue was used to remove water from the capillary tube by absorption, until the water level reached the graduation line. The pycnometer was then removed from the thermostatic bath, thoroughly dried, and weighed within 60 seconds; the resulting measurement is termed m_1 . The specimen to be measured was then cleaned in ethanol in an ultrasonic cleaner, dried, weighed (to yield mass m_2), and placed inside the water-filled pycnometer. The same procedure as above was then repeated, but with the sample placed within the pycnometer, to yield mass m_3 . The water bath temperature was carefully monitored to be within 0.1°C of its value at the time of measurement of m_1 . A polynomial curve fit of water density data versus temperature was computed [98, p.6-8], and used to determine the exact water density $\rho_w(T)$ at the temperature of measurement. The volume of the specimen was then computed from:

$$V = \frac{m_1 + m_2 - m_3}{\rho_w(T)} , \quad (4.4-1)$$

and its density from:

$$\rho = \frac{m_2}{V} = \frac{m_2 \rho_w(T)}{m_1 + m_2 - m_3} . \quad (4.4-2)$$

This density measurement was repeated at least three times to verify consistency for each specimen, and the average value of all the results was computed as the final measurement. A typical variation between two measurements is 0.001gcm^{-3} for aluminum-based composites and 0.01gcm^{-3} for copper-based composites (see the discussion in Section 4.4.2 below). The volume fraction of alumina fibers in the composites was then calculated using the rule of mixtures as:

$$V_f = \frac{\rho_c - \rho_m}{\rho_f - \rho_m} , \quad (4.4-3)$$

with subscripts c , f , and m referring to composite, fiber, and matrix, respectively.

4.4.1.2 Xylene Pycnometry

Knowledge of the densities of the composite constituents is critical to the accuracy of the fiber volume fraction determination method described above. The fiber density ρ_f is in particular subject to question, because of the possibility for closed porosity within fibers. Error or variability in the value of ρ_f used can, therefore, cause error in the value of V_f computed using Eq. (4.4-3). The magnitude of this error depends on the difference between ρ_f and ρ_m , and is therefore larger with aluminum-based matrices than with Cu-based matrices (see Section 4.4.2 below).

Values for ρ_f and ρ_m were therefore also measured in order to check the validity of data cited in the literature. The procedure followed was the same pycnometric method described in the previous section, save for measurements on 3M Nextel 610 fibers, where xylene was used instead of water because of its superior wetting properties: in water, bubbles formed between fibers inside the submerged fiber bundle proved impossible to remove completely, despite the use of ultrasonic agitation. In xylene, wetting of the fibers was significantly improved; however, the measurement susceptibility to temperature fluctuations was also significantly increased. Best stability was obtained by letting the xylene-filled pycnometer equilibrate at room temperature on the balance for 10 minutes before each weighing. The following polynomial curve fit of xylene (mixed xylenes or m-xylene) density

data versus temperature, obtained from standard ASTM D3505-91 (Density or Relative Density of Pure Liquid Chemicals), was then used to compute the density of xylene at the relevant ambient temperature T:

$$\rho_{m-Xylene}(T [^{\circ}C]) = 0.8809567 - 8.31026 \cdot 10^{-4} T - 4.1548 \cdot 10^{-7} T^2 \quad . \quad (4.4-4)$$

Samples of 99.999% aluminum and Fiber FP were also measured in xylene in order to verify consistency between water and xylene pycnometry results.

4.4.2 Error Analysis in Pycnometry

All weighings were performed on a Mettler AE163 balance (Mettler-Toledo, Inc. of Heightstown, NJ). The standard deviation for the settings used (160g range) is $\sigma_m = 0.0001$ g, which is taken as the precision of the mass determination. In measuring m_i , additional error is introduced due to error in the volume of water used to fill the pycnometer. This error is mainly due to the possible presence of microscopic bubbles and/or impurities inside the pycnometer. Its extent is difficult to quantify, but it is minimized by the fact that m_1 is determined for each individual measurement. In addition m_1 and m_3 are measured at the same temperature, and hence any thermal expansion/contraction of the pycnometer does not need to be taken into account.

The temperature was measured to a precision of $\pm 0.1^{\circ}C$. It was determined experimentally that for a typical measurement, the temperature inside the pycnometer drops by $0.6^{\circ}C$ between the time the temperature of the bath is read and the time the pycnometer is weighed. This temperature drop was taken into account in the determination of volume V using Eq. (4.4-1). The corresponding experimental error in the water density is $\Delta\rho_w = 0.0002 \text{ g}\cdot\text{cm}^{-3}$.

Experimental error in pycnometry arising from all factors was measured by performing a series of ten measurements using water, performed over a period of four days, of the density of a sample of 99.999% pure unreinforced Al processed identically to the Al/FP and Al/3M composites (this sample was cast in the same

run as 1•Al/FP and machined and annealed as all Al/FP and Al/3M samples). The average value measured was computed as $2.700 \text{ g}\cdot\text{cm}^{-3}$. This value is within $0.001 \text{ g}\cdot\text{cm}^{-3}$ of the density cited in the literature [99, p.1.49], of $2.6989 \text{ g}\cdot\text{cm}^{-3}$, for 99.996% pure aluminum at the same temperature. The precision of the pycnometric density measurement is thus deemed good, and free of bias.

The intrinsic experimental error of the technique was evaluated by computing the standard deviation of the ten measurements, to yield $0.001 \text{ g}\cdot\text{cm}^{-3}$ (the computed value was $\sigma_{n-1}=0.00081 \text{ g}\cdot\text{cm}^{-3}$). Three measurements were also performed for the same sample using xylene as liquid, to find a mean density of $2.700 \text{ g}\cdot\text{cm}^{-3}$, and the standard deviation on the three measurements of $0.0055 \text{ g}\cdot\text{cm}^{-3}$. The technique is thus free of bias with xylene as well, and its experimental error is seemingly slightly higher than with water.

In measurements of the density of composites of fiber reinforced aluminum, the computed standard deviation of the three measurements performed for each sample was of the order of $0.001 \text{ g}\cdot\text{cm}^{-3}$, confirming the estimate of experimental error in the technique with water. With fiber reinforced pure copper, on the other hand, the computed experimental error for each series of three measurements was significantly higher than $0.001 \text{ g}\cdot\text{cm}^{-3}$: the average standard deviation of the Cu/FP composite density over 30 series of three measurements was $0.01 \text{ g}\cdot\text{cm}^{-3}$. We therefore take this value as an estimate of experimental error in the measurement of the density of pure Cu matrix composites. Causes for this increase in uncertainty can be traced to the smaller size of copper matrix composite samples, and their greater surface roughness (these could not be machined to the same surface smoothness as aluminum matrix composites because of the very low copper/alumina bond strength), which must have rendered wetting of the sample by the liquid somewhat less reproducible. There may, for this reason, also be some slight bias towards an underestimation of the density of pure copper matrix specimens (and therefore towards overestimation of V_f).

4.4.2.1 Composite Constituents

The density of pure aluminum is given as $\rho_m = 2.6989 \text{ g}\cdot\text{cm}^{-3}$ [99]. Having confirmed this value experimentally, we adopt it as known with negligible uncertainty, so that we take $\frac{\Delta\rho_m}{\rho_m} \ll \frac{\Delta\rho_c}{\rho_c}$ for pure Al. Similarly, for other constituents, measured values are listed in Table 4–2, and compared with data from the literature, where available. The experimental error was similarly estimated as the higher of $0.001 \text{ g}\cdot\text{cm}^{-3}$ (measured on pure aluminum) and the computed standard deviation of the measurements, of which there were at least three for each sample.

All our measurements agree with the values quoted in the literature, when available. With metals other than pure aluminum, however, the uncertainty on ρ_m is such that $\frac{\Delta\rho_m}{\rho_m}$ must be taken into account in the computation of $\frac{\Delta V_f}{V_f}$ (see Eq. (4.4–5) below). For Fiber FP alumina fibers, experimental measurements of density, performed here using both water pycnometry (with extensive ultrasonic and manual stirring of the fibers in the liquid), as well as Xylene pycnometry, were in agreement with published values; there is, however, significant variation in the latter (probably due to slight adjustments in the manufacturing process with time). We therefore use the density measured in our work, of $\rho_f = 3.91 \text{ g}\cdot\text{cm}^{-3}$, and use the corresponding experimental error for $\Delta\rho_f$ of $0.015 \text{ g}\cdot\text{cm}^{-3}$.

The density of 3M Nextel 610 fibers is given by the manufacturer as $\rho_f = 3.85 \text{ g}\cdot\text{cm}^{-3}$ † [100]. These fibers have a much smoother surface than Fiber FP and a smaller diameter ($12\mu\text{m}$ for Nextel 610, $20\mu\text{m}$ for Fiber FP). Consequently these fibers have a greater tendency to stick together under the action of capillary forces than Fiber FP, and achieving perfect wetting was very difficult, even in Xylene (a

† This value corresponds to fiber lots used in the present study. Other lots may have a slightly different density.

number of preliminary measurements had to be discarded after it became apparent that some bubbles still remained trapped between fibers in the pycnometer). Measurements by xylene pycnometry on Nextel 610 fibers extracted by dissolution from sample 1-1•Al/3M, yielded $\rho_f = 3.82 \pm 0.02 \text{ g}\cdot\text{cm}^{-3}$. This is most certainly a lower limit, since it is likely that a few bubbles remained in the fiber bundle, despite extensive stirring.

We therefore conclude that our experimental measurement of the density of Nextel 610™ fibers is in reasonable agreement with the value quoted by the manufacturer, of $\rho_f = 3.85 \text{ g}\cdot\text{cm}^{-3}$, and adopt the latter value as the fiber density. Since this value was measured at 3M using several techniques (helium pycnometry, transmission electron microscopy, and refractive index measurement [100]), we take the precision in this value to be higher than in our measurement, and on the order of an increment in the last significant digit, namely $\Delta\rho_f \approx 0.01 \text{ g}\cdot\text{cm}^{-3}$.

4.4.2.2 Experimental Error in the Volume Fraction

The experimental error ΔV_f in the measured value of V_f is then given from Eq. (4.4-3), page 60, as:

$$\frac{\Delta V_f}{V_f} = \frac{\Delta\rho_c}{|\rho_c - \rho_m|} + \frac{\Delta\rho_f}{|\rho_f - \rho_m|} + \left| \frac{\rho_c - \rho_f}{(\rho_f - \rho_m)(\rho_c - \rho_m)} \right| \Delta\rho_m \quad (4.4-5)$$

Resulting estimations of ΔV_f for each composite system considered are given in Table 4-3, page 68. It is noted that the greater error in composite density measurement for copper matrix composites is compensated by the greater difference between matrix and fiber density.

Table 4-2 - Measured constituent densities and corresponding values from the literature

System	Density from literature (g/cm ³)	Measured density (g/cm ³)	Experimental error (g/cm ³)
99.999% Aluminum (1)	2.6989 (a) (99.996% Al)	2.700	0.001
Al-4.5wt%Cu (1) (As Cast)	2.77 (a) (Al 2024)	2.787	0.001
Al-4.5wt%Cu (T4)	—	2.793	0.001
Al-0.9wt%Mg (2)	2.70 (a) (Al 6061)	2.689	0.006
99.996% Copper (3) (C10100)	8.96 (Pure Cu) (a) 8.94 (C10100) (b) 8.932 (Pure Cu) (c)	8.936	0.003
Cu-7wt%Al (2)	7.8 (C95200: 88Cu- 3Fe-9Al) (a) 7.64 (C95200) (d)	7.90	0.01
Cu-1wt%Ti (4) (As Cast)	—	8.852	0.006
Cu-1wt%Ti (4) (Heat Treated)	—	8.862	0.001
DuPont Fiber FP	3.90 (e) 3.92 (f) 3.9-3.95 (g)	3.91	0.015
3M Nextel 610 Fiber	3.85 (h)	3.82 (underestimate)	0.01

(1) Received from ALCOA (Pittsburgh, PA)

(2) Cast at MIT

(3) From Sambo Copper Alloy Co. Ltd (Osaka, Japan)

(4) Received from Olin Corp. (New Haven, CT)

(a) ASM Metals Handbook, Desk Edition, p. 1-49 [99]

(b) ASM Metals Handbook, Vol.2, p. 275 [101]

(c) Barrett and Massalski [102]

(d) ASM Metals Handbook, Vol.2, p. 429 [101]

(e) Champion, *et al.* [103]

(f) Romine [104]

(g) Dhingra [76]

(h) Deve [100]

4.4.3 Matrix Dissolution

To confirm the accuracy of the fiber volume fraction determined by density measurements, fibers from samples selected from each system investigated were extracted by acid digestion of the matrix, in accordance with standard ASTM D 3553-76 (Reapproved 1989), with the following two differences:

1) Aqua Regia (mixed in the proportions (1 part HNO_3 , 3 parts HCl) + $\frac{2}{3}\text{H}_2\text{O}$) was used rather than sodium hydroxide, because some dissolution of alumina in NaOH has been documented [8];

2) one large specimen (weighing typically 4 to 5 g) was used rather than five smaller ones (at least 300 mg each in ASTM D3553) because of the increased precision in volume measurement associated with larger samples.

After mechanical testing was completed, the specimen was cut in the middle of its gage section. One half was weighed (m_c) and its volume V determined by pycnometry. It was then placed in Aqua Regia heated at 60°C . Dissolution times were typically 3 to 4 hours for copper and at least 9 hours for aluminum matrix composites. Aluminum composite samples were usually left in Aqua Regia overnight to ensure complete matrix dissolution. Fibers were filtered onto a 15 ml tared sintered-glass filter (porosity D, 10-20 μm for Fiber FP; porosity E, 4-8 μm for Nextel 610) under vacuum and rinsed with water, followed by acetone. The filter and fibers were placed in an oven at 120°C overnight, then cooled to room temperature in a dessicator and weighed. The fiber volume fraction was then determined from the resulting fiber weight m_f using the fiber density ρ_f :

$$V_{f(\text{from } \rho_f)} = \frac{m_f}{\rho_f V} , \quad (4.4-6)$$

and, alternately, from the matrix weight $m_m = m_c - m_f$, using the matrix density ρ_m , which is known with a higher accuracy than that of the fiber:

$$V_{f(\text{from } \rho_m)} = 1 - \frac{m_m}{\rho_m V} . \quad (4.4-7)$$

4.4.3.1 Experimental Error in Matrix Dissolution

In order to confirm that alumina fibers are inert in the acid used, 1.4g of as-received Nextel 610 fibers were immersed in Aqua Regia at 60°C for 7 hours, filtered, and dried overnight at 120°C following the same procedure as during composite dissolution. The amount of fibers recovered was 99.94% of the initial weight. It was concluded that Aqua Regia has no effect on alumina fibers during dissolution and furthermore that the error on the measured fiber weight (due to possible fiber loss in the filtering process as well as to uncertainty inherent to the weighing procedure itself) is negligible compared to the uncertainty on the fiber density.

Eq. (4.4-6) can be written

$$V_{f(\text{from } \rho_f)} = \frac{m_f \cdot \rho_c}{\rho_f \cdot m_c} , \quad (4.4-8)$$

and the corresponding experimental error is

$$\frac{\Delta V_{f(\text{from } \rho_f)}}{V_{f(\text{from } \rho_f)}} = \frac{\Delta m_f}{m_f} + \frac{\Delta \rho_f}{\rho_f} + \frac{\Delta \rho_c}{\rho_c} + \frac{\Delta m_c}{m_c} \approx \frac{\Delta \rho_f}{\rho_f} + \frac{\Delta \rho_c}{\rho_c} , \quad (4.4-9)$$

where $\frac{\Delta m}{m} \approx 10^{-5}$ is negligible compared to the other quantities. Similarly, from Eq. (4.4-7),

$$\frac{\Delta V_{f(\text{from } \rho_m)}}{V_{f(\text{from } \rho_m)}} = \frac{\Delta m_m}{m_m} + \frac{\Delta \rho_m}{\rho_m} + \frac{\Delta \rho_c}{\rho_c} + \frac{\Delta m_c}{m_c} \approx \frac{\Delta \rho_m}{\rho_m} + \frac{\Delta \rho_c}{\rho_c} . \quad (4.4-10)$$

Using results from the previous section (Table 4-2, page 65), the experimental error in V_f obtained from measurements by matrix dissolution can be calculated for each system, Table 4-3.

It is important to note that these error estimates do not take into account the possible presence of impurities and/or porosity in the composites.

Table 4-3- Estimated experimental errors on measured stress and fiber volume fraction V_f

System	Error on stress $\frac{\Delta\sigma}{\sigma}$ (%)	Average V_f of system (%)	Uncertainty on V_f from pycnometry		Uncertainty on V_f from fiber dens. ρ_f		Uncertainty on V_f from matrix dens. ρ_m	
			$\Delta V_f/V_f$	ΔV_f (%)	$\Delta V_f/V_f$	ΔV_f (%)	$\Delta V_f/V_f$	ΔV_f (%)
99.999%Al/ Fiber FP	0.04	42	0.016	0.69	0.004	0.2	0.001	0.04
99.999%Al/ Nextel 610	0.04	62	0.011	0.69	0.003	0.2	0.001	0.06
Al- 4.5wt%Cu/ Fiber FP	0.04	42	0.017	0.72	0.004	0.2	0.001	0.04
Al- 0.9wt%Mg/ Fiber FP	0.06	40	0.031	1.25	0.005	0.2	0.004	0.2
99.996%Cu/ Fiber FP	0.6	60	0.007	0.45	0.006	0.4	0.002	0.1
Cu-7wt%Al/ Fiber FP	0.3	51	0.009	0.44	0.005	0.2	0.002	0.1
Cu-7wt%Al/ Nextel 610	0.3	69	0.007	0.51	0.005	0.3	0.003	0.2
Cu-1wt%Ti/ Fiber FP	0.2	52.7	0.005	0.26	0.004	0.2	0.001	0.06
Cu-1wt%Ti/ Nextel 610	0.3	73.2	0.003	0.23	0.003	0.2	0.001	0.09

4.4.4 Volume Fraction Determination From the Stress-Strain Curve

Another method of estimation of the fiber volume fraction is from the composite modulus in regions of the stress-strain curve where both constituents are elastic. From a practical point of view, it is noted that with samples tested in tension first, the initial elastic loading stage (Stage I) may be very small because of the large residual tensile stresses present in the matrix. It was therefore deemed preferable, with samples tested initially in tension, to use elastic unloading after initial loading into the plastic deformation range to evaluate the composite tensile modulus.

In regions of the composite stress-strain curves where both constituents are elastic, V_f can be computed from Eq. (3.2-1) page 32 as:

$$V_{f(\text{from } \sigma-\epsilon)} = \frac{\theta_{c,el} - E_m - \theta_{h,el}}{E_f - E_m} , \quad (4.4-11)$$

where E_f and E_m are the fiber and matrix elastic moduli, respectively, and the composite elastic slope $\theta_{c,el}$ is determined as described below, in Section 4.5.1, page 71. The contribution due to Poisson's ratio effects in the elastic regime, $\theta_{h,el}$, is small for systems of present interest, Eq. (3.2-4).

Uncertainty in V_f evaluated using this technique can result from several causes:

- (i) uncertainty in stress and strain measurements (error $\Delta\theta_{c,el}$)
- (ii) variations in matrix modulus with crystalline orientation (error ΔE_m)
- (iii) uncertainty in fiber modulus due to porosity (error ΔE_f)
- (iv) deviations in composite behavior from the rule of mixtures.

The error on the fiber volume fraction computed from Eq. (4.4-11) is thus:

$$\frac{\Delta V_{f(\text{from } \sigma-\epsilon)}}{V_{f(\text{from } \sigma-\epsilon)}} = \frac{\Delta\theta_{c,el} + \Delta\theta_{h,el}}{|\theta_{c,el} - E_m - \theta_{h,el}|} + \frac{\Delta E_f}{|E_f - E_m|} + \left| \frac{\theta_{c,el} - \theta_{h,el} - E_f}{(\theta_{c,el} - E_m - \theta_{h,el})(E_f - E_m)} \right| \Delta E_m . \quad (4.4-12)$$

The error arising from measurement of composite slope, $\Delta\theta_{c,el}$, is discussed below in Section 4.5.3 page 74. Cause (ii), namely anisotropy in matrix modulus, can

introduce significant uncertainty in the evaluation of V_f in some cases: with copper, in particular, the elastic modulus can vary by a factor of as much as 2.8 depending on crystal orientation and texture. Hence, this method of V_f measurement is not viable with copper-based matrices; however, with aluminum, the orientation dependence of the matrix elastic modulus is low, and only introduces an error in V_f of about 1%, Table 4-4.

Table 4-4 - Orientation dependence of modulus and resulting error in fiber volume fraction

System	Elastic Modulus E_m (GPa)	Corresponding Hypothetical V_f (%)	ΔV_f (from σ - ϵ) due to variation in E_m (%)
Aluminum			
No preferred orientation	69†; 70‡*; 70.3♦	50.0	
(111)	76†*; 76.1♦	49.0	1.1
(100)	62†; 63.7♦; 64*	51.1	
Copper			
No preferred orientation	110†; 115□; 121*; 129.8♦	50	
(111)	193†; 192*; 191◇; 191.1♦	29	15
(100)	69†; 67*◇; 66.7♦	58	

† Carter and Paul [105, p.40]

‡ ASM Metals Handbook, Desk Edition [99]

♦ Hertzberg [73, p.7 and 15]

* Courtney [72, p.60]

□ ASM Metals Handbook, Vol.2 (C10100 p.275) [101]

◇ Kelly and Lilholt [4]

The error on fiber modulus (cause (iii) above) is proportional to fiber density. It was estimated not to exceed 1% (see Section 4.5.2 page 74). Uncertainty arising from a deviation in composite behavior from the rule of mixtures (cause (iv) above) was discussed in Section 3.1 page 29, where relevant numerical values are given.

It appears clearly from what precedes that the pycnometric method of determination of V_f yields much more accurate results than the method presented in this section. Values of V_f determined by pycnometry were therefore used throughout this work. In aluminum-based systems, $V_f(\text{pyc})$ was confirmed from mechanical test results *via* Eq. (4.4–11).

4.5 Analysis of Stress-Strain Curves

4.5.1 Determination of Composite Rate of Work Hardening Curves

The strains measured on each side of a sample were averaged and the composite stress-average strain plotted and analyzed using the program Yield! II, written specifically for this purpose (see description in Appendix **B**). The slope of this curve versus average composite strain, or “Theta curve” ($\theta = \frac{d\sigma}{d\varepsilon}$), was computed using a running least-square linear fit of the composite σ - ε curve. To this end, a fixed number of data points, or “window size”, was first chosen to span on average 0.020%-0.025% strain. The linear fit over this window yielded one point on the θ - ε curve. The window was then translated by one point and the linear fit repeated, until the whole loading (resp. unloading) portion of the σ - ε curve was spanned. The contributions of the fibers ($E_f V_f$) and of Poisson’s ratio effects (Hill’s bounds θ_h , see Section 3.1, page 29) was then plotted as well on these curves. In Stage II, the difference between the composite θ value and $E_f V_f$ compensated for the influence of lateral contraction mismatch (*i.e.*, $E_f V_{f'} + \theta_h$), gives the matrix contribution to the composite work-hardening rate.

To reduce uncertainty in measurement of the composite modulus within linear regions of the stress-strain curve, a linear fit over a strain window of maximum width is preferable. In systems with high $V_{f'}$, the transition between deformation stages can involve only very small and/or gradual variations in slope; hence an

arbitrary determination of a yield stress could lead to large errors. It was found that maximizing the correlation coefficients of linear fits with varying window sizes was not effective, as all the coefficients were very close to 1. Hence, a different procedure was developed to measure composite elastic moduli.

In this procedure, the starting point of the region of interest (*e.g.*, the first data point of the unloading cycle) was held fixed and the end point gradually incremented. For each successive (increasingly large) window w , the least-square linear fit σ_{ls} was computed (as for θ above) as $\sigma_{ls} = a\varepsilon + b$, with the regression coefficients given by [106]:

$$a = \frac{w \sum \sigma \varepsilon - (\sum \sigma)(\sum \varepsilon)}{w \sum \varepsilon^2 - (\sum \varepsilon)^2}, \quad b = \frac{\sum \sigma - a \sum \varepsilon}{w}, \quad (4.5-1)$$

and the standard deviation of regression $S_{\sigma\varepsilon}$ given by

$$S_{\sigma\varepsilon} = \sqrt{\frac{\sum (\sigma - \sigma_{ls})^2}{w}} = \sqrt{\frac{\sum \sigma^2 - b \sum \sigma - a \sum \sigma \varepsilon}{w}}. \quad (4.5-2)$$

The corresponding LabVIEW™ code (part of the Yield! II program) can be found in Appendix C. An example is given in Figure 4-8 for a test on a Nextel 610 reinforced Cu-7wt%Al composite. It shows how $S_{\sigma\varepsilon}$ plotted versus strain gives the best estimate of the strain at which the unloading portion of the composite σ - ε curve starts to deviate from linearity. A confirmation of this can be found by looking at the apparent *in-situ* matrix stress-composite strain curve computed from that of the composite (see Figure 5-15 (c), page 117), where the change in slope is more pronounced. In practice, the $S_{\sigma\varepsilon}$ - ε curve either showed a minimum as in Figure 4-8 or a plateau followed by a sharp increase in $S_{\sigma\varepsilon}$. The strain corresponding to the end of the plateau was taken as the end of the elastic region of the corresponding composite stress-strain curve.

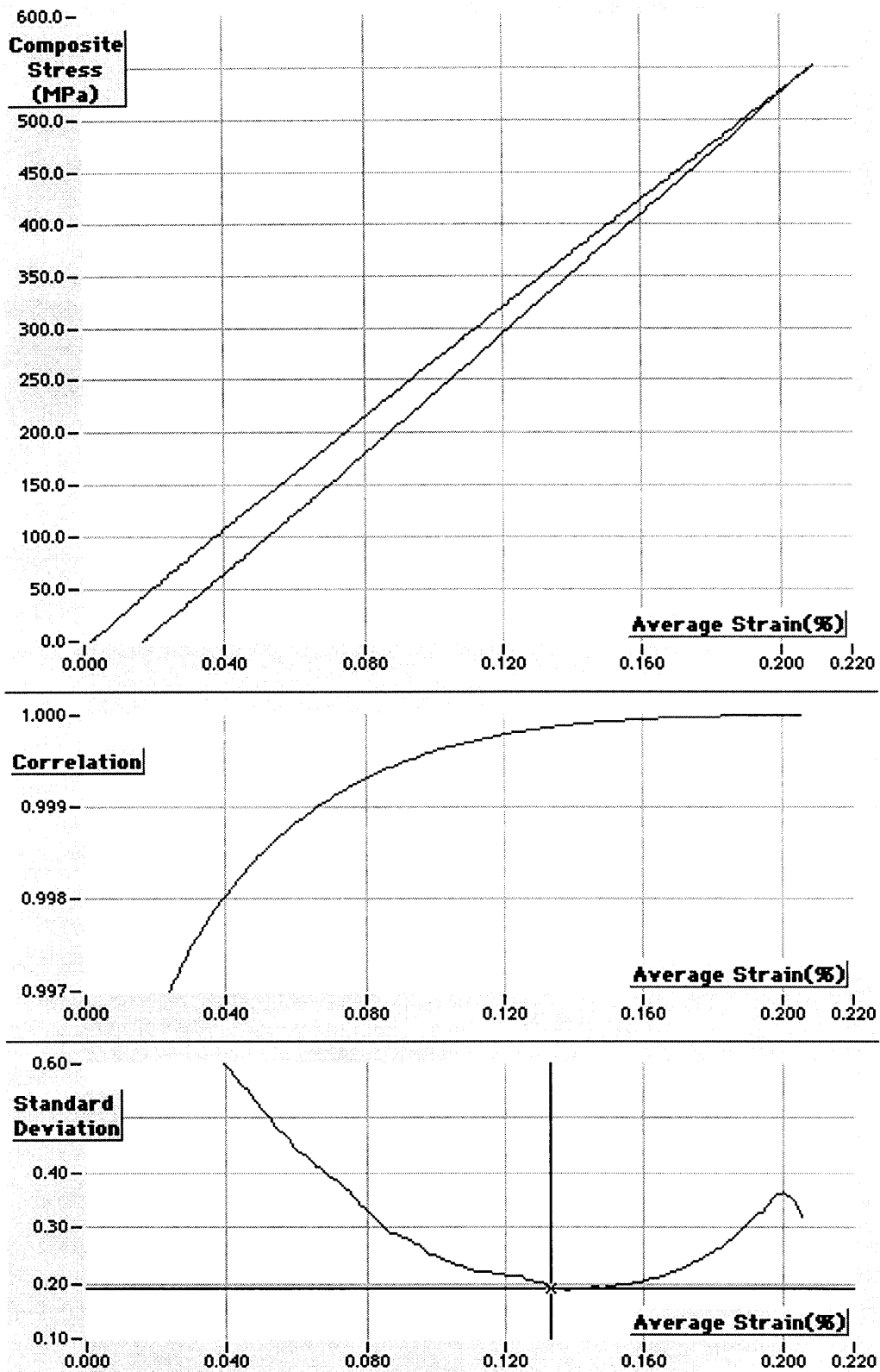


Figure 4-8 - Example of determination of yield stress (taken as point at which departure from linearity occurs) after elastic unloading (data from 1-3•CuAl/3M Test1, computed and plotted in Yield! II program).

4.5.2 Uncertainty on Fiber Modulus

The fiber elastic modulus E_f was taken as 379 GPa, as specified by the manufacturers (see Section 4.1.1 page 36); however, no mention has been found of the uncertainty on E_f . Since the latter is due to porosity in the fibers, ΔE_f was estimated using Mackenzie's formula for the effective elastic modulus of a solid containing a low density of spherical holes [107]:

$$\frac{G_0 - G}{G_0} = 5 \frac{3K_0 + 4G_0}{9K_0 + 8G_0} \left(1 - \frac{\rho}{\rho_0} \right), \quad (4.5-3)$$

where the subscript 0 indicates the fully dense material's moduli and density. This can be rewritten in terms of Young's modulus as :

$$E = E_0 \left(\frac{\nu + 1}{\nu_0 + 1} \right) \left(1 - \frac{15(1 - \nu_0)}{7 - 5\nu_0} \left(1 - \frac{\rho}{\rho_0} \right) \right). \quad (4.5-4)$$

Assuming that Poisson's ratio of the fiber is not affected by the (limited) porosity, we take $\nu_f \approx \nu_{0, Al_2O_3} \approx 0.24$ (see Table 3-1 page 30) to obtain:

$$E_f \approx E_{0,f} \left(1.97 \frac{\rho_f}{\rho_{0,f}} - 0.97 \right), \quad (4.5-5)$$

therefore:

$$\Delta E_f = 1.97 E_{0,f} \frac{\Delta \rho_f}{\rho_{0,f}}. \quad (4.5-6)$$

From fiber density data (see Table 4-2 page 65), the resulting uncertainty on the fiber modulus is $\Delta E_{FP} \approx 3$ GPa and $\Delta E_{Nextel\ 610} \approx 2$ GPa.

4.5.3 Uncertainty on Stress-Strain Slope

It was seen in Section 4.3.4.6 page 52 that all sources of error associated with the measurement of composite stress and strain are negligible compared to the error ΔA on the sample cross-section. In addition, it was verified that the procedure used to

determine θ_c , described above in Section 4.5.1 page 71, introduces an error in the value of the composite slope which is smaller by at least an order of magnitude compared with the error arising from stress and strain measurement. It follows that the uncertainty on the slope of the composite stress-strain curve at any stage of deformation for strain ranges pertinent to this investigation (*i.e.* $\epsilon \leq 0.5\%$) is simply given by:

$$\Delta\theta_c = \theta_c \frac{\Delta A}{A} . \quad (4.5-7)$$

4.6 Metallography

Composite samples were examined under an Olympus VANOX-T microscope (Model AHMT, from Olympus Corp., Lake Success, NY) to check for fiber distribution, absence of porosity, and absence of reaction at the fiber-matrix interface. After sectioning on a low speed diamond saw, the grinding/polishing procedure was as follows:

- rough grinding with 400 grit SiC paper or lower to produce flat surface;
- 600 grit SiC paper;
- 6 μm , 3 μm , then 1 μm diamond paste;
- Final polishing: Mastermet™ (colloidal silica) or Magomet™ (MgO powder) (trademarks of Buehler, Lake Bluff, IL).

Table 4–5 lists the etchants used for each matrix.

Copper composites were also polished to 1 μm diamond paste, slightly electropolished to remove the surface layers damaged from mechanical polishing, then etched to reveal dislocations that intersect {111} grain surfaces by etch-pitting [108, 109]. This technique was used to assess grain size in pure copper matrix specimens.

Additional metallographic characterization was conducted using scanning electron microscopy of fibers and of fracture surfaces; the microscopes used were a

conventional Cambridge SEM, an Electro Scan Environmental SEM, and a JEOL JSM 6320FV Field Emission SEM. Gold coating was applied to the fibers and composite samples to prevent charging inside the microscopes.

Table 4-5 - Etchants

System	Etchant name	Etchant composition
Aluminum 99.999%, Al-4.5wt%Cu, Al-0.9wt%Mg	Keller's etch	2 ml HF (48%) 3 ml HCl 5 ml HNO ₃ 190 ml H ₂ O
	Barker's electrolytic etch	2 ml HBF ₄ 100 ml H ₂ O Several min at 20 V Observe under polarized light, with 530 nm tint plate
	Potassium permanganate etch	2 g NaOH 4 g KMnO ₄ 1000 ml H ₂ O
Copper 99.996% (Prepare surface by electropolishing in H ₃ PO ₄ before etching)	Livingston's etch [108, 109]	By volume: 1 part Br ₂ 15 parts CH ₃ COOH 25 parts HCL (38%) 90 parts H ₂ O
	Hydrogen peroxide etch [99, 110]	40 ml NH ₄ OH 20 ml H ₂ O 1 ml H ₂ O ₂ (30%)
Cu-7wt%Al	Iron (III) chloride etch [111]	20 ml HCl 5 ml FeCl ₃ · 6H ₂ O 100 ml H ₂ O
Cu-1wt%Ti	Potassium dichromate etch [111]	10 g K ₂ Cr ₂ O ₇ 5 ml H ₂ SO ₄ 2 drops HCl (immediately before use) 80 ml H ₂ O

5. Results

5.1 Composite Characterization

5.1.1 Infiltration

Aluminum and binary aluminum alloy composites were cast without significant difficulty. The aluminum-alumina bond was found to be strong, there was no reaction at the interface, and no detectable porosity in the composites. Chemical analyses of the master alloy and composite samples (by Luvak, Inc., Boylston, MA) showed that there was some level of copper macrosegregation across Al-Cu samples, the copper concentration increasing somewhat from the top to the bottom of the cast bars. The copper concentration was low at the top of the casting and increased in its lower portions, such that it may have exceeded locally the 5.65wt% solubility limit of Cu in Al. For this reason, the CuAl_2 second phase could not be put fully into solid solution, even when solutionizing times were extended to three and five days. The measured average composition in the gage section of Al-Cu composites, namely 4.8wt%, remained close, however, to that of the original Al-4.5wt%Cu master alloy. No comparable segregation was observed in the Al-Mg composites. Results of chemical analyses are given in Table 5-1.

In contrast to the Al/ Al_2O_3 system, Cu/ Al_2O_3 composites were considerably more difficult to produce. The bond between pure copper and alumina was found to be weak to the point of rendering the composites fragile during handling, and composite infiltration results were also unpredictable. A decrease in solidification time after pressure infiltration appeared to increase the likelihood of obtaining a successfully infiltrated composite; it may be, therefore, that observed infiltration problems emanated from a tendency of the matrix to dewet the fibers after infiltration. Surface roughness on Fiber FP alumina fibers seemed to improve bonding between matrix and fiber somewhat, as compared with the smooth surface of Nextel 610. This observation is consistent with published results on copper-alumina bonding [112]. The higher volume fraction fiber attained in a fully packed

Table 5-1 - Results of chemical analyses

Aluminum-Copper	Weight(%) Cu	Weight(%) Si	Weight(%) Al
<u>Unreinforced 1•AlCu/NoFibers</u> †	4.58	0.017	balance
<u>AlCu/FP composite</u> ‡			
Top of casting (from 3•AlCu/FP)	2.98, 2.99	0.024	balance
Gage section (from 3-6•AlCu/FP)	4.82	0.035	95.1
Aluminum-Magnesium	Weight(%) Mg	Weight(%) Si	Weight(%) Al
<u>Unreinforced AlMg master alloy</u> □			
Top of casting	0.93	0.010	99.0
Bottom of casting	0.94	<0.005	99.0
<u>AlMg/FP composite and unreinforced AlMg tensile bars</u> ‡			
Bottom of casting	0.88	0.12	99.0

† Machined from master alloy as received from ALCOA (Pittsburgh, PA)
‡ Pressure cast
□ Cast conventionally from high purity Al and Mg

fiber preform with Nextel 610, combined with the smaller fiber diameter, increased the difficulty of producing a sound composite with this fiber in copper.

Cu/FP composites were successfully cast (see Figure 5-1), machined, and tested. Efforts to produce Cu/Nextel 610 composites were unsuccessful as bars of this system, even when fully infiltrated, proved too brittle for handling. In an attempt to improve the matrix-fiber bond strength, binary copper alloy matrices were

therefore also produced. Aluminum, which bonds strongly to the fibers, was added to copper for this reason. Cu-7wt%Al indeed showed a marked improvement in bond strength over pure copper, although the resulting interface was still weak, especially in Nextel 610 reinforced composites. The addition of titanium to copper has been shown to increase the work of adhesion between copper and alumina by reducing the Cu/Al₂O₃ interfacial tension. This results in the formation of an oxide of titanium at the interface and produces a strong chemical bond with polycrystalline α -Al₂O₃ [113-115]. Cu-1wt%Ti composites indeed displayed strong interfaces comparable to aluminum composites. Nextel 610 reinforced Cu-1wt%Ti failed prematurely in tension, however. Fiber degradation due to the reactive wetting was suspected, although SEM observations combined with X-ray analysis of CuTi/3M showed no conclusive evidence of a reaction layer. A qualitative evaluation of the fiber/matrix bond strength in all the systems tested is given in Table 5-2.

Table 5-2 - Qualitative measure of fiber/matrix bond strength in composite systems investigated

Matrix ↓	Fiber →	Fiber FP	Nextel 610
99.999% Al		Strong	Strong
Al-4.5wt%Cu		Strong	—
Al-0.9wt%Mg		Strong	—
99.996% Cu		Poor	Unusable
Cu-7wt%Al		Medium	Nearly unusable
Cu-1wt%Ti		Strong	Strong, causing premature composite failure in tension

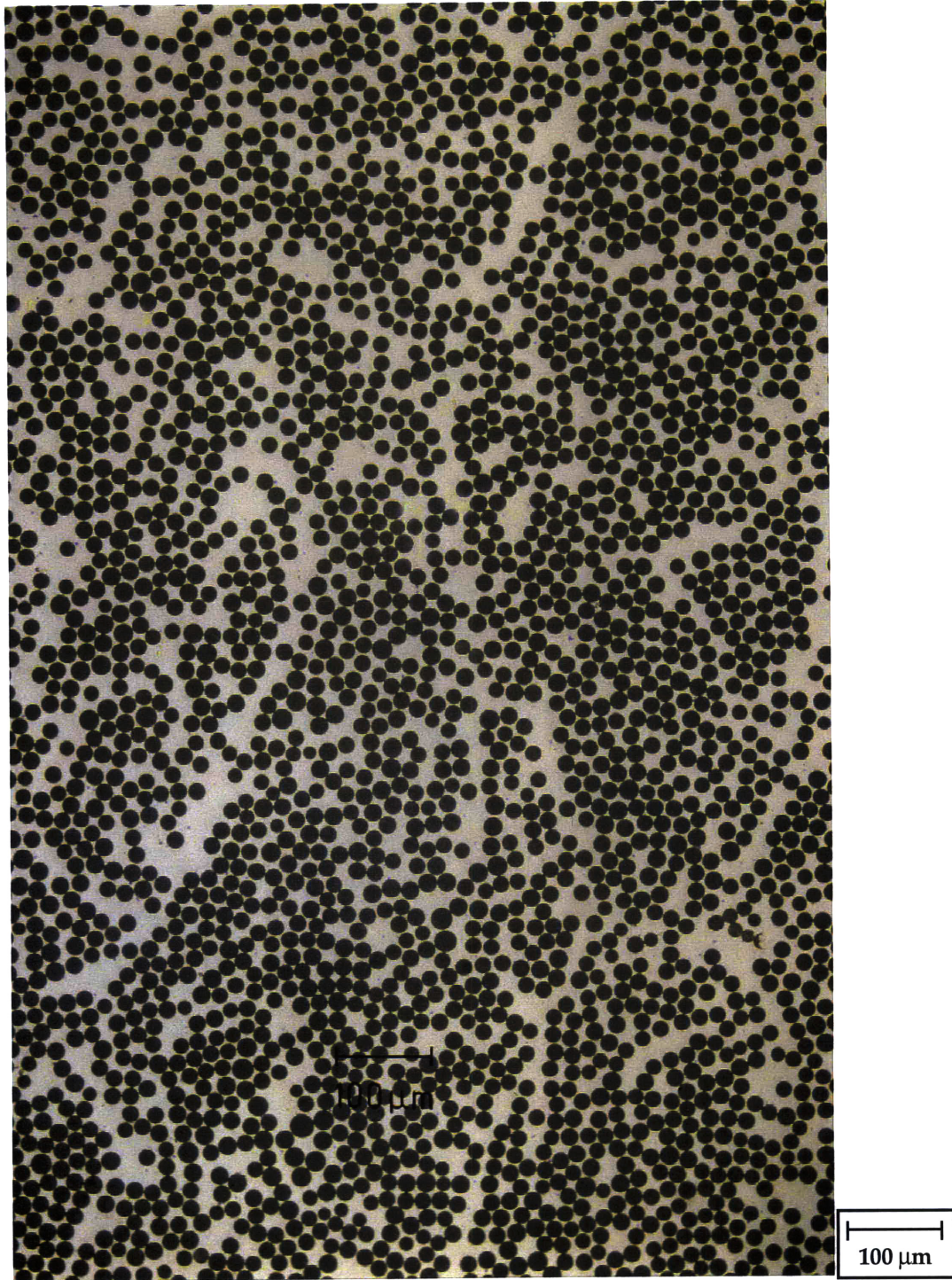


Figure 5-1 - Annealed 99.996%Cu reinforced with 60% Fiber FP, after mechanical testing, showing complete infiltration and uniform fiber distribution (Sample 1-1•Cu/FP).

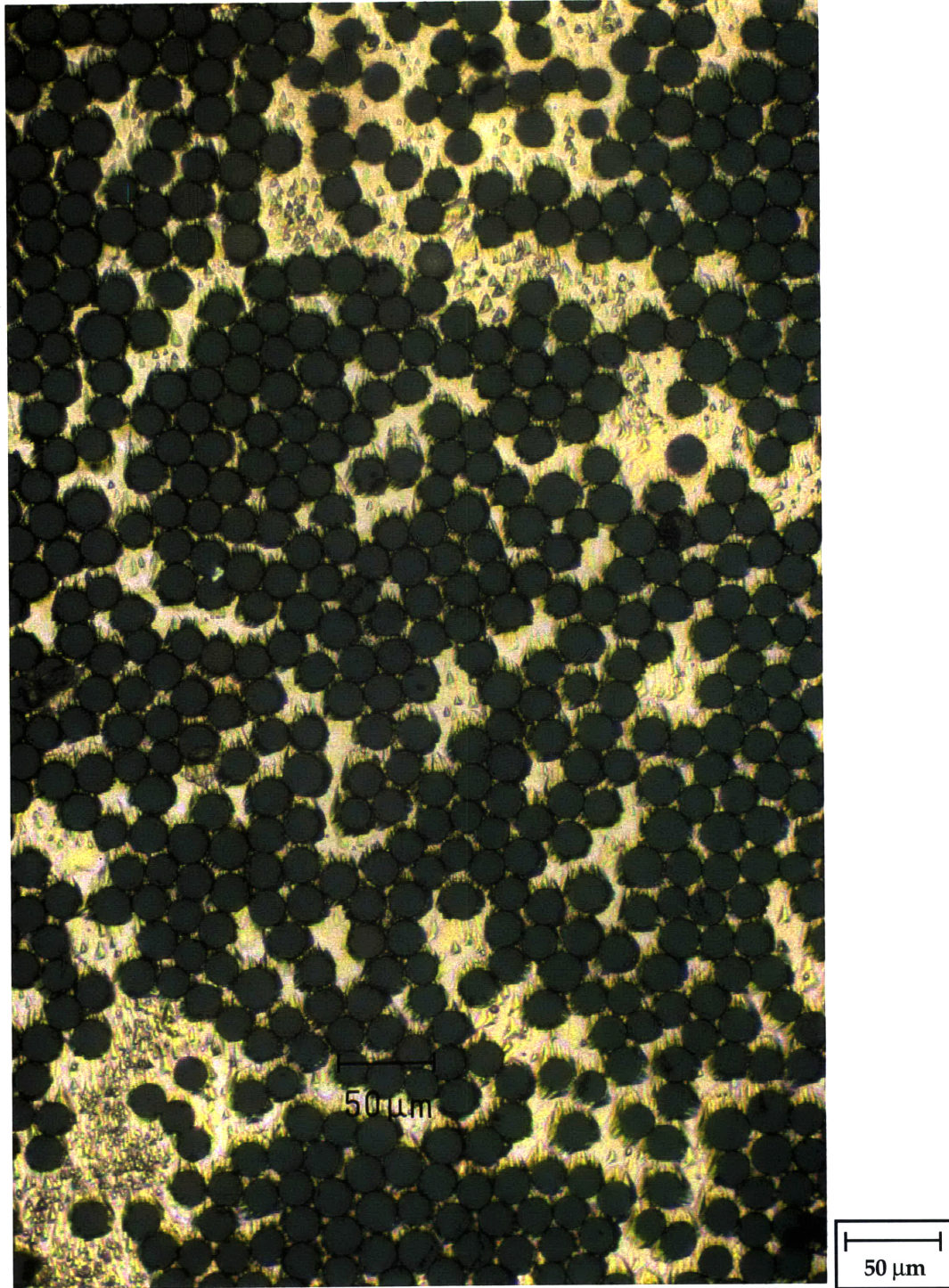


Figure 5-2 - As-cast and annealed 99.996%Cu reinforced with 60% Fiber FP, hydrogen peroxide etch (Table 4-5). Etch pits with identical orientation and shape show large grain size (Sample 0-3•Cu/FP).

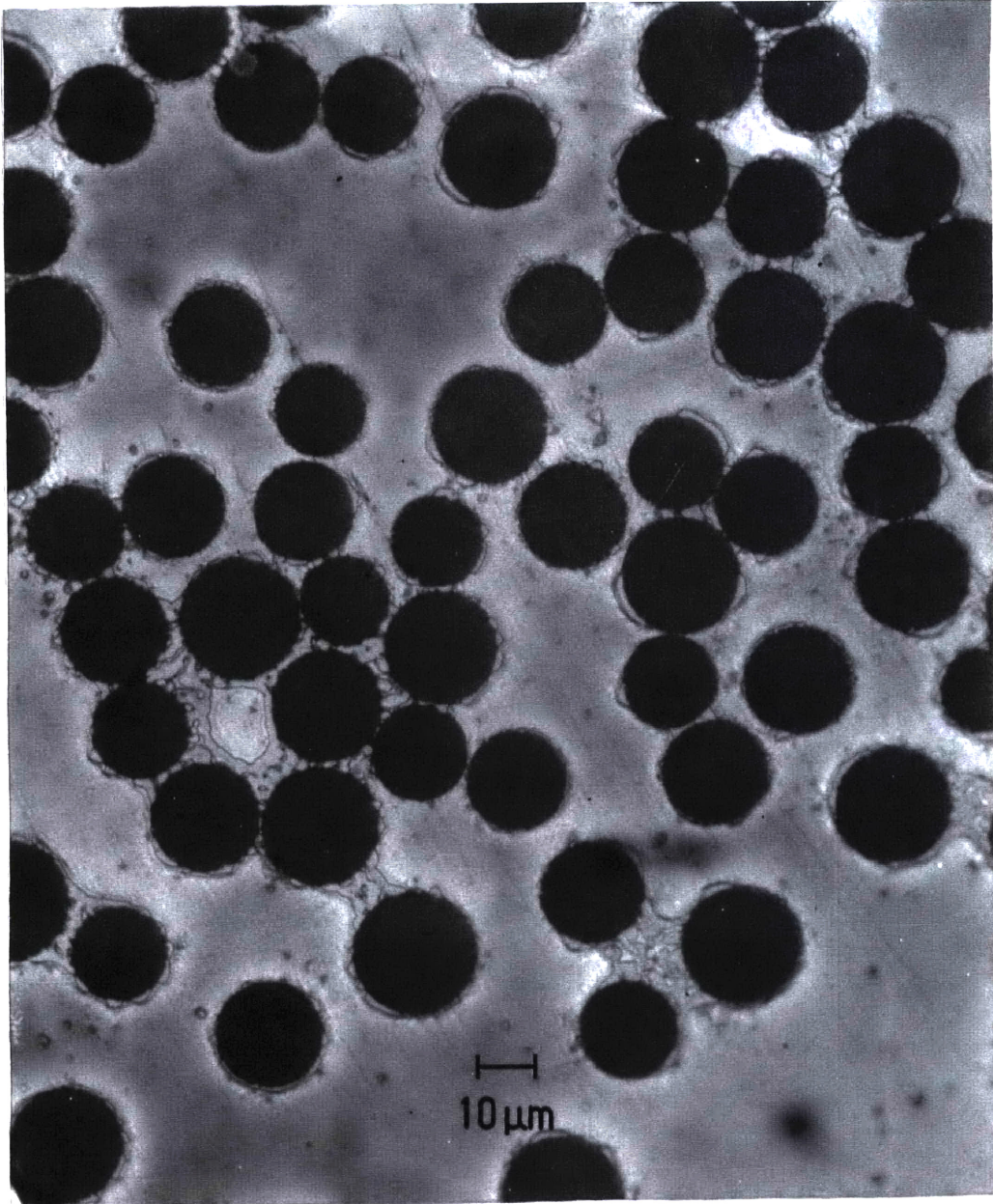


Figure 5-3 - As-cast Al-4.5wt%Cu reinforced with approximately 42% Fiber FP. Keller's etch shows the presence of θ (CuAl_2) phase at the fiber-matrix interface.

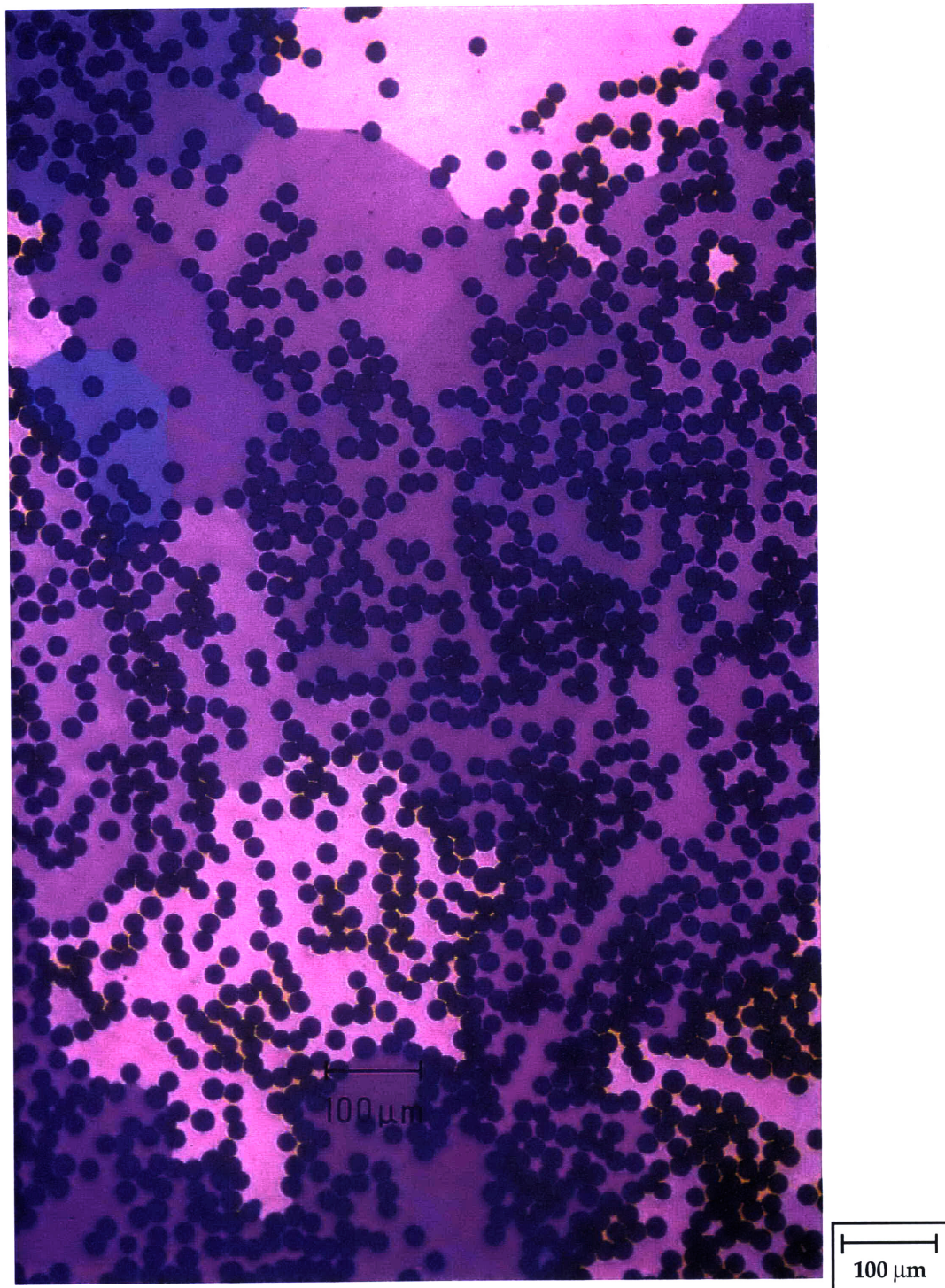


Figure 5-4 - As-cast Fiber FP reinforced Al-0.9wt%Mg. Low volume fraction ($V_f = 34\%$) allows large grains, revealed by Barker's etch, to be clearly distinguishable under polarized light, with grain boundaries pinned at fibers (Sample 10•AlMg/FP).

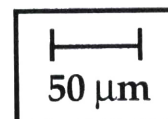
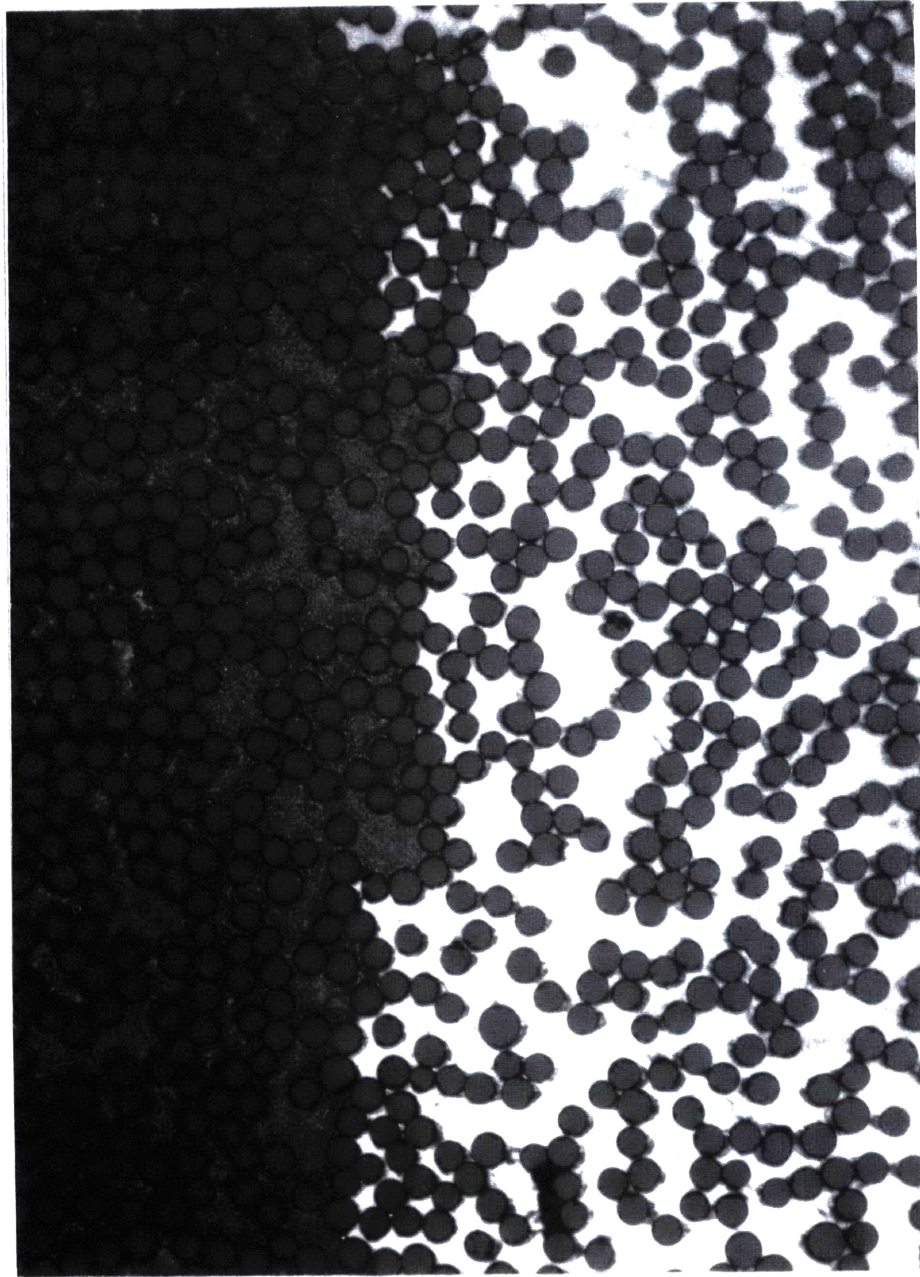


Figure 5-5 - As-cast Cu-1wt%Ti reinforced with 53% Fiber FP, etched in potassium dichromate (Table 4-5), showing a grain boundary (Casting number 1•CuTi/FP).

5.1.2 Microstructure

Samples cut parallel and perpendicular to the fiber direction were prepared. The grain size in all systems was assessed using optical metallographic techniques. Transverse to the fibers, grain diameters were found to be on the order of 100 μm for AlCu/FP (T4) composites, 400 μm for AlMg/FP (AC) and Cu/FP composites, and greater than 2 mm for CuAl/FP, CuAl/3M, CuTi/FP & CuTi/3M (AC) composites, Figure 5-5. The grain size in infiltrated Al/FP composites was determined in earlier work to be about 300 μm [24]. In all composites investigated, therefore, the matrix grain size was significantly larger than the fiber diameter.

5.1.3 Fiber Volume Fraction

Results from fiber volume fraction measurements using the two techniques of (i) pycnometry and (ii) matrix dissolution, are given in Table 5-3. It is seen that V_f measurements by the two techniques show good agreement in all Fiber FP reinforced composites, within the uncertainty in pycnometric measurements of this quantity (Section 4.4.2, page 61). With Nextel 610 fiber reinforced aluminum composites, V_f measurements by pycnometry lie somewhat below values measured by dissolution. This could arise due to the presence of porosity within the composites, either within the fiber itself, or within the matrix between closely spaced fibers.

Our measurement of the fiber density by pycnometry in xylene yielded the value 3.82 g cm^{-3} : this value is a lower bound of the fiber density (since any bubble within the fiber bundle would lower the measurement significantly), and can only account for half of the difference in V_f values obtained by the two techniques for these composites. We therefore view as most plausible that pores within the matrix of these composites account for the discrepancy between the two measurements, and retain the measurement of V_f by pycnometry computed using the fiber density value given by the manufacturer, of 3.85 g cm^{-3} as the most precise, with the implication

that, for consistency, the fiber modulus used in computing the matrix stress is also that provided by the manufacturer, of 379 GPa, for all Nextel 610 fiber reinforced composites.

Table 5-3 - Comparison of fiber volume fraction determined from density ($V_f(\rho_{pyc})$) and from matrix dissolution using fiber density ($V_f(\rho_f)$) and matrix density ($V_f(\rho_m)$)

Specimen	$V_f(\rho_{pyc})$ (%)	$V_f(\rho_f)$ (%)	$V_f(\rho_m)$ (%)
0-5•Al/FP	48.6	48.0	47.7
1-1•Al/3M	56.1	57.6	58.3
1-62•Al/3M	51.8	54.1	55.1
2-4•Al/3M	67.5	70.3	71.6
3-6•AlCu/FP	45.3	45.3	45.4
3-1•Cu/FP	60.0±1.5	56.1	58.4
3-4•Cu/FP	63.2	61.5	62.5
4-1•Cu/FP	56.5	54.4	55.6
4-2•Cu/FP	60.0	58.7	59.5
1-1•CuAl/FP	50.4	49.1	49.7

Finally, it should be pointed out that the values of V_f presented in Table 5-3 for pycnometry measurements were conducted using the portions of the respective composite bars that were subsequently dissolved. These are therefore not always

exactly equal to the corresponding values of $V_f(\text{pyc})$ used to compute the apparent *in-situ* matrix stress-strain curves (given in Table 5-5 and Table 5-6, page 94, and Table A- 4, page 162), which were measured on whole bars prior to testing. The (possible) difference between the two values reflects the (small) variation in V_f throughout a single composite bar as well as uncertainty in the measurement of V_f .

5.2 Mechanical Tests

5.2.1 Unreinforced Matrix Reference

Bars of unreinforced matrix from each system were prepared and tested under the same conditions as the composites to provide a reference for the computed apparent *in-situ* matrix stress-strain curves. The unreinforced Al-4.5wt%Cu was machined directly from the master alloy as received from ALCOA (Pittsburgh, PA). All the other reference samples were pressure cast as part of the same run as the corresponding composites.

All bars were then heat treated identically to the respective composites prior to testing, and aluminum tabs were glued in the grip sections as well. The unreinforced matrices were then subjected to several tension-compression cycles (the sole exception was Al-0.9wt%Mg, which was tested in tension only) in the strain range of the composite tests, *i.e.*, less than 1%. The strains attained in the compressive portions of the cycles were generally lower than in the composites because the lower stiffness of the unreinforced bars was accompanied by an earlier onset of buckling (this was detectable by comparison of the signals from the two strain gages). Stress-strain curves of the unreinforced matrices are presented in Figure 5-6 and Figure 5-7.

Young's modulus of 99.999% pure aluminum at room temperature, measured in the early elastic loading portion of the first tension, was 69 GPa and dropped to 64 GPa in all the subsequent elastic loading and unloading portions of each cycle. The slope in the plastic regime varied from 1 GPa in the first cycle (at 0.15% strain) to 0.5

GPa in the 10th cycle (at 0.85% strain). When pure aluminum was tested at 77 K, Young's modulus increased to 81 GPa (a value which is in reasonable agreement with that of 78 GPa given in the literature [93, 116]), and the slope in the plastic regime increased to 1.9 GPa. The tension-compression stress amplitude (at 0.4% strain amplitude) also roughly doubled, from about 35 MPa at room temperature to 60 MPa at 77 K.

The experimentally determined elastic moduli of all unreinforced matrices are given in Table 5-4, page 93. The slopes in the plastic regime at strains relevant to this study can be found in Table 5-5 and Table 5-6, page 94, and the corresponding approximate stress amplitudes are summarized in Table 6-1, page 147.

Two samples each of 99.996%Cu and Cu-1wt%Ti were tested, exhibiting different values for Young's modulus in each case. This result is not unexpected, owing to the orientation dependence of the modulus in copper (see Table 4-4, page 70).

One Cu-1wt%Ti sample was re-annealed after the first series of tests, heated to 120°C for 1h, and re-tested to investigate the influence, if any, of such heating (required for mounting tabs onto CuTi/3M samples) on the mechanical response of Cu-1wt%Ti.

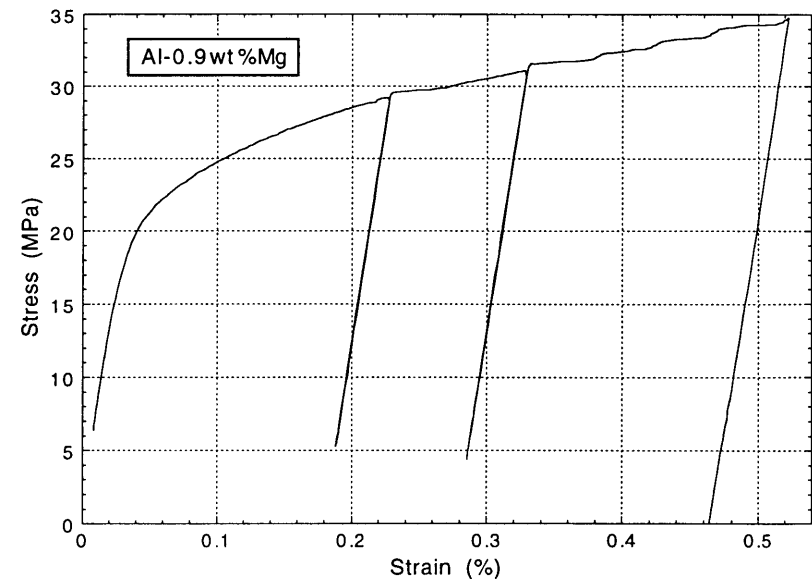
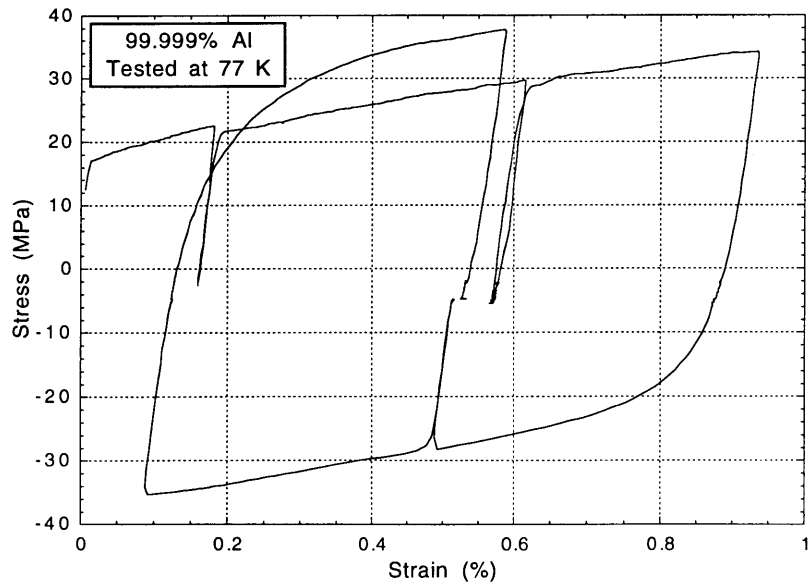
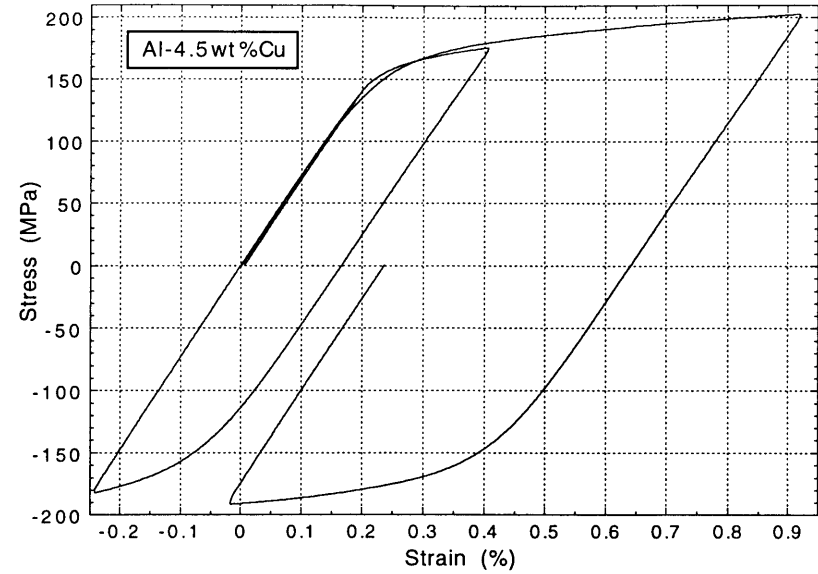
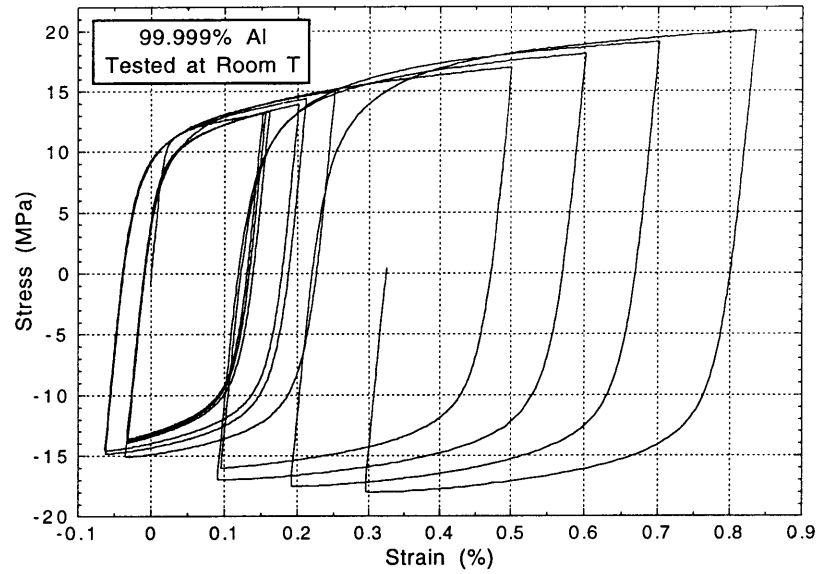
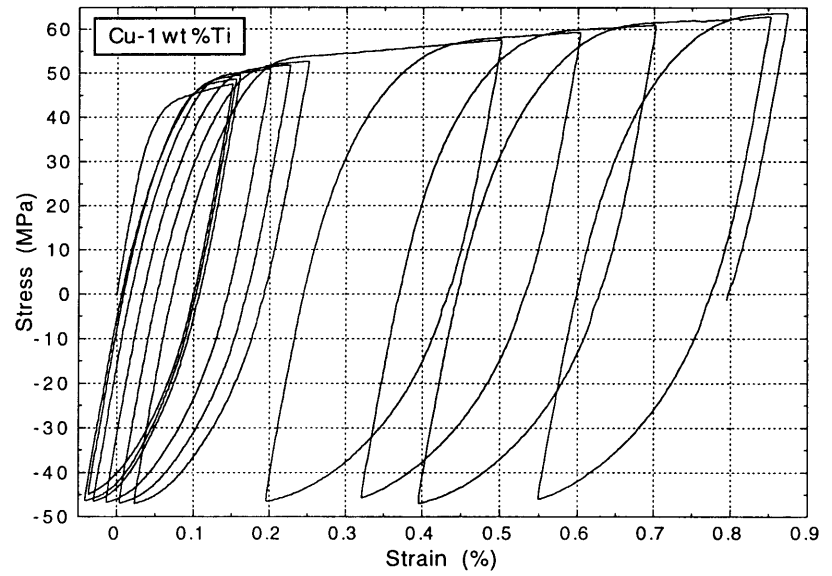
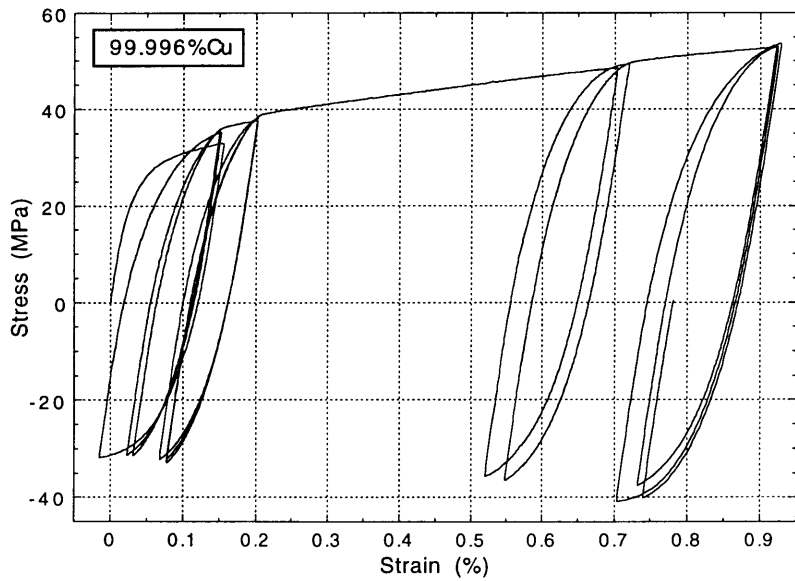
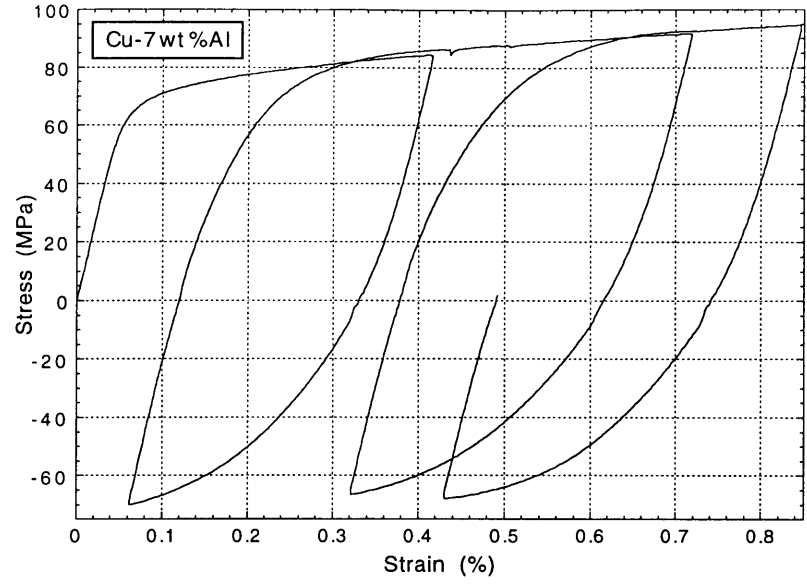
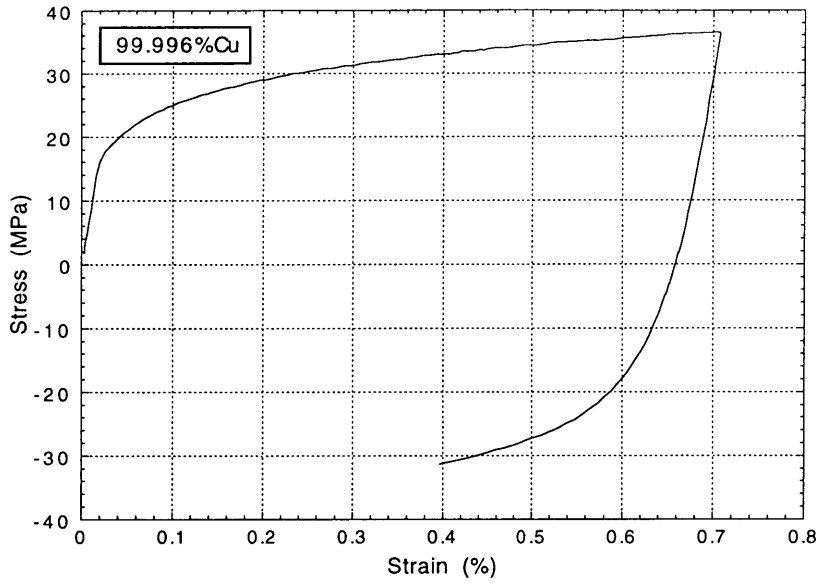


Figure 5-6 - Unreinforced matrix reference stress-strain curves of pure aluminum (tested at room temperature and at 77 K) and of Al-4.5wt%Cu and Al-0.9wt%Mg.



06

Figure 5-7 - Unreinforced matrix reference stress-strain curves of pure copper (tested once and eleven times in tension-compression) and of Cu-7wt%Al and Cu-1wt%Ti.

5.2.2 Composites

Several samples for each system were tested monotonically and in tension-compression to varying strain amplitudes. All mechanical tests conducted are summed up for all systems and samples in Table A- 4, page 162.

Experimental problems encountered during tests included occasional tab debonding, especially in Nextel fiber reinforced composites. This resulted in the presence of gaps in some of the recorded composite stress-strain curves; however, since strain was measured using strain gages, this problem was not deemed to invalidate the test when it occurred on a minor scale. A second occasional source of stress-strain curve imperfection was found to be generated by the screw-driven mechanism of the testing apparatus during transitions from composite tension to compression and vice-versa. This caused the formation of small spikes near zero strain (but not zero stress) on some matrix *in-situ* stress-strain curves.

An example of the stress-strain curves recorded is given for each system in Figure 5-8 to Figure 5-17 (pages 96 to 123). Each figure shows (a) the composite stress-strain curves; (b) the corresponding θ curves; (c) the corresponding apparent *in-situ* matrix stress, computed using Eq. (3.2-7), page 33, with V_f determined by pycnometry, plotted versus composite strain; and (d) error bounds on the apparent matrix stress, computed from Eq. (3.3-3), page 34. It is seen that for all composites investigated, composite stress-strain curves display, upon initial tension or initial compression to sufficient strain, the classical two-stage bilinear shape. The corresponding composite theta curves show that, for all examples given, the composite rate of work-hardening in Stage II tends towards a constant value, which generally lies in the vicinity of $E_f V_f$.

Computed matrix *in-situ* stress-strain curves result from the subtraction of two large numbers; hence any noise or other defects (such as the small spike occasionally generated upon stress reversal) in the original composite curve appears significantly amplified. Also, since uncertainty in V_f and other quantities is inherent to the matrix *in-situ* stress-strain curve computation, an overall "tilted" appearance is often found in these curves, as discussed in more detail below.

Therefore, strongly negative apparent rates of matrix work-hardening, which were found in several samples, particularly with Cu/FP and Cu-7wt%Al/3M systems, do not imply work softening of the matrix during plastic deformation in the composite.

The experimentally determined average slopes in elastic and plastic ranges of matrix deformation are given in Table 5-4 and Table 5-5 for each system investigated, together with the uncertainty, itemized by source, on these slopes, evaluated as described in Section 4.5.1, page 71. These slopes were computed from those of the composite stress-strain curves *via* Eq. (3.2-2), page 32, using an average value of V_v , determined by pycnometry, and θ_h given by Eq. (3.2-4), page 33, for elastic deformation, and by Eq. (3.2-3) for plastic matrix deformation. Values given are averages of all available measurements on the composite stress-strain curves for each system. The corresponding slopes of the unreinforced matrices are given as well for comparison in the respective tables.

Apparent *in-situ* matrix elastic moduli, although somewhat low for Al/FP and Al-0.9wt%Mg/FP, compare acceptably in all other systems, being within experimental uncertainty of values measured with the corresponding unreinforced matrices (keeping in mind the large orientation-dependent variations which can occur in Young's modulus of Cu-based matrices, see Table 4-4 page 70).

It is seen in Table 5-5 and Table 5-6 that the plastic deformation rate of work hardening in compression is always greater than that measured in tension, for all systems. In Al-4.5wt%Cu and Al-0.9wt%Mg composites, the limited strain range did not allow complete yielding in compression and the slope in compression is hence overestimated. In the other systems, complete compressive yielding appears to have been reached and the difference between tensile and compressive slopes is real.

Tension-compression tests show a marked difference in yielding behavior, for binary alloy matrix composites, between initial loading in tension, which features very abrupt yielding, and subsequent tension cycles as well as all compression cycles, which feature much more gradual yielding.

Table 5-4 - Matrix elastic slope $\theta_{m,el}$ in the composite and associated experimental uncertainty (Averages of all available measurements; in GPa)

System	Elastic slope of unreinforced matrix reference	Average V_f (%)	Composite elastic slope $\theta_{c,el}$ (GPa)	Slope of matrix $\theta_{m,el}$ (GPa) in the composite	Uncertainty on $\theta_{m,el}$ (GPa) due to ΔV_f	Uncertainty on $\theta_{m,el}$ (GPa) due to ΔE_f	Uncertainty on $\theta_{m,el}$ (GPa) due to $\Delta\theta_{c,el}$ and $\Delta\theta_{h,el}$	Total estimated uncertainty $\Delta\theta_{m,el}$ (GPa)
99.999% Al/ FiberFP (room T)	64.0	30.3	152.2	53	3.5	1	0.5	5
99.999% Al/ FiberFP (77K)	81.0	46.8	231.8	96	3.5	2.5	1	7
99.999% Al/ Nextel 610	64.0	50.2	222.3	63	4	2	1	7
		55.7	238.6	61	5	2.5	1	8.5
		66.7	277.4	73	6.5	4	1	11.5
Al-4.5%Cu/ Fiber FP	72.7	42.8	203.7	72	4	2	1	7
Al-0.9%Mg/ Fiber FP	62.0	37.3	172.9	50	6.5	2	0.5	9
99.996% Cu/ Fiber FP	90; 103	59.6	261.4	86	3	4.5	4.5	12
Cu-7%Al/ Fiber FP	127	51.1	244.1	102	2.5	3	2	7.5
Cu-7%Al/ Nextel 610	127	69.4	290.5	88	4.5	4.5	4	13
Cu-1%Ti/ Fiber FP	100; 120	53.0	253.0	110	1.5	3.5	1.5	6.5
Cu-1%Ti/ Nextel 610	100; 120	73.2	298.9	85	2.5	5.5	3.5	11.5

Table 5-5 - Matrix slope $\theta_{m,pl}$ in stage II and associated experimental uncertainty for aluminum-based matrices (Averages of all measurements; Shaded values are averages for each system; in GPa)

System	Plastic slope of unreinforced matrix reference	V_f (%)	Composite slope $\theta_{c,pl}$ (GPa) in tension	Composite slope $\theta_{c,pl}$ (GPa) in compression	Slope of matrix $\theta_{m,pl}$ (GPa) in the composite, in tension	Slope of matrix $\theta_{m,pl}$ (GPa) in the composite, in compression	Uncertainty on $\theta_{m,pl}$ (GPa) due to ΔV_f	Uncertainty on $\theta_{m,pl}$ (GPa) due to ΔE_f	Uncertainty on $\theta_{m,pl}$ (GPa) due to $\Delta\theta_{c,pl}$ and $\Delta\theta_{h,pl}$	Total estimated uncertainty $\Delta\theta_{m,pl}$ (GPa)				
99.999%Al/ FiberFP (RT) ($\theta_{h,pl}=3.0$ ± 1.5)	0.5-1.0	30.3	108.4	114.4	-13	-5	4	1.5	2	7.5				
		21.4	75.1	76.0	-12	-11								
		27.9	100.2	107.7	-12	-2								
		34.8	124.5	130.6	-16	-7								
		36.9	133.9	143.4*	-14	1*								
99.999%Al/ FiberFP (77K) ($\theta_{h,pl}=3.0$ ± 1.5)	1.9	47.0	186.9	194.7	7	21	5	2.5	2.5	10				
		48.0	174.7	—	-25	—								
		47.6	197.0	196.4	21	19								
		45.5	189.4	—	21	—								
		48.5	197.3	204.4	15	31								
		48.6	197.4	206.7	14	34								
		46.2	185.3	—	8	—								
		43.4	167.0	171.4	-5	-0.7								
		37.2	144.3	—	-3	—								
99.999%Al/ Nextel 610 ($\theta_{h,pl}=3.0$ ± 1.5)	0.5-1.0	50.2	192.4	—	-1.8	—	5.5	2	3	10.5				
		51.7	192.0	—	-15	—								
		48.8	192.8	—	10	—								
		55.7	212.6	214.1	-3	0.2					6	2.5	3.5	12
		56.2	215.9	217.0	0.3	3								
		55.2	209.2	211.3	-7	-2								
	66.7	255.9	265.2	3	31	7	4	4	15					
	65.5	247.0	—	-10	—									
	67.4	264.0	267.2	19	29									
	66.6	256.8	263.5	7	27									
	67.2	255.8	265.0	-4	24									
	Al-4.5%Cu/ Fiber FP ($\theta_{h,pl}=3.0$ ± 1.5)	3.3	42.8	165.5	182(*)					1	14(*)	4.5	2.5	2.5
40.7			162.1	—	8	—								
41.2			161.1	—	3	—								
42.3			163.6	—	0.2	—								
41.7			165.7	—	8	—								
44.5			172.4	182(*)	2	19(*)								
46.2			168.2	183(*)	-18	9(*)								
Al-0.9%Mg/ Fiber FP ($\theta_{h,pl}=3.0$ ± 1.5)	1.6	37.3	135.1	145(*)	-15	1(*)	8	1.5	2.5	12				
		39.9	144.2	156(*)	-17	2(*)								
		38.2	140.3	153(*)	-12	8(*)								
		33.8	120.8	127(*)	-16	-6(*)								

* Slope in compression is overestimated due to incomplete matrix yield in limited strain range explored.

Table 5-6 - Matrix slope $\theta_{m,pl}$ in stage II and associated experimental uncertainty for copper-based matrices (Averages of all measurements; Shaded values are averages for each system; in GPa)

System	Plastic slope of unreinforced matrix reference	V_f (%)	Composite slope $\theta_{c,pl}$ (GPa) in tension	Composite slope $\theta_{c,pl}$ (GPa) in compression	Slope of matrix $\theta_{m,pl}$ (GPa) in the composite, in tension	Slope of matrix $\theta_{m,pl}$ (GPa) in the composite, in compression	Uncertainty on $\theta_{m,pl}$ (GPa) due to ΔV_f	Uncertainty on $\theta_{m,pl}$ (GPa) due to ΔE_f	Uncertainty on $\theta_{m,pl}$ (GPa) due to $\Delta\theta_{c,pl}$ and $\Delta\theta_{h,pl}$	Total estimated uncertainty $\Delta\theta_{m,pl}$ (GPa)
99.99%Cu/ Fiber FP ($\theta_{h,pl}=4.0 \pm 1.5$)	1.0-1.7	59.6	211.4	224.5	-33	-19	4.5	4.5	7	16
		59.3	216.5	—	-30	—				
		60.3	218.8	—	-35	—				
		63.3	237.3	260(*)	-19	43(*)				
		62.1	228.6	231.5	-28	-20				
		55.6	188.8	201(*)	-59	-30(*)				
		60.3	221.7	247(*)	-27	35(*)				
		59.4	216.4	239(*)	-31	24(*)				
		58.1	212.3	—	-28	—				
		58.2	206.7	217.5	-43	-17				
Cu-7%Al/ Fiber FP ($\theta_{h,pl}=4.0 \pm 1.5$)	2.1	51.1	190.0	204.7	-16	14	3.5	3	4.5	11
		50.2	185.9	202(*)	-17	15(*)				
		50.1	183.9	194.2	-20	1				
		52.1	196.8	213(*)	-10	25(*)				
		52.2	193.5	210(*)	-17	17(*)				
Cu-7%Al/ Nextel 610 ($\theta_{h,pl}=3.1 \pm 1.2$)	2.1	69.4	250.9	266.5	-49	2	6.5	4.5	6.5	17.5
		68.6	245.0	257.5	-58	-18				
		70.1	256.8	275.5	-40	23				
Cu-1%Ti/ Fiber FP ($\theta_{h,pl}=4.0 \pm 1.5$)	1.2	53.0	205.1	214.3	0.5	22	2	3.5	4	9.5
		53.6	212.9	—	12	—				
		53.9	207.9	218.2	-0.4	22				
		52.2	200.5	209.2	-3	16				
		52.3	199.0	215.5	-7	28				
Cu-1%Ti/ Nextel 610 ($\theta_{h,pl}=3.1 \pm 1.2$)	1.2	73.2	275.7	283.1	-18	18	3	5.5	5	13.5
		72.6	277.1	283.1	-3.5	18				
		73.8	274.3	—	-33	—				

* Slope in compression is overestimated due to incomplete matrix yield in limited strain range explored.

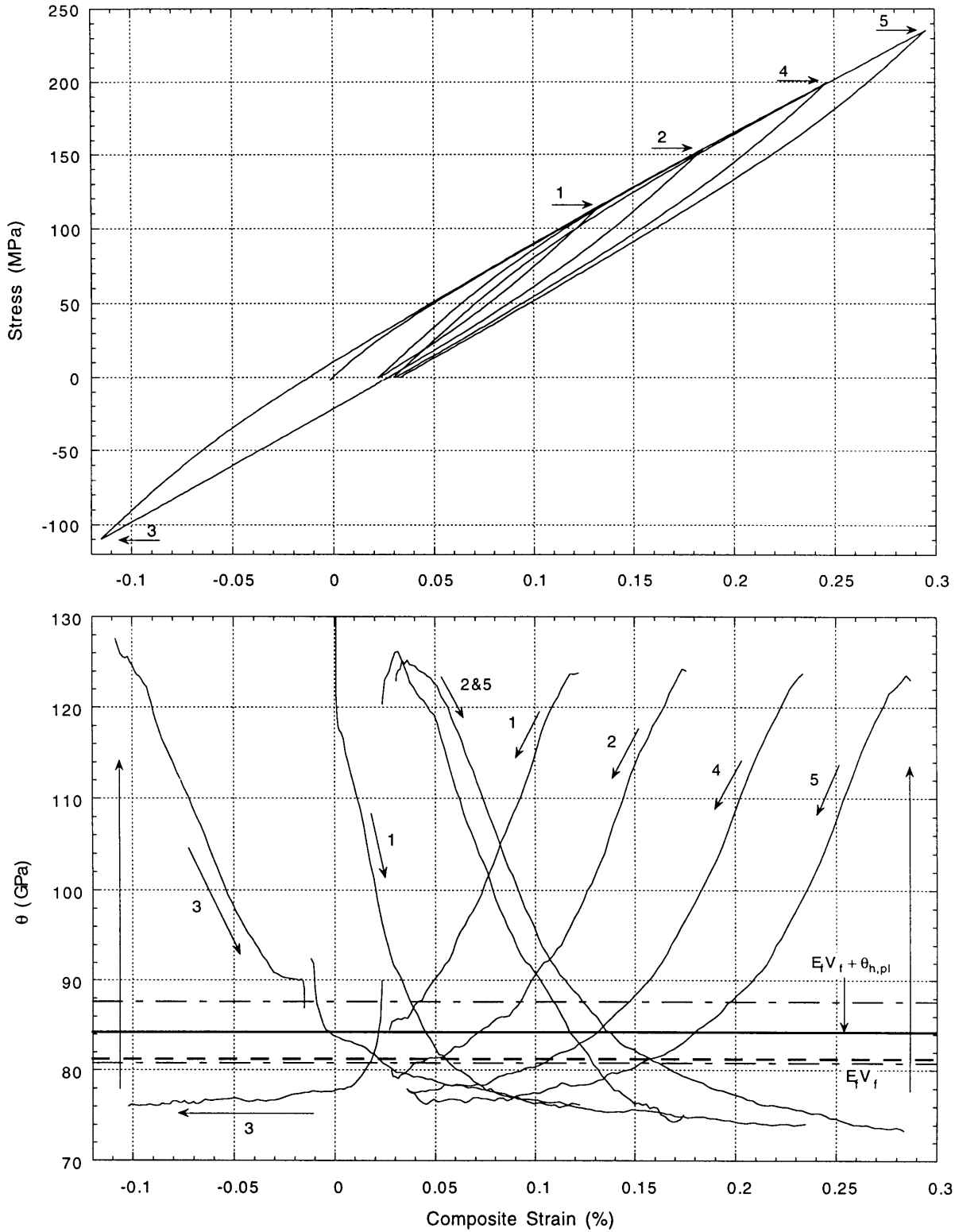


Figure 5-8 - (a) Stress-strain curve of pure aluminum composite reinforced with 21.4% Fiber FP, tested at room temperature (Sample 1-1•Al/FP) (top graph).
 (b) Corresponding Theta curves for each cycle (bottom graph). Horizontal lines represent $E_f V_f$ (dashed line) and $E_f V_f + \theta_{h,pl} \pm \Delta(E_f V_f + \theta_{h,pl})$.

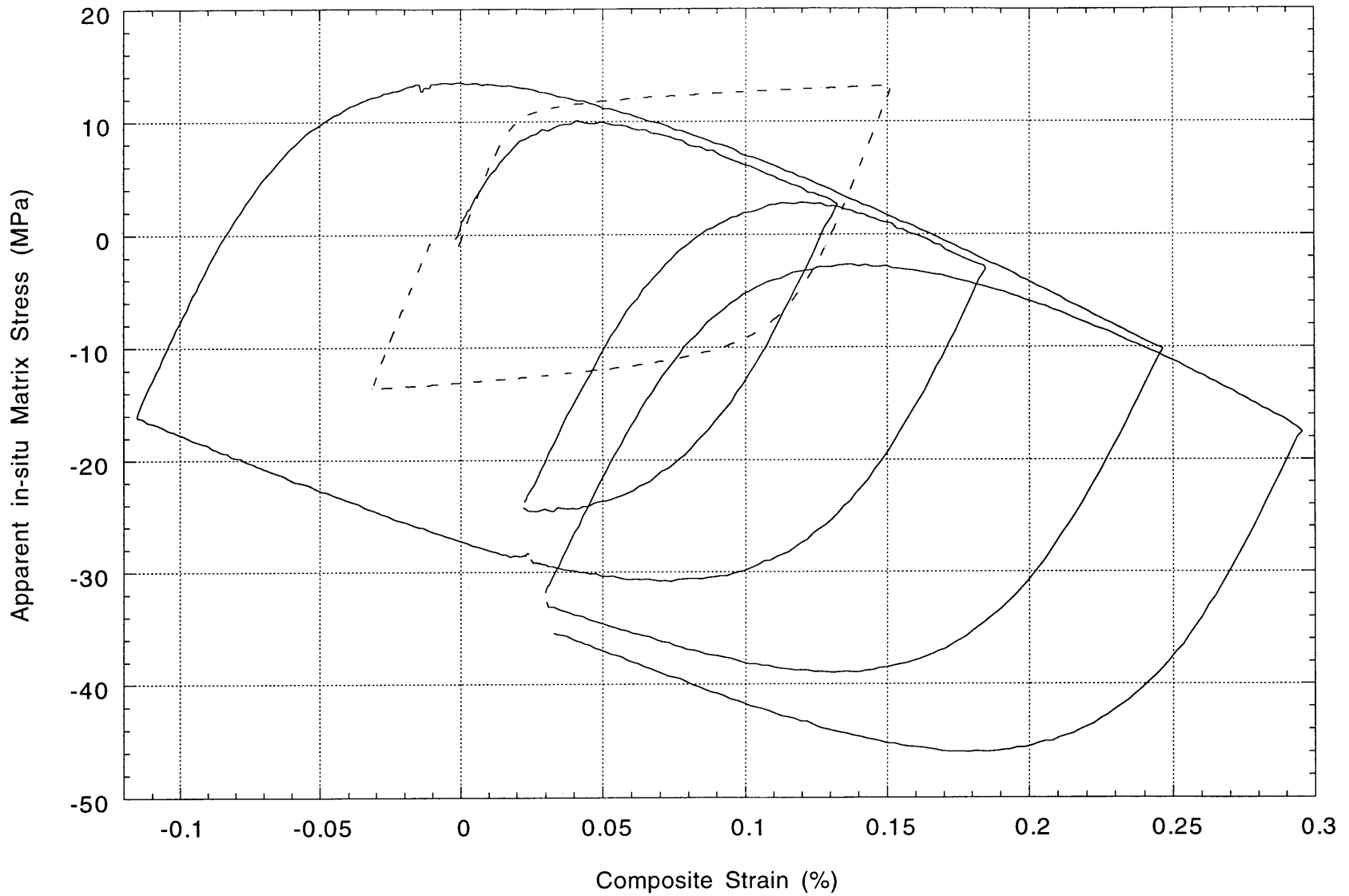


Figure 5-8 - (c) Apparent *in-situ* matrix stress-strain curve of pure aluminum computed from composite reinforced with 21.4% Fiber FP, tested at room temperature (Sample 1-1 • Al/FP). Dashed line shows unreinforced matrix tested as reference.

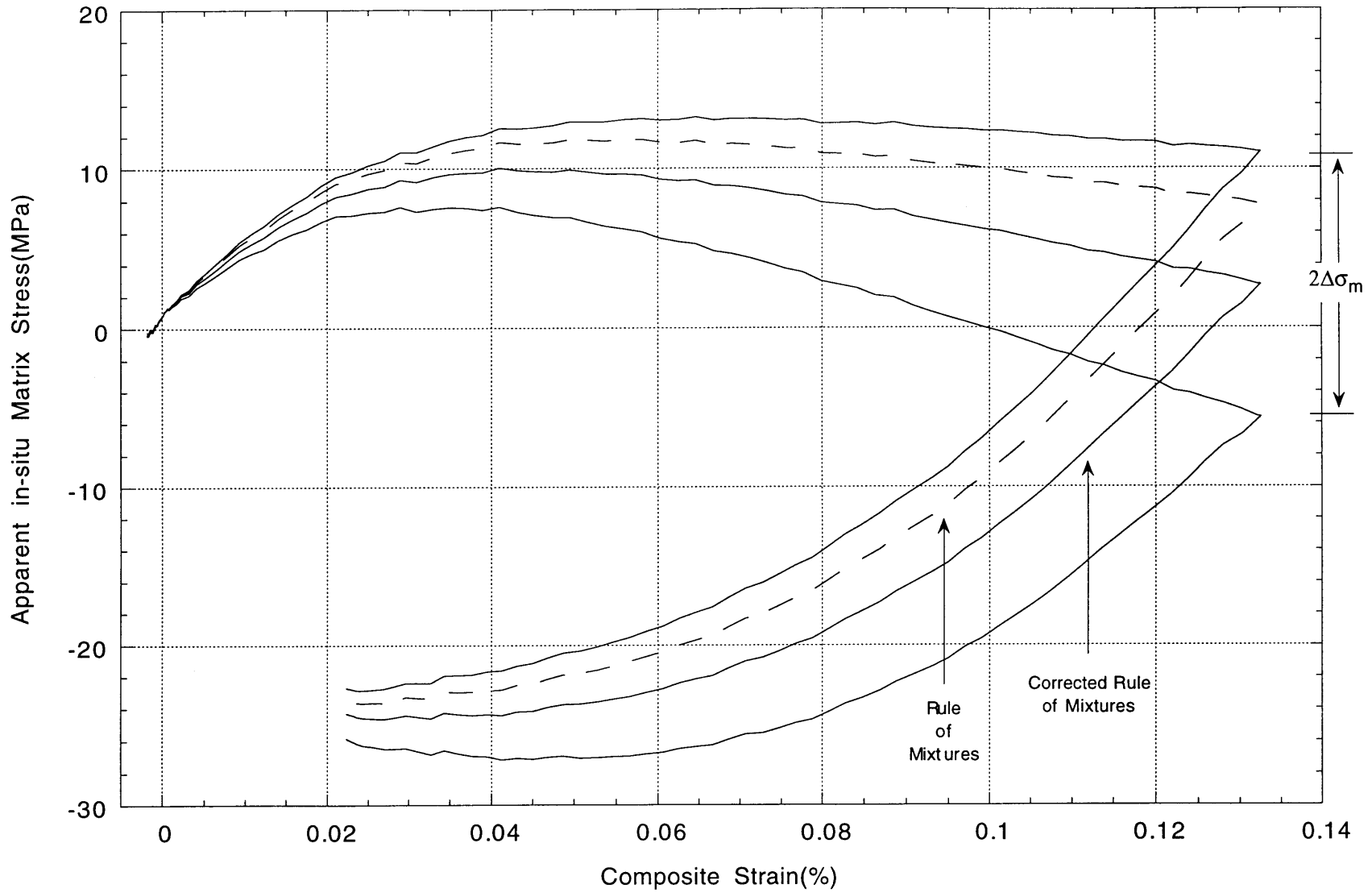


Figure 5-8 - (d) Total estimated uncertainty on apparent *in-situ* matrix stress-strain curve of pure aluminum computed from composite reinforced with 21.4% Fiber FP, tested at room temperature (Sample 1-1•Al/FP).

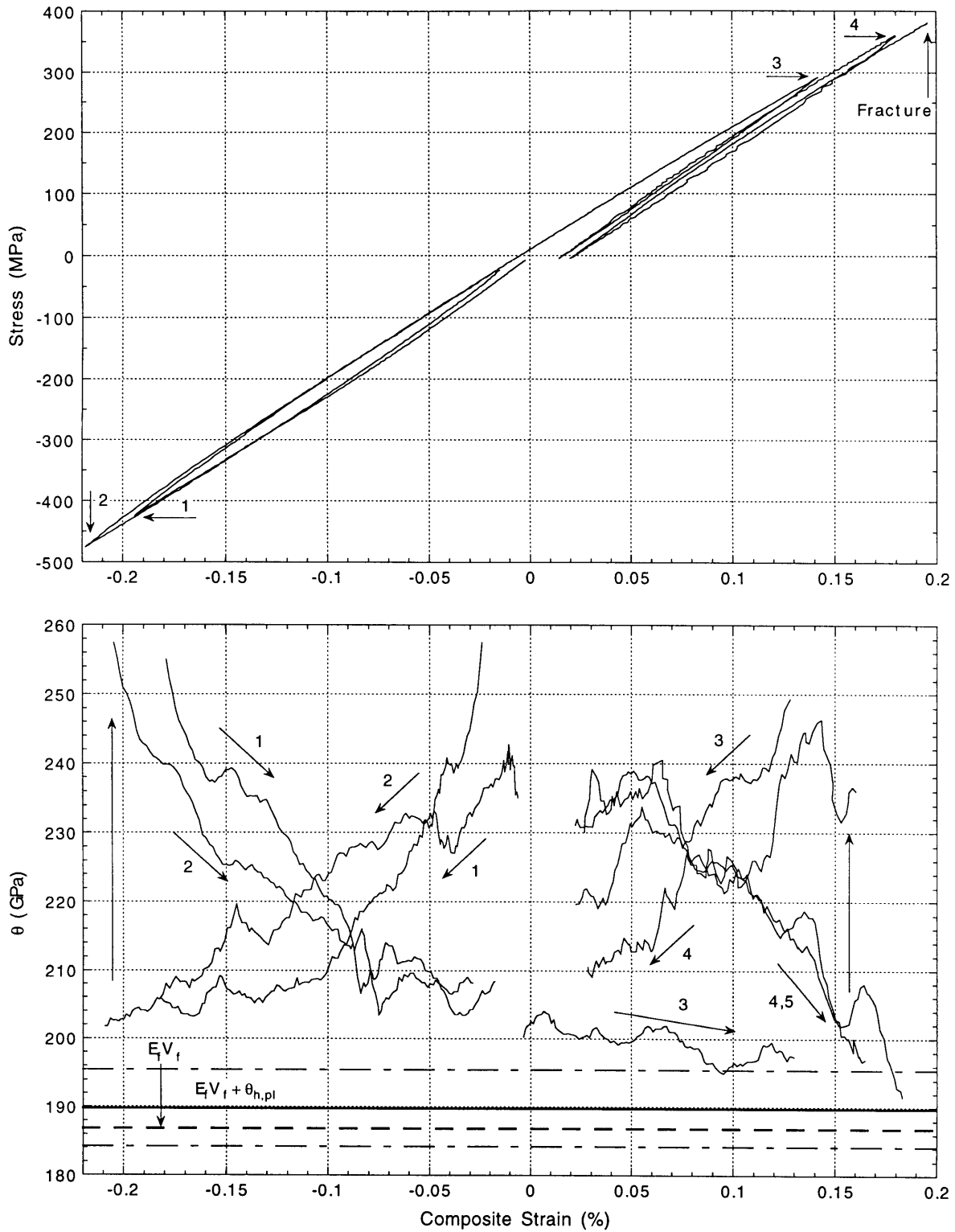


Figure 5-9 - (a) Stress-strain curve of pure aluminum composite reinforced with 48.5% Fiber FP, tested at 77 K (Sample 0-4•Al/FP) (top graph).
 (b) Corresponding Theta curves for each cycle (bottom graph). Horizontal lines represent $E_f V_f$ (dashed line) and $E_f V_f + \theta_{h,pl} \pm \Delta(E_f V_f + \theta_{h,pl})$.

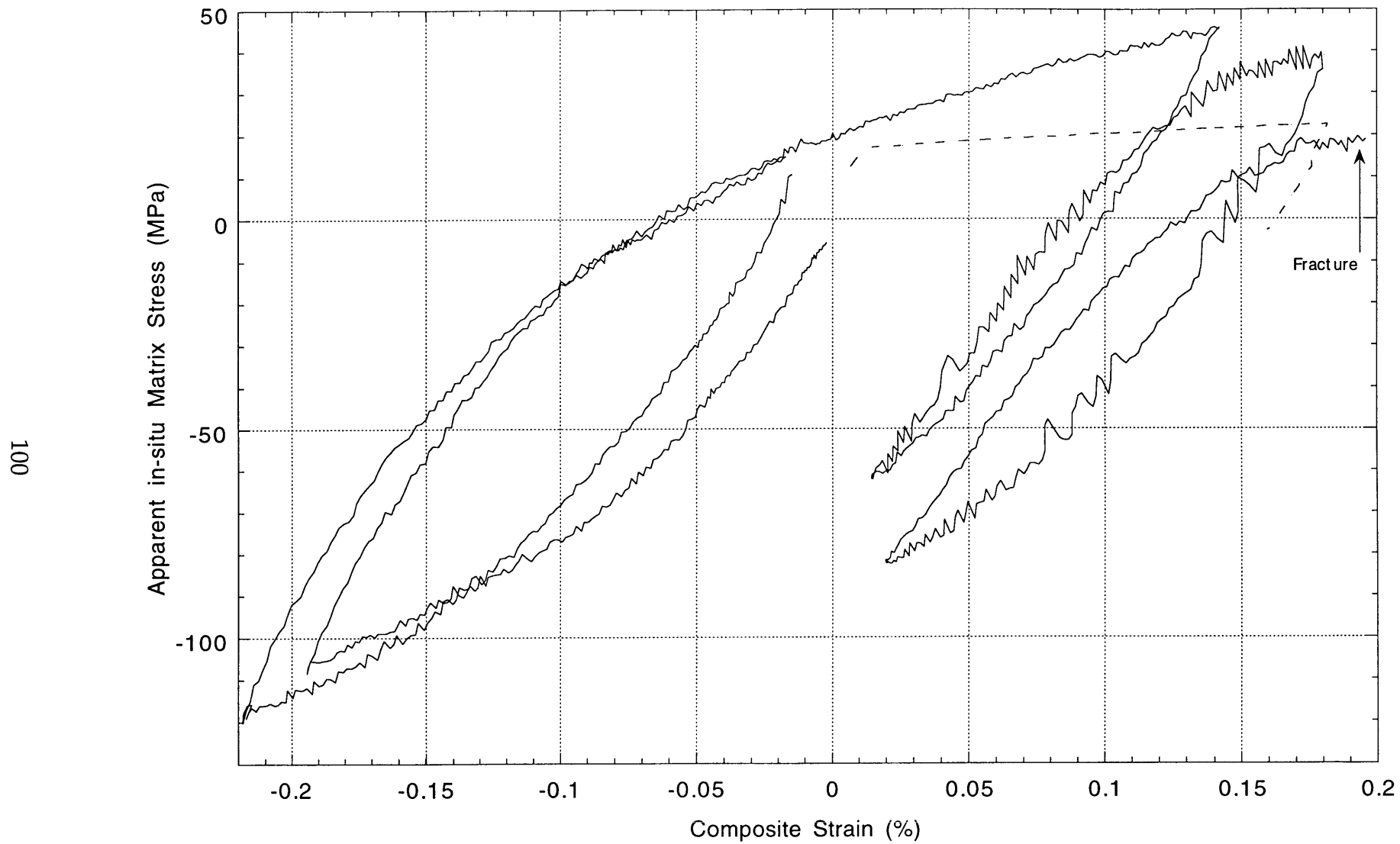


Figure 5-9 - (c) Apparent *in-situ* matrix stress-strain curve of pure aluminum computed from composite reinforced with 48.5% Fiber FP, tested at 77 K (Sample 0-4•Al/FP). Dashed line shows unreinforced matrix tested as reference.

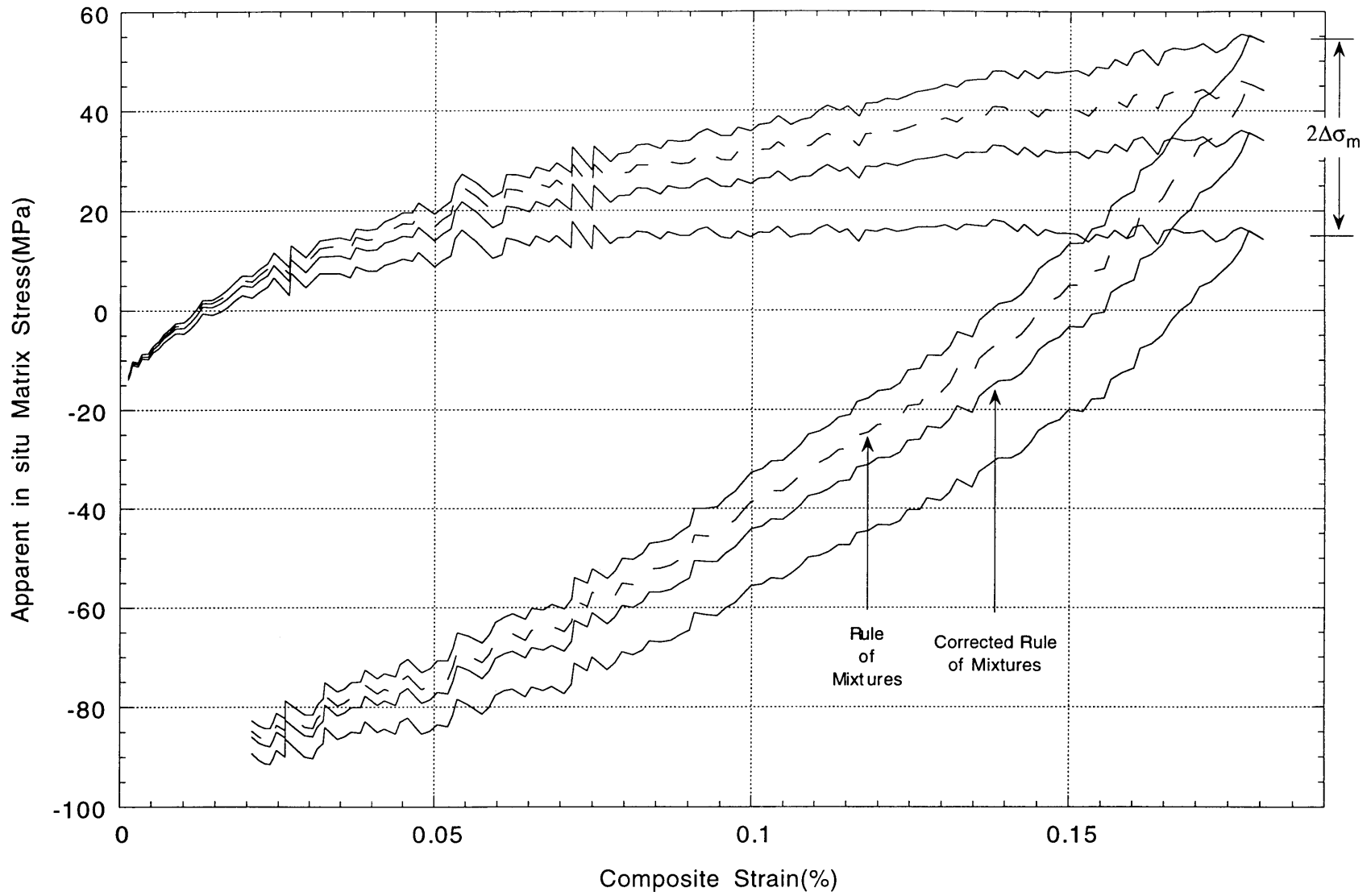


Figure 5-9 - (d) Total estimated uncertainty on apparent *in-situ* matrix stress-strain curve of pure aluminum computed from composite reinforced with 46.2% Fiber FP, tested at 77 K (Sample 0-6•Al/FP).

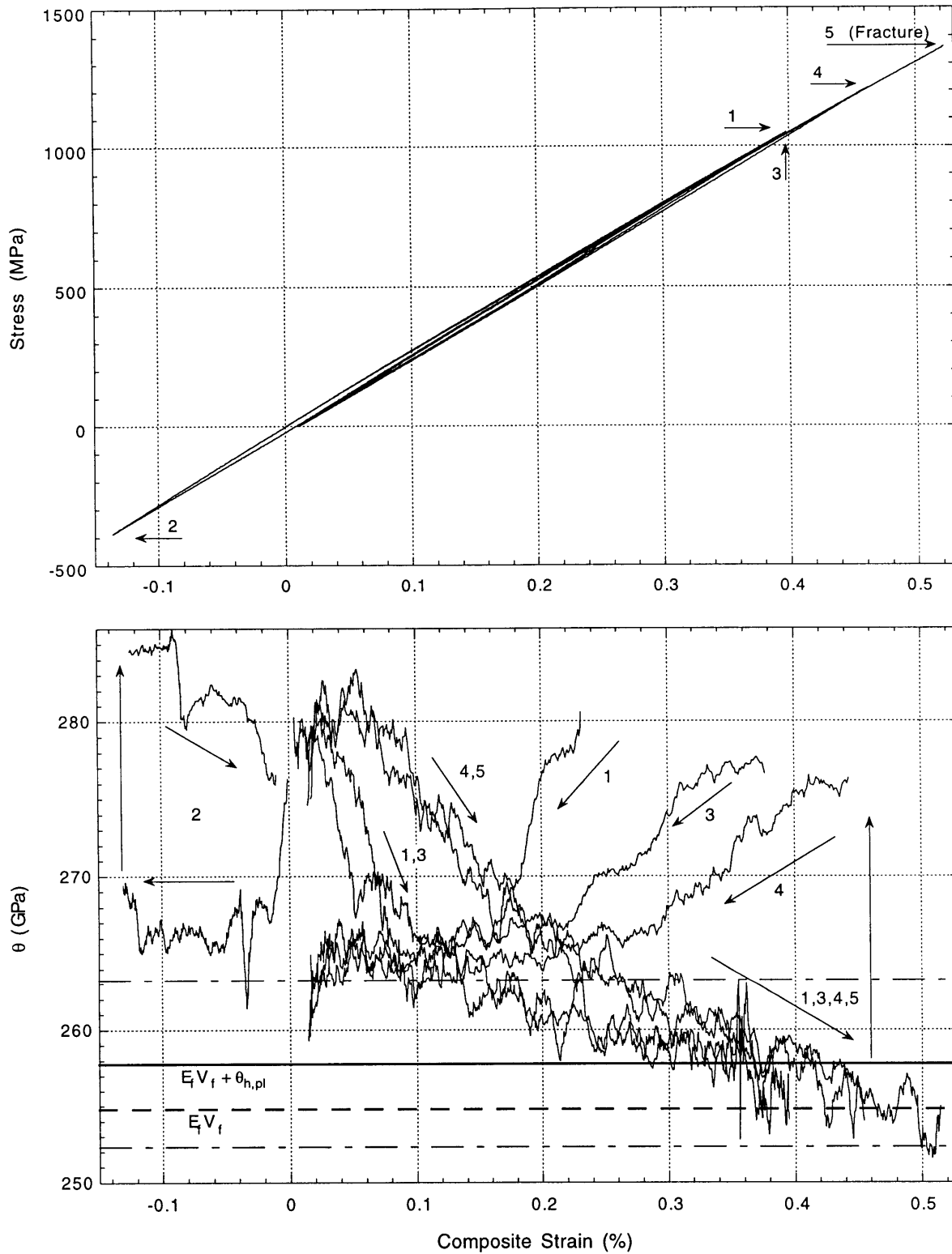


Figure 5-10 - (a) Stress-strain curve of pure aluminum composite reinforced with 67.2% Nextel 610 fibers (Sample 2-9•Al/3M) (top graph).
 (b) Corresponding Theta curves for each cycle (bottom graph). Horizontal lines represent $E_f V_f$ (dashed line) and $E_f V_f + \theta_{h,pl} \pm \Delta(E_f V_f + \theta_{h,pl})$.

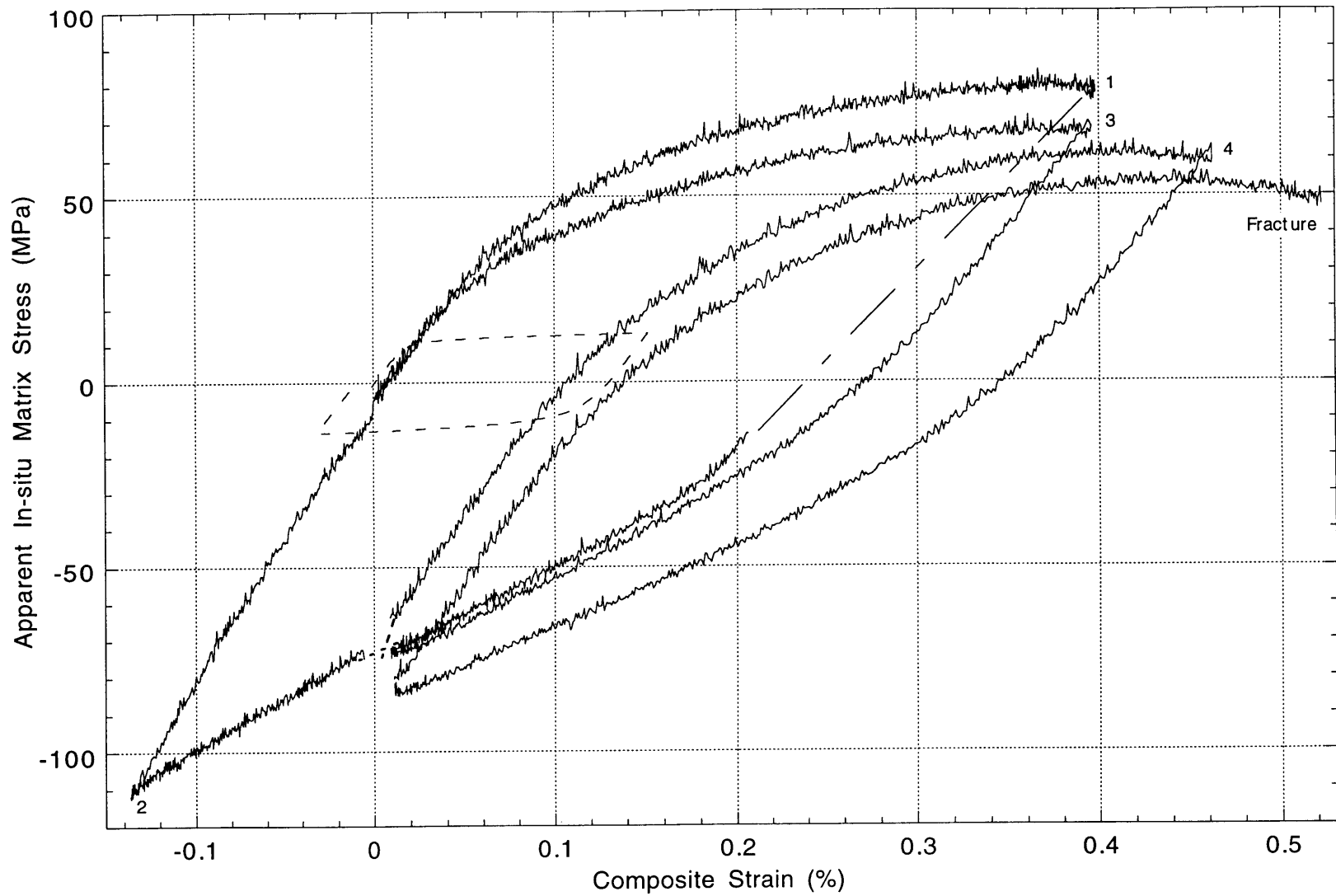


Figure 5-10 - (c) Apparent *in-situ* matrix stress-strain curve of pure aluminum computed from composite reinforced with 67.2% Nextel 610 fibers (Sample 2-9•Al/3M). Dashed line shows unreinforced matrix tested as reference.

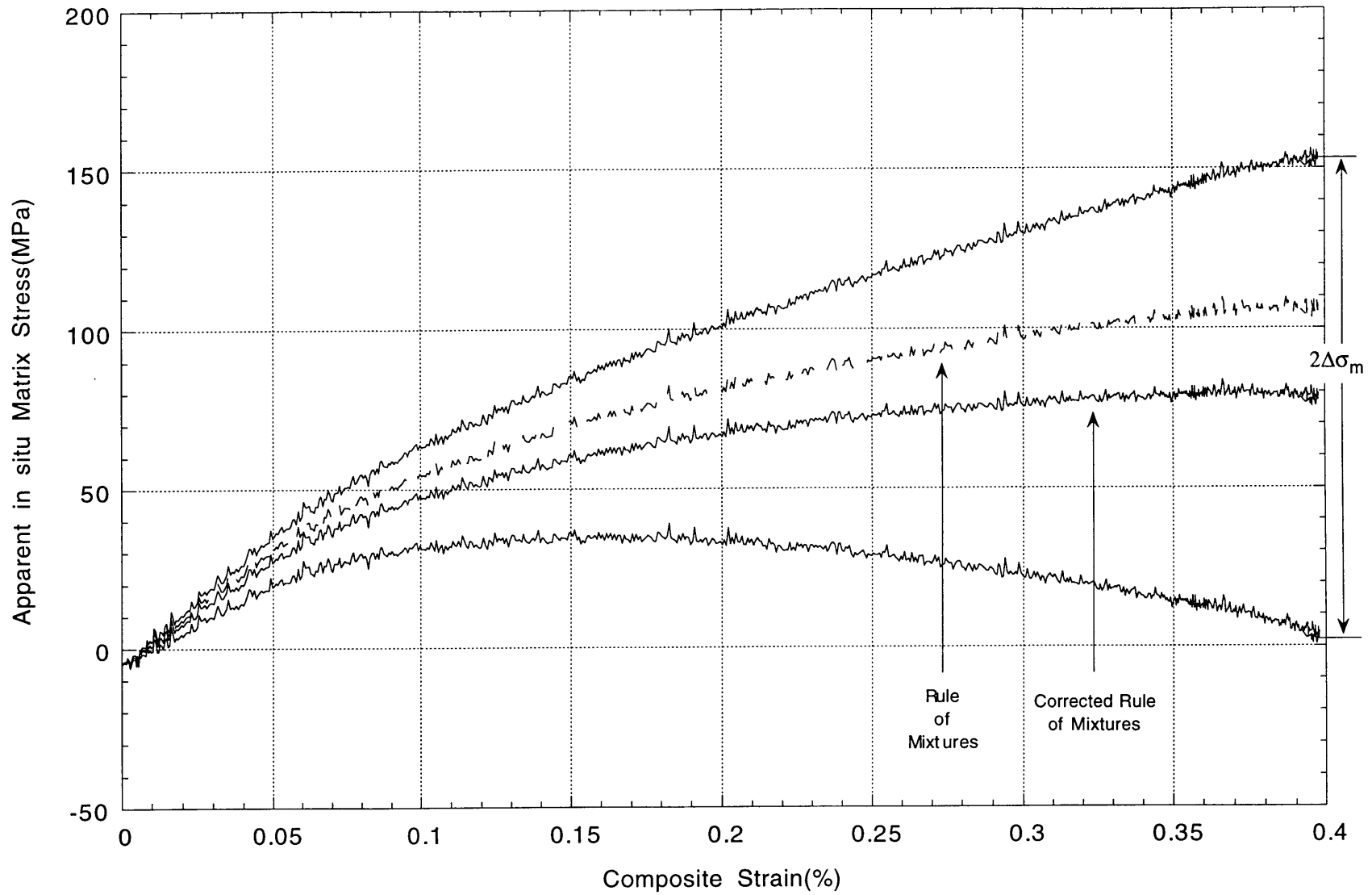


Figure 5-10 - (d) Total estimated uncertainty on apparent *in-situ* matrix stress-strain curve of pure aluminum computed from composite reinforced with 67.2% Nextel 610 fibers (Sample 2-9•Al/3M).

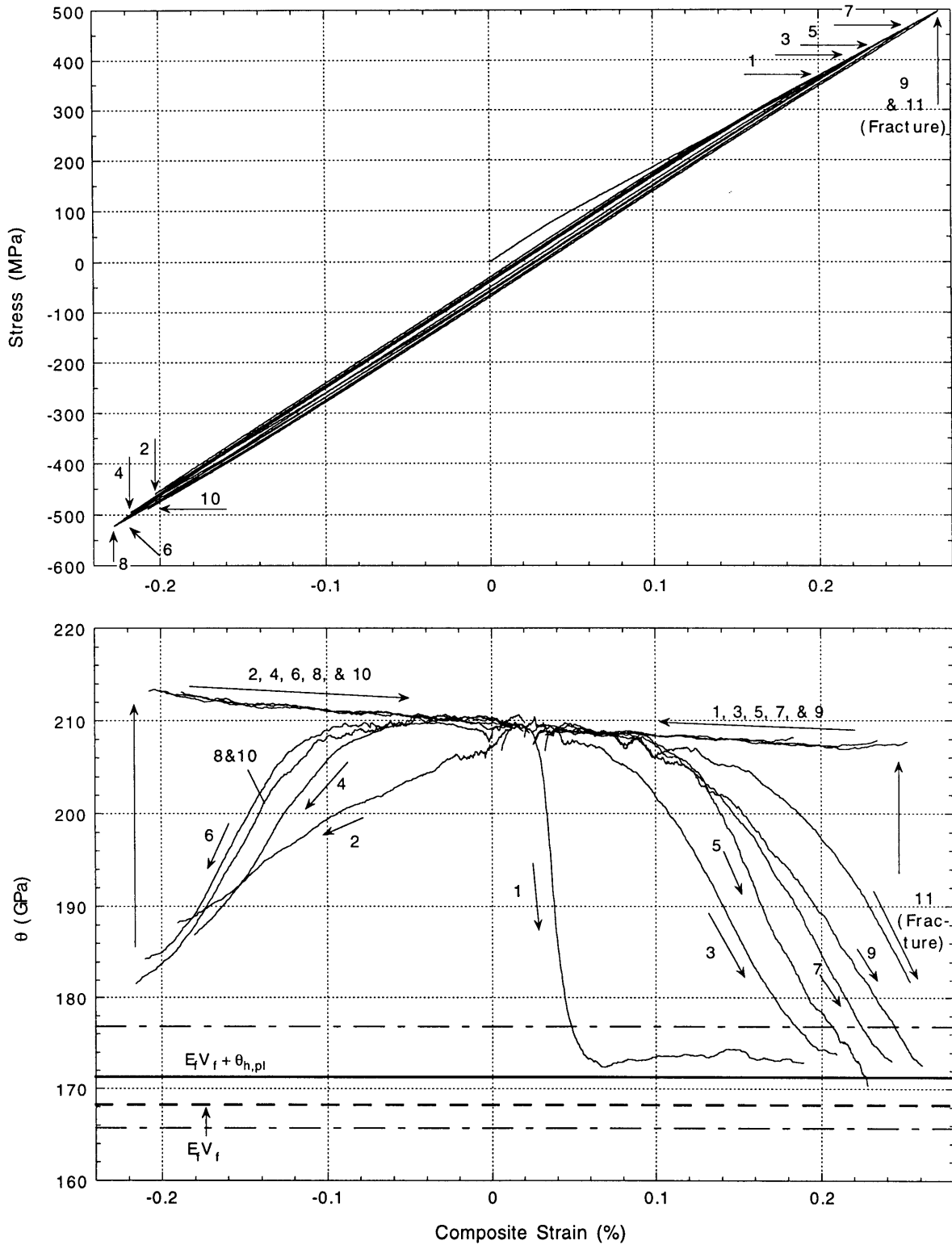


Figure 5-11 - (a) Stress-strain curve of Al-4.5wt%Cu composite reinforced with 44.5% Fiber FP (Sample 3-6•AlCu/FP) (top graph).
 (b) Corresponding Theta curves for each cycle (bottom graph). Horizontal lines represent $E_f V_f$ (dashed line) and $E_f V_f + \theta_{h,pl} \pm \Delta(E_f V_f + \theta_{h,pl})$.

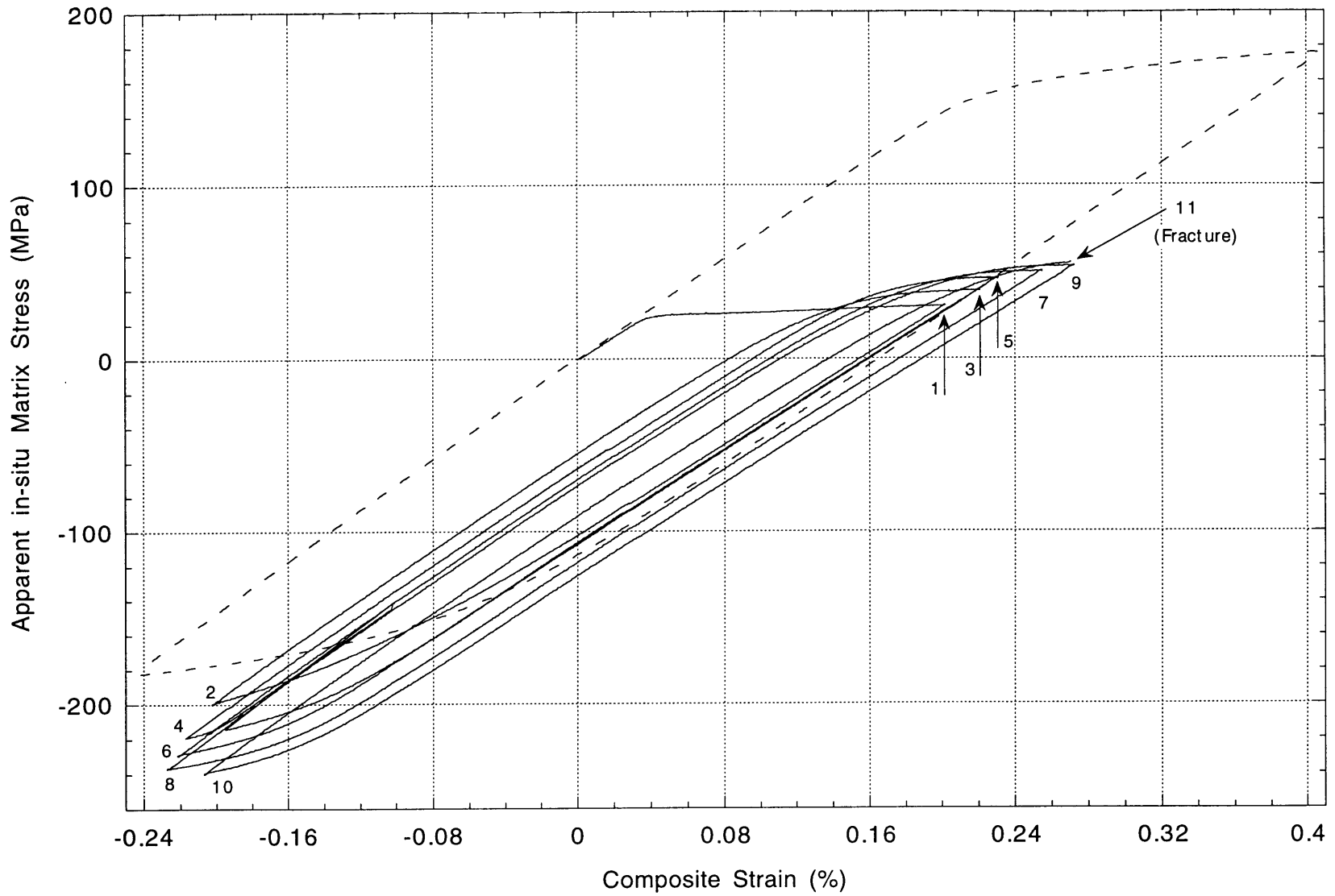


Figure 5-11 - (c) Apparent *in-situ* matrix stress-strain curve of Al-4.5wt%Cu computed from composite reinforced with 44.5% Fiber FP (Sample 3-6•AlCu/FP). Dashed line shows unreinforced matrix tested as reference.

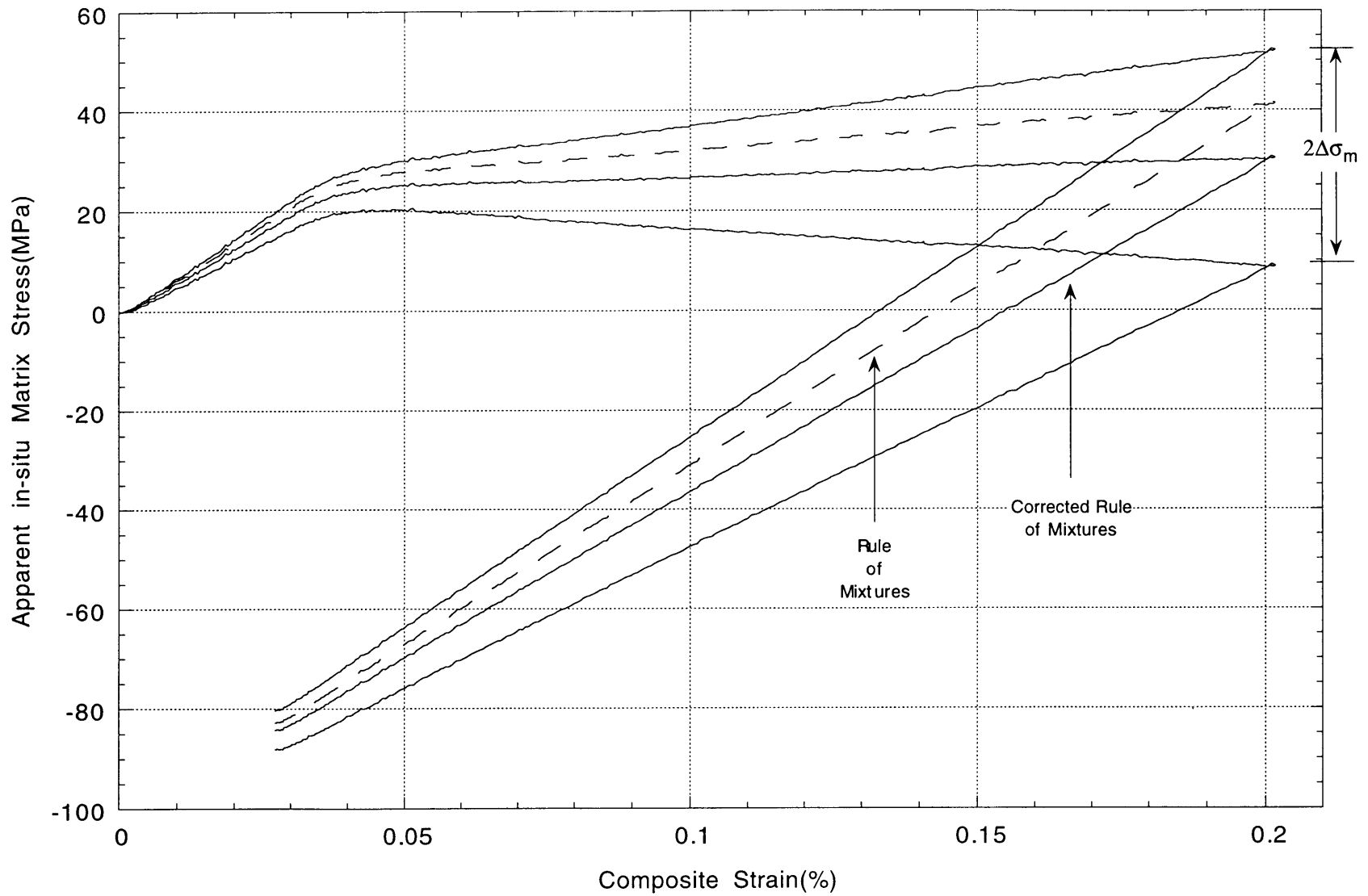


Figure 5-11 - (d) Total estimated uncertainty on apparent *in-situ* matrix stress-strain curve of Al-4.5wt%Cu computed from composite reinforced with 44.5% Fiber FP (Sample 3-6•AlCu/FP).

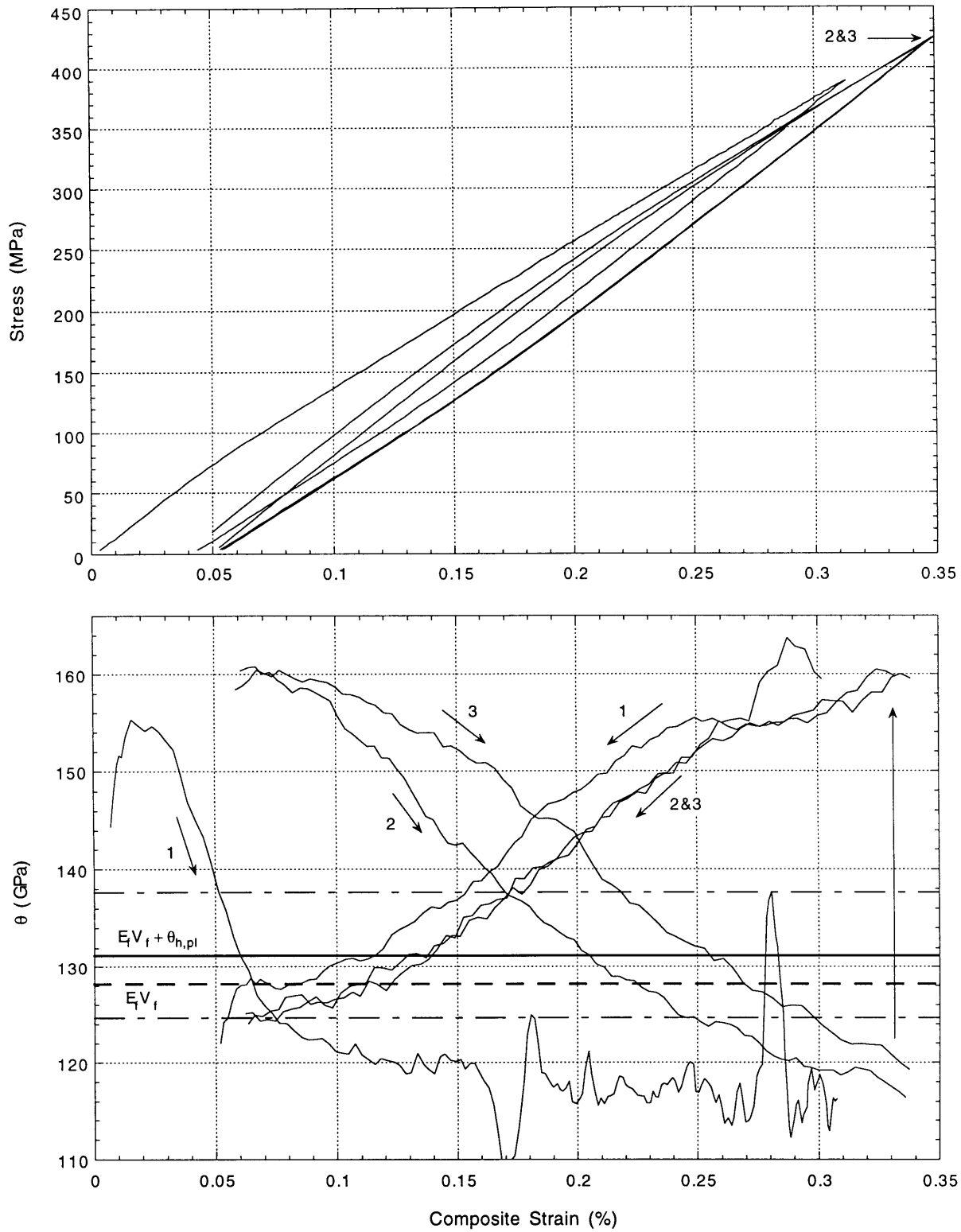


Figure 5-12 - (a) Stress-strain curve of Al-0.9wt%Mg composite reinforced with 33.8% Fiber FP (Sample 10•AlMg/FP) (top graph).
 (b) Corresponding Theta curves for each cycle (bottom graph). Horizontal lines represent $E_f V_f$ (dashed line) and $E_f V_f + \theta_{h,pl} \pm \Delta(E_f V_f + \theta_{h,pl})$.

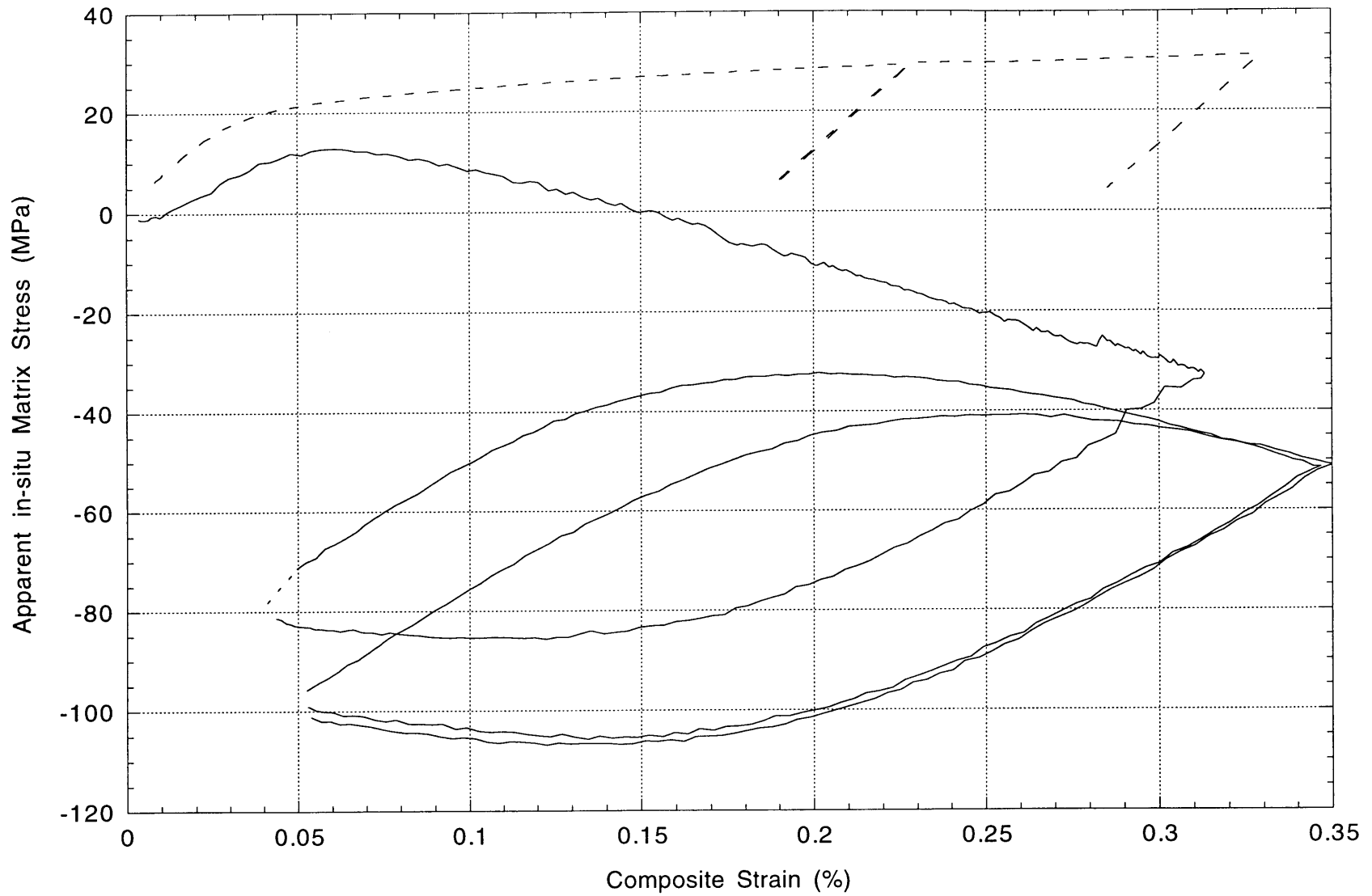


Figure 5-12 - (c) Apparent *in-situ* matrix stress-strain curve of Al-0.9wt%Mg computed from composite reinforced with 33.8% Fiber FP (Sample 10•AlMg/FP). Dashed line shows unreinforced matrix tested as reference.

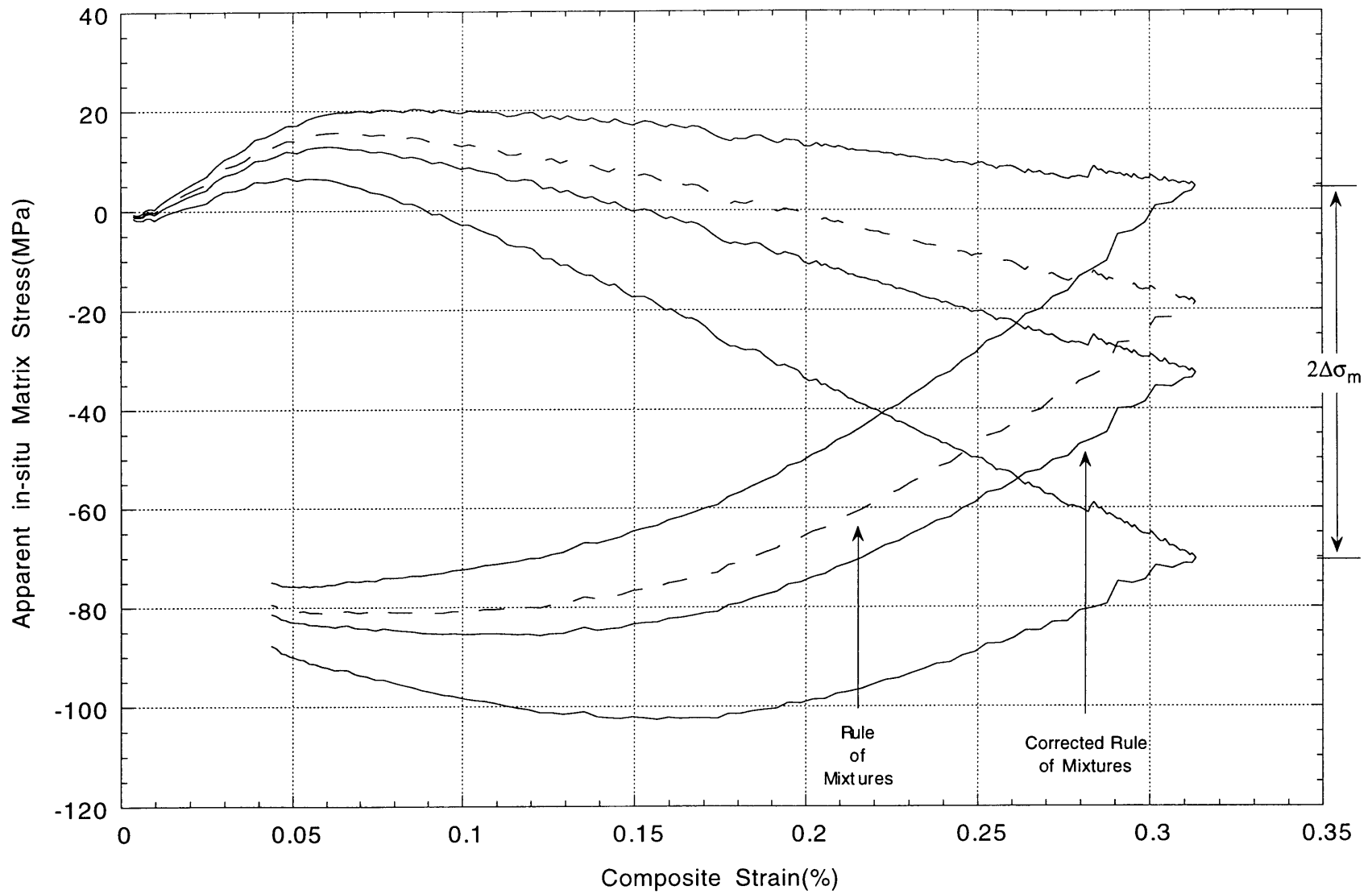


Figure 5-12 - (d) Total estimated uncertainty on apparent *in-situ* matrix stress-strain curve of Al-0.9wt%Mg computed from composite reinforced with 33.8% Fiber FP (Sample 10•AlMg/FP).

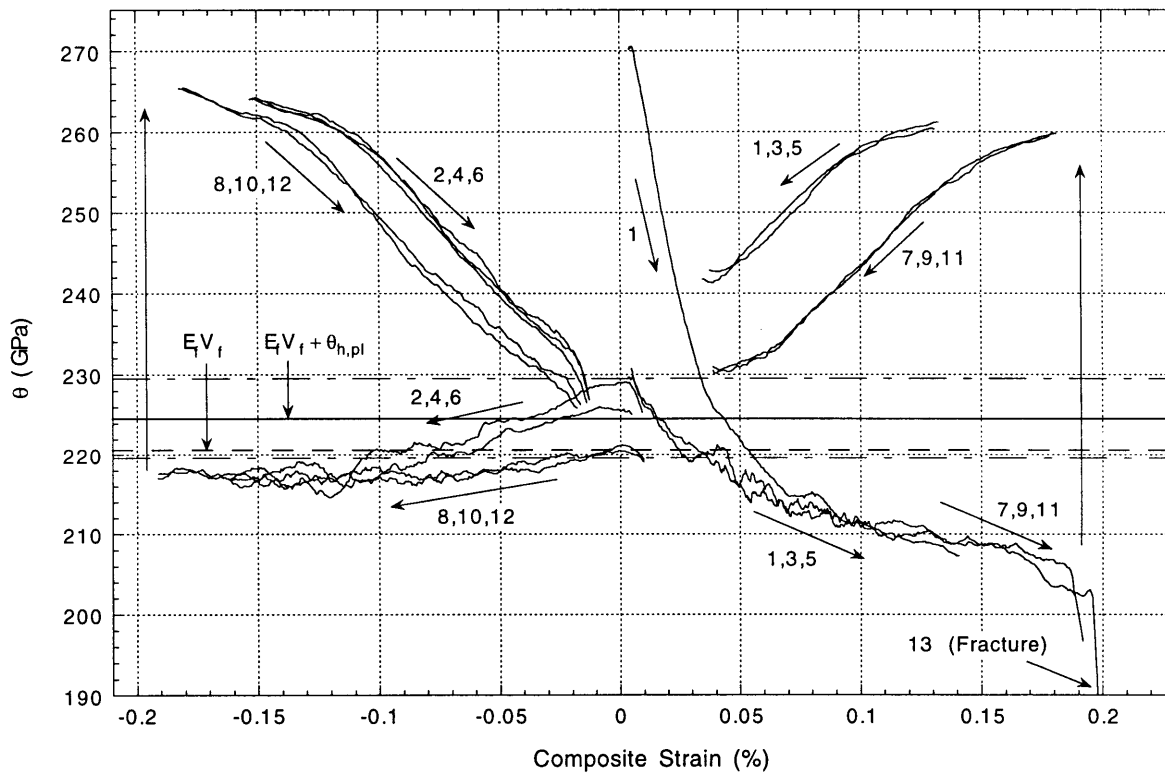
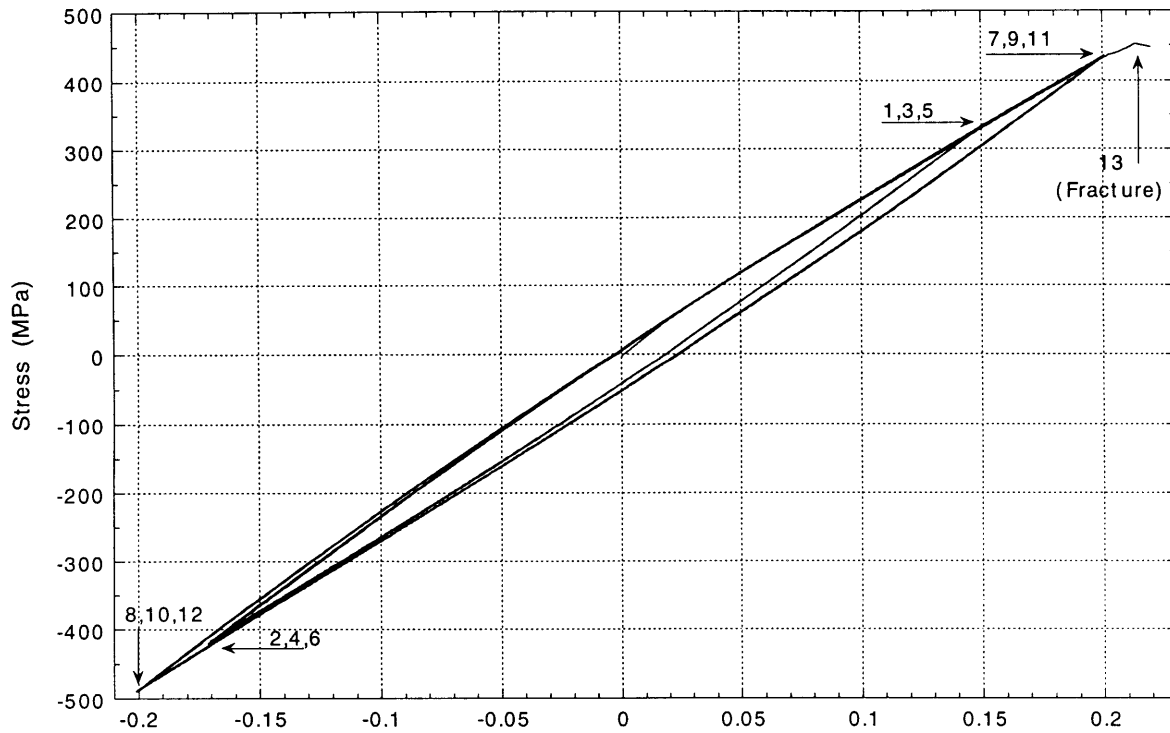


Figure 5-13 - (a) Stress-strain curve of pure copper composite reinforced with 58.2% Fiber FP (Sample 4-5•Cu/FP) (top graph).
 (b) Corresponding Theta curves for each cycle (bottom graph). Horizontal lines represent $E_f V_f$ (dashed line) and $E_f V_f + \theta_{h,pl} \pm \Delta(E_f V_f + \theta_{h,pl})$.

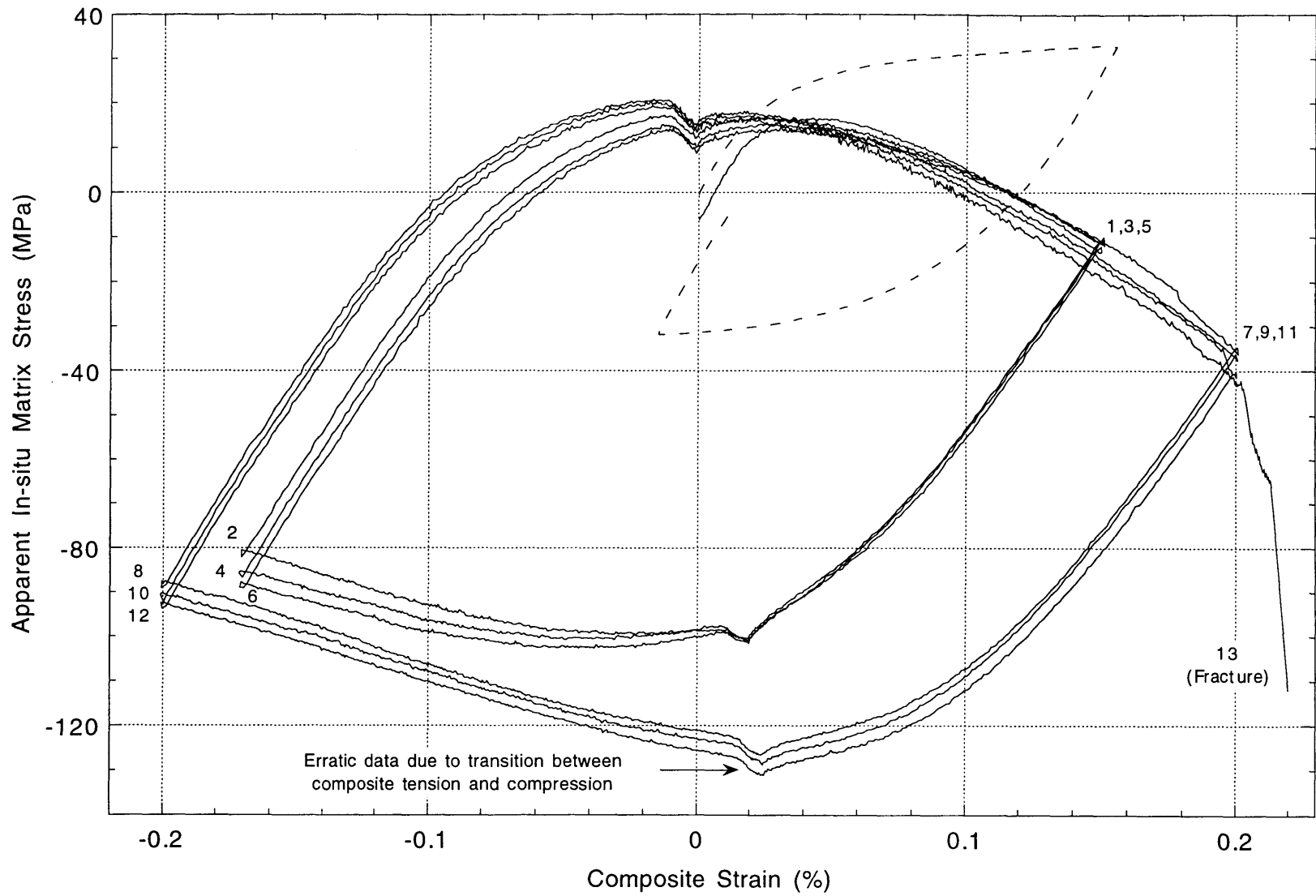


Figure 5-13 - (c) Apparent *in-situ* matrix stress-strain curve of pure copper computed from composite reinforced with 58.2% Fiber FP (Sample 4-5•Cu/FP). Dashed line shows unreinforced matrix tested as reference.

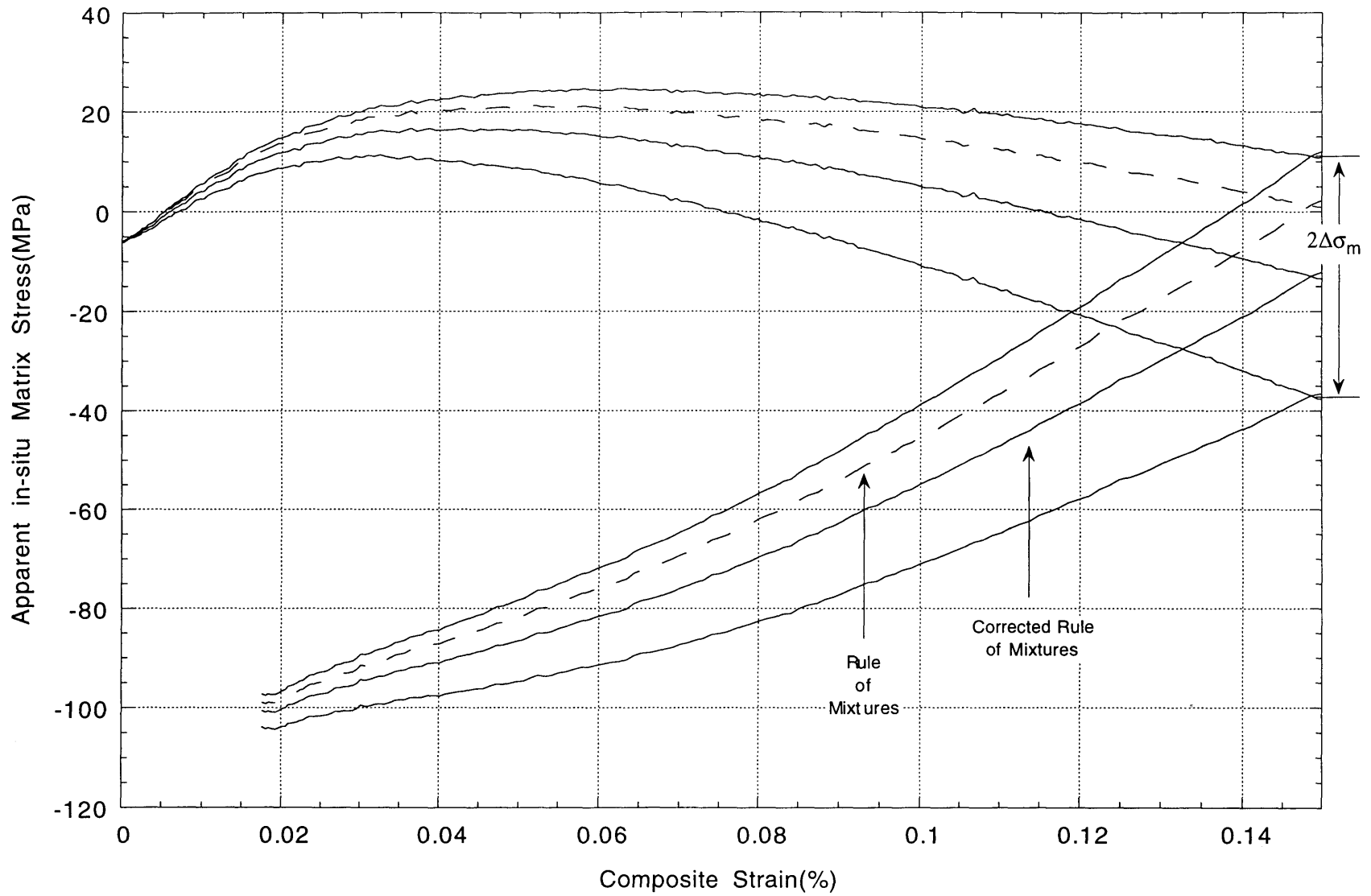


Figure 5-13 - (d) Total estimated uncertainty on apparent *in-situ* matrix stress-strain curve of pure copper computed from composite reinforced with 58.2% Fiber FP (Sample 4-5•Cu/FP).

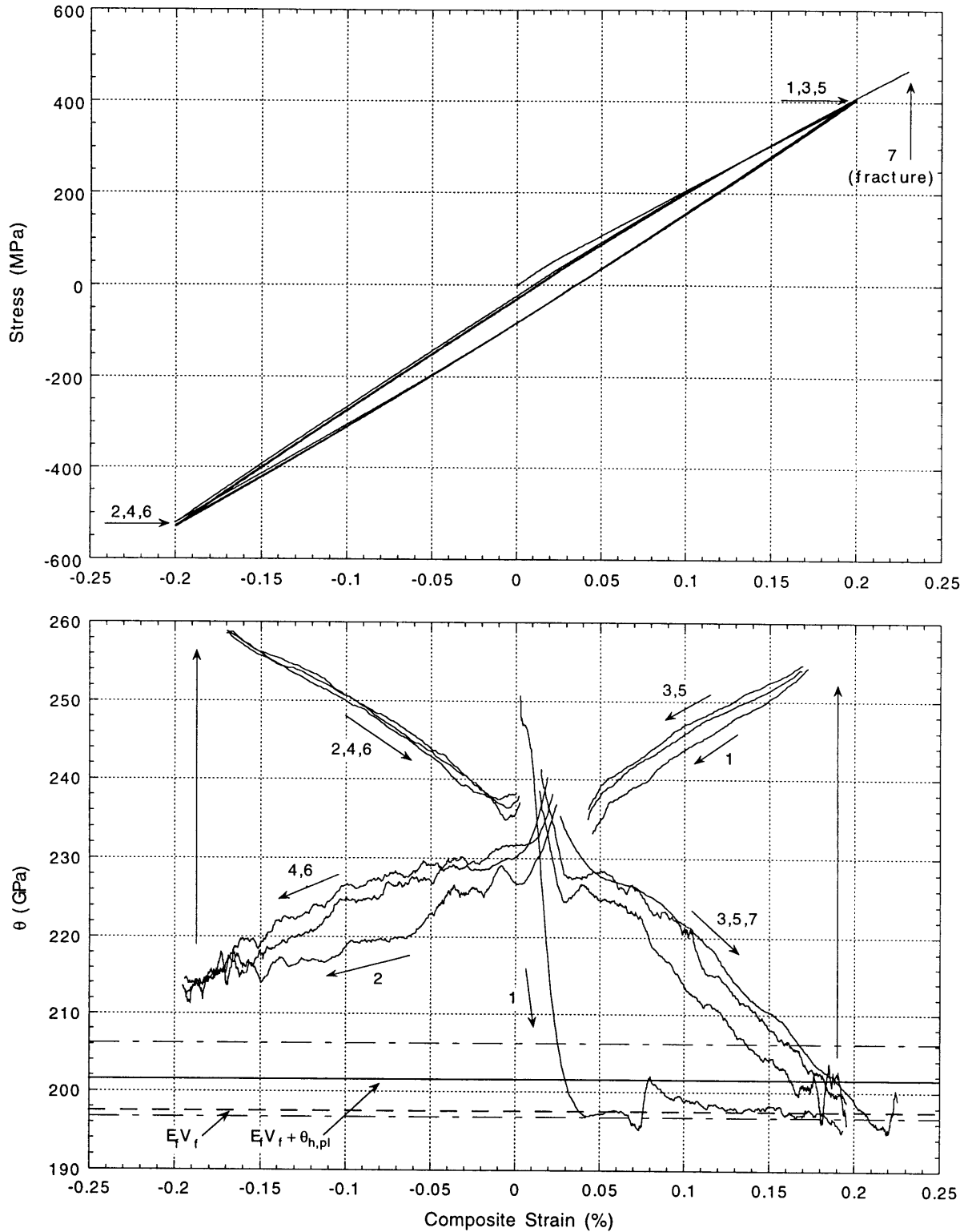


Figure 5-14 - (a) Stress-strain curve of Cu-7wt%Al composite reinforced with 52.1% Fiber FP (Sample 1-3•CuAl/FP) (top graph).
 (b) Corresponding Theta curves for each cycle (bottom graph). Horizontal lines represent $E_f V_f$ (dashed line) and $E_f V_f + \theta_{h,pl} \pm \Delta(E_f V_f + \theta_{h,pl})$.

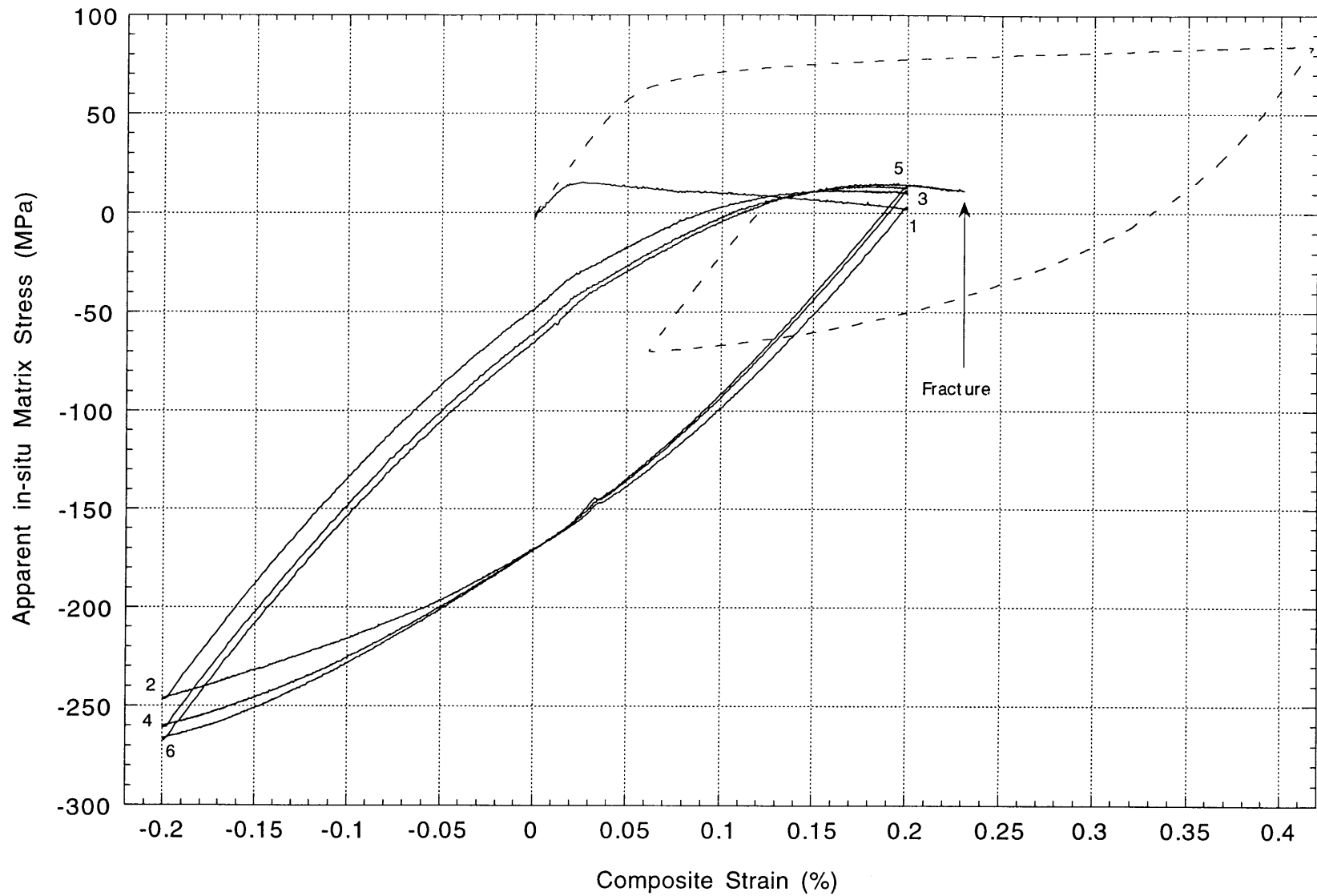


Figure 5-14 - (c) Apparent *in-situ* matrix stress-strain curve of Cu-7wt%Al computed from composite reinforced with 52.1% Fiber FP (Sample 1-3•CuAl/FP). Dashed line shows unreinforced matrix tested as reference.

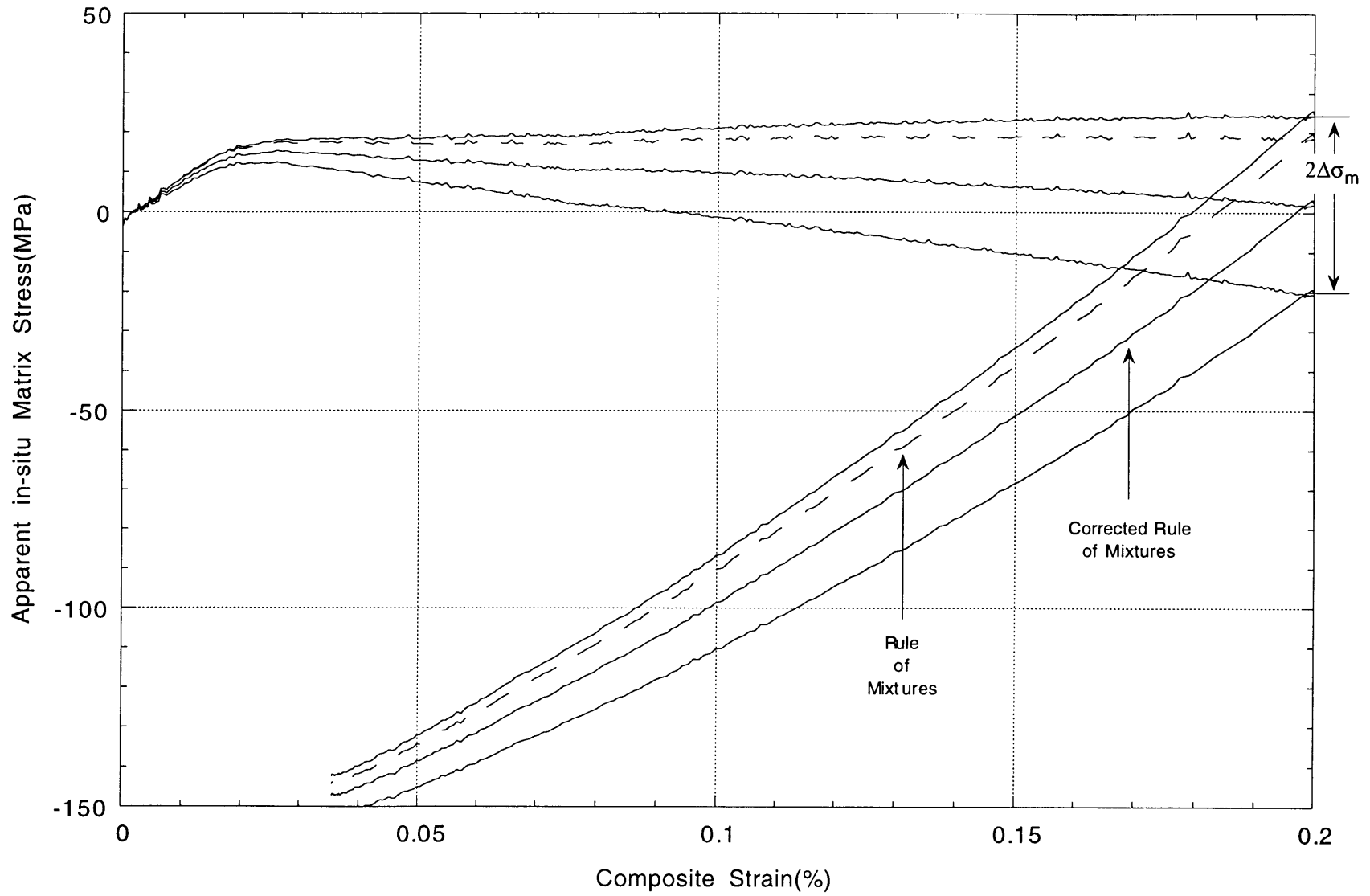


Figure 5-14 - (d) Total estimated uncertainty on apparent *in-situ* matrix stress-strain curve of Cu-7wt%Al computed from composite reinforced with 52.1% Fiber FP (Sample 1-3•CuAl/FP).

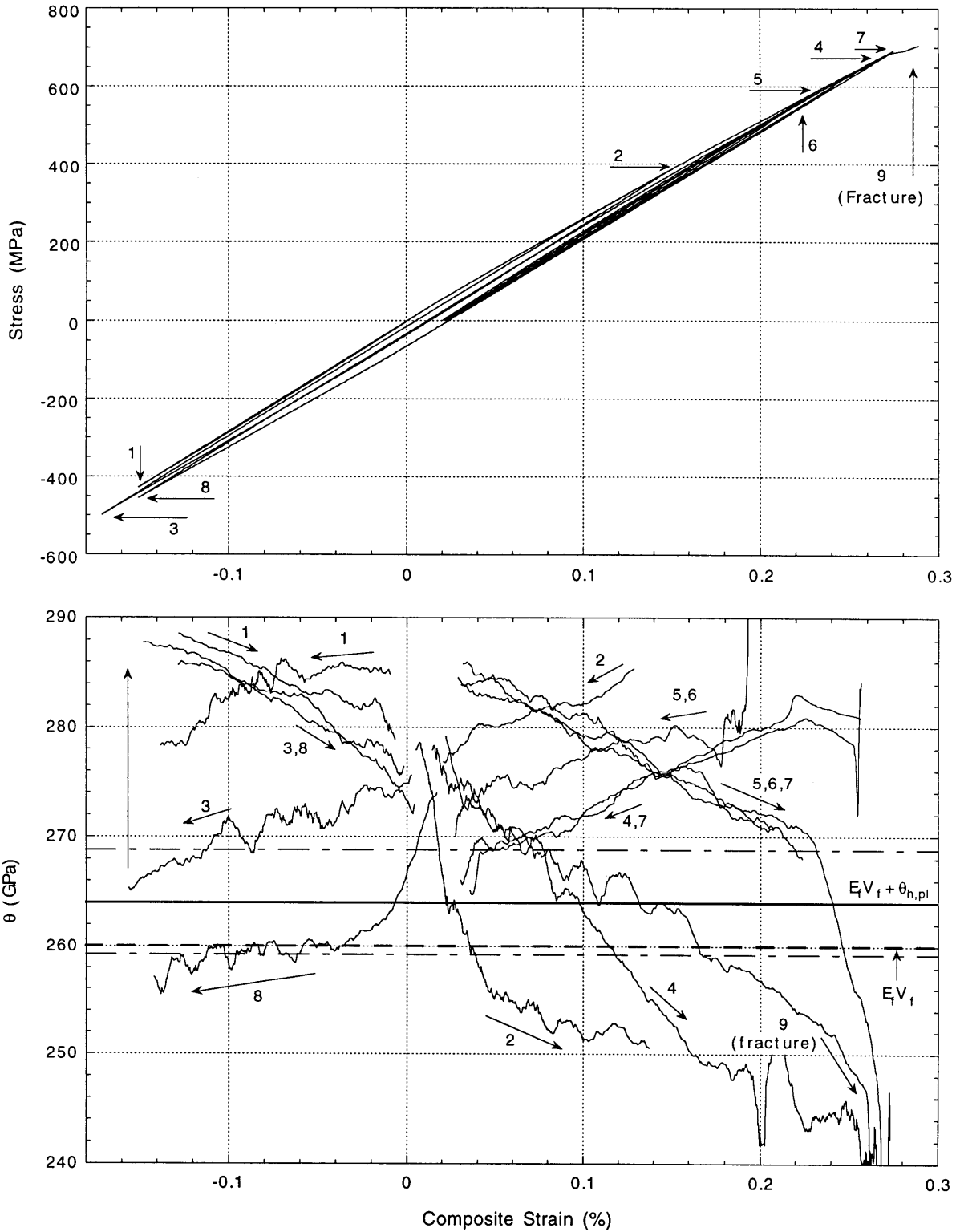


Figure 5-15 - (a) Stress-strain curve of Cu-7wt%Al composite reinforced with 68.6% Nextel 610 fibers (Sample 1-2•CuAl/3M) (top graph).
 (b) Corresponding Theta curves for each cycle (bottom graph). Horizontal lines represent $E_f V_f$ (dashed line) and $E_f V_f + \theta_{h,pl} \pm \Delta(E_f V_f + \theta_{h,pl})$.

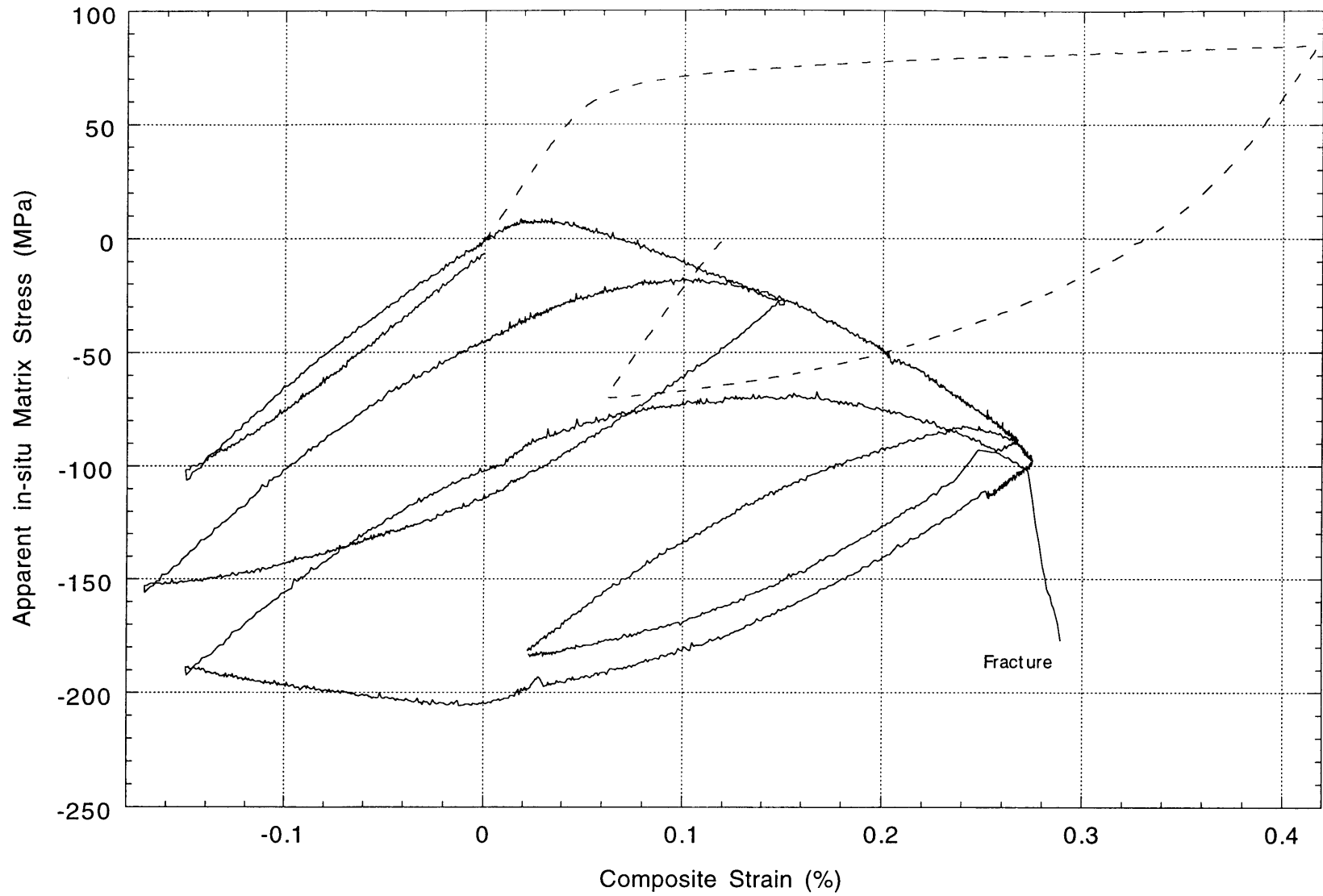


Figure 5-15 - (c) Apparent *in-situ* matrix stress-strain curve of Cu-7wt%Al computed from composite reinforced with 68.6% Nextel 610 fibers (Sample 1-2•CuAl/3M). Tests number 5 and 6 (see preceding figure) were not plotted for greater clarity.

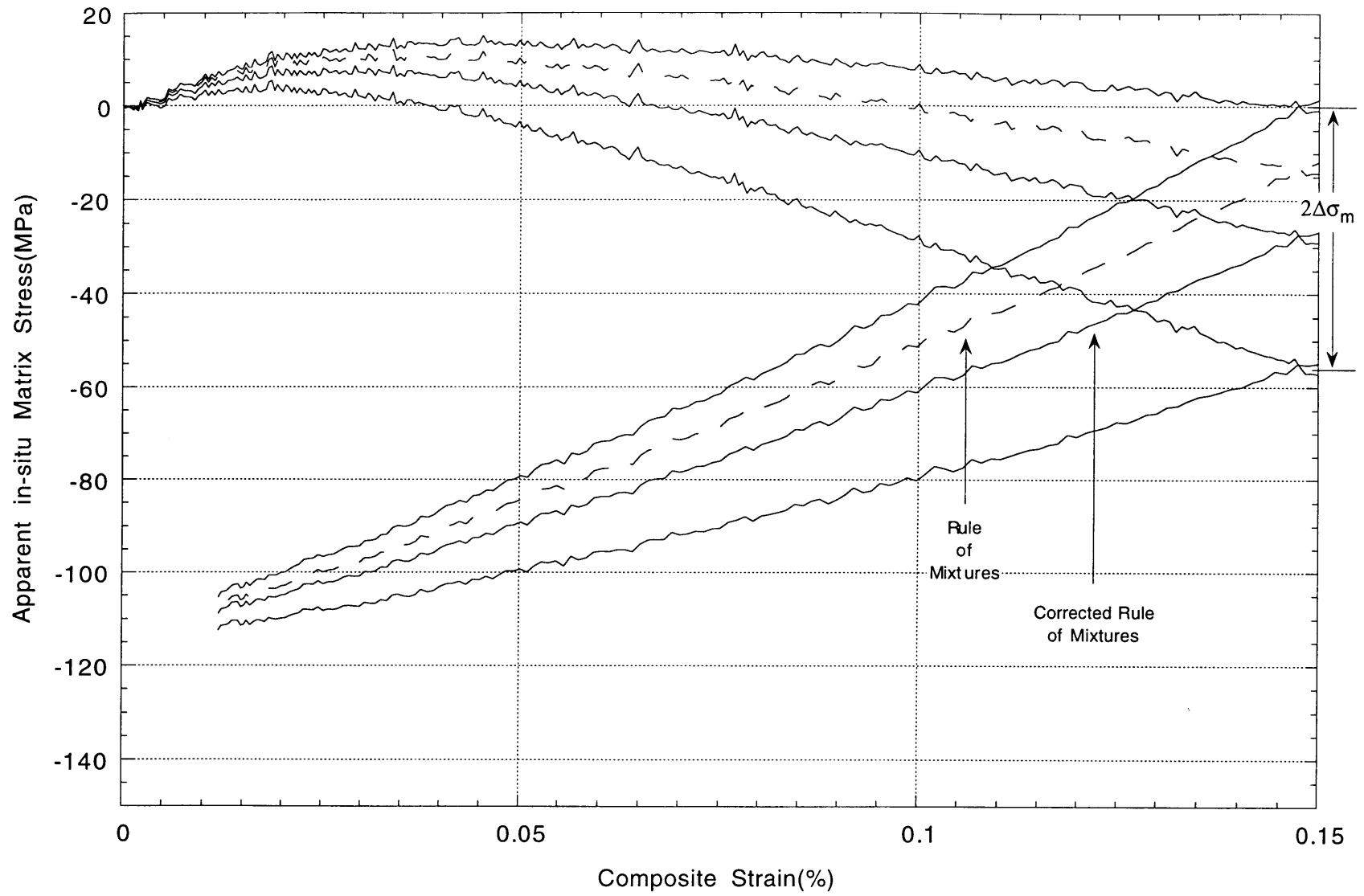
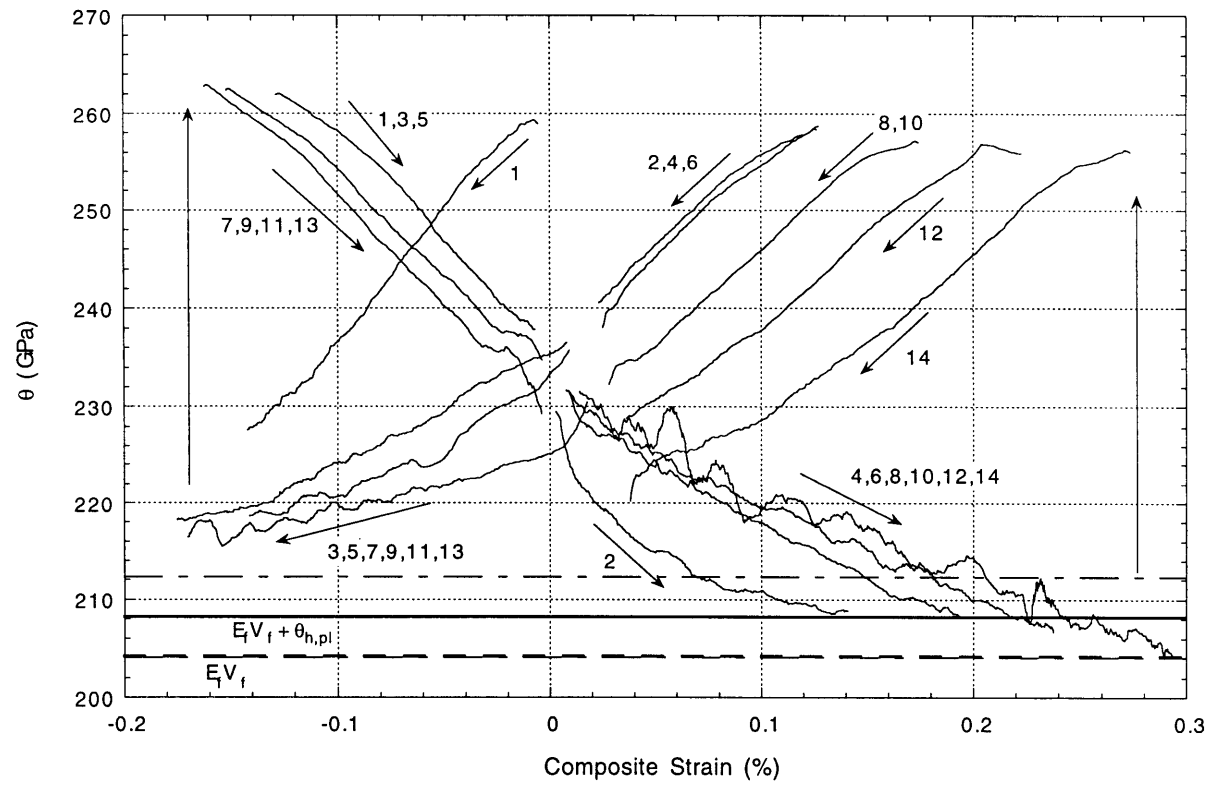
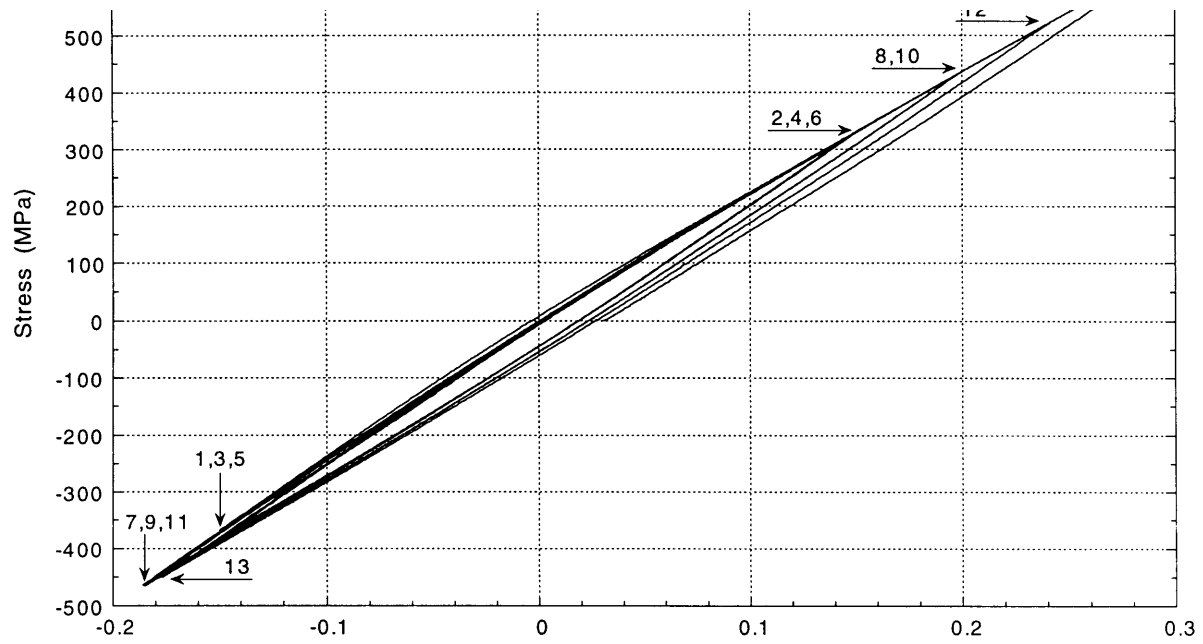


Figure 5-15 - (d) Total estimated uncertainty on apparent *in-situ* matrix stress-strain curve of Cu-7wt%Al computed from composite reinforced with 68.6% Nextel 610 fibers (Sample 1-2•CuAl/3M).



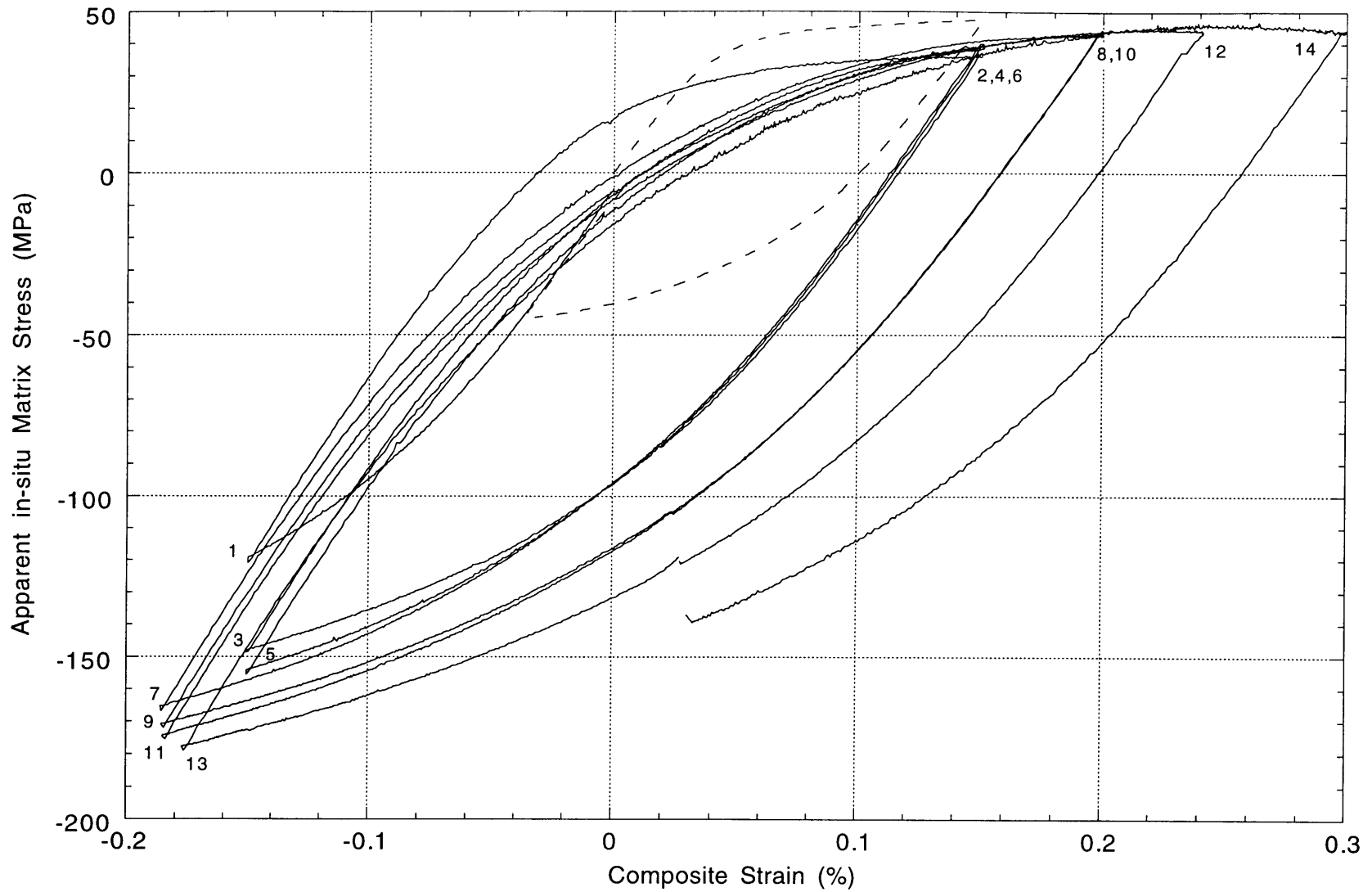


Figure 5-16 - (c) Apparent *in-situ* matrix stress-strain curve of Cu-1wt%Ti computed from composite reinforced with 53.9% Fiber FP (Sample 1-2•CuTi/FP). Dashed line shows unreinforced matrix tested as reference.

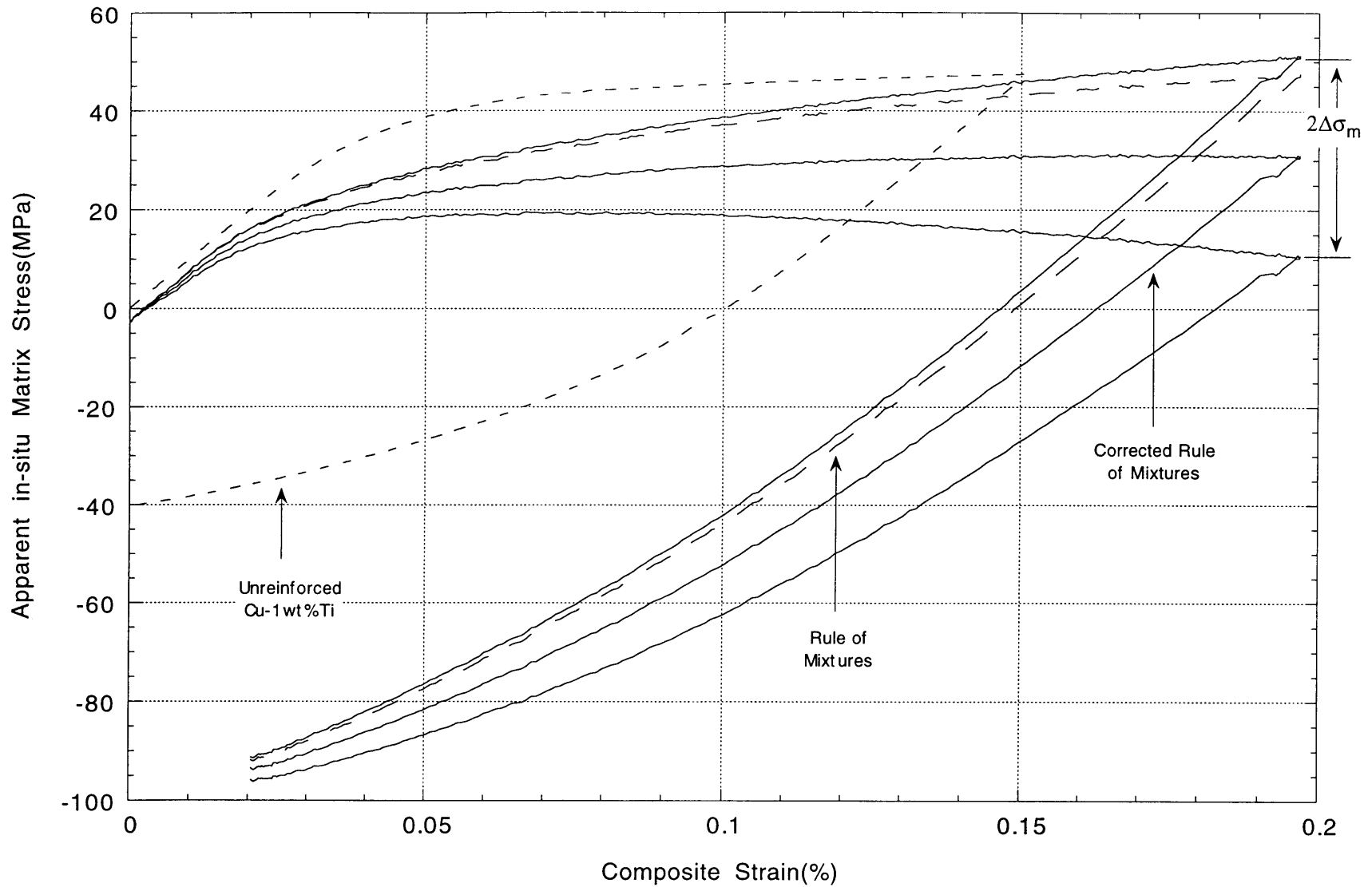


Figure 5-16 - (d) Total estimated uncertainty on apparent *in-situ* matrix stress-strain curve of Cu-1wt%Ti computed from composite reinforced with 52.2% Fiber FP (Sample 1-3•CuTi/FP).

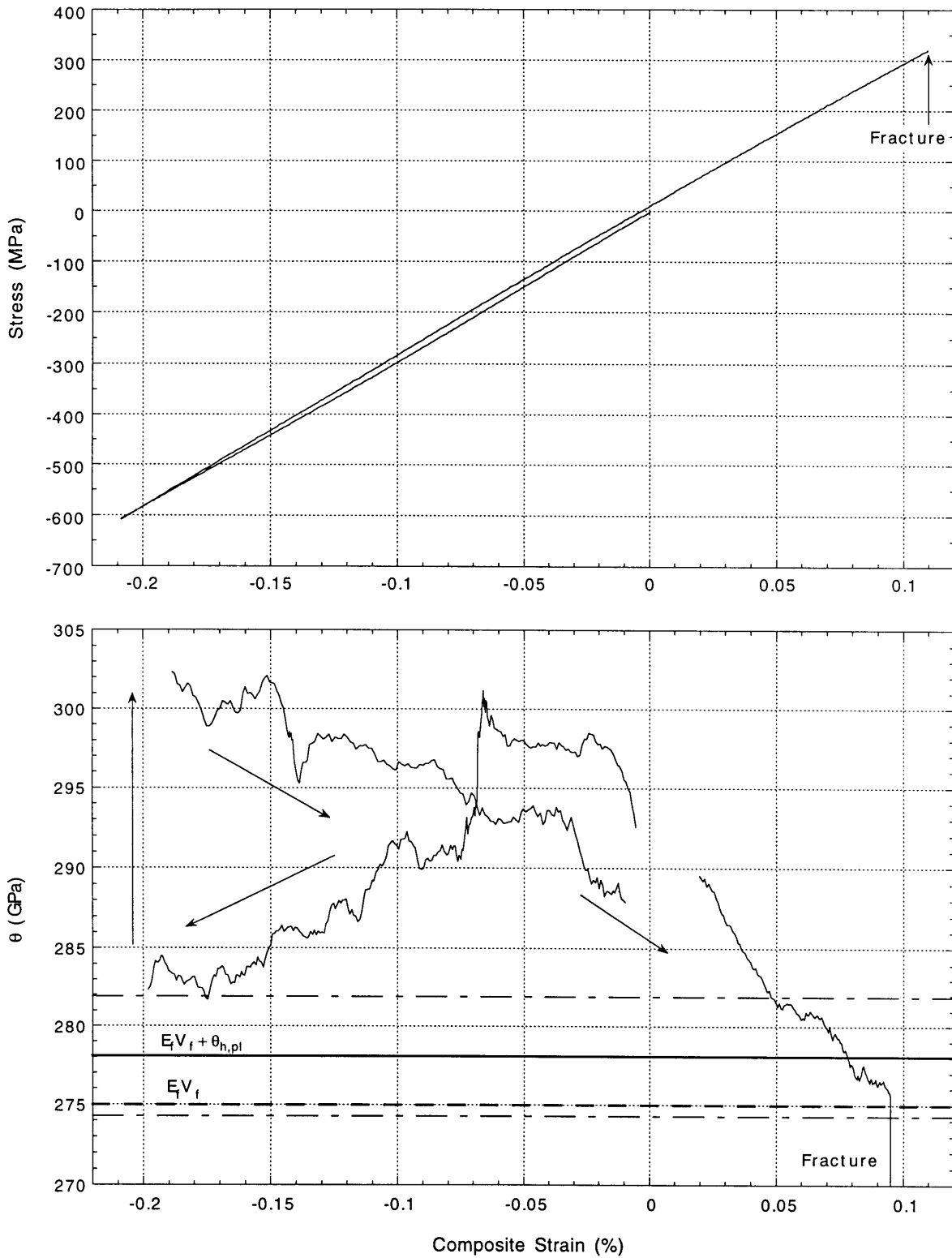


Figure 5-17 - (a) Stress-strain curve of Cu-1wt%Ti composite reinforced with 72.6% Nextel 610 fibers (Sample 1-1•CuTi/3M) (top graph).
 (b) Corresponding Theta curves for each cycle (bottom graph). Horizontal lines represent $E_f V_f$ (dashed line) and $E_f V_f + \theta_{h,pl} \pm \Delta(E_f V_f + \theta_{h,pl})$.

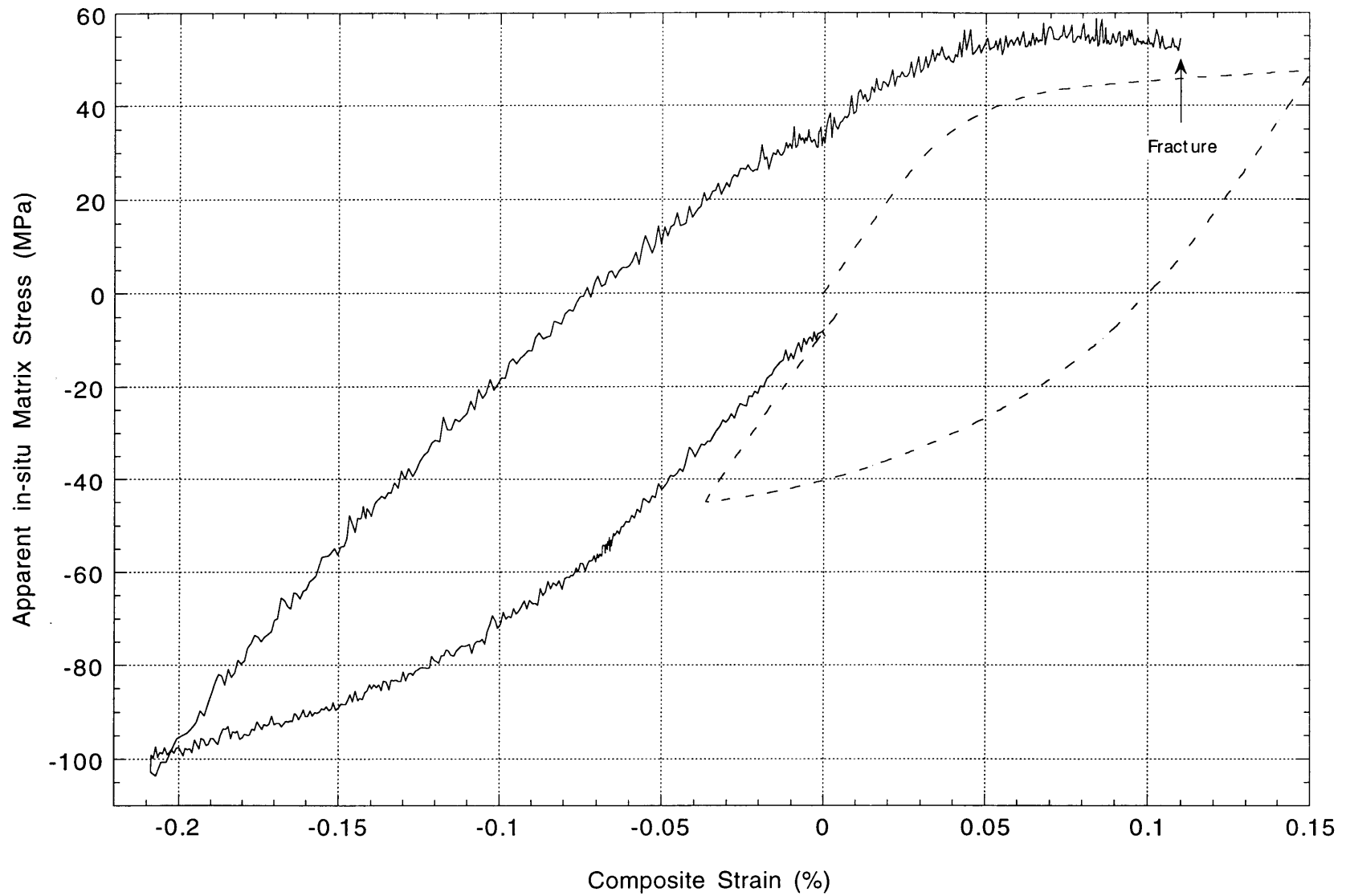


Figure 5-17 - (c) Apparent *in-situ* matrix stress-strain curve of Cu-1wt%Ti computed from composite reinforced with 72.6% Nextel 610 fibers (Sample 1-1•CuTi/3M). Dashed line shows unreinforced matrix tested as reference.

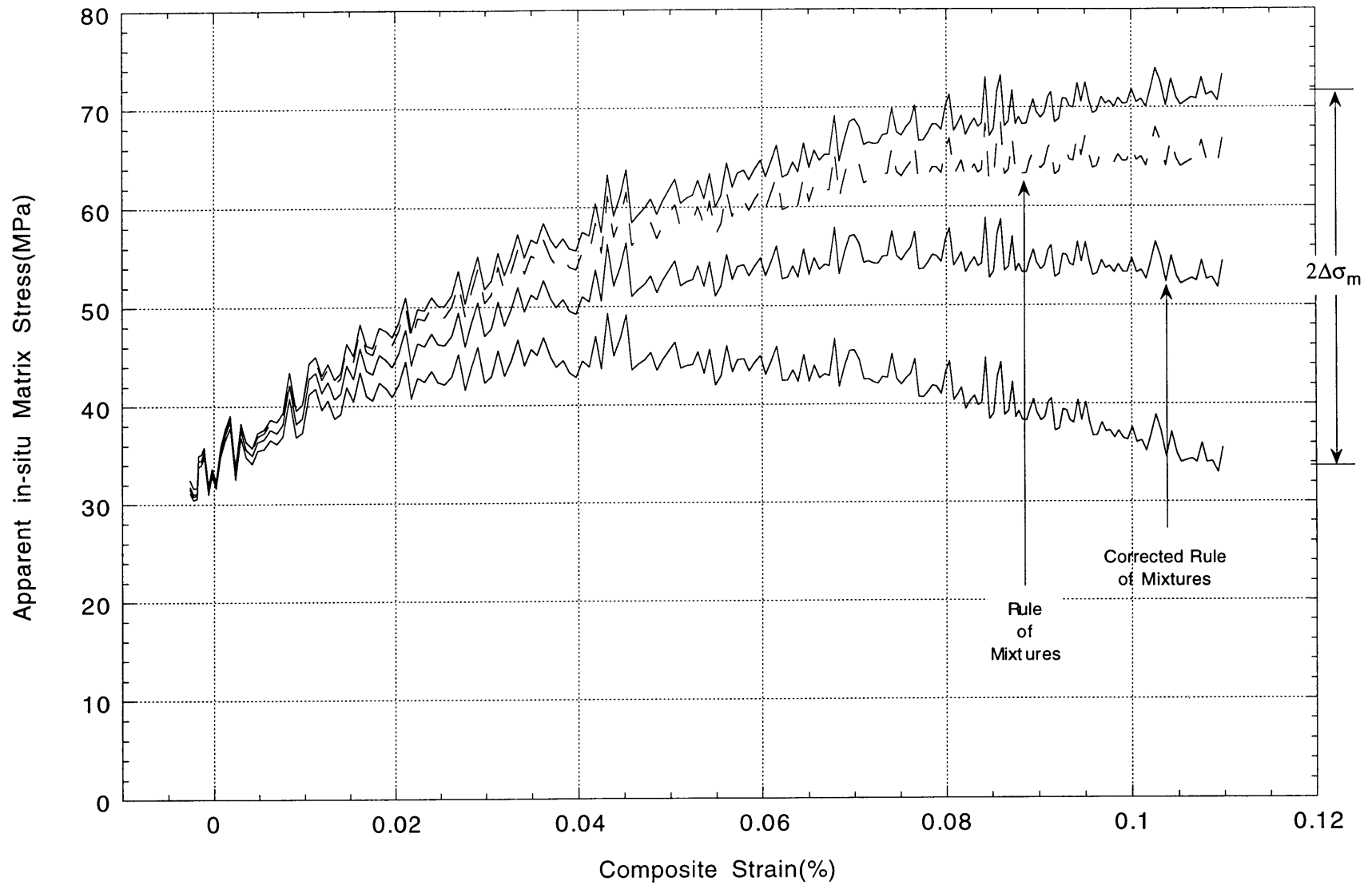


Figure 5-17 - (d) Total estimated uncertainty on apparent *in-situ* matrix stress-strain curve of Cu-1wt%Ti computed from composite reinforced with 72.6% Nextel 610 fibers (Sample 1-1•CuTi/3M).

5.2.3 Fracture

In most cases, fracture occurred in the grips or at the tab edges rather than in the gage section, presumably due to stress concentrations. For this reason, and because most bars were cycled several times before fracture, the ultimate tensile strength is not reported.

The fracture type and surface morphology varies widely between the different systems investigated. It ranges from extremely brittle with no fiber pull-out in CuTi/3M (where the fracture surface is indistinguishable to the naked eye from that produced by a diamond saw cut, except in poorly infiltrated regions of some samples, which were discarded) to highly irregular with extreme fiber pull-out in CuAl/3M (where the fracture surface typically extends across half the bar length). Some macroscopic steps (several mm) at the fracture surface occur in Cu/FP, especially after tension-compression cycling, and in Al/3M and low volume fraction Al/FP. Macroscopic steps are also observed on bars of Al/FP tested to fracture in liquid nitrogen. The other composite systems (AlCu/FP, CuAl/FP, and CuTi/FP) all show similarly rough but rather regular fracture surfaces with steps not exceeding 0.5 mm on average. Progressive fracture, particularly in systems featuring weak fiber/matrix interfaces, is also apparent as a finite drop in flow stress followed by further deformation before general fracture in a few stress-strain curves.

SEM observations of fracture surfaces of all composite systems show some microscopic steps but few individually pulled-out fibers. Matrix fracture between fibers was ductile. Local debonding between fibers and matrix occurred in Cu/FP. A strong fiber-matrix interface is evident in all other systems, except Cu-7wt%Al, which represents an intermediate case (see Figure 5-18 to Figure 5-24). These observations fully agree with the macroscopic qualitative assessment of bond strength of Table 5-2, page 79. Individual fiber fracture surfaces are relatively flat and perpendicular to the fiber axis (especially in CuTi/3M, Figure 5-24), except in CuAl/FP and Al/FP tested to fracture in liquid nitrogen. In the latter system, fiber fracture is uneven, in some cases even extending parallel to the fiber axis (as seen in Figure 5-19) and the overall fracture surface is composed of large steps, Figure 5-18.

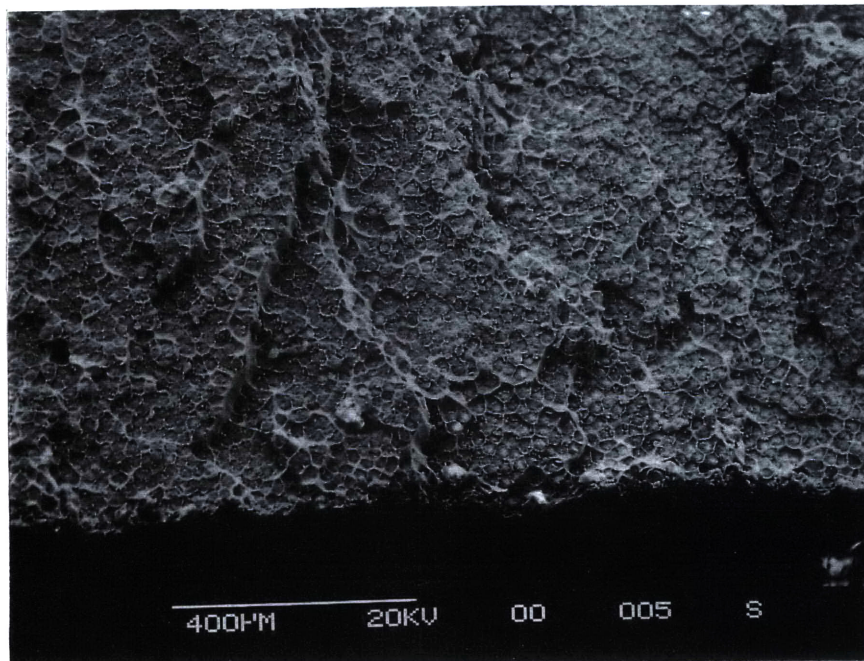
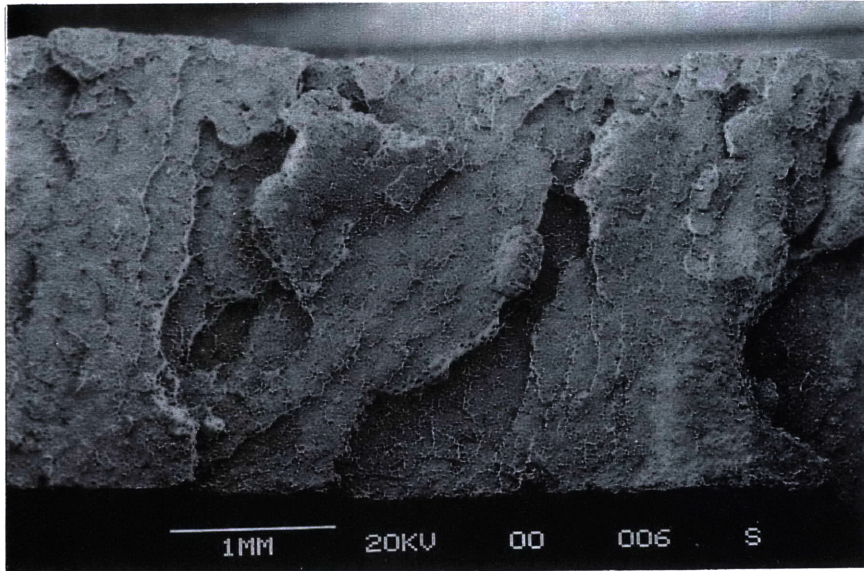


Figure 5-18 - Fracture surface of Fiber FP reinforced pure aluminum tested at 77 K (Sample 0-4•Al/FP).

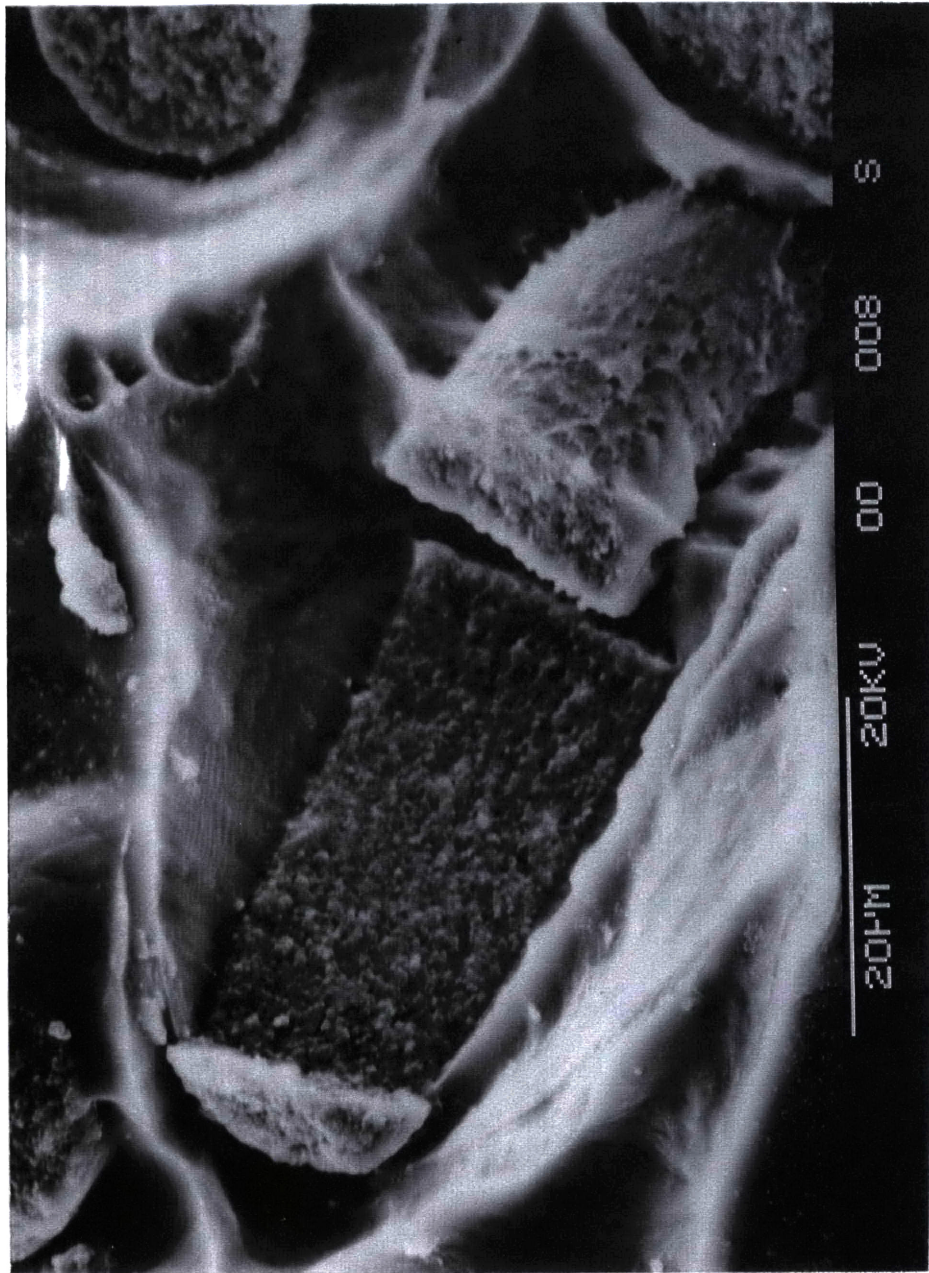


Figure 5-19 - Longitudinally split fiber in Fiber FP reinforced pure aluminum tested at 77 K, showing strong interfacial bonding (Sample 0-4•Al/FP).

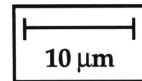
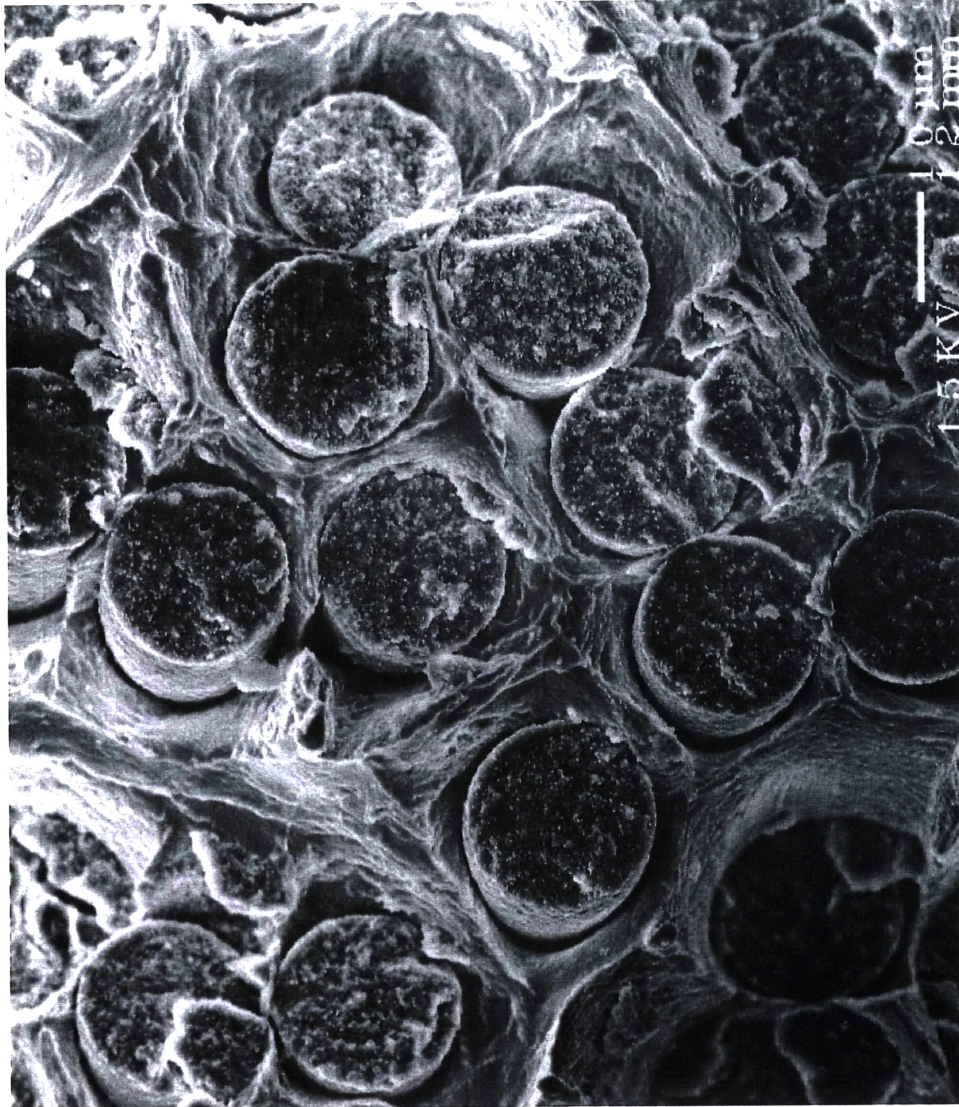


Figure 5-20 - Fracture surface of Fiber FP reinforced Cu-7wt%Al, showing intermediate interfacial bond strength (Sample 1-1•CuAl/FP).

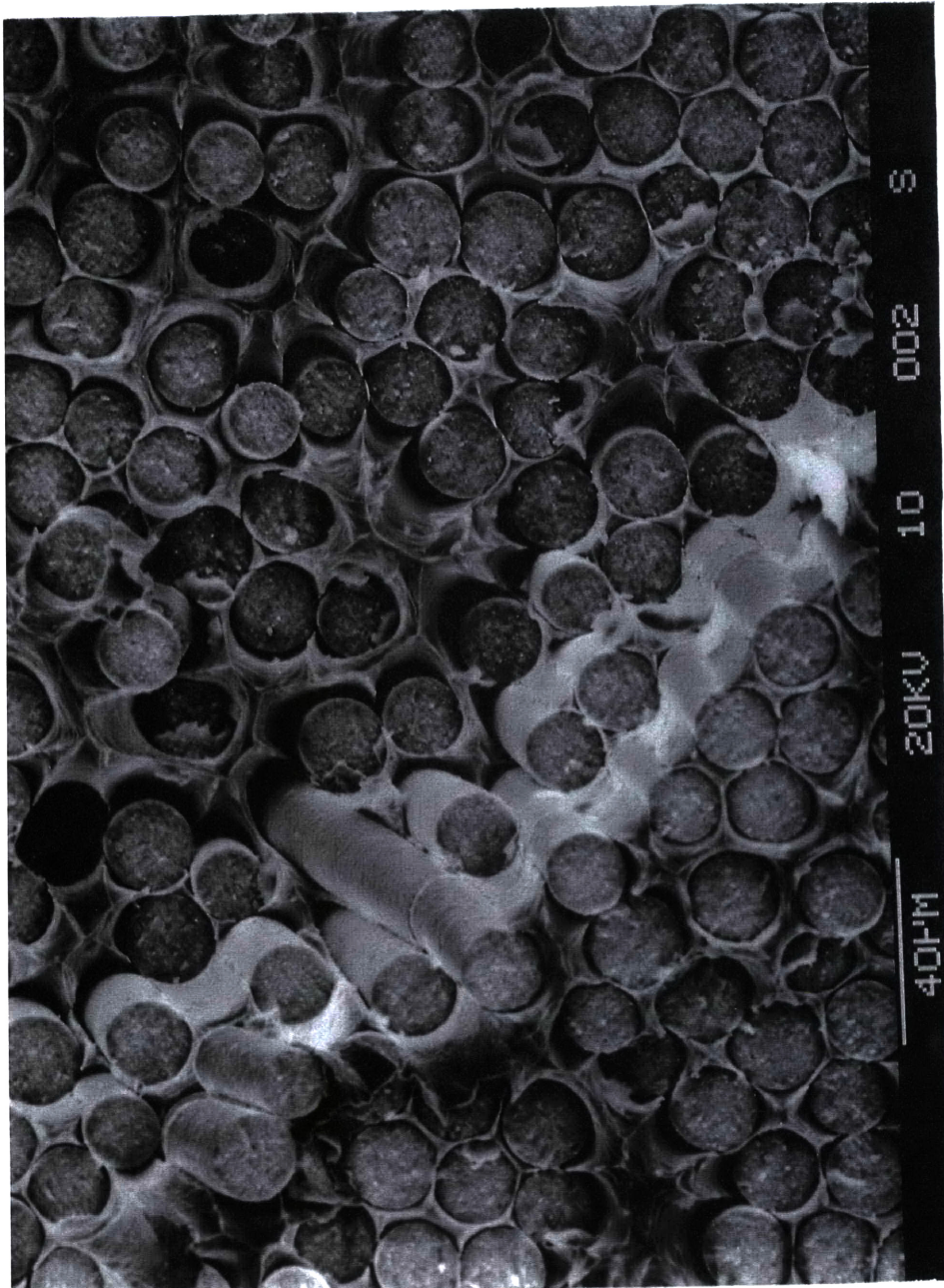


Figure 5-21 - Fracture surface of Fiber FP reinforced pure copper, showing fiber-matrix debonding (Sample 0-3•Cu/FP).

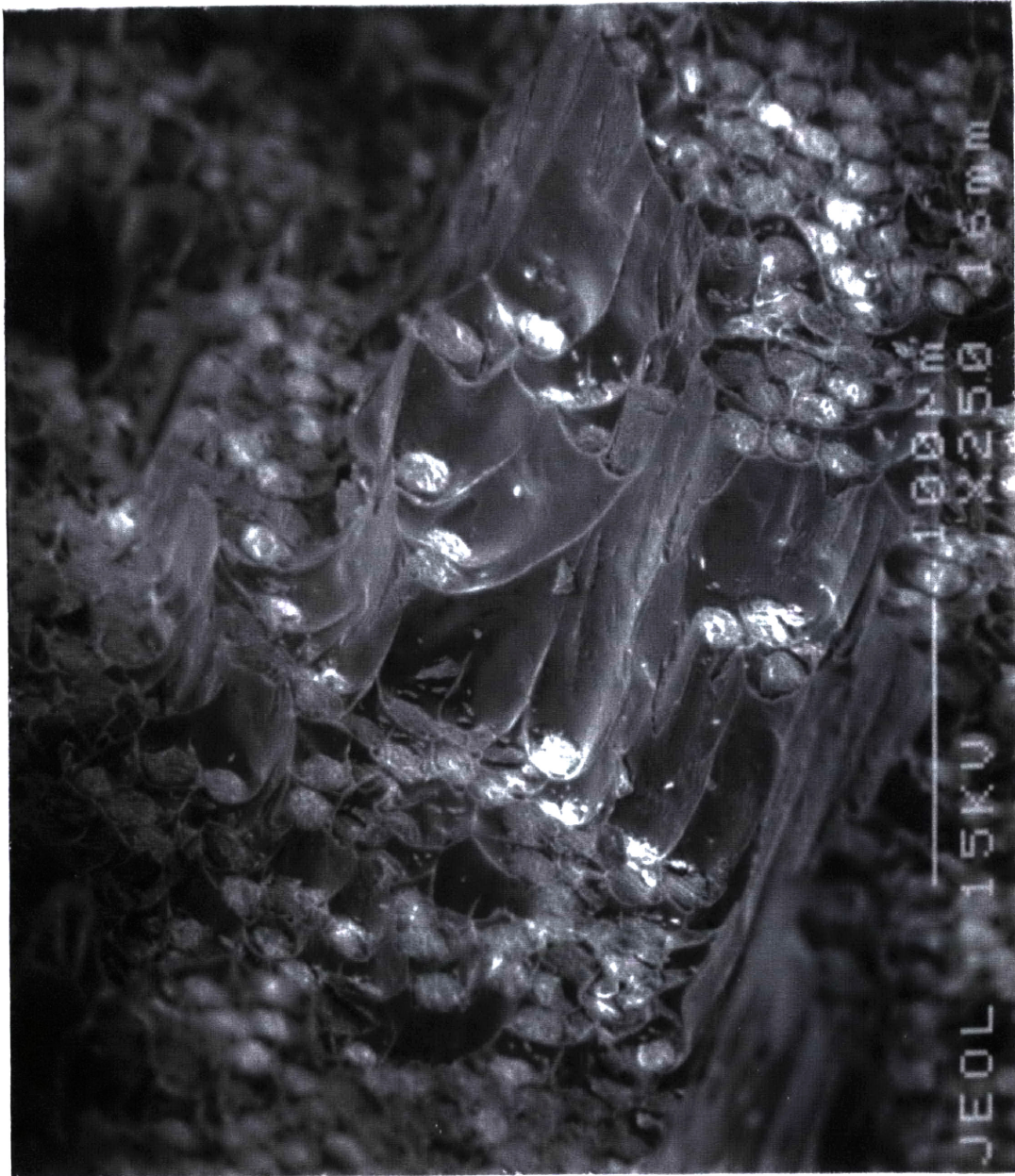


Figure 5-22 - Fracture surface of Fiber FP reinforced Al-0.9wt%Mg, showing strong interfacial bonding (Sample 2•AlMg/FP).

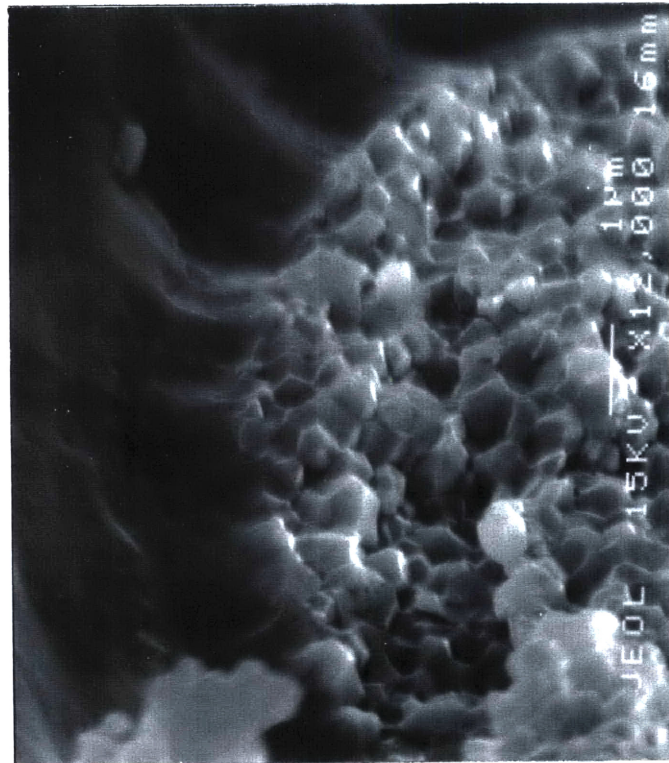


Figure 5-23 - Detail of fracture surface of Fiber FP reinforced Al-0.9wt%Mg, showing strong interfacial bonding. Fiber FP grains, of average size 0.5 μm , are clearly visible (Sample 2•AlMg/FP).

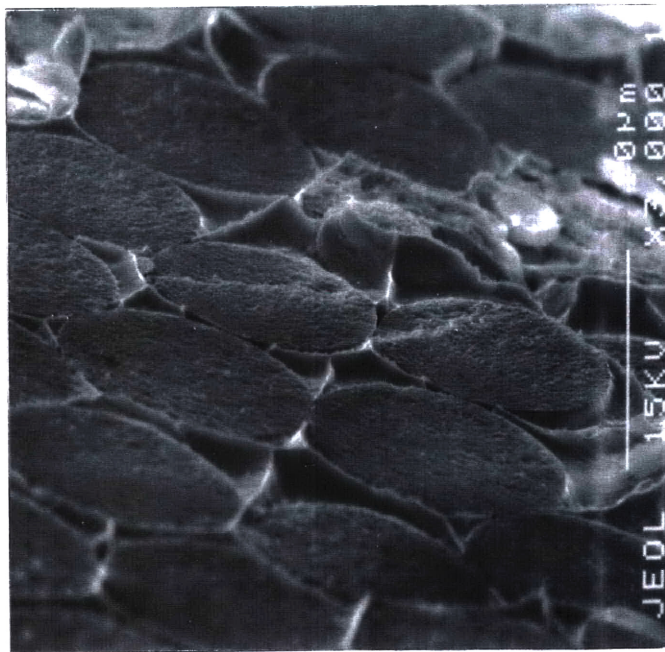
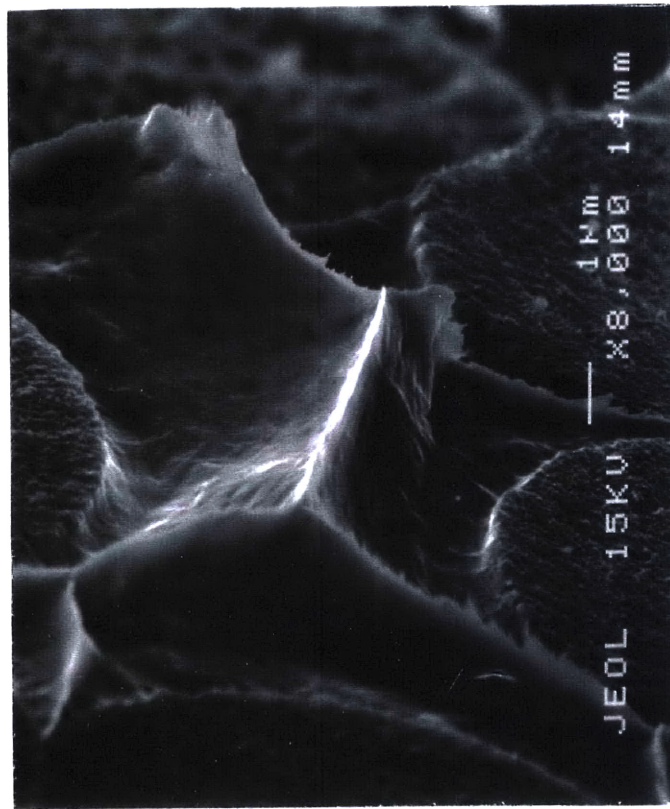


Figure 5-24 - Fracture surface of Nextel 610 fiber reinforced Cu-1wt%Ti, showing strong interfacial bonding. Note planar character of fiber fracture (Sample 1-1•CuTi/3M).

6. Discussion

6.1 Unreinforced Matrices

Elastic moduli for unreinforced metal samples were found to be slightly lower than values cited in the literature (*e.g.*, Table 4-4, page 70); this is expected because the present static method of determination of the modulus uses stresses several orders of magnitude higher than the more adequate dynamic methods (*e.g.*, resonance or pulse techniques, which avoid non-linear effects [93]).

The nature of hardening of the unreinforced matrices was analyzed as proposed by Asaro [117, 118]. Kinematic (type I) hardening was computed using forward tension data $\sigma = f(\epsilon)$ to model the compressive portion of the σ - ϵ loop by writing:

$$\sigma = 2f\left(\frac{1}{2}\epsilon\right). \quad (6.1-1)$$

For unreinforced aluminum-based matrices, the hardening behavior observed varied somewhat with the alloy, and was intermediate between kinematic and isotropic. Inhomogeneous flow in the form of steps on the stress-strain curve was observed in the plastic regime of Al-0.9wt%Mg. Such a behavior, a manifestation of the Portevin-Le Chatelier effect, is classical in Al-Mg alloys (see *e.g.* [119]).

Multiple cycling of pure Cu increased the amplitude of the hysteresis loops appreciably; the sample thus displayed cyclic hardening, as expected given its annealed condition. Hardening was more kinematic than isotropic. The occurrence of cyclic creep may be noted, as cyclic stress-strain curves were not strain-controlled because the strain range in compression was limited by the onset of buckling.

In Cu-7wt%Al and Cu-1wt%Ti, hardening was nearly perfectly kinematic, the more so with continued cycling. Multiple cycling increased the amplitude of the hysteresis loops only slightly.

In Cu-1wt%Ti, the stress-strain curve obtained upon retesting after a new anneal and heating for 1h at 120°C was essentially the same as for the original test. It is therefore concluded that gluing tabs with 3M Scotchweld AF-163-2™ (which requires curing at 120°C for 1h) does not significantly affect the mechanical

properties of Cu-1wt%Ti (although such heating may cause the onset of spinodal decomposition in this alloy [84-86, 120]).

It is worth noting that, although unreinforced matrix bars were annealed, these samples are likely to have experienced some straining during cooldown from casting temperatures due to differential thermal contraction between these samples and their surrounding mold. This may explain why these samples have some features of a previously deformed metal.

6.2 Uncertainty on Matrix Stress, and Broken Fibers in Pure Copper Matrix Composites

Because the reinforcement in the composites is far stiffer than the matrix, the fraction of the applied load carried by the fibers is high in comparison with that carried by the matrix. Therefore, the matrix stress, when deduced from the composite stress-strain curve, is computed as the small difference between two large numbers, Eq. (3.2-7), page 33. As a consequence, experimental uncertainty in the derived *in-situ* matrix stress-strain curves is generally quite large with fiber reinforced metal composites.

The main sources of error for most composite systems stem from uncertainty on fiber volume fraction V_f and modulus E_f , as illustrated in Table 5-4, Table 5-5, and Table 5-6, page 93. Potential sources of error were presented and analyzed above. Figure 5-8 (d) to Figure 5-17 (d) illustrate, for each composite system, the magnitude of the uncertainty on the apparent *in-situ* matrix stress of a representative monotonic loading cycle. It is seen that this uncertainty is, indeed, not negligible.

The possible presence of broken fibers in the composites has so far been considered negligible. In aluminum-based matrix composites and in Nextel 610 fiber reinforced composites, no significant fiber fracture was detected after matrix dissolution; hence this issue is considered to be of no concern in those systems. In Cu/FP composites, on the other hand, the measured volume fraction was higher than expected, which could imply that some fiber fracture occurred during preform packing. This suspicion was corroborated by qualitative examination of fibers

extracted by dissolution, which indicated the presence of a significant number of short fibers. Additionally, most results from tests on pure copper matrix composites (see Section 5.2) show apparent *in-situ* matrix stress-strain curves with a negative slope in the plastic regime. This could be due to the presence of broken fibers: whenever a fiber breaks, it ceases locally to carry the applied load. Since no systematic lowering of the flow stress was observed in consecutive cycles of tension-compression mechanical tests (*i.e.*, the matrix displayed apparent saturated cyclic behavior for the limited number of cycles explored; see Figure 5-13 (c), page 111), the origin of such broken fibers in FP reinforced copper can be traced to the processing of the composites.

The deficit in load carried by the fibers caused by one fiber break can be estimated if, as is classically assumed, load transfer from fiber to matrix is governed by a constant shear stress at the matrix/fiber interface equal to the matrix plastic flow stress in shear, τ_f . Load transfer from fiber to matrix is then given by:

$$\pi r^2 \frac{d\sigma_f}{dx} = 2\pi r \tau_f, \quad (6.2-1)$$

where r is the fiber radius and $\sigma_f = E_f \epsilon_c$ the full fiber stress corresponding to the average composite strain ϵ_c . The increase in load from matrix to fiber is then constant until the fibers are fully loaded to σ_f . This occurs over a distance l given by:

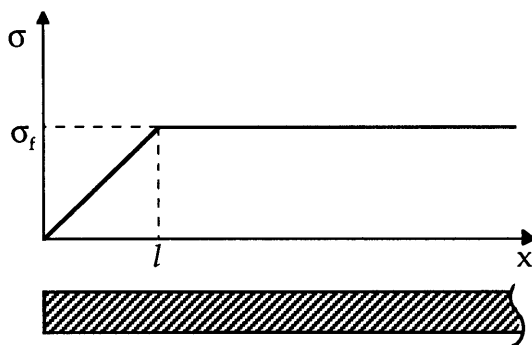


Figure 6-1 - Load carried by a broken fiber

$$l \approx \frac{E_f \epsilon_c}{\frac{d\sigma_f}{dx}} = \frac{E_f \epsilon_c r}{2\tau_f}. \quad (6.2-2)$$

The total deficit in average load carried by each fiber caused by n breaks over total length l_0 is then easily deduced by integration as equal to:

$$\frac{\Delta\sigma_f}{\sigma_f} = n \frac{l}{l_0}, \quad (6.2-3)$$

such that the fibers in the composite have on average an apparent modulus equal to:

$$E_{app} = E \left(1 - n \frac{l}{l_0} \right) . \quad (6.2-4)$$

The presence of broken fibers may thus cause a decrease in the apparent load carried by the fibers if the fiber contribution to composite stress is assumed to be $E_f V_f$.

The average failure strain of Fiber FP reinforced composites is 0.3%. Using $E_f=379\text{GPa}$, $r_{FP} = 10 \mu\text{m}$, and $\tau_{Cu} \approx 20 \text{MPa}$ in Eq. (6.2-2), we determine that the critical fiber length for full load transfer from matrix to fiber is $l = 284 \mu\text{m}$.

To quantify the number of broken fibers per unit length, a sample cut from Specimen 4-2•Cu/FP parallel to the fiber direction was ground carefully with 600 grit SiC paper over a surface approximately equal to 1cm^2 . This was followed by polishing with $6 \mu\text{m}$, $3 \mu\text{m}$, and $1 \mu\text{m}$ diamond paste for at least 1 hour at each step. Final polishing was done for 15 minutes with Mastermet™ (trademark of Buehler, Lake Bluff, IL). A sequence of adjacent pictures spanning the whole area of the sample was taken at 5x and 10x magnification. The pictures were pasted together, the total length of fibers was measured and the number of fiber breaks counted. Although no excessive pressure was used, some fibers were still broken during polishing because of the weak fiber-matrix interface in Cu/FP. These fiber breaks, however, were clearly distinguishable from the pre-existing ones (see Figure 6-2) and were not included in the final count.

On a total composite area of 0.09cm^2 , $n=58$ fiber breaks per meter of Fiber FP were counted (where one break is equivalent to two non-contiguous fracture surfaces). Hence, in this sample, the apparent fiber modulus is altered by a factor $(1-58 \times 284 \cdot 10^{-6}) \approx 0.984$. Fiber breaks thus cause a decrease of $0.016 \times 379 \approx 6 \text{GPa}$ in the fiber modulus. This value is twice the estimated uncertainty of 3 GPa on the elastic modulus of Fiber FP (see Section 4.5.2). By examination of Table 5-5 and Table 5-6, page 94, it is seen that broken fibers in pure Cu can introduce a systematic error on the order of - 10 GPa in the measured apparent *in-situ* matrix work hardening rates



Figure 6-2 - Longitudinal cross-section of Sample 4-2•Cu/FP ($V_f = 60\%$). The area shown is approximately one fifth of that used to estimate the proportion of broken fibers.

for this system. The experimentally determined plastic slope of the matrix of specimen 4-2•Cu/FP in tension is $-27 \text{ GPa} \pm 16 \text{ GPa}$ (see Table A- 4, page 162). The effect of broken fibers is thus appreciable, being on the order of the experimental error in the curves, and accounts at least for a significant fraction of the systematic downwards tilt observed in matrix in-situ stress-strain curves measured with this particular composite system.

Alloyed copper-based matrix composites showed comparatively lower fiber volume fractions, which were in accordance with nominal values selected to avoid fiber fracture during fiber preform packing. No significant fiber breakage was thus assumed to occur in these composites; this was verified by inspection of fibers in one sample of Cu-Al matrix composite after matrix dissolution (Table 5-3, page 86). Exceptions to the above statement were two samples of Nextel 610 reinforced Cu-1wt%Ti (designated 1-3•CuTi/3M and 1-4•CuTi/3M), which exhibited higher volume fractions than expected. Fiber breakage was not suspected in those cases (due to the greater toughness of these fibers compared to Fiber FP). Rather, the presence of macropores in the matrix, presumably due to solidification shrinkage, could explain these findings. This was confirmed by the samples' fracture mode: whereas the well infiltrated CuTi/3M samples showed an extremely flat fracture surface, 1-3 and 1-4•CuTi/3M exhibited large localized areas of fiber pull-out. Mechanical test results of the latter two samples were therefore not taken into consideration. A third sample, 1-2•CuTi/3M, showed a flat fracture surface with no fiber pull-out, but also had a rather high fiber volume fraction and may thus be subject to caution.

The effect of a change in temperature on the volume fraction was also investigated. The calculation, presented in Appendix C, shows that the variation in V_f due to differential thermal contraction between the composite phases upon cooling from room temperature to 77 K is negligible compared to experimental uncertainty on V_f . The volume fractions, determined by pycnometry at room temperature, of composites subsequently tested in liquid nitrogen remain therefore valid at 77 K.

6.3 Matrix Yielding

In all composites produced in this work, initial matrix yielding in tension was found to take place at a positive value of the applied stress; in other words, a finite, albeit small in some systems, Stage I was observed. Overall, it is apparent that the difference between the initial yield stress in tension and that in compression is greater for composite matrices than for corresponding bars of unreinforced metal, with the exception of Al-4.5wt%Cu, most likely because for this one system the bar of unreinforced material was machined directly from the DC cast bar.

In binary alloy matrix composites, initial yield in tension, be it initial yield for a test started in tension, or the first matrix yield in tension following a test started in compression, always tended to be significantly more abrupt than (i) subsequent yield in tension for tension-compression tests, and (ii) yield in compression, for both initial and subsequent cycles. This is seen in Figure 5-11 (c), Figure 5-12 (c), Figure 5-14 (c), and Figure 5-15 (c). This tendency was less marked with non-alloyed matrices, as visible, *e.g.*, in Figure 5-10 (c) for pure Al reinforced with Nextel fibers. Also, after stress/strain cycling, this difference in matrix yielding behavior with straining direction disappeared: for all systems, it was found that the second and subsequent stress-strain loops were highly symmetrical near the transition from elastic to plastic deformation, as seen, *e.g.*, in Figure 5-14 (c).

The greater difference in yield stresses between tension and compression, and the difference in the onset of matrix plastic deformation upon initial straining, can be attributed to matrix deformation due to differential thermal strains during composite cooldown. Since thermal contraction of the matrix is greater than that of the fibers, matrix dislocations are generated during cooldown of the composite from processing temperatures, causing significant alterations in matrix substructure and the build-up of internal stresses within matrix and fibers; these effects are amply documented in the literature [15, 17-19], and have also been modeled using finite element analysis [38, 43-46, 121-125].

In all systems, the apparent *in-situ* yield stress in initial compression exceeded that measured in initial tension. Significant tensile residual stresses are thus

present in all composite matrices. The physical origin of these is also well-known, namely differential contraction during composite cooldown from processing and heat-treating temperatures. Consequently, the real zero-stress zero-strain origin of the matrix *in-situ* stress-strain curves is translated below the origin of the measured curves, which corresponds to zero composite stress and strain.

Dislocational matrix hardening, which resulted during cooling of the composite, proves that thermal mismatch strains were of sufficient magnitude to induce plastic flow in the matrix, at least on a local basis. This conclusion is borne out by calculations, in particular by plane strain and generalized plane strain numerical simulations based on the finite element method, which show that, for differences in coefficient of thermal expansion between matrix and fiber on the usual order of 10^{-5} K^{-1} and temperature excursions during cooldown on the order of several hundred degrees, significant plastic flow is generated in the matrix during cooldown [40, pp. 174-190, 45, 46, 125].

It is interesting, then, that a finite Stage I of deformation is observed for most of the composite systems in this work; if the matrix was deforming plastically under the action of thermal mismatch during cooldown, it is expected to be at its tensile yield flow stress upon initial straining, and should therefore display no Stage I deformation, as predicted in finite-element calculations [45, 46, 125]. Two reasons can be invoked to explain this effect, namely (i) that after cooldown, relaxation of internal stresses occurred in the composite at the testing temperature, or (ii) that during cooldown, before reaching the testing temperature, the final stage of composite deformation was elastic.

To discriminate between these two interpretations, we quantify the latter, using the fact that, in fiber reinforced metals, predictions of composite expansion derived from simple unidimensional models of the kind first used by Garmong [126, 127] and de Silva and Chadwick [128] show good agreement both with experiment [124, 126-131], with analytical models derived using cylindrically symmetric unit cells [129, 132, 133], and with plane-strain finite element analysis [124, 125, 131], even though thermal-strain generated plastic flow and the distribution of residual stresses within the matrix, are highly inhomogeneous [40 pp. 174-190, 45, 46, 125]. Hence, for

the analysis of internal stresses generated by thermal strains within the matrix, the simple rule of mixtures, which assimilates the composite to a series of small independent bars of each phase stressed in uniaxial tension, provides an adequate tool for first analysis because longitudinal stresses dominate the longitudinal thermal expansion.

We thus consider a composite cooling down from an elevated temperatures at which the matrix is annealed and stress-free. Denoting by ε_i strain and σ_i the average stress within each phase along the fiber direction, with subscript $i = f$ for the fibers, c for the composite, and m for the matrix, during cooldown of the composite with no applied stress, the following relations hold:

$$\sigma_f = E_f \varepsilon_f = - \frac{(1-V_f)}{V_f} \sigma_m \quad (6.3-1)$$

since the average longitudinal stress is zero and since the fibers only deform elastically, and:

$$\varepsilon_c = \varepsilon_m + \alpha_m (T - T_0) = \varepsilon_f + \alpha_f (T - T_0) \quad (6.3-2)$$

since longitudinal strain is equal within all phases. At elevated temperatures the matrix deforms predominantly by creep and its plastic flow stress is low. As temperature decreases, the importance of creep decreases, and it is reasonable to assume that at some intermediate temperature, at which the matrix plastic flow stress is low, matrix deformation due to thermal strain mismatch is predominantly plastic, as witnessed by the observation that composite matrices are hardened by enhanced dislocation densities. Since the matrix then deforms plastically, σ_m equals the average plastic flow stress within the matrix. As the composite cools further by a temperature decrement $dT < 0$, the average increase in matrix longitudinal strain $d\varepsilon_m$ is given by:

$$d\varepsilon_m = (\alpha_f - \alpha_m) dT - \frac{(1-V_f)}{E_f V_f} d\sigma_m \quad (6.3-3)$$

from a combination of Eqs. (6.3-1) and (6.3-2), where $d\sigma_m$ is the increment in matrix plastic flow stress, assuming the matrix deforms plastically. During cooling, the first term on the right-hand side of Eq. (6.3-3) is positive (because the fibers stretch the matrix, inducing tensile and hence positive strain in the matrix), while the second term is negative because σ_m increases with decreasing temperature (this stands to reason since matrix hardening reduces the fiber-induced matrix elongation by straining the fibers in compression). Now, the matrix strain, $d\epsilon_m$, can be decomposed into elastic and plastic terms, $d\epsilon_{m,el}$ and $d\epsilon_{m,pl}$ respectively, such that Eq. (6.3-3) becomes:

$$-\frac{d\epsilon_{m,pl}}{dT} = (\alpha_m - \alpha_f) - \left[\frac{1}{E_m} + \frac{1-V_f}{E_f V_f} \right] \left(-\frac{d\sigma_m}{dT} \right) \quad (6.3-4)$$

Hence, for plastic deformation to occur during the temperature decrement ($-dT$), the left-hand side of this equation must be positive and we must have:

$$\frac{(\alpha_m - \alpha_f)}{\frac{1}{E_m} + \frac{1-V_f}{E_f V_f}} > -\frac{d\sigma_y}{dT} \quad (6.3-5)$$

where σ_y is the matrix flow stress at temperature T and for the level of average matrix work-hardening caused by prior cooling.

If the rate of increase in σ_y with decreasing temperature is sufficiently high, therefore, the matrix ceases to deform plastically, elongating elastically instead.

Computation of the left-hand side of Eq. (6.3-5) for the present systems yields values between 0.7 and 0.9 MPa K^{-1} for composites containing from 50 to 70 % fibers in both Al and Cu matrix composites, and 0.6 MPa K^{-1} for Al-20% Fiber FP. These values exceed (but in some cases only slightly) the average rate of increase with decreasing temperature in the yield stress of aluminum and copper metal matrices explored in this work [101].

This leads to the conclusion that some relaxation of internal stresses has occurred within the composites at room temperature before testing. That this

should occur is plausible since, for example, relaxation of dislocation structures generated during deformation of dispersion-hardened copper is indeed observed at room temperature [134]. Relaxation of internal stresses in fiber reinforced metals has also been proposed in studies of their thermal expansion which, furthermore, show no evidence of composite matrices leaving their yield surface during cooldown (this would be evident in an increase in the apparent composite CTE) [124, 129-131, 135, 136].

Reasons for differences observed between matrices in the presence or extent of Stage I deformation must therefore result from differences in the mechanisms and level of stress relaxation after cooldown. In particular, that no clear evidence of Stage I deformation in composites tested at 77 K was detected stands to reason, given the low temperature of these tests, and the fact that straining was initiated immediately after final cooldown of the composites.

The relatively abrupt nature of initial tensile yield can also be explained as resulting from thermal mismatch straining of the matrix during cooldown: if, as is suggested both by microstructural examination of reinforced metal substructures and by micromechanical analysis, there are inhomogeneities in the level of hardening within the matrix, there are also gradients in both the intrinsic flow stress, and the longitudinal residual stress within the composite. Ignoring the influence of relaxation processes, yield is then expected to occur relatively abruptly in initial tensile deformation because all regions of the matrix are already at predominantly tensile yield within the composite, so yield is expected to occur relatively simultaneously throughout the matrix. During initial yield in compression, on the other hand, locally harder matrix regions require a higher local stress decrease to start yielding; hence more progressive yielding is expected in compression. That relaxation processes between cooldown and testing do not erase this difference is an indication that these must lower the overall internal stress relatively uniformly, without erasing gradients in internal matrix stress.

A difference in yielding behavior between initial tension and following compression and tension cycles can also be observed in some of the unreinforced matrices cast with the composites, namely Cu-1wt%Ti and Cu-7wt%Al (Figure 5-7);

however, the effect was less pronounced than in composite matrices, and was absent from the Al-4.5 wt %Cu sample machined from the as-received ingot. It could be attributed, by analogy with the composite matrices, to differential contraction between these unreinforced samples and their mold during cooldown in the infiltration apparatus. A similar difference between initial yielding in tension and compression can also be seen in pure aluminum tested at 77 K (Figure 5–6), where it can be explained by imperfect compensation of the sample’s thermal contraction during cool-down, which probably resulted in cycling slightly above the yield stress prior to testing (the sample had to be gripped before cooling).

6.4 Dislocation Densities

An estimation of the dislocation density initially present in the matrix of the composites can be obtained using the well-known correlation between matrix flow stress σ and dislocation density ρ :

$$\sigma = \sigma_0 + \alpha G b \sqrt{\rho} \quad , \quad (6.4-1)$$

where G is the matrix shear modulus, b the magnitude of the Burgers vector of dislocations, σ_0 a constant corresponding to the flow stress of a perfectly annealed matrix and α a constant on the order of one. Constants σ_0 and α are documented in the literature for all matrices explored here, with the exception of Cu-1wt%Ti, for which the same constants as for Cu-7wt%Al were used, Table A– 3, page 161.

The matrix flow stress σ corresponding to the dislocation density present within the matrix can therefore be estimated from the *in-situ* matrix tension-compression stress amplitude for a fixed strain amplitude, sufficiently large to exceed the range of elastic deformation upon straining direction reversal. Results are given in Table 6–1, together with the strain amplitudes used for the measurement.

Computed dislocation densities in composite matrices fall in a range spanning about one and a half order of magnitude, centered around 10^{14} m^{-2} . This agrees with

the value estimated for pure Al/45% Fiber FP composites on the basis of electron microscopic characterization of the matrix [24].

These dislocation densities far exceed values predicted using simple models based on consideration of geometrically necessary dislocation loops which have radii commensurate with the fiber radius (*e.g.*, [15]). Significant amplification of the dislocation length required to compensate for thermal strain mismatch during composite cooldown thus occurs, a conclusion that is in agreement with previous work [15, 24]. One possible cause for this was proposed in Ref. [24], namely that roughness of the surface of Fiber FP causes punching of dislocation loops far smaller than the fiber radius; it would seem, given that much smoother Nextel fiber composites contain many more dislocations than are geometrically necessary, that this is not the only operative mechanism.

It is seen that, in composites of pure aluminum reinforced with alumina fibers, computed dislocation densities vary by one and a half orders of magnitude as the fiber radius, fiber volume fraction, and the test temperature, vary. If dislocations are predominantly emitted at the fiber/matrix interface during composite cooldown, one would expect that the total length of dislocations emitted per unit composite volume be roughly proportional to the number of fibers present per unit composite volume, and inversely proportional to the fiber radius r_f if it is assumed that punched dislocation configurations are dependent on fiber dimensions (as in simple geometrically necessary dislocation punching models). It is also expected that the density of punched dislocations be proportional to the total mismatch strain, which is in turn proportional to the difference ΔT between the sample temperature and that at which thermal mismatch strains are no longer accommodated by creep, in the vicinity of 500 K for pure aluminum.

Computed dislocation densities divided by $\Delta T V_f (1-V_f)^{-1} r_f^{-1}$ should therefore be approximately constant. This is indeed found to be the case, with values obtained varying by a factor of at most 2, compared with one and a half orders of magnitude for ρ . It can therefore be concluded that enhanced dislocation densities created in the matrix by thermal mismatch during cooldown are consistent with geometrically

necessary dislocation punching models. However, the total punched length is about one thousand times higher.

Table 6-1 - Average tension-compression stress amplitude, in MPa (for given strain amplitude, in %) and corresponding dislocation density in the matrix (with fiber volume fraction in %), computed from Eq. (6.4-1) , page 145

	Unreinforced matrix (MPa)		Matrix in Fiber FP reinforced composite (MPa)		Matrix in Nextel 610 reinforced composite (MPa)	
	Average stress amplitude, MPa (Strain amplitude, %)	Average dislocation density, 10^{12} m^{-2}	Average stress amplitude, MPa (Strain amplitude, %)	Average dislocation density, 10^{12} m^{-2} (V_f , %)	Average stress amplitude, MPa (Strain amplitude, %)	Average dislocation density, 10^{12} m^{-2} (V_f , %)
99.999% Al at Room Temp.	35 (0.4%)	20	45 (0.4%)	40 (30%)	130 (0.4%)	300 (56%)
					200 (0.4%)	720 (67%)
99.999% Al at 77 K	60 (0.35%)	50	170 (0.35%)	420 (47%)	—	—
Al-4.5wt%Cu	350 (0.5%)	740	320 (0.5%)	620 (43%)	—	—
Al-0.9wt% Mg	60 \diamond (0.3%)	10	110 (0.3%)	90 (37%)	—	—
99.996% Cu	70 (0.4%)	8	140 (0.4%)	30 (60%)	—	—
Cu-7wt%Al	150 (0.4%)	40	280 (0.4%)	140 (51%)	230 (0.4%)	90 (69%)
Cu-1wt%Ti	100 (0.4%)	20	240 (0.4%)	110 (53%)	170 (0.3%)	70 (73%)

\diamond Taken as twice the stress amplitude of the sample tested in tension.

6.5 Flow Stress in Tension-Compression and Hardening Behavior

Despite indications of an initially dislocated matrix substructure due to thermal stresses, no softening was found in cycles imposed on the samples. If any evolution in matrix flow stress was observed, it was rather a tendency for slight cyclic hardening, although the number of cycles explored was small and the strain range in compression limited.

The hardening behavior of the respective matrices in the composites was analyzed as for the unreinforced metals using Asaro's method [117, 118], Eq. (6.1-1), page 134, with the origin of the apparent matrix stress-strain curve deduced from an estimate of the residual stresses (the method for determining the residual stresses is described in the following section). No correlation in hardening behavior was found between the unreinforced and reinforced matrices. Whereas the former had a tendency to go from an isotropic or intermediate character in the initial tension-compression cycle towards kinematic hardening with continued cycling, as expected [117], no such behavior was apparent in the reinforced matrices, which showed neither hardening character. Indeed, the asymmetry between the tensile and compressive slopes in Stage II of a given stress-strain cycle (see work hardening rates in Table 5-5 and Table 5-6, page 94, and discussion in Section 6.6) indicate an apparently greater than isotropic behavior in compression (when the actual compressive portion of the σ - ϵ curve was compared with an expected compression curve computed from the tensile portion of the σ - ϵ curve), while no isotropic behavior was observed in tension, where hardening in successive cycles was minimal.

This is also apparent on composite "theta curves", which show that in compression, the rate of composite, and hence of matrix, work hardening has a tendency to remain higher than in tension, in both the initial and subsequent tests.

This is indicative that residual stress patterns set up in the composite during cooldown, although somewhat reduced during tension-compression testing since the abrupt nature of matrix yield found upon initial tensile straining is lost, are partly retained for the strain amplitudes explored here. Indeed, if more highly

dislocated matrix regions retain both a higher flow stress amplitude and a higher tensile residual stress along the fiber direction, these will remain elastic and increase the average matrix rate of work hardening before they yield.

6.6 Residual Stresses

The presence of a finite tensile internal stress in the composite matrices was also clearly noticeable during tension-compression testing: matrix stress-strain loops are, in all systems, centered around a horizontal line that lies below the origin of *in-situ* matrix stress-strain curves derived from the composite curves. For the systems and strain ranges explored in this work, thus, composite deformation does not erase the internal stresses generated during composite cooldown.

The gradual stabilization of stress-strain loops in tension-compression testing allowed a determination of a well-defined origin on matrix *in-situ* stress-strain curves from the resulting loops, and hence provided a means of assessing the matrix internal stress σ_r . It was noticed that σ_m - ϵ curve loops are, in the portion extending from the onset of yield to the last point prior to unloading, symmetric about a single point, which can be determined graphically with relative ease as the single intersection of lines running mid-way between several pairs of tangents to the curves (an example is shown in Figure 6-3, page 152). This point was, thus, taken to belong to the line of zero matrix stress on σ_m - ϵ plots. This method yielded consistent and reproducible results in all tests, provided that the (several) points on the hysteresis loop used to determine the center of symmetry were not too close to the elastic portion of the loop. This method also yielded a relatively well-defined single point even when used for initial yielding curves, including cases where the onset of yielding was more abrupt in tension than compression (see discussion in Section 6.3, page 140). It was also verified experimentally, using this technique, that the initial hysteresis loops of all the unreinforced matrices tested have a center of symmetry at $\sigma = 0$. It should be noted that this last statement does not necessarily imply the absence of a Bauschinger effect in the matrix.

The above described method of determination of the origin of *in-situ* matrix stress-strain curves was deemed superior to the alternative and more classical technique of taking the mid-point between stress extrema on a hysteresis loop extending far enough in the plastic regime, such that the tangents measured at each extremum be parallel and close to horizontal. This condition was often not met in the present tests because, as indicated in the previous section, the slope in the plastic regime in compression usually remained, at compressive strain amplitudes which were explored here, higher than that in tension. A second and significant advantage of the present method of determination of the origin is that, since relevant data points are taken at low composite strain, it is relatively independent of several sources of experimental error (such as error on V_f) in the matrix *in-situ* stress-strain curves. It can be used, in particular, even in cases where such sources of error cause a downward tilt in the *in-situ* matrix stress-strain curves.

Knowing the stress origin, the internal stress could then be determined for each sample. For the initial tension-compression cycle, it was found that there is no significant variation in the residual stress from sample to sample of a given composite system: typically 2-5 MPa for aluminum-based systems and 5-10 MPa for copper-based systems, *i.e.*, a quantity within experimental error on the stress. This result was expected given the relative constancy of fiber volume fraction and the identical annealing procedure applied to all samples of a given system. The average value of the residual stress thus determined is given for the composite systems investigated in Table 6-2. These values are governed, in each system, by the combined influences of matrix flow stress increase due to dislocation punching during cooldown from processing temperatures, and by relaxation processes at room temperature following cooldown, as shown above.

Furthermore, it was found that, by application of this method for successive loops on stress-strain curves of the matrix of the same sample, there was relatively little shift (if any) in the origin (provided the center of symmetry of the loop in question remained near $\epsilon=0$): typically, origins thus determined shifted negligibly between loops for aluminum-based systems, and by not more than 10 MPa for most

copper-based composites[†]. When that shift occurred with successive loops, its direction always tended to be towards a lowering of the origin, which would correspond to an increase in the influence of tensile residual stress with cyclic straining; however experimental uncertainty precludes a clear conclusion on this point.

[†] The shift was larger in one sample of each Cu-Al composite system (20 MPa in 1-3•CuAl/FP and 45 MPa in 1-2•CuAl/3M).

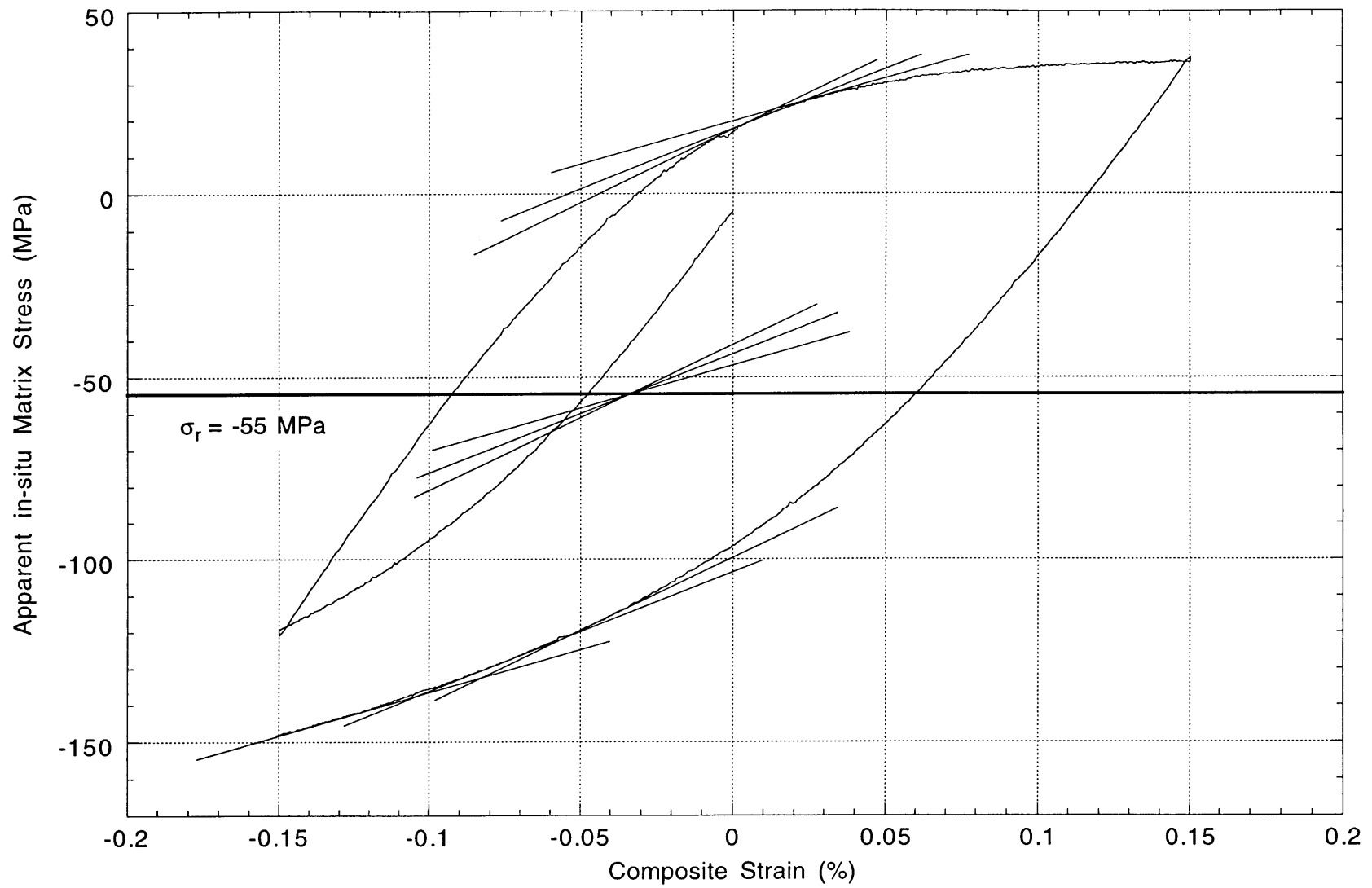


Figure 6-3 - Example of graphical determination of the residual stress from the center of symmetry of an *in-situ* matrix stress-strain tension-compression test (Cu-1wt%Ti matrix from composite reinforced with 53.9% Fiber FP; Initial cycle; Sample 1-2•CuTi/FP).

Table 6-2 - Apparent *in-situ* matrix yield stress and residual stress (computed as described in Section 6.6) from stress-strain curves (MPa)

System	Yield in tension (MPa)	Yield in compression (MPa)	Residual stress (MPa)
99.999%Al/ Fiber FP	6	-23	-10
99.999%Al/ Fiber FP at 77 K			-50
99.999%Al/ Nextel 610	22	-50	-7
Al-4.5wt%Cu/ Fiber FP	25	-95	-90
Al-0.9wt%Mg/ Fiber FP	14	—	-35
99.996%Cu/ Fiber FP	14	-70	-40
Cu-7wt%Al/ Fiber FP	17	-70	-90
Cu-7wt%Al/ Nextel 610	6	-107	-90
Cu-1wt%Ti/ Fiber FP	14	-46	-50
Cu-1wt%Ti/ Nextel 610	14	-60	-20

6.7 Matrix Work-Hardening Rate

Experimental error on the *in-situ* rate of matrix work hardening resulted from uncertainty in the values of V_f , E_f , $\theta_{c,pl}$ and $\theta_{h,pl}$. As seen in Figure 5–8 (d) to Figure 5–17 (d), the resulting uncertainty in the slopes of derived stress-strain curves is significant, yet it is below 15% of the matrix modulus for most systems (20% for Al/3M with high V_f). In each test, for all composite systems, it was found that the measured tensile *in-situ* rate of matrix work hardening decreased steadily with increasing strain, towards a relatively constant large-strain value which remained the same from cycle to cycle for each sample.

Values of this average tensile *in-situ* rate of matrix work hardening, measured using a strain range $\Delta\varepsilon = 0.05\%$ extending immediately before unloading of the composite or before composite rupture, are given in Table 5–5 and Table 5–6, page 94, for each system explored. It is seen that, for all composites, there is no *in-situ* rate of matrix work hardening that fluctuates about a systematically high value representing a large fraction of the matrix modulus. Although *in-situ* matrix stress-strain curves measured with composites produced here did, in several samples, display high slopes, no systematic deviation of measured matrix work hardening rates beyond the range that can be ascribed to experimental uncertainty was found - if anything, average values of the apparent *in-situ* rate of matrix work hardening were negative, an effect explained, within experimental error, for pure copper by fiber breakage during preform preparation.

It was found in a previous investigation of Fiber FP reinforced pure aluminum at room temperature that the *in-situ* rate of matrix work hardening in that system is low, being zero within (significant) experimental error. This earlier finding agrees with the present results for pure aluminum reinforced with Nextel fibers, thus reinforcing the conclusion that in pure aluminum reinforced with continuous fibers in the size range used to produce engineering composites (above a few micrometers), the room temperature behavior displays no feature that is not explained as resulting from dislocation punching and internal stress buildup during composite cooldown from processing temperatures.

Most remaining composite matrices explored in this work, comprising aluminum tested at 77K, aluminum-magnesium, copper, Cu-1wt%Ti and Cu-7wt%Al, represent a series of systems for which cross-slip is rendered increasingly more difficult compared with pure aluminum. No noticeable enhancement in tensile *in-situ* rate of matrix work hardening was found for any of these systems either. This result thus represents a significant extension of the conclusion reached with aluminum that, in metal matrix composites, the observed *in-situ* matrix plastic flow rheology is that expected to result from the sole influence of differential contraction between matrix and reinforcement during cooldown from processing temperatures, with no other noticeable influence exerted on the creation and motion of dislocations within the composite.

Our findings thus disagree with results from previous and similar studies conducted with copper reinforced with tungsten wires 10 and 20 μm in diameter, where it was found that the apparent matrix rate of work hardening can be spectacularly high in composites, exceeding one-half of the matrix modulus at high fiber loadings (see Section 2.4, page 21). The present work therefore raises doubt on the notion, supported by various authors and theories over the past twenty-five years, that high rates of matrix work hardening are systematically observed in metal matrices reinforced with fibers around ten micrometers in diameter.

The question remaining then is, why were spectacular rates of work hardening observed in the copper-tungsten system? Despite the significant experimental uncertainty inherent in matrix *in-situ* stress measurement from the composite, we leave unquestioned the validity of the data by Kelly and Lilholt and Lee and Harris, which provide the most careful and eloquent body of evidence of this effect. We note that the explanation originally proposed by Kelly and Lilholt, namely that a portion of the matrix remains elastic during Stage II deformation, can in turn be explained as resulting from significant, but not unrealistic, dislocational hardening of a portion of the matrix by dislocation punching from the fibers during composite cooldown, followed by relaxation of internal stresses, as observed in the present copper-matrix composites.

7. Conclusion

Continuous alumina fiber reinforced composites were produced by pressure infiltration, featuring metallurgically simple matrices based on the face-centered cubic metals aluminum and copper. These composites were tested uniaxially parallel to the fibers, to derive, using the rule of mixtures, the *in-situ* matrix flow stress. Although this technique yields data with significant quantitative uncertainty due to the subtraction of two large numbers involved in the computation of matrix flow stress, the physical clarity of the data generated is greater than with other composite or mechanical test configurations when the reinforcement diameter falls below about 100 μm .

It is found that matrix *in-situ* plastic deformation differs in the composite from that of the same matrix deformed and processed analogously. Essential differences found in this work between the matrix and the unreinforced metal were an increased flow stress, a change in the detailed features of yield with stress cycling, and the presence of residual stresses in the matrix. These could all be rationalized as results of the generation of internal stresses due to differential matrix/fiber contraction during cooldown of the composite from processing temperatures, and concomitant dislocation emission within the matrix. No clear evidence was found for very large rates of *in-situ* matrix work hardening, such as have been observed in copper reinforced with tungsten fibers of diameter similar to that of the fibers used in this work, namely 10 to 20 micrometers.

Suggestions For Future Work

Observations of the microstructure of the various matrices by transmission electron microscopy would help explain the presence, in all cases, of a higher than predicted dislocation density. This has been done successfully on the Fiber FP reinforced pure aluminum system [8, 24], despite the difficulty associated with the preparation of thin sections. Ion milling, which induces in the sample a temperature excursion of the order of 200 K (both with and without a cold stage), is likely to cause dislocation rearrangements due to differential thermal contraction between matrix and fiber, a fact rarely recognized in the literature. Jet-polishing, which only thins the metal matrix, thus becomes the method of choice, with the added difficulty of having to use careful preliminary mechanical grinding. The weak fiber-matrix interface in pure copper/FP composites and erratic results during preparation of Al-4.5wt%Cu/FP thin sections prevented the successful observation, in the present work, of the microstructure in these two systems. Cu-Ti and Al-Mg matrix composites, with their strong interfacial bond, appear as the most likely candidates in this respect.

Tension-compression cycling of pressure cast copper reinforced with a high volume fraction of tungsten fibers (for uniform reinforcement distribution), with the samples annealed prior to testing, would allow a more direct comparison with the present results. A diameter of the order of 10 μm is below that of most standard tungsten fibers used in industry. The high cost of the very large quantity of fibers required for such an experiment is a liability which should be kept in mind.

It would also be of interest to measure, on the composites used in this work, the thermal expansion during cooldown from elevated temperatures. These measurements could ascertain that matrix deformation remains plastic during the lower-temperature portion of the cooldown cycle, confirming experimentally the calculations above. In this regard, it would be interesting to explore the thermal expansion of composites which have matrices featuring a yield strength that increases rapidly with decreasing temperature, or a sufficiently low value of the left-

hand side of Eq. (6.3–5), page 143, to explore the second mechanism of formation of a finite range of Stage I composite tensile deformation.

Appendix A: Materials Constants and Summary of Test Results

Table A-1 - Elastic moduli and densities used in this work

Material	Elastic modulus E (GPa)	Shear modulus G (GPa) †	Density
Pure Al at Room T	70	26	2.6989
at 77 K	78	29	—
Al-0.9wt%Mg	62 \diamond	23	2.689 \diamond
Al-4.5wt%Cu as cast	—	—	2.787 \diamond
T4	72.7 \diamond	27	2.793 \diamond
Pure Cu	115	43	8.936 \diamond
Cu-7wt%Al	127 \diamond	47	7.90 \diamond
Cu-1wt%Ti as cast	—	—	8.852 \diamond
heat treated	110 \diamond	41	8.862 \diamond
Fiber FP at Room T	379 \pm 3	153	3.91 \diamond
at 77 K	385 \pm 3	155	—
Nextel 610	379 \pm 2	153	3.85

\diamond Values measured in this work.

† Values computed from Eq. (3.1-2), page 29.

Table A-2 - Poisson's ratio, coefficient of thermal expansion, and magnitude of Burger's vector

Material	Poisson's ratio ν	CTE ($10^{-6}/K$)	Magnitude of Burger's vector b (nm)
Al	0.345 (298 K)	23.5 \diamond (293 to 373 K)	0.2864 \diamond
	0.337 (77 K)	18 (298 to 77 K)	
Cu	0.343	16.5	0.25561 \star
Al ₂ O ₃	0.24	8.5 (293 to 373 K)	
		3.4 (298 to 77 K)	

\diamond Cullity [137, p. 506]

\star Liu and Bassim [138]

\diamond Smithells Metals Reference [139]

Table A-3 - Stacking fault energies and constants entering Eq (6.4-1), page 145

Matrix	Stacking fault energy γ (mJ/m ²)	σ_0 (MPa)	α
Pure Al	166 †; 250 ‡	0 †	0.5 †
Al-Mg	110 † (Al-0.7wt%Mg at 170°C)	65 † ◆ (Al-3wt%Mg; Al-5wt%Mg)	0.66 † (Al-3wt%Mg; Al-5wt%Mg)
Al-4.5wt%Cu	—	0 †	0.83 †
Pure Cu	78 †; 90 ‡	0 †	1.1 †
Cu-7wt%Al	2.5 †	0 †	1.0 †
Cu-1wt%Ti	—	0 ★	1 ★

† Murr [140, p.145]

‡ Suresh [141]

† Swann [142, p142]

† Guyot and Reynaud [143]

◆ $\sigma_0 = 15$ MPa, estimated from the yield stress of unreinforced Al-0.9wt%Mg tested in the present work, was used in the computation of average dislocation density in Al-0.9wt%Mg

† Sahoo and Lund [144]

† Various authors [108, 109, 145-148]

★ Estimated by comparison to other Cu systems [146]

Values of γ for Al-4.5wt%Cu and Cu-1wt%Ti were not found in the literature. However, since alloying decreases the stacking fault energy of copper, $\gamma_{\text{Cu-1wt\%Ti}}$ is expected to be well below 80 mJ/m². $\gamma_{\text{Al-4.5wt\%Cu}}$, on the other hand, while likely somewhat lower than γ_{Al} , is still very high, because stacking faults do not occur in Al-Cu alloys (although stacking faults have been observed in θ' precipitates of Al-Cu alloys [149]).

Values of σ_0 and α for Cu-1wt%Ti were not found in the literature, but they were considered to be of the same order as in the other copper systems, because they vary little with alloying in copper [146].

Table A- 4 (a) - Summary of samples tested, with test sequence (Tension or Compression), and volume fraction determined by pycnometry: aluminum-based systems

System	Sample	Test Sequence	Vf(pyc)
Pure Al/FP at Room T	2•Al/No Fibers	(TC)x10	0
	1-1•Al/FP	T-T-C-T-T(F)	21.44
	1-2•Al/FP	T-T(F)	27.91
	1-3•Al/FP	C-C-T-T	34.84
	1-5•Al/FP	T	36.85
Pure Al/FP at -196 °C	1•Al/No Fibers	T-T-C-T-C-C-T	0
	0-1•Al/FP	T(preload)-T(F)	48.00
	0-2•Al/FP	(T-C)x3	47.58
	0-3•Al/FP	T-T(F)	45.51
	0-4•Al/FP	C-C-T-T-T(F)	48.51
	0-5•Al/FP	C-C-T(F)	48.56
	0-5•Al/FP Top	Top half after test	48.61
	0-6•Al/FP	T	46.24
	0-8•Al/FP	T-T-C-C-T-T	43.37
	1-4•Al/FP	T(F)	37.16
Pure Al/3M at Room T	1-1•Al/3M	T-T-C-C-T	56.15
	1-1•Al/3M Bot	Bottom half after test	56.09
	1-2•Al/3M	T-T-T-C-T-T-T	55.21
	1-2•Al/3M-NewTest	T-T-T	
	1-61•Al/3M	T-T-T(F)	51.69
	1-62•Al/3M	T-T(F)	48.75 (Lower Vf than below due to large vein of matrix at fract. surf.)
	1-62•Al/3M Main	Main piece after fracture	51.80
	2-2•Al/3M	T-T-T-T	65.52
	2-2•Al/3M-again	(T)x4-T(F)	
	2-4•Al/3M	T-T-C-(T)x5	67.10
	2-4•Al/3M-NewTest	C-T(F)	67.63
	2-4•Al/3M Top	Top half after test	67.47
	2-5•Al/3M	C-C-T-T-T	66.27
	2-5•Al/3M-NewTest	T-T-C-T-TT	66.86
	2-5•Al/3M-LastTest	T-C-T-T-T	
	2-5•Al/3M-NewConfig	T-T-T-TC	66.86
	NC#5-10 (22-27total)	T-T-C-T-C-T	
	NC#11-15(28-32total)	T-T-T-C-T	
	2-5•Al/3M-NewAnneal	T-C-T-T	66.86
	NA#5-8 (37-40 total)	T-C-T-T	
2-9•Al/3M	T-C-T-T-T(F)	67.22	
Al-4.5wt% Cu(T4)/FP at Room T	1•AlCu/No Fibers	T-TC-TC-T	NA
	2-1•AlCu/FP	C	NA
	2-2•AlCu/FP	T	NA
	2-3•AlCu/FP	T	NA
	2-4•AlCu/FP	T-T(F)	NA
	2-5•AlCu/FP	T-T-T(F)	NA
	2-6•AlCu/FP	C	NA
	3-1•AlCu/FP	T(F)	39.67
	3-2•AlCu/FP	C-T	40.67
	3-3•AlCu/FP	T	41.22
	3-4•AlCu/FP	C-T-C-T-T(F)	42.33
	3-5•AlCu/FP	C-T	41.72
	3-6•AlCu/FP	(T-C)x5-T(F)	44.46
	3-6•AlCu/FP Mid	Dissolved by Luvak	45.29
3-7•AlCu/FP	(T-C)x9	46.18	
Al-0.9wt% Mg/FP at RT	1•AlMg/No Fibers	T	0
	1•AlMg/NoFibers again	T-T	0
	8•AlMg/No Fibers	T-T-T	0
	2•AlMg/FP	T(F)	41.66
	3•AlMg/FP	T	39.90
	4•AlMg/FP	T	38.24
	10•AlMg/FP	T	33.84
10•AlMg/FP again	T-T		

Table A- 4 (b) - Summary of samples tested, with test sequence (Tension or Compression), and volume fraction determined by pycnometry: copper-based systems

System	Sample	Test Sequence	Vf(pyc)
Pure Cu/FP at Room T	3-5•Cu/No Fibers	T-T	0
	3-5•Cu/NoF-NewTest	T	0
	1•Cu/No Fibers	(T-C)x11	0
	0-1•Cu/FP	T	59.25
	0-2•Cu/FP	C	59.01
	0-3•Cu/FP	T(F)	60.12
	0-4•Cu/FP	T-T-T	59.57
	0-4•Cu/FP-New Test	C-C(F)	
	1-1•Cu/FP	(T)x8-T(F)	60.29
	1-2•Cu/FP	T(F)	62.38
	1-4•Cu/FP	C-T	63.34
	1-4•Cu/FP	After test	63.64
	3-1•Cu/FP	T	59.36
	3-1•Cu/FP	After test-whole bar	59.84
	3-1•Cu/FP Bot	Bottom grip section	60.0 ± 1.5
	3-2•Cu/FP	T(F)	61.70
	3-3•Cu/FP	T(F)	58.64
	3-4•Cu/FP	(T-C)x7-T(F)	62.05
	3-4•Cu/FP Main	Main piece after fracture	63.09
	4-1•Cu/FP	T-T-C-C-T(F)	55.63
4-1•Cu/FP Main	Main piece after fracture	56.33	
4-2•Cu/FP	C-C-T-T	60.29	
4-2•Cu/FP Bot	Bottom half after test	59.92	
4-3•Cu/FP	C-C-T-T(F)	59.38	
4-4•Cu/FP	T-T(F)	58.10	
4-5•Cu/FP	(T-C)x6-T(F)	58.19	
Cu-7wt%Al/NoFibers	1•CuAl/No Fibers	TC-TC-TC	0
Cu-7wt%Al/FP	1-1•CuAl/FP	T-C-T(F)	50.21
	1-1•CuAl/FP Top	Top half after test	50.36
	1-2•CuAl/FP	C-T-C-T	50.08
	1-3•CuAl/FP	(T-C)x3-T(F)	52.08
	1-4•CuAl/FP	C-T-C-T(F)	52.15
Cu-7wt%Al/3M	1-1•CuAl/3M	(C-T)x3-C(F)	69.58
	1-2•CuAl/3M	C-T-C-Tx4-C-T(F)	68.60
	1-3•CuAl/3M	T-C-T-T(F)	70.09
Cu-1wt%Ti/NoFibers	1•CuTi/No Fibers	(TC)x10-T	0
	2•CuTi/No Fibers	TC-TC-TC	0
	2•CuTi/NoF NewTest	T-C-T	0
Cu-1wt%Ti/FP	1-1•CuTi/FP	T-T-C-T-T-T-T(F)	53.60
	1-2•CuTi/FP	(C-T)x7	53.86
	1-3•CuTi/FP	(T-C)x2-T-T-T	52.20
	1-4•CuTi/FP	C-T-C-T(F)-C-T-T	52.30
Cu-1wt%Ti/3M	1-1•CuTi/3M	C-T(F)	72.55
	1-2•CuTi/3M	T(F)	73.81
	1-3•CuTi/3M	(C-T)x4-C-T(F)	74.13
	1-4•CuTi/3M	T-C-T(F)	76.13

Table A-5 - Summary of all mechanical test results, by system (see next page through p. 176)

Pure Al Matrix Dupont FP Fibers at Room T				Matrix Em (GPa)	Dupont FP Ef (GPa)	ΔE_f (GPa)	ΔV_f for Al/FP (%)	$\Delta \theta_c / \theta_c$ Al/FP (%)	Hill el. bounds θ_{el} (GPa)	Error on el. bnds $\Delta \theta_{el}$ (GPa)	Hill pl. bounds θ_h (GPa)	Error on pl. bnds $\Delta \theta_h$ (GPa)								
Sample ID	Date Cast	Date Annealed	Date Tested	(C)omp. or (T)ens.	Max Stress (MPa)	Max Strain (%)	V_f (pyc) (%)	Composite Slope in Stage I (GPa)	Composite Slope in Elast. Unld. (GPa)	Composite Slope in Stage II - Tension (GPa)	Composite Slope in Stage II - Compr. (GPa)	Matrix Elastic Slope fm V_f (Pyc) (GPa)	Total Error on θ_m el. (GPa)	Mat. St.II Slope fm V_f (Pyc) - Tension (GPa)	Total Error on θ_m ,pl. (T) (GPa)	Mat. St.II Slope fm V_f (Pyc) - Compr. (GPa)	Total Error on θ_m ,pl. (C) (GPa)			
Pure Al Matrix Dupont FP Fibers at Room T				70.0	379	3	0.69	0.04	0.5	0.3	3.0	1.5								
2*Al/NoFibers	10-Nov-94	29-Mar-95	10-Apr-96	(TC)x10	13.145	0.15142	NA	63.9	64.0	1.0	NA									
Al/NoFibers Tested at Room T				2	-13.603	-0.03163		NA	NA	NA	(1.8)									
				3	13.210	0.15504														
				4	-13.783	-0.03151														
				5	13.321	0.16052														
				6	-13.919	-0.03121														
				7	13.886	0.20107														
				8	-14.583	-0.06275														
				9	14.392	0.21122														
				10	-14.837	-0.06188														
									15.014	0.25119										
					-15.082	-0.03586														
					16.979	0.5003														
					-16.013	0.09915														
					18.134	0.60127														
					-16.983	0.09445														
					19.108	0.70208														
					-17.506	0.19452														
					20.0629	0.83519		NA	62.4	0.4	NA									
					-18.017	0.29951		NA	64.2	NA	0.6									
							Avg:	63.9	63.5	0.7	0.6									
1-1*Al/FP	10-Nov-94	23-Dec-94	28-Dec-94	T	113.84	0.13259	21.44	120.4	123.0	76.6	NA									
Al/FP Tested at Room T				T	153.25	0.18477		124.2	124.7	75.2	NA									
				C	-109.70	-0.11512		NA	127.6	NA	76.0									
				T	199.76	0.24656		NA	124.2	74.6	NA									
				T	235.35	0.29575		124.2	123.0	74.1	NA									
				T(F)	253.4 (F)	?														
							Avg:	21.44	Avg El. Slope: 123.9	75.1	76.0	53.6	4.1	-11.6	6.2	-10.5	6.2			
1-2*Al/FP	10-Nov-94	23-Dec-94	30-Dec-94	T	205.23	0.193	27.91	143.9	142.8	100.7	107.7									
				T(F)	240.52	0.226		145.9	NA	99.8	NA									
							Avg:	27.91	Avg El. Slope: 144.2	100.2	107.7	52.6	4.8	-11.9	7.0	-1.5	7.0			
1-3*Al/FP	10-Nov-94	27-Dec-94	3-Jan-95	C	-237.58	-0.165	34.84	164.1	167.9	NA	130.7									
				C	-292.50	-0.208		168.1	170.3	NA	130.4									
				T	228.61	0.175		NA	167.5	124.2	NA									
				T	278.55	0.216		180.3	167.1	124.7	NA									
							Avg:	34.84	Avg El. Slope: 169.3	124.5	130.6	56.4	5.6	-16.2	8.2	-6.9	8.1			
1-5*Al/FP	10-Nov-94	3-Jan-95	5-Jan-95	T	264.95	0.188	36.85	163.5	171.4	133.9	143.4	49.4	5.9	-13.8	8.5	1.1	8.4			
							Gen. Avg:	30.3	Avg El. Slope: 152.2	108.4	114.4	53.1	5.1	-13.3	7.4	-4.7	7.3			

Pure Al Matrix Dupont FP Fibers at 77K				Matrix Em (GPa)	Dupont FP Ef (GPa)	ΔEf (GPa)	ΔVf for Al/FP (%)	$\Delta \theta c/\theta c$ Al/FP (%)	Hill el. bounds θ_{el} (GPa)	Error on el. bnds $\Delta \theta_{el}$ (GPa)	Hill pl. bounds θ_h (GPa)	Error on pl. bnds $\Delta \theta_h$ (GPa)								
Sample ID	Date Cast	Date Annealed	Date Tested	(C)omp. or (T)ens.	Max Stress (MPa)	Max Strain (%)	Vf(pyc) (%)	Composite Slope in Stage I (GPa)	Composite Slope in Elast. Unid. (GPa)	Composite Slope in Stage II - Tension (GPa)	Composite Slope in Stage II - Compr. (GPa)	Matrix Elastic Slope fm Vf(Pyc) (GPa)	Total Error on θ_m el. (GPa)	Mat. St.II Slope fm Vf(Pyc) - Tension (GPa)	Total Error on θ_m ,pl. (T) (GPa)	Mat. St.II Slope fm Vf(Pyc) - Compr. (GPa)	Total Error on θ_m ,pl. (C) (GPa)			
1•Al/NoFibers	10-Nov-94	29-Mar-95	7-Apr-95	T	22.51	0.18172	NA	82.2	(115.9)	(2.8)	NA									
Al/NoF Tested at 77K				T	29.66	0.61647		84.3	80.0	1.9	NA									
				T	34.20	0.93700		80.8	81.2	1.7	NA									
				C	-28.19	0.48854		NA	83.4	NA	2.2	NA								
				C	-35.26	0.08830		79.9	78.0	NA	1.9	NA								
				T	37.77	0.58823		NA	79.9	NA	NA	NA								
Re-annealed 11-Dec-1995							Avg:	81.8	80.5	1.8	2.1									
0-1•Al/FP	Cast by JAI	4-Oct-94	21-Oct-94	T	85.24	0.034259	48.00	(254.9)	NA	(200.0)	NA									
Al/FP Tested at 77K				T(F)	351.10	0.17289		241.2	NA	174.7	NA									
				Avg:	48.00	Avg El. Slope	241.2	174.7	NA	107.5	7.2	-25.2	11.2	NA	NA					
0-2•Al/FP	Cast by JAI	4-Oct-94	11-Oct-94	T	220.06	0.11122	47.58	NA	226.7	(192.4)	NA									
				C	-240.87	-0.09943		NA	230.5	195.3	(203.5)									
				T	295.53	0.15349		NA	225.2	NA	197.1	NA								
				C	-341.41	-0.14459		NA	234.9	NA	198.7	NA								
				T	420.15	0.21864		NA	218.2	NA	195.6	NA								
				C	-411.84	-0.17745		NA	225.8	NA	196.4	82.4	7.5	20.6	10.5	19.4	10.6			
Avg:	47.58	Avg El. Slope	226.9	197.0	196.4	82.4	7.5	20.6	10.5	19.4	10.6									
0-3•Al/FP	Cast by JAI	4-Oct-94	18-Oct-94	T	385.12	0.20390	45.51	NA	225.2	189.4	NA									
				T(F)	414.02	0.21946		228.7	NA	(197.9)	NA									
				Avg:	45.51	Avg El. Slope	227.0	189.4	NA	94.0	6.9	20.6	10.0	NA	NA					
0-4•Al/FP	Cast by JAI	26-Oct-94	7-Dec-94	C	-424.81	-0.19444	48.51	232.9	236.8	NA	205.2									
				C	-476.17	-0.21833		231.3	246.1	NA	203.6									
				T	292.67	0.14184		NA	235.6	197.3	NA									
				T	360.90	0.17993		230.8	232.9	(200.5)	NA									
				T(F)	381.44	0.19587		234.7	NA	(205.1)	NA									
				Avg:	48.51	Avg El. Slope	235.1	197.3	204.4	93.0	7.5	14.7	10.9	28.5	10.7					
0-5•Al/FP	Cast by JAI	26-Oct-94	17-Nov-94	C	-391.4	-0.17672	48.56	230.8	228.2	NA	206.6									
				C	-416.16	-0.18765		232.2	229.2	NA	206.7									
				T(F)	335.74	0.16737		NA	NA	197.4	NA									
Avg:	48.56	Avg El. Slope	230.1	197.4	206.7	82.9	7.7	14.5	10.9	32.5	10.6									
0-6•Al/FP	Cast by JAI	26-Oct-94	1-Nov-94	T	344.88	0.18041	46.24	229.3	228.9	185.3	NA									
								46.24	Avg El. Slope	229.1	185.3	NA	94.1	7.1	7.9	10.4	NA	NA		
				Avg:	46.24	Avg El. Slope	229.1	185.3	NA	94.1	7.1	7.9	10.4	NA	NA					
0-7•Al/FP	Cast by JAI	21-Nov-94	Not Tested																	
0-8•Al/FP	Cast by JAI	21-Nov-94	22-Dec-94	T	273.65	0.16111	43.37	(190.0)	231.7	166.2	NA									
				T	332.21	0.19299		233.5	NA	NA	NA									
				C	-263.77	-0.12094		NA	NA	NA	164.3									
				C	-362.55	-0.18671		NA	NA	NA	178.4									
				T	285.88	0.16528		NA	238.8	167.8	NA									
				T	368.20	0.21511		NA	229.3	NA	NA									
Avg:	43.37	Avg El. Slope	233.3	167.0	171.4	116.3	6.3	-5.2	9.8	2.4	9.7									
General average, excluding 1-4•Al/FP (which has low Vf):							46.8	Avg El. Slope	231.8	186.9	194.7	96.0	7.1	6.8	10.5	21.5	10.3			
1-4•Al/FP	10-Nov-94	3-Jan-95	5-Jan-95	T(F)	227.83	0.15375	37.16	187.3	NA	144.3	NA									
								37.16	Avg El. Slope	187.3	144.3	NA	69.6	5.8	-2.8	8.5	NA	NA		
				Gen. Avg:	45.6	Avg El. Slope	226.2	181.6	194.7											

Pure Al Matrix 3M Nextel 610 Fibers				Matrix Em (GPa)	Nextel 610 Ef (GPa)	ΔE_f (GPa)	ΔV_f for Al/3M (%)	$\Delta \theta_c / \theta_c$ Al/3M (%)	Hill el. bounds θ_{el} (GPa)	Error on el. bnds $\Delta \theta_{el}$ (GPa)	Hill pl. bounds θ_h (GPa)	Error on pl. bnds $\Delta \theta_h$ (GPa)						
				70.0	379	2	0.69	0.04	0.5	0.3	2.3	1.1						
Sample ID	Date Cast	Date Annealed	Date Tested	(C)omp. or (T)ens.	Max Stress (MPa)	Max Strain (%)	Vf(pyc) (%)	Composite Slope in Stage I (GPa)	Composite Slope in Elast. Unld. (GPa)	Composite Slope in Stage II - Tension (GPa)	Composite Slope in Stage II - Compr. (GPa)	Matrix Elastic Slope fm Vf(Pyc) (GPa)	Total Error on θ_m el. (GPa)	Mat. St.II Slope fm Vf(Pyc) - Tension (GPa)	Total Error on $\theta_m, pl.$ (T) (GPa)	Mat. St.II Slope fm Vf(Pyc) - Compr. (GPa)		
1-1•Al/3M	15-Nov-94	19-Apr-95	25-Aug-95	T	576.18	0.261256	56.15	241.8	238.8	216.8	NA							
				T	747.49	0.340602		241.5	237.5	216.0	NA							
				C	-142.02	-0.05559		NA	242.0	NA	217.1							
				C	-709.14	-0.31655		241.4	240.3	NA	216.8							
				T	755.73	0.342763		NA	242.0	215.0	NA							
				Avg:		56.15	Avg El. Slope:	240.7	215.9	217.0	62.4	8.5	1.9	11.2	4.2			
1-2•Al/3M	15-Nov-94	19-Apr-95	9-Oct-95	T	448.96	0.20539	55.21	235.6	235.0	210.5	NA							
				T	627.59	0.29070		238.1	235.9	207.6	NA							
				T	523.33	0.24157		238.0	236.9	212.0	NA							
				C	-555.08	-0.24729		NA	238.7	NA	211.3							
				T	521.61	0.23906		NA	235.9	209.6	NA							
1-2•Al/3M-NewTest	15-Nov-94	19-Apr-95	1-Nov-95	T	596.22	0.27672		238.5	235.8	210.1	NA							
				T	615.43	0.28844		240.4	237.1	209.6	NA							
				T	578.05	0.26742		235.9	234.6	209.8	NA							
				T	716.06	0.33389		NA	233.9	206.0	NA							
				T	742.62	0.34718		236.9	234.4	207.6	NA							
				Avg:		55.21	Avg El. Slope:	236.6	209.2	211.3	59.9	8.3	-5.3	11.0	-0.6			
				Average of 1-1 & 1-2:		55.7	Avg El. Slope:	238.6	212.6	214.1	61.1	8.4	-1.7	11.1	1.8			
1-61•Al/3M	15-Nov-94	13-Oct-95	17-Nov-95	T	657.92	0.330202	51.69	221.8	221.6	193.0	NA							
				T	902.16	0.45829		223.6	220.1	192.8	NA							
				T(F)	988.73	0.50804		224.4	NA	190.3	NA							
				Avg:		51.69	Avg El. Slope:	222.3	192.0	NA	53.6	7.6	-12.8	10.2	NA			
1-62•Al/3M	15-Nov-94	13-Oct-95	1-Nov-95	T	640.68	0.32217	48.75	222.8	220.6	192.1	NA							
				T(F)	737.66	0.37385		223.3	NA	193.5	NA							
				Avg:		48.75	Avg El. Slope:	222.2	192.8	NA	72.2	6.8	11.2	9.2	NA			
				Average of 1-61 & 1-62:		50.2	Avg El. Slope:	222.3	192.4	NA	63.2	7.2	-0.4	9.6	NA			
2-1•Al/3M	2-Dec-94	23-Dec-94	Not tested															
2-2•Al/3M	2-Dec-94	23-Dec-94	28-Dec-94	T	343.74	0.13181	65.52	273.3	273.3	(256.7)	NA							
2-2•Al/3M-again	2-Dec-94	23-Dec-94	5-Jan-95	T														
				T														
				T														
				T														
				T														
				T(F)	906.27	0.35013		269.6	NA	247.0	NA							
				Avg:		65.52	Avg El. Slope:	272.1	247.0	NA	67.5	11.2	-10.4	15.1	NA			
2-4•Al/3M	2-Dec-94	27-Dec-94	30-Dec-94	T	360.70	0.13561	67.10	281.8	281.5	263.5	NA							
				T	445.37	0.16823		NA	282.3	NA	267.1							
				C	-395.05	-0.13974												
				T														
				T	688.26	0.26136		NA	NA	264.4	NA							

AI/3M Nextel 610 (continued)				T																					
2-4*AI/3M - NewTest	2-Dec-94	29-Mar-95	6-Apr-95	T	-595.50	-0.21563	67.63	280.5	282.2	NA	267.3														
				C	912.84	0.34948																			
					Avg:	67.37	Avg El. Slope:	281.7	264.0	267.2	79.2	11.7	19.4	15.4	29.4										
2-5*AI/3M	2-Dec-94	27-Dec-94	3-Jan-95	C	-430.78	-0.16140	66.27	273.8	277.1	NA	263.1														
				C	-449.95	-0.16856						278.4	278.1	NA	(269.7)										
				T	470.32	0.17625						NA	276.2	258.6	NA										
				T	688.87	0.26041						277.6	277.2	261.6	NA										
2-5*AI/3M - NewTest	New anneal	29-Mar-95	6-Apr-95	T	707.79	0.26843	66.86	NA	NA	254.9	NA														
				T	572.75	0.21831						276.1	274.8	259.1	NA										
				T	714.29	0.27604						NA	NA	258.6	NA										
				C	-445.39	-0.15687						280.5	274.6	258.6	NA										
2-5*AI/3M - Last Test	Last old config	25-Apr-95	25-Apr-95	C	-445.39	-0.15687	66.86	NA	NA	NA	262.9														
				T	Lost test3 (Superscope crash)																				
				T																					
				T																					
2-5*AI/3M-New Config	Config	4-Aug-95	4-Aug-95	T	Lost test3 (Superscope crash)		66.86	NA	NA	NA	262.9														
				T	Noise pbs with new config.																				
				T																					
				TC																					
2-5*AI/3M-New Config	Config	17-Aug-95	17-Aug-95	T	Noise pbs with new config.		66.86	NA	NA	NA	262.9														
				T	Noise pbs fixed																				
				C																					
				T																					
2-5*AI/3M - NewAnneal	New anneal	20-Feb-96	23-Feb-96	T	Noise pbs fixed		66.86	NA	NA	NA	262.9														
				C																					
				T																					
				T																					
New Anneal Tests#5-8 (#37-40 total)	Tests#5-8 (#37-40 total)	29-Feb-96	29-Feb-96	T	Pb with Instron Load reading for first 2 T (Tests 11&12/New config TO BE DISCARDED); remaining 3 tests OK		66.86	NA	NA	NA	262.9														
				C																					
				T																					
				T																					
2-5*AI/3M - NewAnneal	New anneal	20-Feb-96	23-Feb-96	C (test14)	-452.11	-0.16842	66.86	NA	280.7	NA	263.0														
				T (test15)	489.78	0.18278						NA	276.7	259.1	NA										
				T	653.13	0.25145						272.5	276.5	257.3	NA										
				C	-655.49	-0.24039						NA	NA	NA	264.7										
New Anneal Tests#5-8 (#37-40 total)	Tests#5-8 (#37-40 total)	29-Feb-96	29-Feb-96	T	657.77	0.25207	66.86	NA	NA	256.0	NA														
				T	752.11	0.28938						NA	NA	256.0	NA										
				T	871.13	0.33663						275.1	275.1	253.3	NA										
				C	-556.16	-0.20050						NA	283.1	NA	263.8										
2-9*AI/3M	2-Dec-94	11-Dec-95	17-Jan-96	T	901.12	0.34878	66.86	NA	275.1	253.1	NA														
				C	857.13	0.33206						277.6	274.9	253.6	NA										
				T																					
				T																					
2-9*AI/3M	2-Dec-94	11-Dec-95	17-Jan-96	Avg:			66.86	NA	276.7	256.8	263.5	71.7	11.6	6.7	15.3	26.7									
				Avg El. Slope:	66.57	276.7											256.8	263.5	71.7	11.6	6.7	15.3	26.7		
				T	1048.74	0.39791											67.22	277.9	NA	254.0	263.6				
				C	-386.74	-0.13619												NA	283.4	NA	266.4				
2-9*AI/3M	2-Dec-94	11-Dec-95	22-Jan-96	T	1039.84	0.39577	66.86	NA	278.0	277.0	259.1	NA													
				T	1208.87	0.46253							279.9	276.8	255.6	NA									
				T	1358.97	0.52254							280.1	NA	254.5	NA									
				T(F)																					
					Avg:	67.22	Avg El. Slope:	279.0	255.8	265.0	72.5	11.8	-3.8	15.8	24.2										

Al-4.5wt%Cu Matrix Dupont FP Fibers				Matrix Em (GPa)	Dupont FP Ef (GPa)	ΔE_f (GPa)	ΔV_f for AlCu/FP (%)	$\Delta \theta_c / \theta_c$ AlCu/FP (%)	Hill el. bounds θ_{el} (GPa)	Error on el. bnds $\Delta \theta_{el}$ (GPa)	Hill pl. bounds θ_h (GPa)	Error on pl. bnds $\Delta \theta_h$ (GPa)							
Sample ID	Date Cast	Date Annealed	Date Tested	(C)omp. or (T)ens.	Max Stress (MPa)	Max Strain (%)	Vf(pyc) (%)	Composite Slope in Stage I (GPa)	Composite Slope in Elast. Unld. (GPa)	Composite Slope in Stage II - Tension (GPa)	Composite Slope in Stage II - Compr. (GPa)	Matrix Elastic Slope fm Vf(Pyc) (GPa)	Total Error on θ_m el. (GPa)	Mat. St.II Slope fm Vf(Pyc) - Tension (GPa)	Total Error on θ_m ,pl. (T) (GPa)	Mat. St.II Slope fm Vf(Pyc) - Compr. (GPa)	Total Error on θ_m ,pl. (C) (GPa)		
1•AlCu/NoFiber	Not cast	21-24 Jan-96	7-Feb-96	T	137.260	0.19448	NA	72.7	72.5	NA	NA								
				TC	175.900	0.40623	NA	72.4	72.3	(8.0)	NA								
					-182.140	-0.24224	NA	74.2	NA	NA	NA								
				TC	202.655	0.92058	NA	72.5	71.5	3.2	NA								
				T	-191.194	-0.01705	NA	74.5	NA	NA	3.5								
					240.759	3.50		72.5	NA	NA	NA								
							Avg:	72.5	73.0	3.2	3.5								
2-1•AlCu/FP	23-Feb-90	4-8 May-90	7-Aug-90	C			NA												
2-2•AlCu/FP	23-Feb-90	4-8 May-90	7-Aug-90	T			NA												
2-3•AlCu/FP	23-Feb-90	4-8 May-90	7-Aug-90	T			NA												
2-4•AlCu/FP	23-Feb-90	4-8 May-90	6-Aug-90	T-T(F)			NA												
2-5•AlCu/FP	23-Feb-90	4-8 May-90	6-Aug-90	T-T-T(F)			NA												
2-6•AlCu/FP	23-Feb-90	4-8 May-90	7-Aug-90	C			NA												
3-1•AlCu/FP	8-Nov-90	4-7 May-94	19-May-94	T(F)	391.81	0.258	39.67	NA	NA	NA	NA								
3-2•AlCu/FP	8-Nov-90	4-7 May-94	19-May-94	C	-207.15	-0.10461	40.67	198.4	199.2	NA	NA								
				T	324.36	0.19072		NA	197.5	162.1	NA								
							Avg:	40.67	Avg El. Slope	198.4	162.1	NA	73.7	6.4	8.4	9.2	NA	NA	
3-3•AlCu/FP	8-Nov-90	4-7 May-94	19-May-94	T	353.29	0.21247	41.22	194.3	197.2	161.1	NA	68.9	6.5	3.2	9.3	NA	NA		
3-4•AlCu/FP	8-Nov-90	21-24 Jan-96	7-Feb-96	C	-452.970	-0.22641	42.33	203.3	205.3	NA	(192.7)	(\leftarrow Limited compression range)							
				T	328.550	0.18886		NA	202.1	166.7	NA								
				C	-245.047	-0.09557		NA	203.7	NA	(197.2)								
				T	472.931	0.27608		NA	201.6	163.7	NA								
				T(F)	509.071	0.29756		202.1	NA	160.3	NA								
							Avg:	42.33	Avg El. Slope	203.0	163.6	NA	73.0	6.7	0.2	9.6	NA	NA	
3-5•AlCu/FP	8-Nov-90	21-24 Jan-96	23-Feb-96	C	-564.633	-0.28514	41.72	202.8	204.9	NA	(187.0)								
				T	398.814	0.23210		NA	201.0	165.7	NA								
							Avg:	41.72	Avg El. Slope	202.9	165.7	NA	76.0	6.5	7.8	9.4	NA	NA	
3-6•AlCu/FP	8-Nov-90	21-24 Jan-96	29-Feb-96	T	363.118	0.20186	44.46	207.9	208.3	172.9	NA								
				C	-459.173	-0.20303		NA	211.5	NA	(188.3)								
				T(2)	400.330	0.22082		NA	208.5	174.0	NA								
				C	-494.752	-0.21758		NA	210.9	NA	(186.9)								
				T(3)	421.747	0.23096		NA	208.3	169.8	NA								
				C	-507.516	-0.22177		NA	211.2	NA	(184.3)								
				T(4)	465.148	0.25497		NA	208.1	172.8	NA								
				C	-521.761	-0.22754		NA	212.7	NA	(181.6)								
				T(5)	497.371	0.27266		NA	207.9	172.4	NA								
				C	-488.616	-0.20723		NA	211.0	NA	(184.1)								
				T(F)	494.621	0.27053		NA	NA	(180.0)	NA								
							Avg:	44.46	Avg El. Slope	209.7	172.4	182.0	73.2	7.0	1.6	10.1	18.9	9.9	
3-7•AlCu/FP	8-Nov-90	21-24 Jan-96	19-Mar-96	T	273.972	0.15053	46.18	204.9	209.0	172.5	NA								
				C	-580.106	-0.27316		NA	211.9	NA	(185.5)								
				T(2)	278.944	0.15002		NA	209.5	173.8	NA								
				C	-544.560	-0.24977		NA	212.3	NA	(184.9)								

Al-4.5wt%Cu (continued)														
			T(3)	281.397	0.15021	NA	209.0	(178.0)	NA					
			C	-519.636	-0.23487	NA	212.2	NA	(190.3)					
			T(4)	368.759	0.20029	NA	208.7	171.7	NA					
			C	-480.521	-0.21000	NA	212.5	NA	(188.4)					
			T(5)	369.237	0.20008	NA	208.7	(178.4)	NA					
			C	-463.890	-0.20055	NA	212.1	NA	(187.3)					
			T(6)	369.440	0.19984	NA	209.6	(185.0)	NA					
			C	-502.423	-0.22028	NA	212.5	NA	(186.2)					
			T(7)	424.382	0.23148	NA	209.5	161.5	NA					
			C	-487.530	-0.21073	NA	211.8	NA	(183.5)					
			T(8)	447.269	0.24447	NA	209.8	153.7	NA					
			C	-488.879	-0.21024	NA	212.6	NA	(182.8)					
			T(9)	459.430	0.25047	NA	209.8	175.7	NA					
			C	-489.779	-0.20966	NA	213.2	NA	(183.1)					
			Avg:	46.18	Avg El. Slope:	210.8	168.2	183.0	65.6	7.5	-18.3	10.8	9.3	10.4
			Gen. Avg:	42.8	Avg El. Slope:	203.7	165.5	182.0	71.8	6.8	0.7	9.7	14.1	9.4

Al-0.9wt%Mg Matrix Dupont FP Fibers				Matrix Em (GPa)	Dupont FP Ef (GPa)	ΔE_f (GPa)	ΔV_f for AIMg/FP (%)	$\Delta \theta_c / \theta_c$ AIMg/FP (%)	Hill el. bounds θ_{el} (GPa)	Error on el. bnds $\Delta \theta_{el}$ (GPa)	Hill pl. bounds θ_h (GPa)	Error on pl. bnds $\Delta \theta_h$ (GPa)							
Sample ID	Date Cast	Date Annealed	Date Tested	(C)omp. or (T)ens.	Max Stress (MPa)	Max Strain (%)	V_f (pyc) (%)	Composite Slope in Stage I (GPa)	Composite Slope in Elast. Unid. (GPa)	Composite Slope in Stage II - Tension (GPa)	Composite Slope in Stage II - Compr. (GPa)	Matrix Elastic Slope fm V_f (Pyc) (GPa)	Total Error on θ_m el. (GPa)	Mat. St.II Slope fm V_f (Pyc) - Tension (GPa)	Total Error on θ_m ,pl. (T) (GPa)	Mat. St.II Slope fm V_f (Pyc) - Compr. (GPa)	Total Error on θ_m ,pl. (C) (GPa)		
1•AIMg/NoFibe	2-Jul-92	10-May-93	13-May-93 5-Aug-93	T T T	44.26	0.72507	NA	64.0	60.7	1.3	NA								
8•AIMg/NoFibe	2-Jul-92	20-Jul-93	22-Jul-93	T	29.21	0.22759	NA	60.5	61.7	(2.8)	NA								
				T	31.10	0.32874		61.4	61.7	1.9	NA								
				T	34.78	0.52304		61.1	61.3	1.7	NA								
				Avg:			61.0	61.6	1.8	NA									
Gen. Avg:				62.5	61.1	1.6	NA												
2•AIMg/FP	2-Jul-92	10-May-93	13-May-93	T(F)	495.98	0.32131	41.66	184.2	NA	143.8	NA	NA	NA	-29.3	13.6	NA	NA		
3•AIMg/FP	2-Jul-92	20-Jul-93	22-Jul-93	T	428.28	0.28703	39.90	178.9	182.5	144.2	156	51.2	9.5	-16.7	12.9	2.4	12.5		
4•AIMg/FP	2-Jul-92	20-Jul-93	22-Jul-93	T	439.42	0.30258	38.24	170.1	177.3	140.3	153	51.6	9.1	-12.3	12.3	7.9	11.9		
10•AIMg/FP	2-Jul-92	10-May-93	13-May-93 19-Jul-93	T	389.34	0.31317	33.84	152.3	157.0	120.0	(126.9)	(=< Limited compression range)							
				T	421.27	0.346903		160.4	159.5	118.8	(126.5)								
				T	425.60	0.350048		159.6	158.7	123.6	(126.7)								
				Avg:			33.84	Avg El. Slope	159.0	120.8	127		45.8	8.4	-15.8	11.4	-6.4	11.2	
Gen. Avg:				37.3	Avg El. Slope	172.9	135.1	145	49.5	9.0	-15.0	12.2	1.3	11.9					

Pure Cu Matrix Dupont FP Fibers				Matrix Em (GPa)	Dupont FP Ef (GPa)	ΔEf (GPa)	ΔVf for Cu/FP (%)	Δθc/θc Cu/FP (%)	Hill el. bounds θel(GPa)	Error on el. bnds Δθel(GPa)	Hill pl. bounds θh (GPa)	Error on pl. bnds Δθh(GPa)					
Sample ID	Date Cast	Date Annealed	Date Tested	(C)omp. or (T)ens.	Max Stress (MPa)	Max Strain (%)	Vf(pyc) (%)	Composite Slope in Stage I (GPa)	Composite Slope in Elast. Unid. (GPa)	Composite Slope in Stage II - Tension (GPa)	Composite Slope in Stage II - Compr. (GPa)	Matrix Elastic Slope fm Vf(Pyc) (GPa)	Total Error on θm el. (GPa)	Mat. St.II Slope fm Vf(Pyc) - Tension (GPa)	Total Error on θm,pl. (T) (GPa)	Mat. St.II Slope fm Vf(Pyc) - Compr. (GPa)	Total Error on θm,pl. (C) (GPa)
3-5•Cu/NoFibers	10-Jan-93	16-Nov-93	15-Dec-93	T	36.59	0.70794	NA	89.8	89.5	1.0	NA	NA					
3-5•Cu/NoF-NewTest(308°C)	18-Aug-94	30-Aug-94		T													
1•Cu/NoFibers	13-Nov-92	9-Feb-96	28-Mar-96	T	33.01	0.155721	NA	104.0	104.8	(3.9)	NA						
				C	-31.82	-0.01493		NA	NA	NA	(4.0)						
				T(2)													
				C													
				T(3)													
				C													
				T(4)													
				C													
				T(5)													
				C													
				T(7)	48.60	0.70404		NA	101.5	1.7	NA						
				C	-35.76	0.51860		NA	101.8	NA	NA						
				T(8)													
				C													
				T(9)	52.92	0.92237		NA	100.7	1.4	NA						
				C	-37.59	0.73240		NA	102.0	NA	NA						
				T(10)	53.03	0.92448		NA	100.8	NA	NA						
				C	-40.88	0.70381		NA	102.9	NA	(2.4)						
				T(11)													
				C													
				Avg:				104.0	102.1	1.6	NA						
0-1•Cu/FP	25-Sep-91	24-Mar-92	31-Mar-92	T	427.22	0.19217	59.25	253.5	250.8	216.5	NA						
							59.25	Avg El. Slope:	252.1	216.5	NA	66.2	12.2	-29.5	15.7	NA	NA
0-2•Cu/FP	25-Sep-91	24-Mar-92	30-Mar-92	C	-335.51	-0.1359											
0-3•Cu/FP	25-Sep-91	24-Mar-92	31-Mar-92	T(F)	487	0.2256											
0-4•Cu/FP	25-Sep-91	Not Annealed	14-Nov-91	T	44.92	0.0188											
				T	212.82	0.09312											
				T	334.87	0.14796											
0-4•Cu/FP-New Test		Not Annealed	30-Mar-92	C	-398.2	-0.162											
				C(F)	-442.0	-0.181											
1-1•Cu/FP	7-Jan-93	16-Nov-93	15-Dec-93	T	402.91	0.17718	60.29	262.6	266.2	218.8	NA						
				T	410.30	0.18159		263.3	265.6	(230.7)	NA						
				T	437.51	0.19338		263.3	259.7	(222.1)	NA						
				T	464.80	0.202					NA						
				T	563.72	0.250					NA						
				T	591.32	0.263					NA						
				T	586.86	0.261					NA						
				T	602.66	0.268					NA						
				T(F)	649.69	0.291					NA						
				Avg:			60.29	Avg El. Slope:	263.5	218.8	NA	86.5	12.6	-34.5	16.3	NA	NA
1-2•Cu/FP	7-Jan-93	16-Nov-93	28-Mar-94	T(F)	480	0.2		NA	NA	NA	NA						
1-4•Cu/FP	7-Jan-93	16-Nov-93	26-Sep-94	C	-327.02	-0.11898	63.34	285.3	289.0	NA	(259.7)						
				T	453.70	0.182910		NA	283.8	237.3	NA						
				Avg:			63.34	Avg El. Slope:	286.0	237.3	259.7	123.8	13.8	-18.5	18.0	42.7	17.6
3-1•Cu/FP	10-Jan-93	16-Nov-93	28-Mar-94	T	457.5	0.2141		NA	NA	NA	NA						

3-2•Cu/FP	10-Jan-93	16-Nov-93	28-Sep-94	T(F)	418.57	0.20593	61.70	245.9	NA	210.6	NA							
3-3•Cu/FP	10-Jan-93	16-Nov-93	29-Sep-94	T(F)	353.74	0.17115	58.64	226.7	NA	199.7	NA							
3-4•Cu/FP	10-Jan-93	16-Nov-93	29-Sep-94	T	260.87	0.10988	62.05	270.1	262.4	230.9	NA							
				C	-259.32	-0.09624			NA	269.4	NA	(238.5)						
Cu/FP (continued)				T(2)	297.74	0.1262		NA	263.6	231.0	NA							
				C	-294.63	-0.11125		NA	266.7	NA	(236.2)							
				T(3)	335.34	0.14289		NA	264.1	230.3	NA							
				C	-332.53	-0.12698		NA	265.1	NA	(233.9)							
				T(4)	362.21	0.15525		NA	263.5	229.4	NA							
				C	-359.70	-0.1387		NA	266.4	NA	(233.7)							
				T(5)	410.70	0.17618		NA	263.4	226.8	NA							
				C	-398.26	-0.15478		NA	266.9	NA	231.0							
				T(6)	449.64	0.19369		NA	263.7	228.4	NA							
				C	-421.95	-0.16472		NA	267.3	NA	231.9							
				T(7)	489.61	0.21214		NA	262.1	225.3	NA							
				C	-426.69	-0.16691		NA	267.3	NA	231.5							
				T(F)	472.59	0.20440		NA	NA	227.0	NA							
				Avg:			62.05	Avg El. Slope:	265.5	228.6	231.5	78.3	13.4	-27.8	17.3	-20.3	17.2	
4-1•Cu/FP	5-Aug-94	28-Oct-94	1-Nov-94	T	398.46	0.19983	55.63	(220.5)	248.9	188.2	NA							
				T	474.89	0.24105		251.4	250.1	188.7	NA							
				C	NA	NA		NA	NA	NA	NA							
				C	-461.12	-0.20075		251.7	257.4	NA	(201.4)							
				T(F)	474.09	0.24001		NA	NA	189.4	NA							
				Avg:			55.63	Avg El. Slope:	251.9	188.8	201.4	91.2	10.7	-58.7	14.1	-30.3	14.0	
4-2•Cu/FP	5-Aug-94	28-Oct-94	7-Dec-94	C	-387.59	-0.15396	60.29	266.8	270.5	NA	(246.8)							
				C	-423.71	-0.16758		267.1	266.7	NA	(246.2)							
				T	391.30	0.16798		NA	262.6	220.7	NA							
				T	436.27	0.1890		267.9	261.0	222.7	NA							
				Avg:			60.29	Avg El. Slope:	266.1	221.7	246.5	93.1	12.5	-27.2	16.2	35.3	15.9	
4-3•Cu/FP	5-Aug-94	28-Oct-94	17-Nov-94	C	-391.70	-0.15821	59.38	252.9	255.2	NA	(236.9)							
				C	-434.45	-0.17694		255.2	253.8	NA	(240.5)							
				T	462.17	0.20408		NA	250.0	216.4	NA							
				T(F)	NA	NA		NA	NA	NA	NA							
				Avg:			59.38	Avg El. Slope:	253.4	216.4	238.7	68.4	12.3	-31.1	15.8	23.8	15.5	
4-4•Cu/FP	5-Aug-94	28-Oct-94	22-Dec-94	T	391.81	0.18579	58.10	248.1	250.5	205.9	NA							
				T(F)	425.41	0.20297		251.8	NA	218.7	NA							
				Avg:			58.10	Avg El. Slope:	251.2	212.3	NA	72.5	11.7	-28.4	15.1	NA	NA	
4-5•Cu/FP	5-Aug-94	28-Oct-94	28-Mar-96	T	332.41	0.15028	58.19	264.9	259.5	208.4	NA							
				C	-416.96	-0.17057		NA	262.0	NA	216.7							
				T(2)	333.99	0.15076		NA	258.7	210.2	NA							
				C	-420.84	-0.17148		NA	261.6	NA	217.6							
				T(3)	335.01	0.15141		NA	258.5	210.7	NA							
				C	-421.09	-0.17099		NA	261.9	NA	217.7							
				T(4)	436.29	0.20087		NA	257.5	201.3	NA							
				C	-487.63	-0.20057		NA	262.5	NA	217.7							
				T(5)	435.22	0.20082		NA	257.0	205.9	NA							
				C	-489.41	-0.20110		NA	262.4	NA	217.5							
				T(6)	432.96	0.20034		NA	256.6	203.6	NA							
				C	-489.21	-0.20067		NA	262.6	NA	217.7							
				T(F)	451.84	0.21353		NA	NA	(152.9)	NA							
				Avg:			58.19	Avg El. Slope:	260.4	206.7	217.5	94.0	11.7	-42.7	15.2	-16.9	15.1	
				Gen. Avg:			59.6	Avg El. Slope:	261.4	211.4	224.5	86.0	12.3	-33.2	16.0	-18.6	16.2	

Cu-7wt%Al Matrix Dupont FP Fibers				Matrix Em (GPa)	Dupont FP Er (GPa)	ΔE_f (GPa)	ΔV_f for CuAl/FP (%)	$\Delta \theta_c / \theta_c$ CuAl/FP (%)	Hill el. bounds θ_{el} (GPa)	Error on el. bnds $\Delta \theta_{el}$ (GPa)	Hill pl. bounds θ_h (GPa)	Error on pl. bnds $\Delta \theta_h$ (GPa)						
Sample ID	Date Cast	Date Annealed	Date Tested	(C)omp. or (T)ens.	Max Stress (MPa)	Max Strain (%)	V_f (pyc) (%)	Composit e Slope in Stage I (GPa)	Composit e Slope in Elast. Unid. (GPa)	Composit e Slope in Stage II - Tension (GPa)	Composit e Slope in Stage II - Compr. (GPa)	Matrix Elastic Slope fm V_f (Pyc) (GPa)	Total Error on θ_m el. (GPa)	Mat. St.II Slope fm V_f (Pyc) - Tension (GPa)	Total Error on θ_m ,pl. (T) (GPa)	Mat. St.II Slope fm V_f (Pyc) - Compr. (GPa)	Total Error on θ_m ,pl. (C) (GPa)	
					127	379	3.0											
1-1•Cu7Al/FF	8-Jul-94	23-Dec-94	27-Jan-96	T C T(F)	479.691 -166.940 497.71	0.250888 -0.049892 0.259701	50.21	221.2 NA NA	224.4 227.7 NA	181.3 NA 190.6	NA 201.8 NA							
					Avg:		50.21	Avg El. Slope:	226.0	185.9	201.8	70.5	7.7	-16.8	10.6	15.0	10.4	
1-2•Cu7Al/FF	8-Jul-94	23-Dec-94	29-Feb-96	C T C T	-461.375 495.074 -440.37 481.26	-0.19745 0.255445 -0.17312 0.246757	50.08	246.9 NA NA NA	249.0 245.9 248.0 244.0	NA 184.2 NA 183.6	(215.6) NA 194.2 NA							
					Avg:		50.08	Avg El. Slope:	246.7	183.9	194.2	112.9	7.4	-19.9	10.6	0.8	10.5	
1-3•Cu7Al/FF	8-Jul-94	23-Dec-94	19-Mar-96	T C T C T C T(F)	404.031 -521.457 407.72 -527.88 408.63 -530.56 469.25	0.200162 -0.20022 0.200125 -0.20013 0.20001 -0.20014 0.230441	52.08	245.7 NA NA NA NA NA NA	252.4 259.5 255.0 259.5 256.3 260.3 NA	195.8 NA 197.3 NA 198.5 NA 195.6	NA 214.1 NA 212.7 NA 213.0 NA							
					Avg:		52.08	Avg El. Slope:	257.2	196.8	213.3	123.5	7.8	-9.6	11.2	24.8	10.9	
1-4•Cu7Al/FF	8-Jul-94	9-Feb-96	10-Apr-96	C T C T(F)	-413.254 433.246 -443.04 529.22	-0.17131 0.218231 -0.17052 0.266676	52.15	245.8 NA NA NA	247.9 242.6 248.4 NA	NA 195.1 NA 191.9	(229.0) NA 209.7 NA							
					Avg:		52.15	Avg El. Slope:	246.3	193.5	209.7	100.4	8.0	-17.0	11.2	16.8	11.0	
					Gen. Avg:		51.1	Avg El. Slope:	244.1	190.0	204.7	101.6	7.7	-15.9	10.9	14.2	10.7	

Cu-7wt%Al Matrix 3M Nextel 610 Fibers				Matrix Em (GPa)	Nextel 610 Ef (GPa)	ΔE_f (GPa)	ΔV_f for CuAl/3M (%)	$\Delta \theta_c / \theta_c$ CuAl/3M (%)	Hill el. bounds θ_{el} (GPa)	Error on el. bnds $\Delta \theta_{el}$ (GPa)	Hill pl. bounds θ_h (GPa)	Error on pl. bnds $\Delta \theta_h$ (GPa)									
Sample ID	Date Cast	Date Annealed	Date Tested	(C)omp. or (T)ens.	Max Stress (MPa)	Max Strain (%)	V_f (pyc) (%)	Composite Slope in Stage I (GPa)	Composite Slope in Elast. Unid. (GPa)	Composite Slope in Stage II - Tension (GPa)	Composite Slope in Stage II - Compr. (GPa)	Matrix Elastic Slope fm V_f (Pyc) (GPa)	Total Error on θ_m el. (GPa)	Mat. St.II Slope fm V_f (Pyc) - Tension (GPa)	Total Error on θ_m ,pl. (T) (GPa)	Mat. St.II Slope fm V_f (Pyc) - Compr. (GPa)	Total Error on θ_m ,pl. (C) (GPa)				
Cu7Al/NoFibers	16-Sep-94	23-Dec-94	27-Jan-96	TC	84.53	0.41695	NA	126.2	128.6	2.8	NA										
				TC(2)	-70.06	0.06250		NA	130.2	NA	NA	NA									
					91.61	0.71872		127.5	126.6	1.9	NA										
					-66.51	0.3208		NA	126.0	NA	NA	NA									
				TC(3)	94.63	0.84599		126.0	127.0	1.6	NA										
					-68.00	0.4313		NA	126.3	NA	(4.4)										
							Avg:	126.6	127.5	2.1	NA										
1-1•Cu7Al/3M	16-Sep-94	9-Feb-96	10-Apr-96	C	-575.66	-0.21147	69.58	295.4	NA	NA	(286.5)										
				T	497.79	0.20036		NA	NA	NA	NA										
				C	-556.72	-0.20170		NA	NA	NA	NA										
				T	497.77	0.20195		NA	NA	NA	NA	NA	NA								
				C	-558.06	-0.20233		NA	NA	NA	NA	NA	NA								
				T	613.05	0.25127		NA	NA	NA	NA	NA	NA								
				C(F)	-716.00	-0.26646		NA	NA	NA	NA	NA	NA								
							69.58	Avg El. Slope:	295.4	NA	NA	102.3	13.1	NA	NA	NA	NA				
1-2•Cu7Al/3M	16-Sep-94	9-Feb-96	17-Apr-96	C	-428.71	-0.15063	68.60	285.0	287.8	NA	(278.6)										
				T	387.33	0.150534		NA	285.2	251.3	NA										
				C	-498.78	-0.17110		NA	287.2	NA	(266.0)										
				T	675.71	0.26741		NA	(280.6)	240.6	NA										
				T	586.16	0.23306		284.0	(279.3)	(269.6)	NA										
				T	555.44	0.21957		282.5	(280.8)	(271.4)	NA										
				T	691.90	0.27461		283.9	(280.0)	239.4	NA										
				C	-455.40	-0.15055		NA	284.5	NA	257.5										
T(F)	704.98	0.28911		NA	NA	248.6	NA														
							Avg:	68.60	Avg El. Slope:	285.0	245.0	257.5	77.7	12.9	-57.8	17.6	-17.9	17.1			
1-3•Cu7Al/3M	16-Sep-94	9-Feb-96	2-Mar-96	T	551.06	0.209052	70.09	285.7	289.3	259.4	NA										
				C	-350.47	-0.10962		NA	295.2	NA	275.5										
				T	776.86	0.29846		NA	289.3	246.0	NA										
				T(F)	790.65	0.31553		290.0	NA	265.0	NA										
											Avg:	70.09	Avg El. Slope:	291.0	256.8	275.5	82.6	13.6	-40.0	18.4	22.6
							Gen. Avg:	69.4	Avg El. Slope:	290.5	250.9	266.5	87.5	13.3	-48.9	18.0	2.4	17.3			

Cu-1wt%Ti Matrix Dupont FP Fibers				Matrix Em (GPa)	Dupont FP Ef (GPa)	ΔEf (GPa)	ΔVf for CuTi/FP (%)	Δθc/θc CuTi/FP (%)	Hill el. bounds θel(GPa)	Error on el. bnds Δθel(GPa)	Hill pl. bounds θh (GPa)	Error on pl. bnds Δθh(GPa)									
Sample ID	Date Cast	Date Annealed	Date Tested	(C)omp. or (T)ens.	Max Stress (MPa)	Max Strain (%)	Vf(%)	Composite Slope in Stage I (GPa)	Composite Slope in Elast. Unid. (GPa)	Composite Slope in Stage II - Tension (GPa)	Composite Slope in Stage II - Compr. (GPa)	Matrix Elastic Slope fm Vf(Pyc) (GPa)	Total Error on θm el. (GPa)	Mat. St.II Slope fm Vf(Pyc) - Tension (GPa)	Total Error on θm.pl. (T) (GPa)	Mat. St.II Slope fm Vf(Pyc) - Compr. (GPa)	Total Error on θm.pl. (C) (GPa)				
1-CuTi/NoFibers	24-Feb-95	11-Feb-96	17-Apr-96 (TC)x10-T	T	47.48	0.15041	NA	100.5	100.2	(4.0)											
				C	-44.95	-0.0365		NA	101.2	NA											
				T(11)	62.99	0.8532		NA	97.7	1.1	NA										
				C	-46.02	.5484		NA	98.4	NA	NA										
				Avg:							100.5	99.4	1.1	NA							
2-CuTi/NoFibers	3-Mar-95	2-Jan-96	17-Jan-96	T	57.01	0.4348	NA	122.5	NA	1.9	NA										
				C	-52.24	-0.0584		NA	122.4	NA	NA										
				T	61.93	0.555			117.7	1.5	NA										
				C	-52.25	0.0557			122.9		NA										
				T	66.90	0.810			119.1	1.2	NA										
2-CuTi/NoFibers	New anneal	11-Feb-96	23-Feb-96	C	-51.40	0.469			122.8												
				T	52.50	0.432		115.9	120.6	1.6	NA										
				C	-48.84	0.068		NA	120.3	NA	(2.8)										
				T	71.01	1.996		NA	129.7	1.0	NA										
				Avg:							119.2	121.9	1.4	NA							
1-1+CuTi/FP	24-Feb-95	2-Jan-96	22-Jan-96	T	238.30	0.10313	53.60	248.8	250.0	(222.1)	NA										
				T	348.53	0.15496		249.2	248.4	213.7	NA										
				C	-167.18	-0.05951		NA	250.6	NA	(229.5)										
				T	407.69	0.18350		NA	247.3	(216.4)	NA										
				T	512.41	0.23403		248.5	246.2	212.4	NA										
				T	601.80	0.27716		247.5	244.3	212.5	NA										
				T(F)	658.80	0.30572		247.6	NA	(215.7)	NA										
				Avg:							53.60	Avg El Slope: 248.0	212.9	(229.5)	95.5	6.8	12.3	9.7	NA	NA	
				1-2+CuTi/FP	24-Feb-95	10-Feb-96	28-Mar-96	C	-367.91	-0.15014	53.86	257.9	261.3	NA	(228.5)						
								T	330.30	0.15044		NA	260.7	208.8	NA						
C	-383.03	-0.15108						NA	261.8	NA	218.8										
T	332.56	0.15122						NA	259.0	(212.8)	NA										
C	-384.67	-0.15055						NA	262.1	NA	219.4										
T	332.75	0.15099						NA	258.4	(214.8)	NA										
C	-463.47	-0.18606						NA	262.7	NA	218.4										
T	435.56	0.19984						NA	256.8	208.7	NA										
C	-465.24	-0.18564						NA	262.0	NA	217.2										
T	436.07	0.19994						NA	257.0	210.3	NA										
1-3+CuTi/FP	24-Feb-95	10-Feb-96	10-Apr-96	T	412.19	0.19682	52.20	244.7	245.2	201.2	NA										
				C	-423.66	-0.17697		NA	248.9	NA	209.5										
				T	522.59	0.24991		NA	245.8	199.6	NA										
				C	-372.93	-0.15005		NA	249.0	NA	209.0										
				T	525.27	0.25069		NA	245.3	201.1	NA										
				T	541.91	0.25916		246.3	244.4	(206.9)	NA										
				T	623.78	0.30014		246.0	244.0	199.9	NA										
				Avg:							52.20	Avg El Slope: 246.0	200.5	209.2	99.4	6.4	-2.9	9.3	15.5	9.3	
				1-4+CuTi/FP	24-Feb-95	10-Feb-96	17-Apr-96	C	-300.02	-0.12225	52.30	259.6	261.7	NA	232.0						
								T	524.03	0.25126		NA	257.3	198.6	NA						
C	-423.19	-0.17036						NA	261.9	NA	207.9										
T(F)	704.62	0.34191						NA	253.6	199.9	NA										
C	-390.56	-0.15019						NA	261.2	NA	206.5										
T	635.57	0.30683						NA	254.4	198.5	NA										
T	633.32	0.30665						258.8	254.9	(206.7)	NA										
Avg:							52.30	Avg El Slope: 258.2	199.0	215.5	124.4	6.4	-6.7	9.4	27.8	9.2					
Gen. Avg:							53.0	Avg El Slope: 253.0	205.1	214.3	109.6	6.6	0.5	9.5	21.7	9.5					

Cu-1wt%Ti Matrix 3M Nextel 610 Fibers				Matrix Em (GPa)	Nextel 610 Ef (GPa)	ΔE_f (GPa)	ΔV_f for CuTi/3M (%)	$\Delta \theta_c / \theta_c$ CuTi/3M (%)	Hill el. bounds θ_{el} (GPa)	Error on el. bnds $\Delta \theta_{el}$ (GPa)	Hill pl. bounds θ_h (GPa)	Error on pl. bnds $\Delta \theta_h$ (GPa)							
Sample ID	Date Cast	Date Annealed	Date Tested	(C)omp. or (T)ens.	Max Stress (MPa)	Max Strain (%)	V_f (pyc) (%)	$\Delta \theta_c / \theta_c$ (%)	Composit e Slope in Stage I (GPa)	Composit e Slope in Elast. Unid. (GPa)	Composit e Slope in Stage II - Tension (GPa)	Composit e Slope in Stage II - Compr. (GPa)	Matrix Elastic Slope fm V_f (Pyc) (GPa)	Total Error on θ_m el. (GPa)	Mat. St.II Slope fm V_f (Pyc) - Tension (GPa)	Total Error on θ_m ,pl. (T) (GPa)	Mat. St.II Slope fm V_f (Pyc) - Compr. (GPa)	Total Error on θ_m ,pl. (C) (GPa)	
1-1•CuTi/3M	3-Mar-95	2-Jan-96	22-Jan-96	C T(F)	-608.63 320.31	-0.20873 0.109819	72.55	0.07	297.3 NA	300.4 NA	NA 277.1	283.1 NA	90.5	9.5	NA -3.5	NA 13.5	18.4 NA	13.4 NA	
							72.55	0.07	Avg El. Slope:	298.9	277.1	283.1	84.9	9.6	-3.5	13.5	18.4	13.4	
1-2•CuTi/3M	3-Mar-95	10-Feb-96	2-Mar-96	T(F)	555.13	0.198515	73.81	0.38	295.2	NA	274.3	NA	56.8	13.8	-32.6	17.8	NA	NA	
							73.81	0.38	Avg El. Slope:	295.2	274.3	NA	56.8	13.8	-32.6	17.8	NA	NA	
							73.81	0.38	Avg El. Slope:	295.2	274.3	NA	56.8	13.8	-32.6	17.8	NA	NA	
							73.2	0.2	Avg El. Slope:	298.9	275.7	283.1	84.9	11.6	-18.0	15.6	18.4	15.4	
1-3•CuTi/3M	3-Mar-95	10-Feb-96	19-Mar-96	C T C T C T C T C T(F)	-732.64 286.611 -728.73 424.53 -870.38 556.63 -873.38 585.88 -872.12 669.27	-0.25393 0.101495 -0.25181 0.15174 -0.30115 0.20042 -0.30123 0.21108 -0.30058 0.24189	74.13	0.65	293.7 NA NA NA NA NA NA NA NA NA	295.4 296.5 295.8 292.4 297.1 291.3 298.1 290.9 298.1 NA	NA 274.8 NA 273.9 NA 273.4 NA 273.8 NA 270.4	283.8 NA 281.9 NA 283.3 NA 280.6 NA 280.9 NA							
							74.13	0.65	Avg El. Slope:	294.9	273.3	282.1	51.7	17.2	-41.7	20.9	-7.6	20.8	
1-4•CuTi/3M	3-Mar-95	10-Feb-96	17-Apr-96	T C T(F)	451.109 -445.139 648.38	0.170842 -0.15311 0.26279	(76.13)	1.00 (?)	(282.3) NA (283.4)	(284.2) (341.6) NA	(249.6) NA (209.6)	NA (265.9) NA							
							Gen. Avg:	73.5	0.3	Avg El. Slope:	296.3	274.9	282.6	64.8	12.7	-25.5	16.6	5.4	16.5

Appendix B: Description of Data Acquisition Program

“Instron Config” is a LabVIEW VI (virtual instrument) designed specifically for acquisition of mechanical data for this work. The front panel, as it appears on the computer screen, is shown in Figure B-1. The program’s block diagrams (*i.e.*, listings written in LabVIEW’s graphical programming language) are listed in the following pages.

The user specifies the cross-section of the sample to be tested and the gage factor of the strain gages. The gain (or input limits) of each channel to be digitized and the sampling rate can also be modified. After a calibrating procedure, a new data file with all relevant information is open before each test. When the test is started, load and strain data (in volts) is acquired continuously and plotted as a function of time at the bottom of the screen. The data is converted to engineering units and stress (MPa) is plotted in real time *vs.* strain1, strain2, and average strain(%) on the right-hand side. The acquired data is also written to file continuously during the test. The program uses the circular buffer technique, whereby data is continuously acquired into a circular acquisition buffer while the VI reads the acquired data and processes it at the same time. Intermediate DAQ (data acquisition) functions are used (AI Config, AI Start, AI Read, AI Clear) as well as the general error handler and custom subVI’s for calibration, data conversion, and writing to file. Data is saved in TEXT format. Each row is a scan and each column a channel; columns are separated by commas and rows by an end-of-line character.

The scan backlog indicates how much data remains in the buffer after each retrieval, and is an indication of how well the application is keeping up with the acquisition rate. If the backlog increases with time, the scanning rate is too high and the circular buffer will eventually be overwritten.

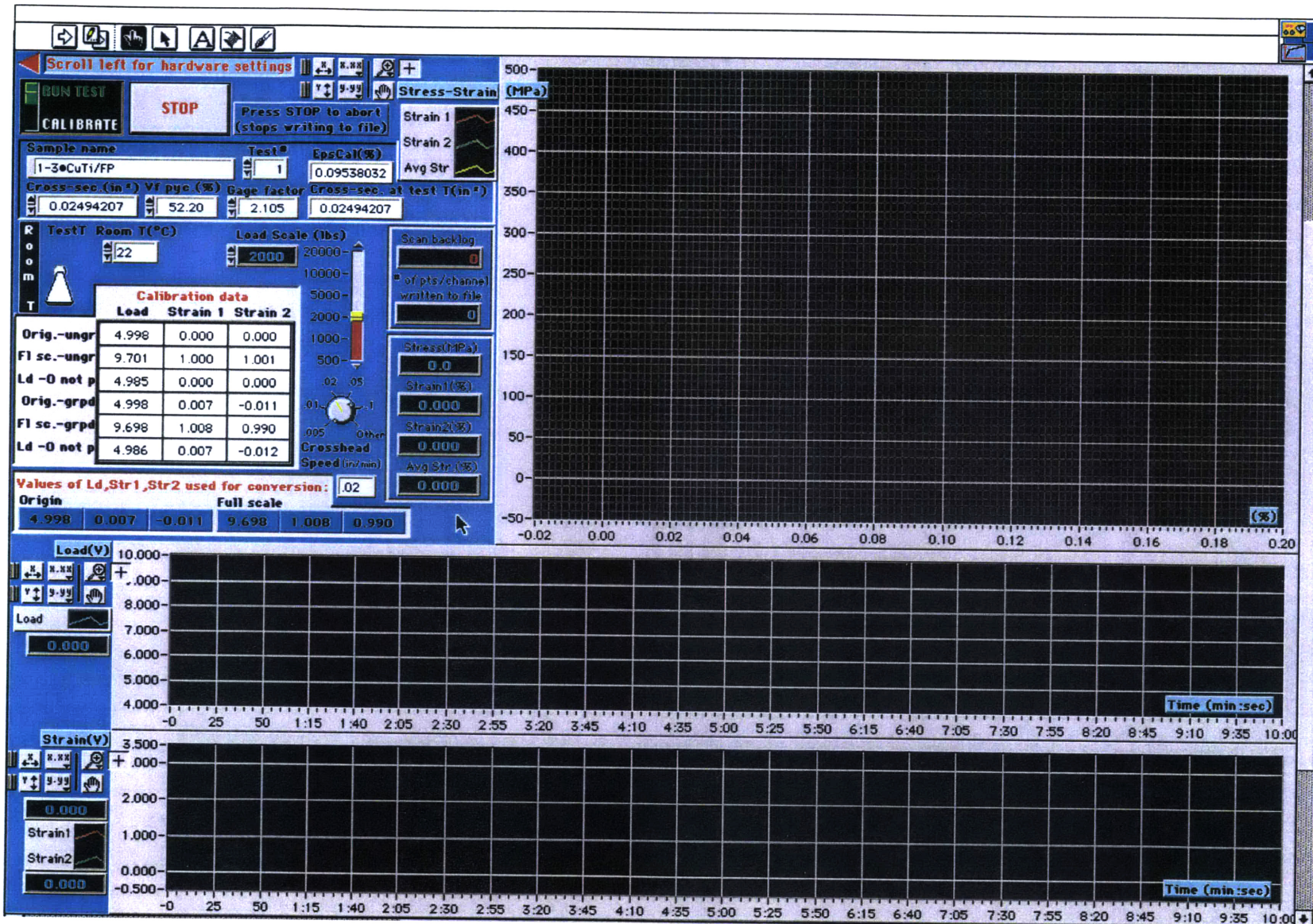


Figure B-1 - Front panel of data acquisition virtual instrument, used to acquire load and strain data in volts, plot stress (MPa) vs. strain (%), and save data in real time (Instron Configuration program, written using the LabVIEW software package).

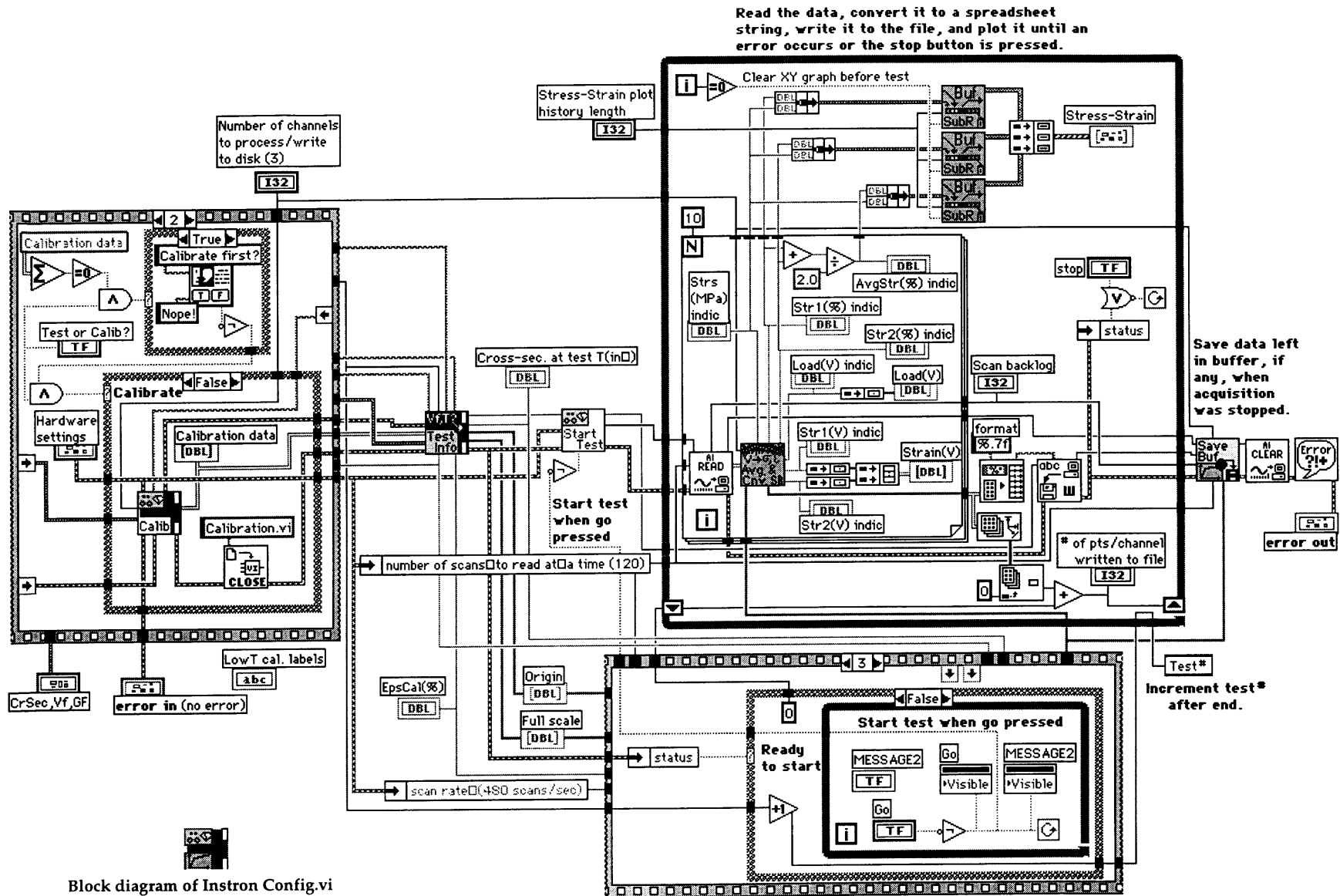


Figure B-2 - Block diagram of data acquisition virtual instrument (Instron Config. vi).

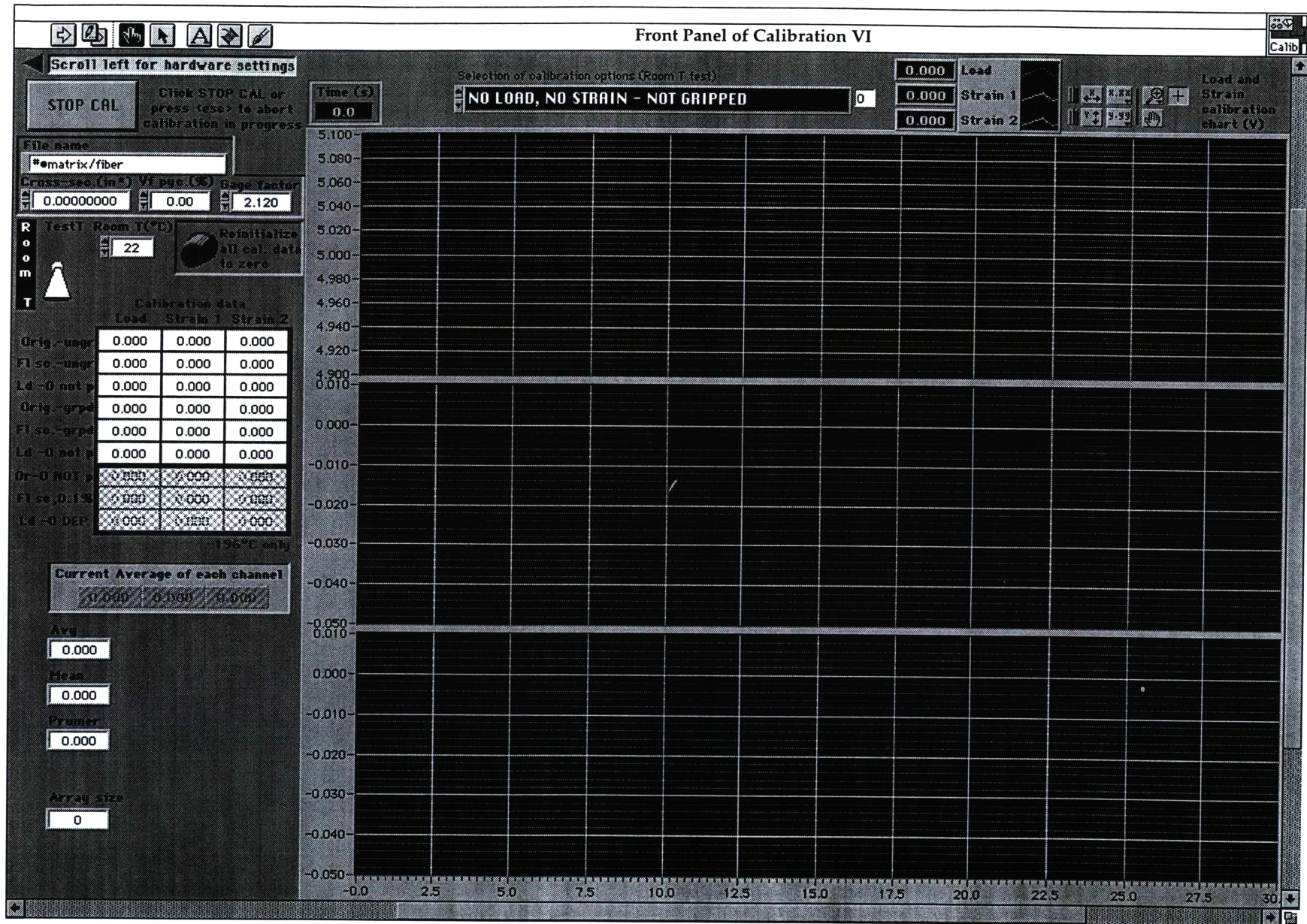


Figure B-3 - Front panel of Calibration vi (Part of Instron Config. vi).

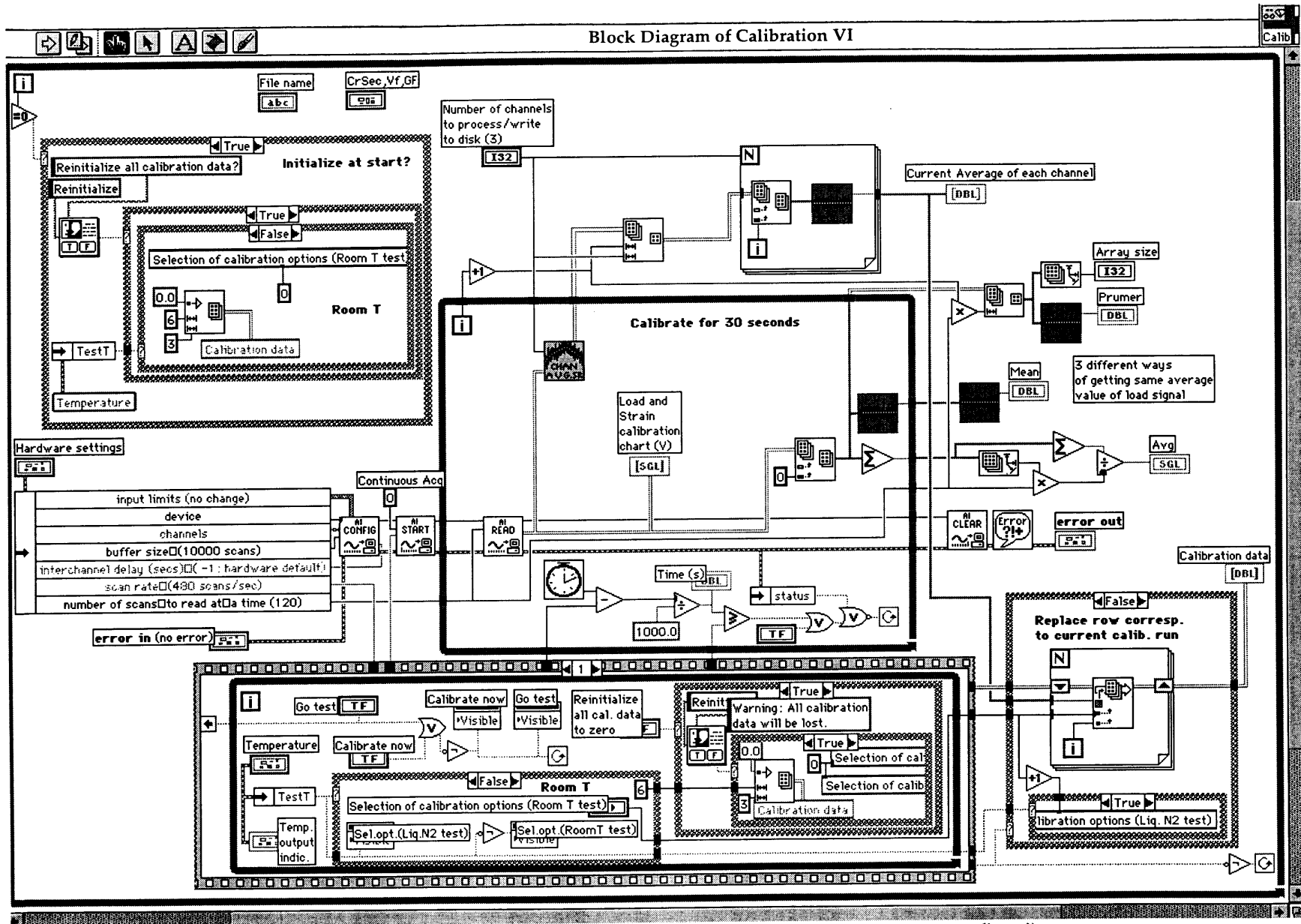
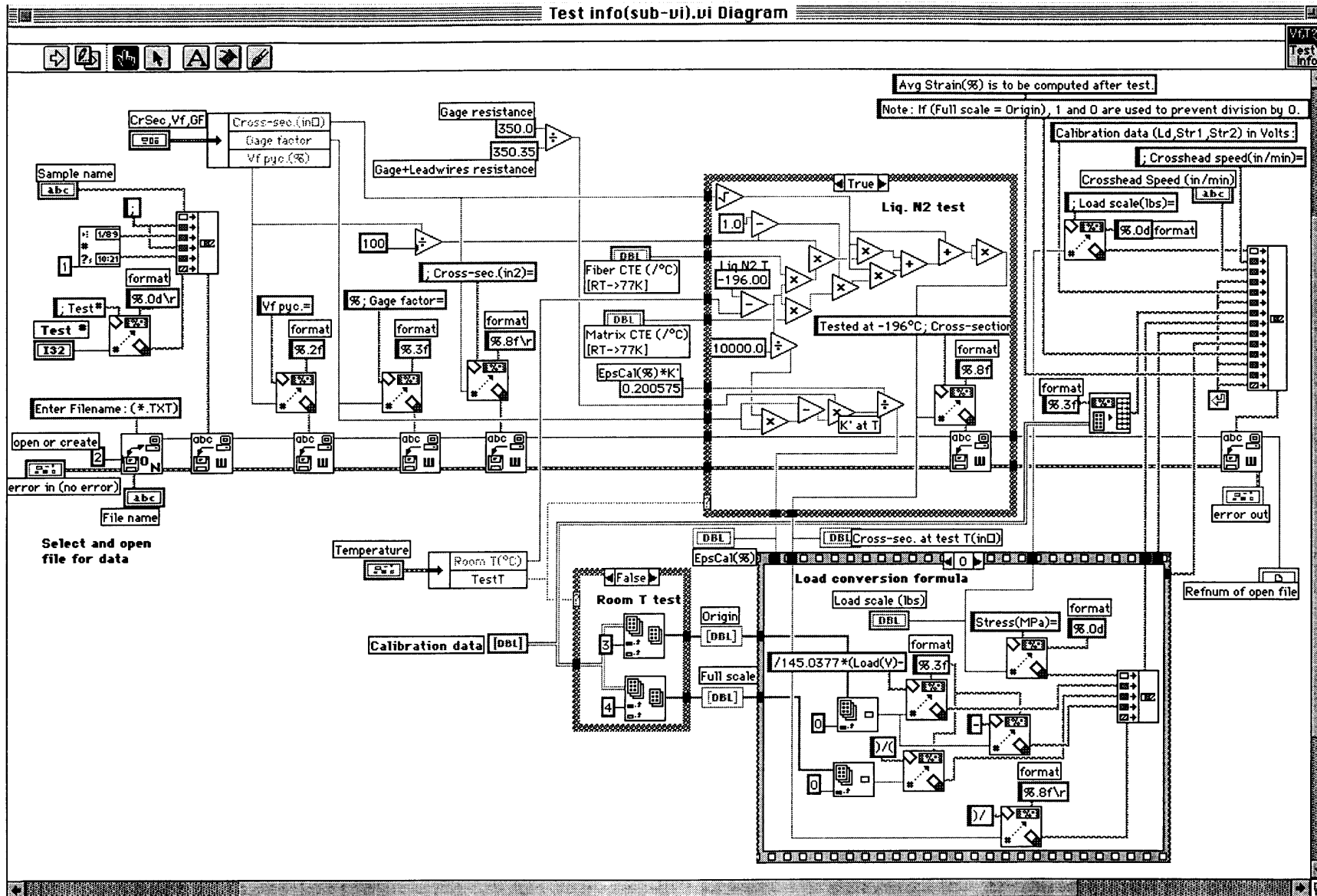


Figure B-4 - Block diagram of calibration vi (Part of Instron Config. vi).

Figures B-5 to B-9 (pages 182 to 186) - Block diagrams of main sub-vi's of Instron Config. vi.

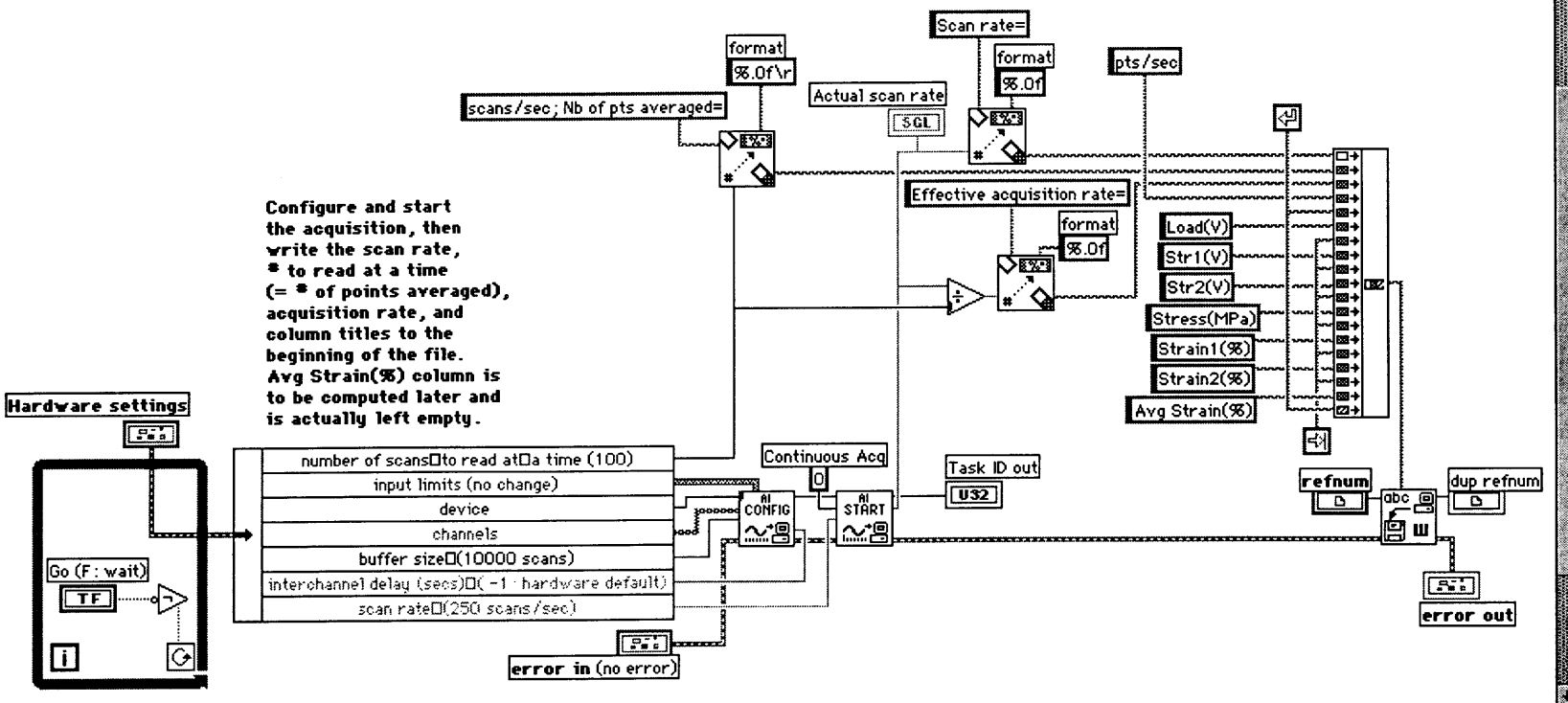


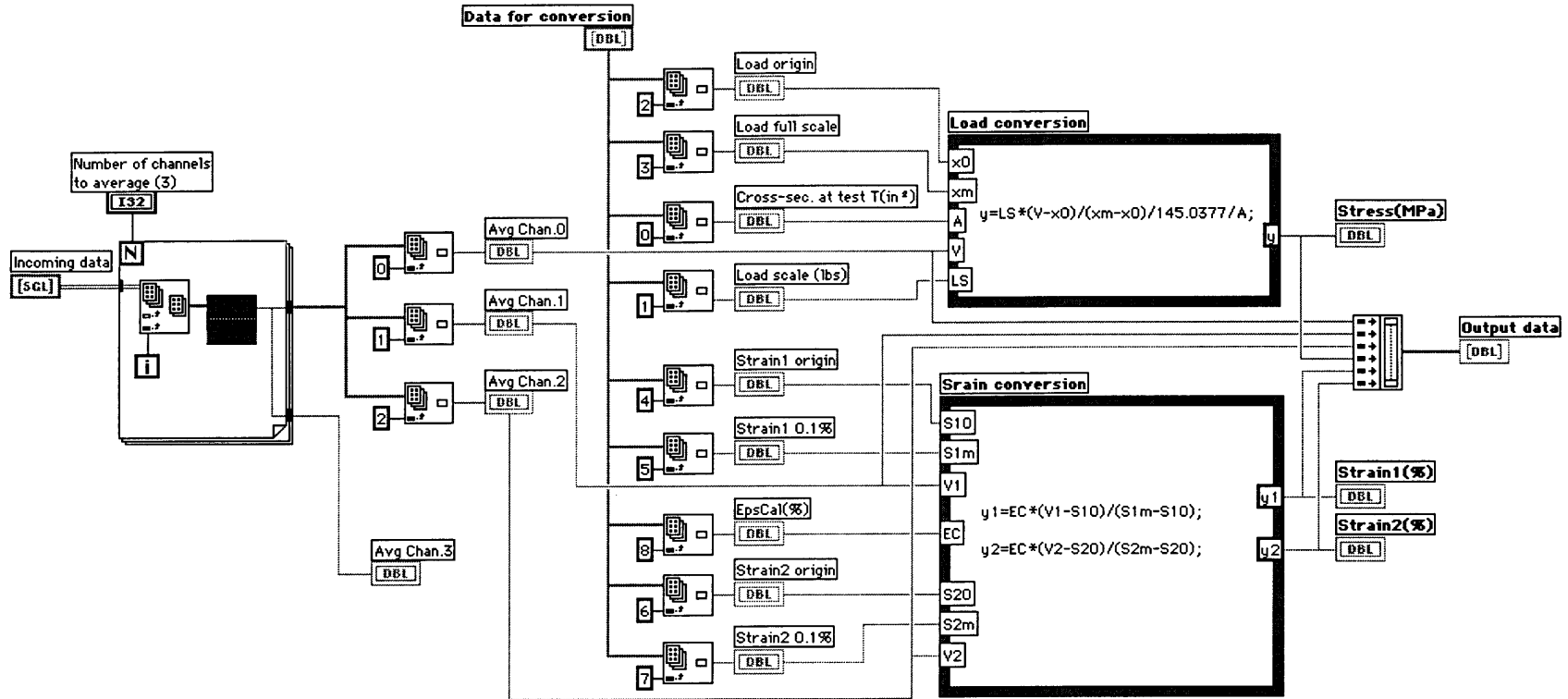
Start Test(sub-vi).vi Diagram

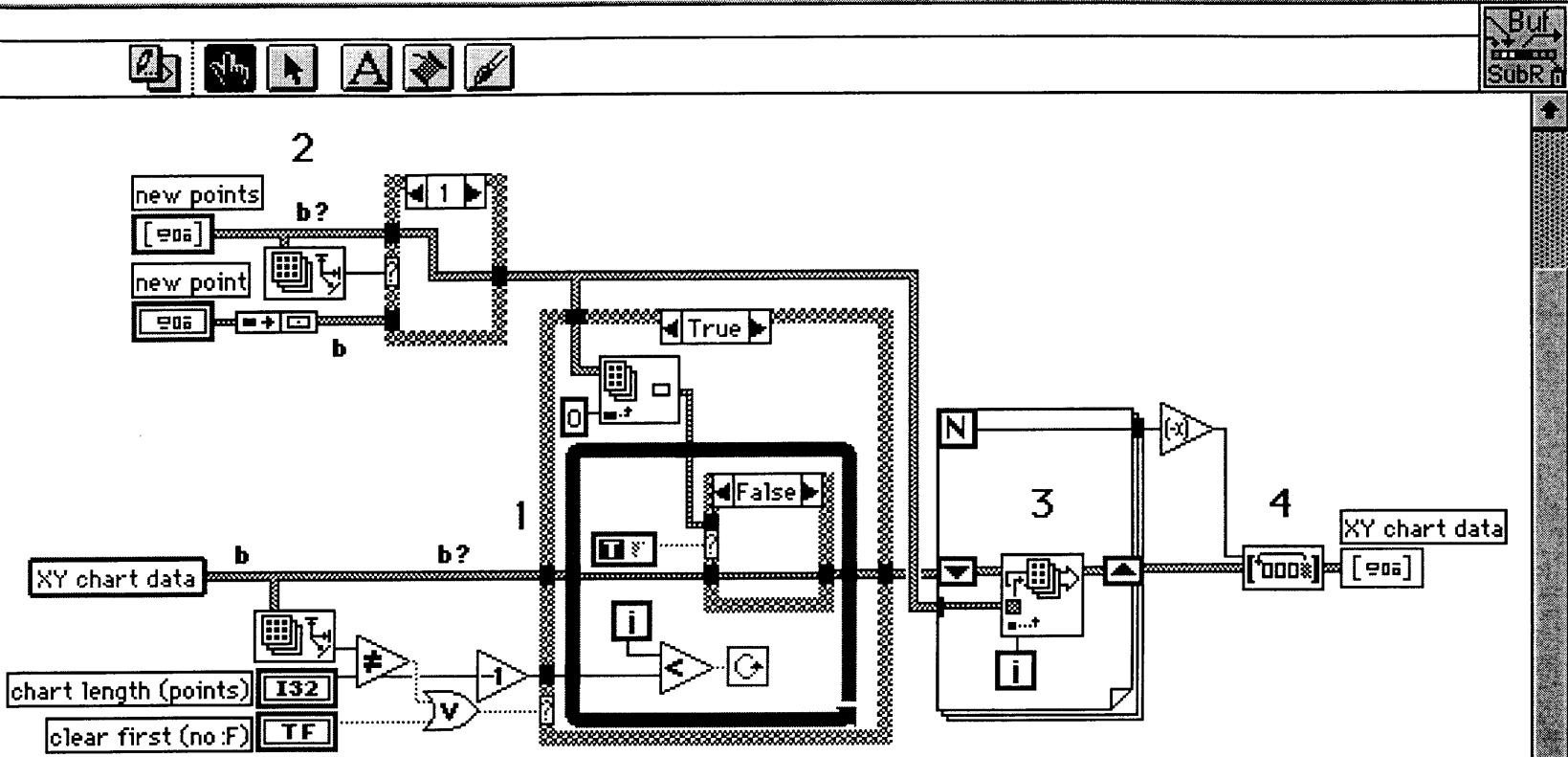


Start Test

Configure and start the acquisition, then write the scan rate, * to read at a time (= * of points averaged), acquisition rate, and column titles to the beginning of the file. Avg Strain(%) column is to be computed later and is actually left empty.



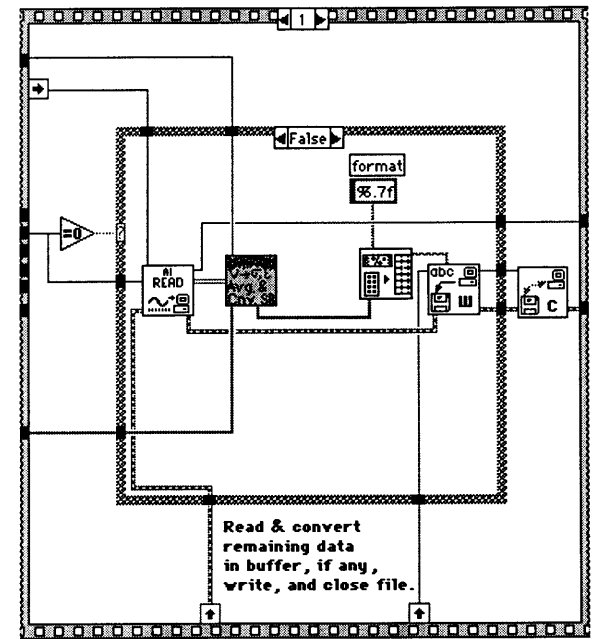
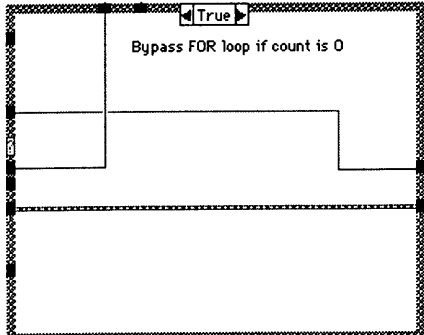
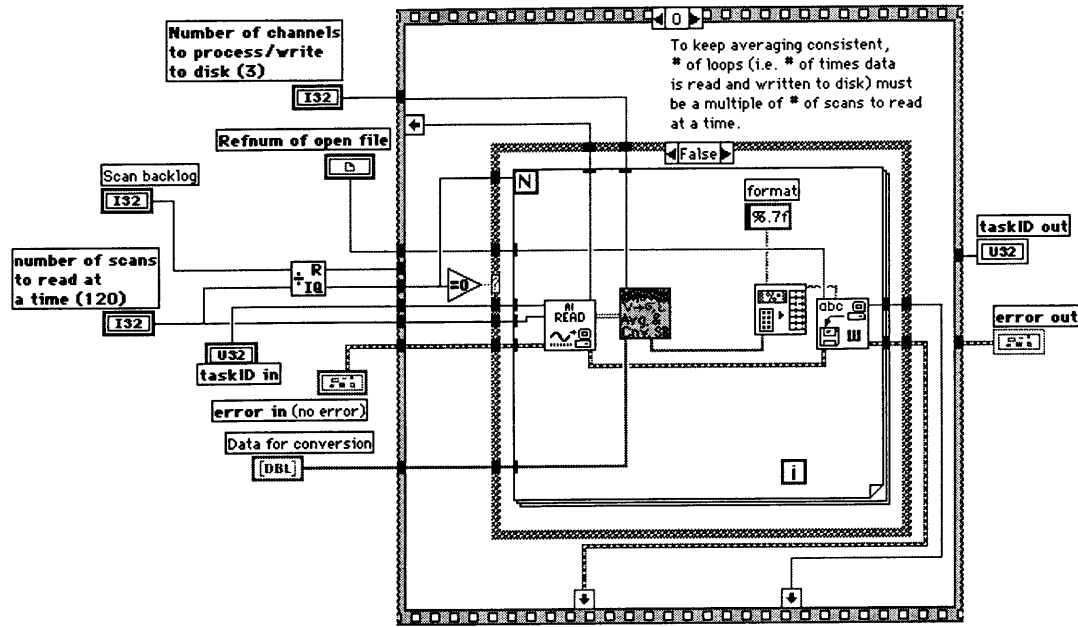




185

1. If **clear first** is TRUE, or if the current length of **XY chart data** is not equal to the desired **chart length**, expand the XY chart data buffer to the desired length. The technique shown mimics the behavior of the Initialize Array function, but without the extra memory buffer created by that function; that is, the output of the While Loop is in-place to the input.
 2. Process the **new points** array if it is not empty; otherwise, build **new point** into an array and process it.
 3. Replace the XY chart elements with the new points.
 4. Rotate the array so that the first element is the oldest one.
- b** marks a diagram array buffer; **b?** marks a buffer that may be in the calling VI.

Read, convert, and write to file data left in buffer, if any, when data acquisition was stopped.



Appendix C: Description of Data Processing Program

Yield!II is a LabVIEW program written specifically to process composite stress-strain data. The front panel is shown in Figure C-1 and the corresponding block diagrams are listed in the following pages.

The program opens TEXT files with composite stress-strain data, plots the composite stress-strain curve and determines its extrema. Least-square linear fits of user-specified regions of the composite stress-strain curve, θ - ϵ curves, and apparent *in-situ* matrix stress-strain curves for various volume fractions of reinforcement can easily be computed. Matrix data is obtained from both the classical and corrected rule of mixtures. All data can be saved in TEXT format.

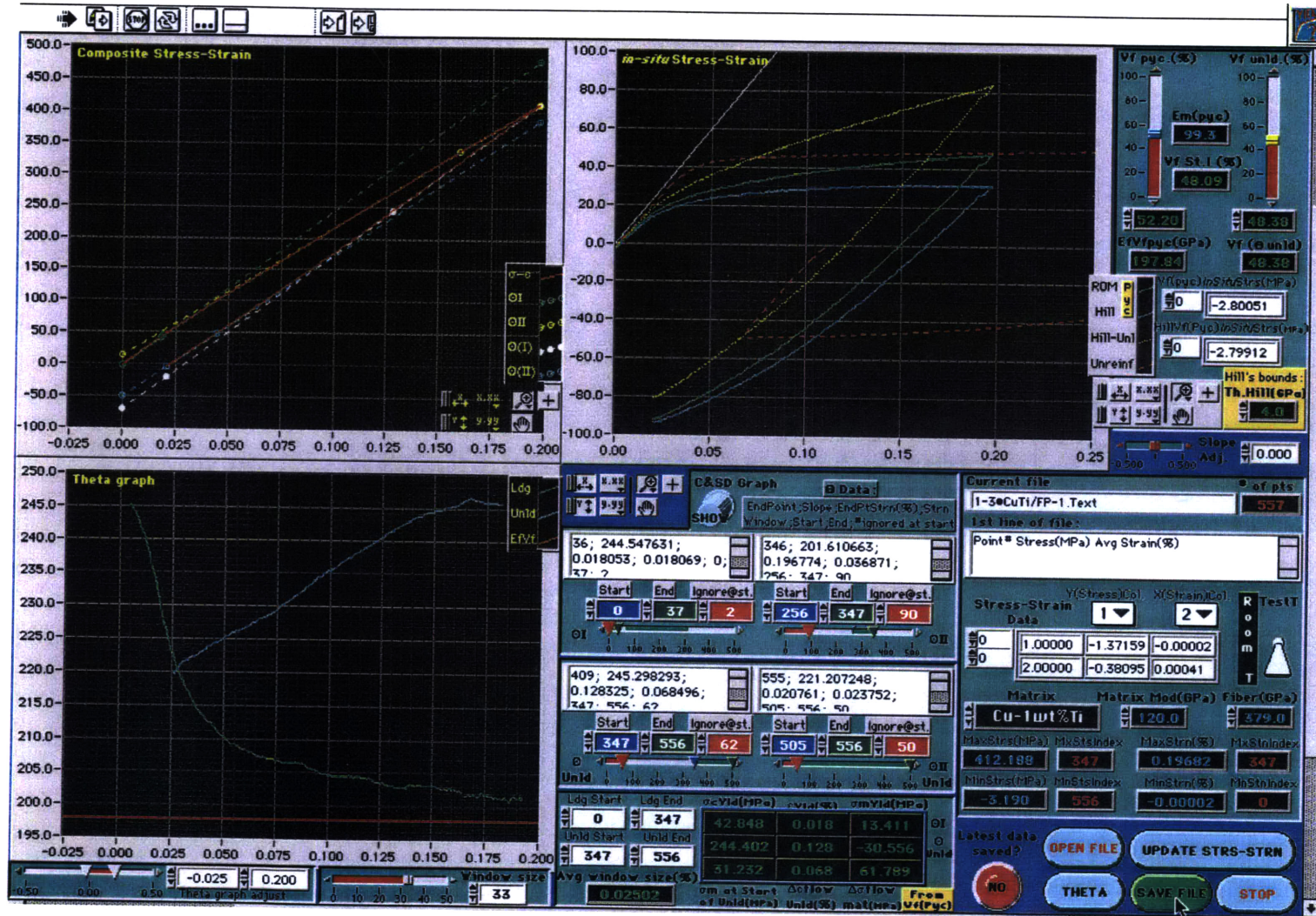
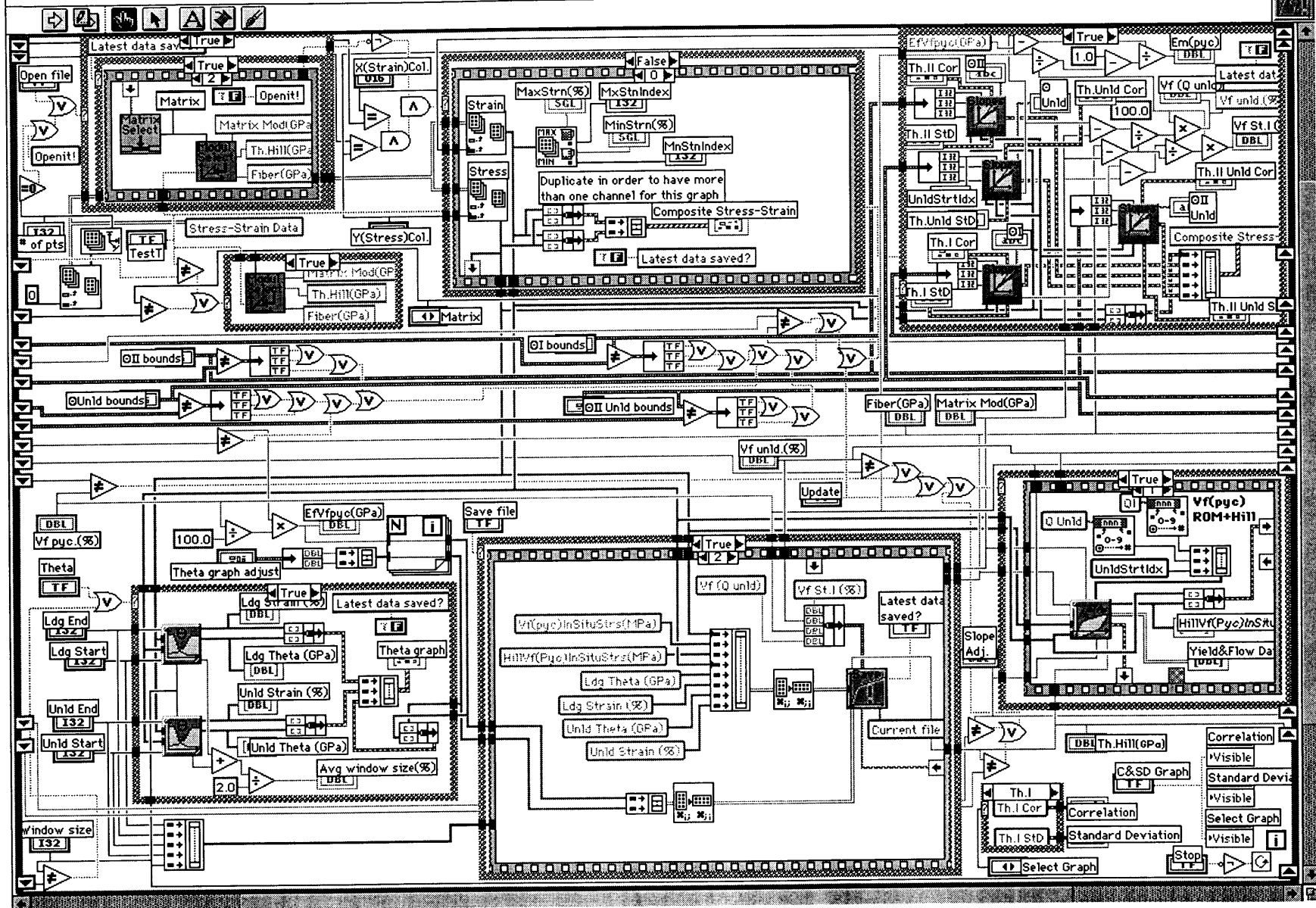


Figure C-1 - Front panel of Yield! II data processing program (written in LabVIEW), showing composite stress-strain curve (upper left; broken lines are least-square fits of linear regions), corresponding θ - ϵ graph (lower left), and apparent *in-situ* matrix σ - ϵ curves (upper right). The latter were computed with $V_f(\text{pyc})=52.2\%$ using the classical (green line) and corrected (blue line) rule of mixtures.

Figure C-2 Yield! II.ui Diagram Part 1



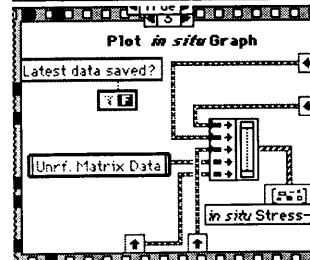
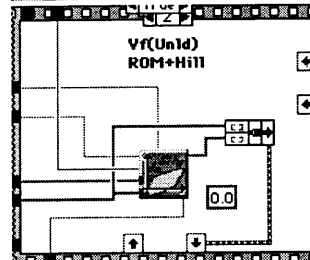
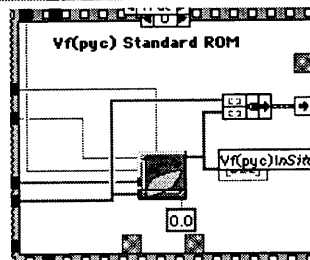
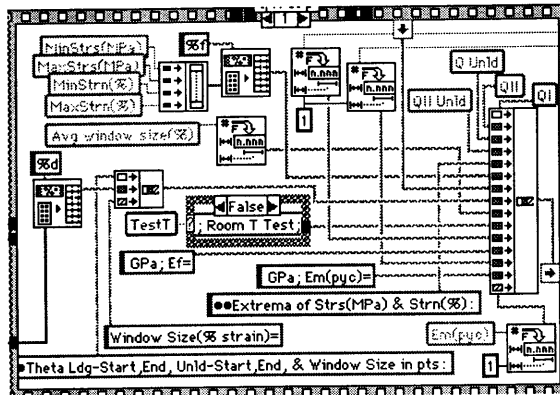
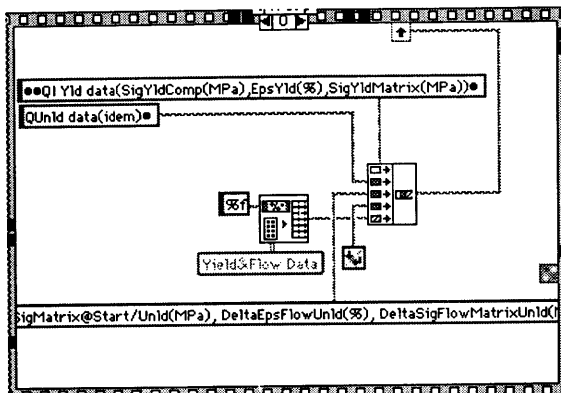
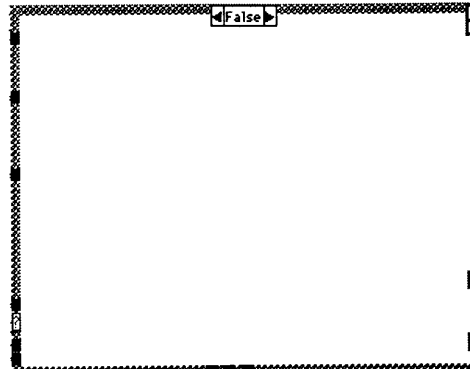
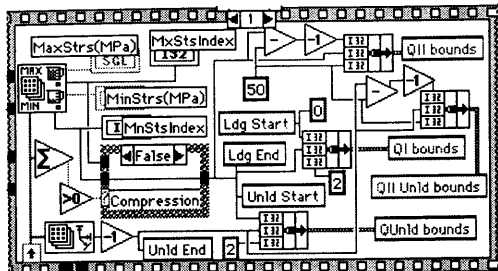
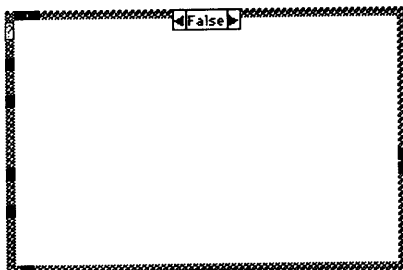
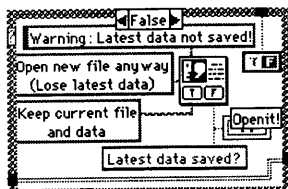
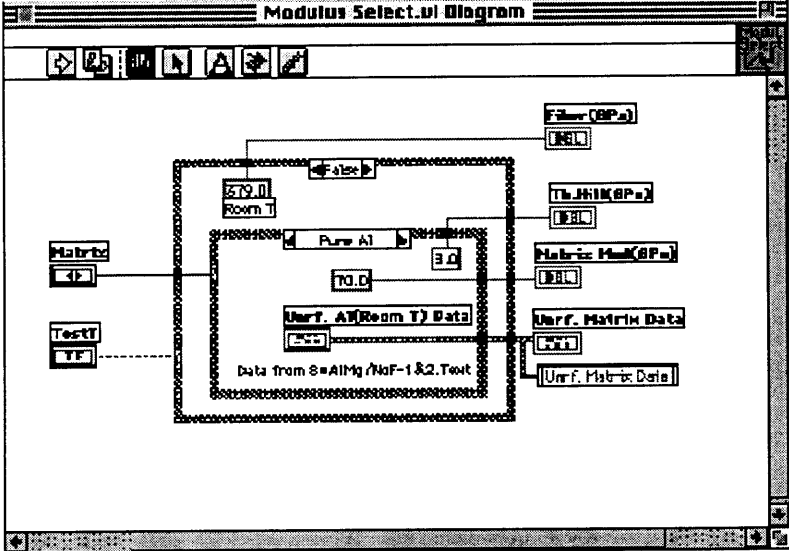
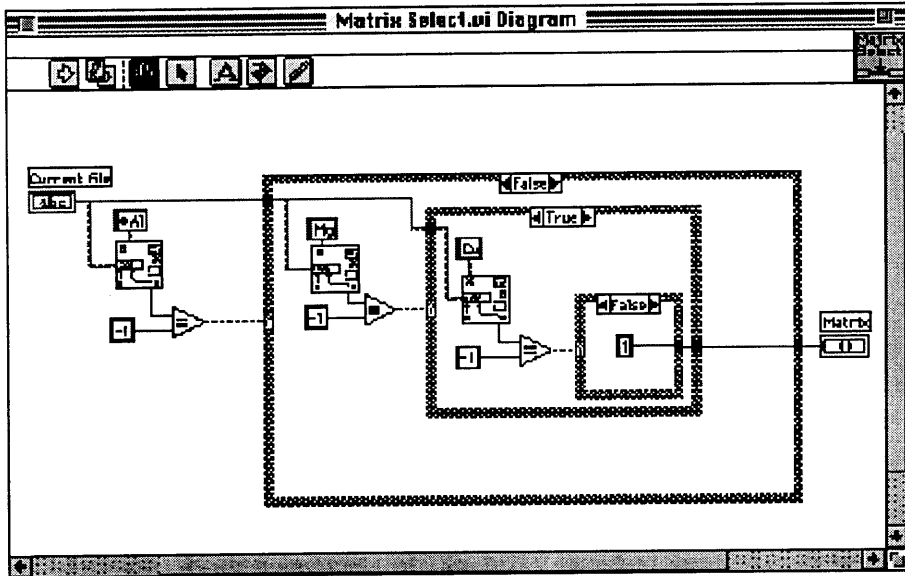
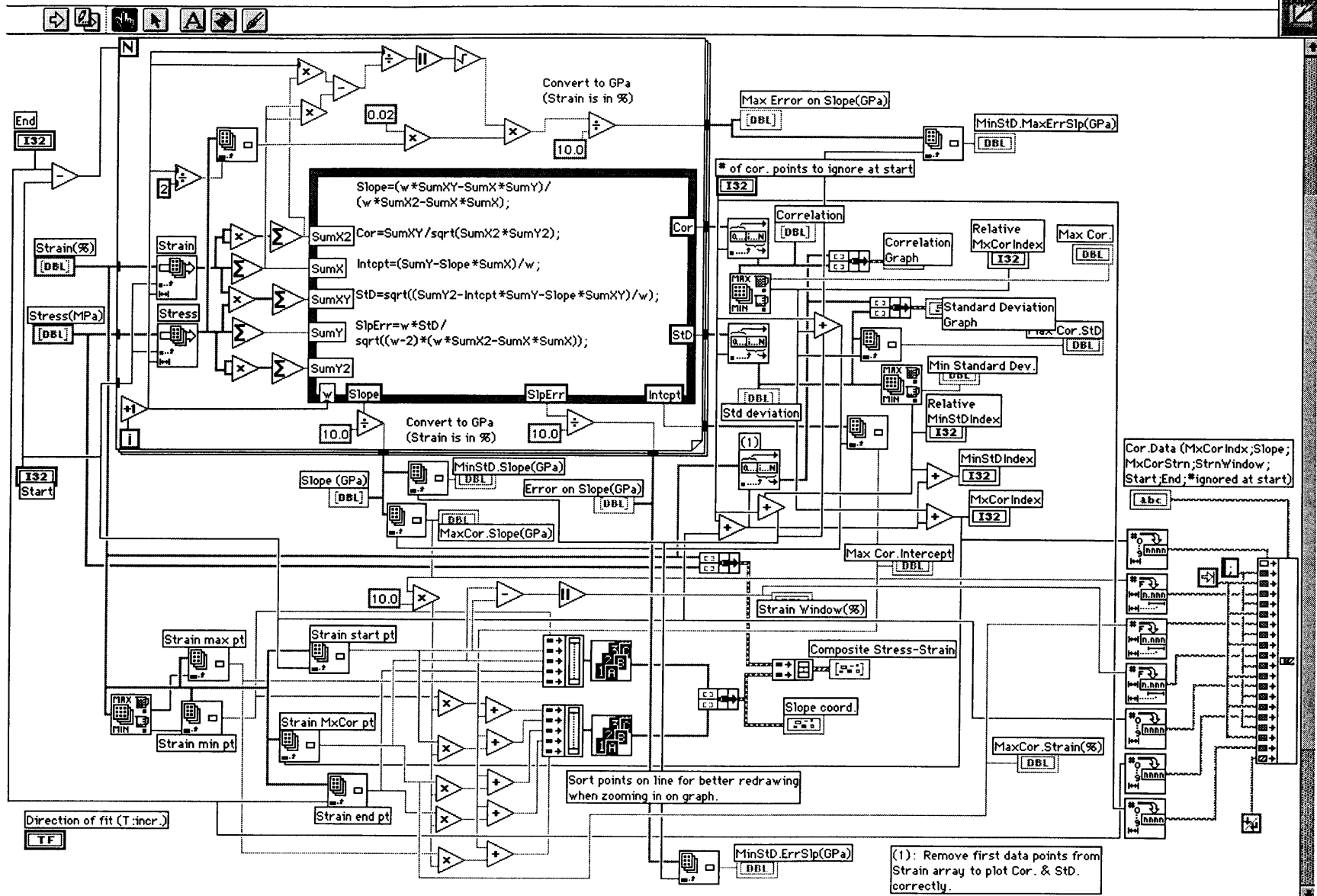
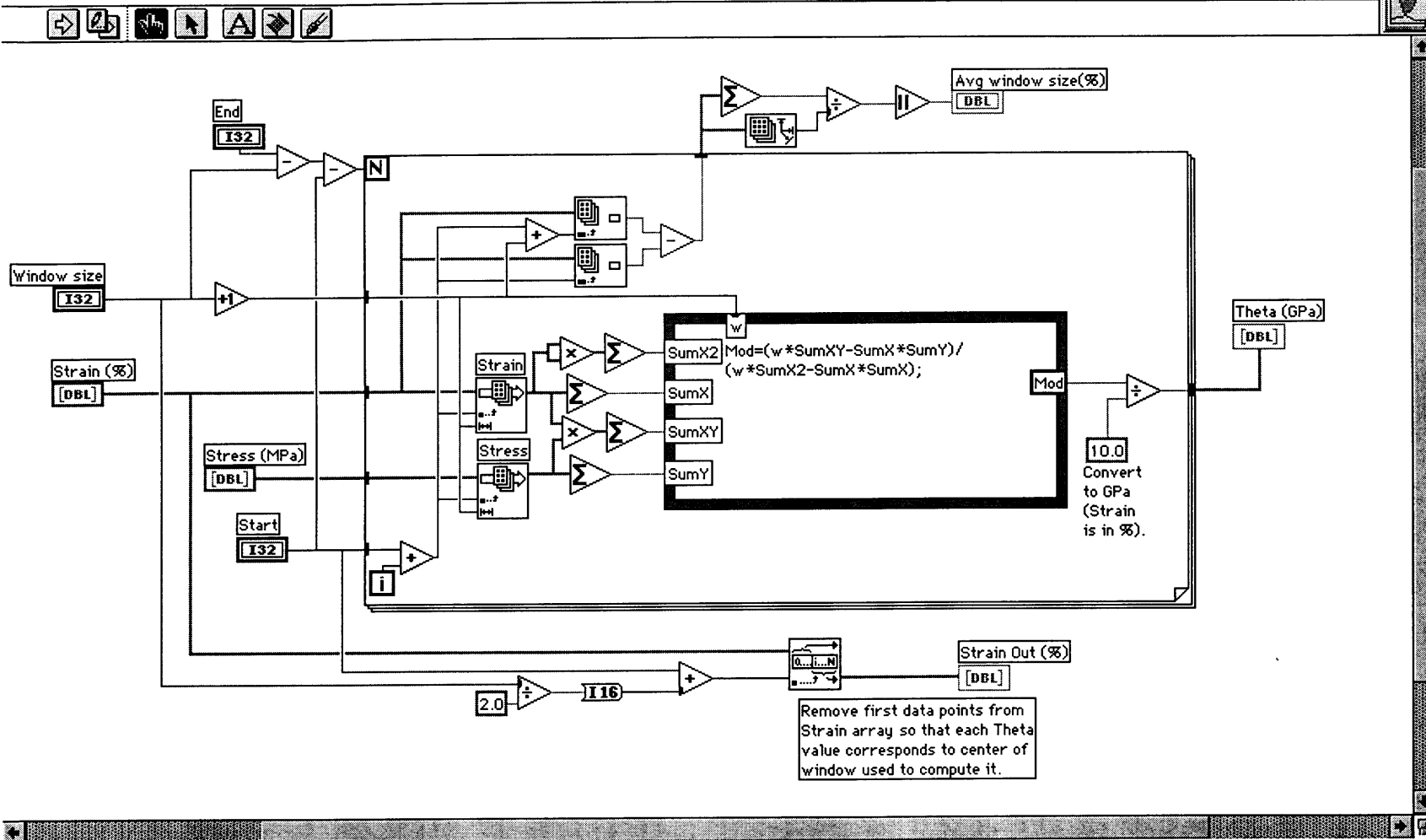


Figure C-2 (continued): additional frames of main Yield!II diagram structures

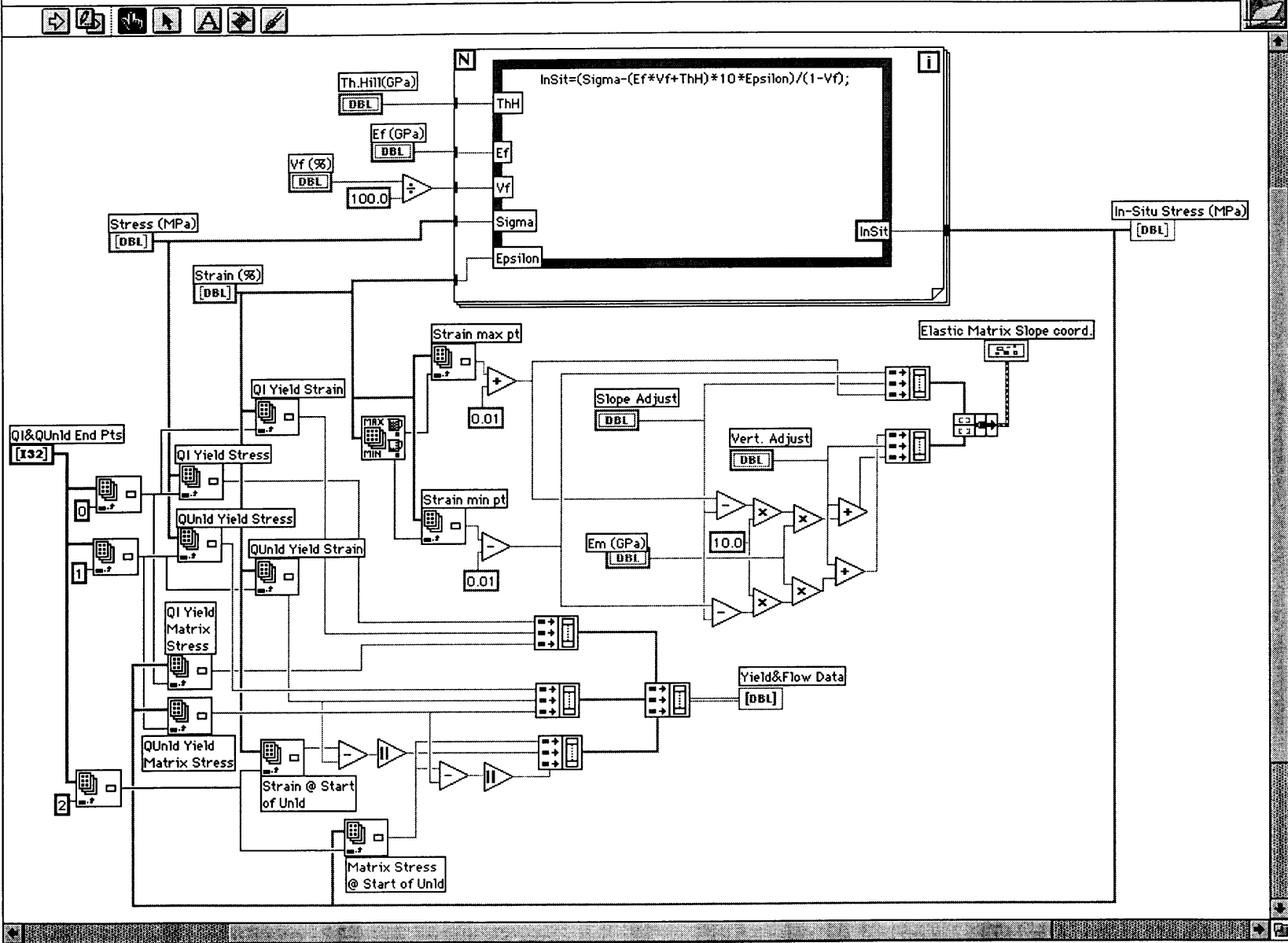
Figures C-3 to C-7 (pages 191 to 195) - Block diagrams of main sub-vi's of Yield!II data processing program.



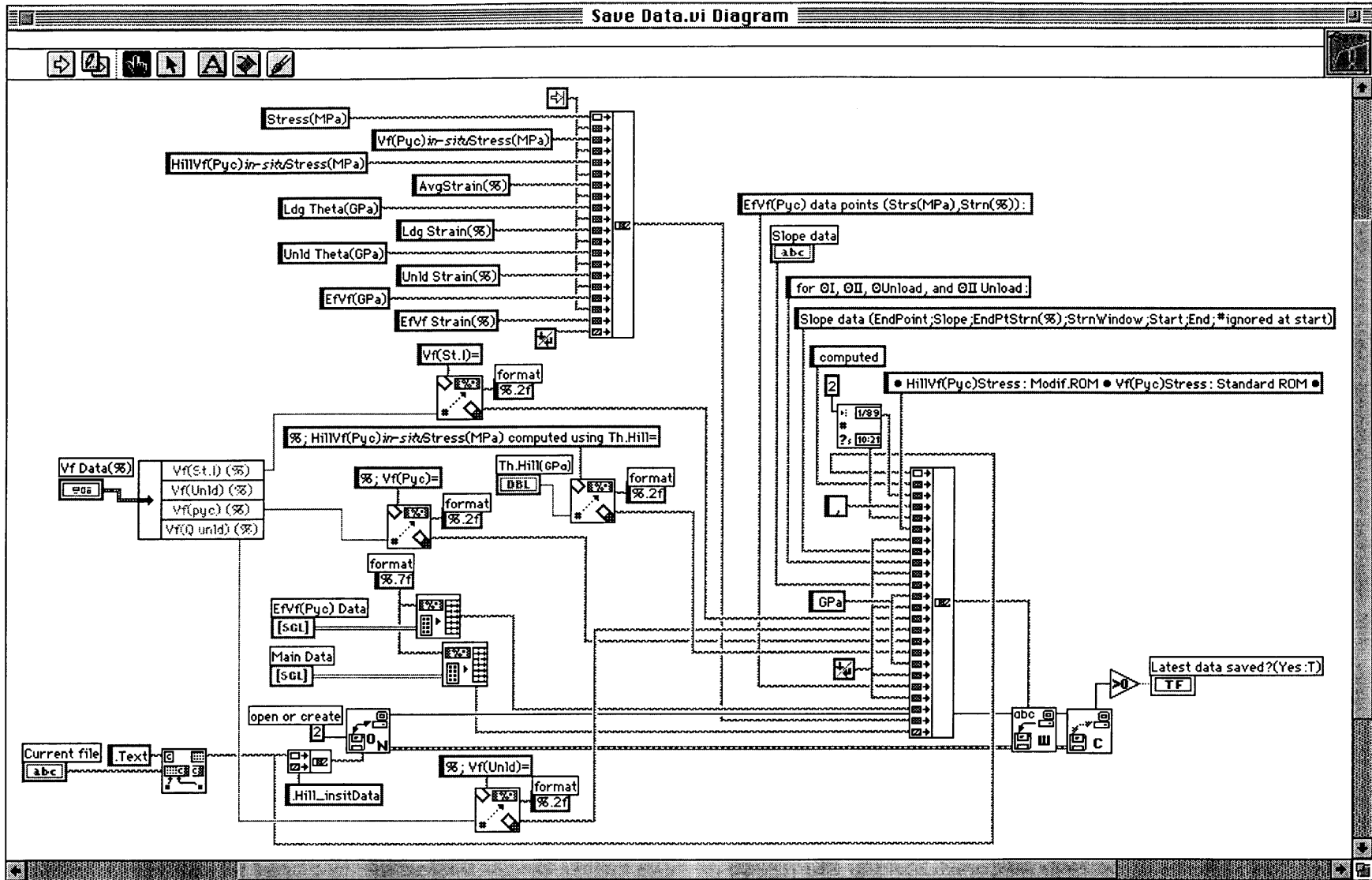




Remove first data points from Strain array so that each Theta value corresponds to center of window used to compute it.



Save Data.vi Diagram



Bibliography

1. A. Cottrell: in *The Science of New Materials*, A. Briggs, ed., Blackwell, Oxford, UK, 1992, pp. 4-31.
2. M.F. Ashby: *Acta Metall. et Mater.*, 1993, vol. 41, pp. 1313-1335.
3. H.E. Deve and C. McCullough: *J. of Metals*, 1995, vol. 47, pp. 33-37.
4. A. Kelly and H. Lilholt: *Phil. Mag.*, 1969, vol. 20, pp. 311-328.
5. R.E. Lee and S.J. Harris: *J. Mater. Sci.*, 1974, vol. 9, pp. 359-368.
6. O.B. Pedersen: *Acta Metall.*, 1990, vol. 38, pp. 1201-1219.
7. O.B. Pedersen and B. Johannesson: in *Advances in Mathematical Modelling of Composite Materials*, K.Z. Markov, ed., World Scientific Publishers, 1994, pp. 1-45.
8. J.A. Isaacs: *Structure and Deformation of Continuous Alumina Fiber Reinforced Aluminum Composites*, Ph.D. thesis, 1991, Massachusetts Institute of Technology.
9. A. Mortensen and I. Jin: *Intern. Mater. Rev.*, 1992, vol. 37, pp. 101-128.
10. V.J. Michaud: in *Fundamentals of Metal Matrix Composites*, S. Suresh, A. Mortensen, and A. Needleman, ed., Butterworth-Heinemann, Stoneham, MA, 1993, pp. 3-22.
11. A. Mortensen and M.C. Flemings: *Metall. Trans.*, 1995, vol. in print, pp.
12. A. Mortensen: *Mater. Sci. & Eng.*, 1993, vol. A173, pp. 205-212.
13. R.J. Arsenault and R.M. Fisher: *Scripta Metall.*, 1983, vol. 17, pp. 67-71.
14. M. Vogelsang, R.J. Arsenault, and R.M. Fisher: *Metall. Trans.*, 1986, vol. 17A, pp. 379-388.
15. M. Taya and J. Arsenault: *Metal Matrix Composites - Thermomechanical Behavior*, 1st ed., Pergamon Press, Oxford, 1989, 264 pages.
16. F.J. Humphreys, A. Basu, and M.R. Djazeb: in *12th Risø International Symposium on Metallurgy and Materials Science: Metal Matrix Composites - Processing, Microstructure and Properties*, Proc. Conf., Roskilde, Denmark, 1991, N. Hansen, D. Juul-Jensen, T. Leffers, H. Lilholt, T. Lorentzen, A.S. Pedersen, O.B. Pedersen, and B. Ralph, ed., Risø National Laboratory, Roskilde, Denmark, pp. 51-66.
17. T.W. Clyne and P.J. Withers: *An Introduction to Metal Matrix Composites*, Cambridge University Press, Cambridge, U.K., 1993, 509 pages.
18. N. Hansen and C. Barlow: in *Fundamentals of Metal Matrix Composites*, S. Suresh, A. Mortensen, and A. Needleman, ed., Butterworth-Heinemann, Stoneham, MA, 1993, pp. 109-118.

19. S. Suresh and K.K. Chawla: in *Fundamentals of Metal Matrix Composites*, S. Suresh, A. Mortensen, and A. Needleman, ed., Butterworth-Heinemann, Stoneham, Mass, 1993, pp. 119-136.
20. P.B. Prangnell and W.M. Stobbs: in *12th Risø International Symposium on Metallurgy and Materials Science: Metal Matrix Composites-Processing, Microstructure and Properties*, Proc. Conf., Roskilde, Denmark, 1991, N. Hansen, D. Juul-Jensen, T. Leffers, H. Lilholt, T. Lorentzen, A.S. Pedersen, O.B. Pedersen, and B. Ralph, ed., Risø National Laboratory, Roskilde, Denmark, pp. 603-610.
21. D.C. Dunand and A. Mortensen: *Acta Metall. et Mater.*, 1991, vol. 39, pp. 127-139.
22. D.C. Dunand and A. Mortensen: *Acta Metall. et Mater.*, 1991, vol. 39, pp. 1405-1416.
23. D.C. Dunand and A. Mortensen: *Acta Metall. et Mater.*, 1991, vol. 39, pp. 1417-1429.
24. J.A. Isaacs and A. Mortensen: *Metallurgical Transactions A*, 1992, vol. 23A, pp. 1207-1219.
25. K. Tanaka and T. Mori: *Phil. Mag.*, 1971, vol. 23, pp. 737-740.
26. T. Mura: *Micromechanics of Solids*, Martinus Nijhoff, The Hague, 1982, pp. 334-388 pages.
27. L.M. Brown and D.R. Clarke: *Acta Metall.*, 1975, vol. 23, pp. 821-830.
28. L.M. Brown and D.R. Clarke: *Acta Metall.*, 1977, vol. 25, pp. 563-570.
29. O.B. Pedersen: *Acta Metall.*, 1983, vol. 31, pp. 1795-1808.
30. O.B. Pedersen: in *Micromechanics and Inhomogeneity - The Toshio Mura 65th Anniversary Volume*, Proc. Conf., 1990, G.J. Weng, M. Taya, and H. Abé, ed., Springer-Verlag, New York, pp. 341-365.
31. P.J. Withers, D.J. Jensen, H. Lilholt, and W.M. Stobbs: in *Sixth International Conference on Composite Materials, ICCM 6*, Proc. Conf., London, 1987, F.L. Matthews, N.C.R. Buskell, J.M. Hodgkinson, and J. Morton, ed., Elsevier Applied Science, London, pp. 2.255-2.264.
32. P.J. Withers, W.M. Stobbs, and O.B. Pedersen: *Acta Metall.*, 1989, vol. 37, pp. 3061-3084.
33. Y.H. Zhao and G.J. Weng: in *Micromechanics and Inhomogeneity - The Toshio Mura 65th Anniversary Volume*, Proc. Conf., 1990, G.J. Weng, M. Taya, and H. Abé, ed., Springer-Verlag, New York, pp. 599-622.
34. Y. Takao: *Adv. Composite Mater.*, 1991, vol. 1, pp. 235-248.
35. G.J. Dvorak: in *Metal Matrix Composites: Mechanisms and Properties*, R.K. Everett and R.J. Arsenault, ed., Academic Press, Boston, MA, 1991, pp. 1-78.
36. P.E. McHugh, R.J. Asaro, and C.F. Shih: in *Fundamentals of Metal Matrix Composites*, S. Suresh, A. Mortensen, and A. Needleman, ed., Butterworth-Heinemann, Stoneham, MA, 1993, pp. 139-157.

37. J.W. Hutchinson and R.M. McMeeking: in *Fundamentals of Metal Matrix Composites*, S. Suresh, A. Mortensen, and A. Needleman, ed., Butterworth-Heinemann, Stoneham, MA, 1993, pp. 158-173.
38. S. Suresh and J. Brockenbrough: in *Fundamentals of Metal Matrix Composites*, S. Suresh, A. Mortensen, and A. Needleman, ed., Butterworth-Heinemann, Stoneham, MA, 1993, pp. 174-190.
39. M.-S. Hu, J. Yang, H.C. Cao, A.G. Evans, and R. Mehrabian: *Acta Metall. et Mater.*, 1992, vol. 40, pp. 2315-2326.
40. S. Suresh, A. Mortensen, and A. Needleman: *Fundamentals of Metal Matrix Composites*, Butterworth-Heinemann, Stoneham, MA, 1993, 342 pages.
41. R. Hill: *Journal of Mechanics and Physics of Solids*, 1964, vol. 12, pp. 199-212.
42. R. Hill: *Journal of Mechanics and Physics of Solids*, 1964, vol. 12, pp. 213-218.
43. J.R. Brockenbrough and S. Suresh: *Scripta Metallurgica et Materiala*, 1990, vol. 24, pp. 325-330.
44. J.R. Brockenbrough, S. Suresh, and H.A. Wienecke: *Acta Metall. et Mater.*, 1991, vol. 39, pp. 735-752.
45. H.J. Böhm: *Computer Based Micromechanical Investigations of the Thermomechanical Behavior of Metal Matrix Composites*, D. Tech. Wiss. thesis, 1991, Technical University of Vienna.
46. T. Nakamura and S. Suresh: *Acta Metall. et Mater.*, 1993, vol. 41, pp. 1665-1681.
47. D.R. Clarke: in *Strength of Metals and Alloys - ICSMA 3*, Proc. Conf., Cambridge, England, 1973, ed., The Institute of Metals, pp. 1-3; Paper 51.
48. M. Dollar, I.M. Bernstein, and A.W. Thompson: *Acta Metall.*, 1988, vol. 36, pp. 311-320.
49. C. Baromeo and T.H. Courtney: *Metall. Trans.*, 1973, vol. 4, pp. 1821-1828.
50. R. Elliott: *Eutectic Solidification Processing; Crystalline and Glassy Alloys*, Butterworths & Co. Ltd., London, 1983, Chapter 7 pages.
51. W.A. Spitzig: *Acta Metall. et Mater.*, 1991, vol. 39, pp. 1085-1090.
52. P.D. Funkenbusch and T.H. Courtney: *Scripta Metallurgica et Materiala*, 1990, vol. 24, pp. 1183-1184.
53. R.J. Arsenault, L. Wang, and C.R. Feng: *Acta Metall. et Mater.*, 1991, vol. 39, pp. 47-57.
54. K.K. Chawla and M. Metzger: *Metallurgical Transactions A*, 1977, vol. 8A, pp. 1681-1687.
55. C.L. Trybus, F.C. Laabs, A.R. Pelton, and W.A. Spitzig: in *Specimen Preparation for Transmission Electron Microscopy of Materials*, Proc. Conf., Boston, MA, USA, 1987, J.C. Bravman, R.M. Anderson, and M.L. McDonald, ed., Materials Research Society, pp. 235-240.
56. A. Kelly and W.R. Tyson: *Journal of Mechanics and Physics of Solids*, 1965, vol. 13, pp. 329-350.

57. D.L. McDanel, R.W. Jech, and J.W. Weeton: *Trans. Metall. Soc. AIME*, 1965, vol. 233, pp. 636-642.
58. H.P. Cheskis and R.W. Heckel: *Metall. Trans.*, 1970, vol. 1, pp. 1931-1942.
59. D.C. Dunand and A. Mortensen: *Mater. Sci. & Eng.*, 1991, vol. A144, pp. 179-188.
60. D.C. Dunand and A. Mortensen: *Scripta Metall. et Mater.*, 1991, vol. 25, pp. 761-766.
61. R.J. Arsenault: in *Metal Matrix Composites: Mechanisms and Properties*, R.K. Everett and R.J. Arsenault, ed., Academic Press, Boston, 1991, pp. 79-100.
62. R.J. Arsenault: *Scripta Metallurgica et Materiala*, 1991, vol. 25, pp. 2617-2621.
63. P. Neumann and P. Haasen: *Phil. Mag.*, 1971, vol. 23, pp. 285-292.
64. L.M. Brown: *Scripta Metall.*, 1977, vol. 11, pp. 127-131.
65. L.M. Brown: in *Strength of Metals and Alloys - ICSMA 5*, Proc. Conf., Aachen, BRD, 1979, P. Haasen, V. Gerold, and G. Kostorz, ed., Pergamon, Toronto, pp. 1551-1571.
66. H. Lilholt: in *Mechanical Properties of Metallic Composites*, S. Ochiai, ed., Marcel Dekker, Inc., New York, NY, 1994, pp. 389-471.
67. L.M. Brown: *Scripta Metall.*, 1977, vol. 11, pp. 315-318.
68. H. Lilholt: *Acta Metall.*, 1977, vol. 25, pp. 571-585.
69. H. Lilholt: *Acta Metall.*, 1977, vol. 25, pp. 587-593.
70. R.E. Stoltz and R.M. Pelloux: *Metall. Trans.*, 1976, vol. 7A, pp. 1295-1306.
71. A. Kelly: *Metall. Trans.*, 1972, vol. 3, pp. 2313-2325.
72. T.H. Courtney: *Mechanical Behavior of Materials*, McGraw-Hill, New York, NY, 1990, 710 pages.
73. R.W. Hertzberg: *Deformation and Fracture Mechanics of Engineering Materials*, 3rd, John Wiley & Sons, New York, NY, 1989, 682 pages.
74. F.S. Galasso: *Advanced Fibers and Composites*, Gordon and Breach Science Publishers, New York, NY, 1989, 178 pages.
75. J.R. Taylor: *An Introduction to Error Analysis - The Study of Uncertainties in Physical Measurements*, Oxford University Press, Mill Valley, CA, 1982, 269 pages.
76. A.K. Dhingra: *Philosophical Transactions of the Royal Society of London A*, 1980, vol. 294, pp. 411-417.
77. A.K. Dhingra: *Philosophical Transactions of the Royal Society of London A*, 1980, vol. 294, pp. 559-564.

78. M.N. Gungor: *Solidification Processing of Al-4.5%Cu / Al₂O₃ Composites*, Sc.D. thesis, 1986, Massachusetts Institute of Technology.
79. J.A. Isaacs, F. Taricco, V.J. Michaud, and A. Mortensen: *Metall. Trans.*, 1991, vol. 22A, pp. 2855-2862.
80. A. Okura: in *Fifth International Conference on Composite Materials ICCM-V, Proc. Conf.*, San Diego, CA, 1985, W.C. Harrigan, J. Strife, and A.K. Dhingra, ed., The Metallurgical Society, Inc., pp. 797-807.
81. R.C. Dorward: *Metall. Trans.*, 1973, vol. 4, pp. 507-512.
82. G. Bradfield and H. Pursey: *Phil. Mag.*, 1953, vol. 44, pp. 437-443.
83. M.J. Saarivirta and H.S. Cannon: *Metal Prog.*, 1959, vol. 72, pp. 81-84.
84. J.L. Murray: *Bull. Alloy Phase Diag.*, 1983, vol. 4, pp. 81-95.
85. D.E. Laughlin and J.W. Cahn: *Acta Metall.*, 1975, vol. 23, pp. 329-339.
86. A. Datta and W.A. Soffa: *Acta Metall.*, 1976, vol. 24, pp. 987-1001.
87. T.K. Vaidyanathan and K. Mukherjee: *J. Mater. Sci.*, 1975, vol. 10, pp. 1697-1710.
88. H.T. Michels, I.B. Cadoff, and E. Levine: *Metall. Trans.*, 1972, vol. 3, pp. 667-674.
89. *Experimental Stress Analysis*, I. Measurements Group, ed., Measurements Group, Inc., Raleigh, NC, 1982-1994, vol.
90. W. Lichten: *Data and Error Analysis in the Introductory Physics Laboratory*, Allyn and Bacon, Inc., Boston, MA, 1988, p. 10 pages.
91. R.A. Schapery: *J. of Comp. Mater.*, 1968, vol. 2, pp. 380-404.
92. R.J. Vaidya and K.K. Chawla: *Composites Sci. and Techn.*, 1994, vol. 50, pp. 13-22.
93. R.P. Reed and A.F. Clark: *Materials at Low Temperatures*, American Society for Metals, Metals Park, Ohio, 1983, 590 pages.
94. Y.S. Touloukian, R.K. Kirby, R.E. Taylor, and P.D. Desai: in *Thermal Expansion - Metallic Elements and Alloys*, ed., IFI/Plenum, New York, NY, 1975, pp. 2-12.
95. Y.S. Touloukian, R.K. Kirby, R.E. Taylor, and T.Y.R. Lee: in *Thermal Expansion - Nonmetallic Solids*, ed., IFI/Plenum, New York, NY, 1977, pp. 176-193.
96. J.B. Wachtman, W.E. Tefft, D.G. Lam, and C.S. Apstein: *Phys. Rev.*, 1961, vol. 122, pp. 1754-1759.
97. O.L. Anderson: *Phys. Rev.*, 1966, vol. 144, pp. 553-557.
98. *CRC Handbook of Chemistry and Physics*, 71st Ed. 1990-1991, D.R. Lide, ed., CRC Press, Inc., Boston, MA, 1991, vol.

99. H.E. Boyer and T.L. Gall: *Metals Handbook - Desk Edition*, 6th printing, May 1991, American Society For Metals, Metals Park, OH, 1985, 1470 pages.
100. H.E. Deve, 3M Corp., St Paul, MN, personal communication, 1995.
101. W.H. Cubberly: *Metals Handbook Ninth Edition Vol.2 - Properties and Selection: Nonferrous Alloys and Pure Metals*, 9th, American Society For Metals, Metals Park, OH, 1979, 855 pages.
102. C.S. Barrett and T.B. Massalski: *Structure of Metals - Crystallographic Methods, Principles and Data*, Third Revised Edition, Pergamon Press, Oxford, 1980, 654 pages.
103. A.R. Champion, W.H. Krueger, H.S. Hartmann, and A.K. Dhingra: in *2nd International Conference on Composite Materials*, Proc. Conf., Toronto, Canada, 1978, ed., AIME, pp. 883-904.
104. J.C. Romine: *Ceram. Eng. Sci. Proc.*, 1987, vol. 9, pp. 755-765.
105. G.F. Carter and D.E. Paul: *Materials Science & Engineering*, 1st, ASM International, Metals Park, OH, 1991, 353 pages.
106. M. Kurtz: *Handbook of Applied Mathematics for Engineers and Scientists*, McGraw-Hill, New York, NY, 1991, 520 pages.
107. J.K. Mackenzie: *Proc. Roy. Soc. Lond.*, 1950, vol. B63, pp. 2-11.
108. J.D. Livingston: *Acta Metall.*, 1962, vol. 10, pp. 229-239.
109. J.D. Livingston: *J. of the Austr. Inst. of Metals*, 1963, vol. 8, pp. 15-24.
110. K. Sangwal: *Etching of Crystals - Theory, Experiment, and Application*, North-Holland, Amsterdam - Oxford - New York - Tokyo, 1987, 497 pages.
111. G. Petzow: *Metallographic Etching*, American Society For Metals, Metals Park, OH, 1978, 131 pages.
112. C. Béraud, M. Courbière, C. Esnouf, D. Juvé, and D. Tréheux: *J. Mater. Sci.*, 1989, vol. 24, pp. 4545-4554.
113. P. Kritsalis, L. Coudurier, and N. Eustathopoulos: *J. Mater. Sci.*, 1991, vol. 26, pp. 3400-3408.
114. N. Eustathopoulos and A. Mortensen: in *Fundamentals of Metal Matrix Composites*, S. Suresh, A. Mortensen, and A. Needleman, ed., Butterworth-Heinemann, Stoneham, MA, 1993, pp. 42-58.
115. P.R. Chidambaram, G.R. Edwards, and D.L. Olson: *Metall. Trans.*, 1994, vol. 25A, pp. 2083-2090.
116. P.M. Sutton: *Phys. Rev.*, 1953, vol. 91, pp. 816-821.
117. R.J. Asaro: *Acta Metall.*, 1975, vol. 23, pp. 1255-1265.
118. N.E. Dowling: *Mechanical Behavior of Materials - Engineering Methods for Deformation, Fracture, and Fatigue*, Prentice Hall, Upper Saddle River, NJ, 1993, pp. 525-569 pages.
119. A. Dlouhy, S. Kumar, and E. Pink: *Scripta Metallurgica et Materiala*, 1994, vol. 30, pp. 129-132.

120. D.E. Laughlin and J.W. Cahn: *Metall. Trans.*, 1974, vol. 5, pp. 972-974.
121. J. Llorca, A. Needleman, and S. Suresh: *Scripta Metallurgica et Materiala*, 1990, vol. 24, pp. 1203-1208.
122. J. Llorca, S. Suresh, and A. Needleman: *Metall. Trans.*, 1992, vol. 23A, pp. 919-934.
123. S. Suresh: in *Morris E. Fine Symposium*, Proc. Conf., Detroit, MI, 1991, P.K. Liaw, J.R. Weertman, H.L. Marcus, and J.S. Santer, ed., TMS, pp. 165-170.
124. H.J. Böhm, H.P. Degischer, W. Lacom, and J. Qu: *Composites Engineering*, 1995, vol. 5, pp. 37-49.
125. H.J. Böhm and F.G. Rammerstorfer: *Mater. Sci. & Eng.*, 1991, vol. A135, pp. 185-188.
126. G. Garmong: *Metall. Trans.*, 1974, vol. 5, pp. 2183-2190.
127. W.R. Tyson: *Metall. Trans.*, 1975, vol. 6A, pp. 1674-1677.
128. A.R.T.d. Silva and G.A. Chadwick: *J. Mech. Phys. Solids*, 1969, vol. 17, pp. 387-403.
129. X. Dumant, F. Fenot, and G. Regazzoni: in *9th Risø International Symposium on Metallurgy and Materials Science*, Proc. Conf., Risø National Laboratory, Roskilde, Denmark, 1988, S.I. Andersen, H. Lilholt, and O.B. Pedersen, ed., Risø National Laboratory, Roskilde, Denmark, pp. 349-356.
130. W. Lacom, J. Qu, H.P. Degischer, T. Schmitt, and H. Leitner: in *International Conference on Light Metals*, Proc. Conf., 1991, T. Khan and G. Effenberg, ed., ASM International, Metals Park, OH, pp. 711-718.
131. D. Masutti, J.P. Lentz, and F. Delannay: *J. of Mater. Sci. Lett.*, 1990, vol. 9, pp. 340-342.
132. G.S. Daehn, P.M. Anderson, and H. Zhang: *Scripta Metall. et Mater.*, 1991, vol. 25, pp. 2279-2284.
133. H. Zhang, P.M. Anderson, and G.S. Daehn: *Metall. Trans.*, 1994, vol. 25A, pp. 415-425.
134. D. Gould, P.B. Hirsch, and F.J. Humphreys: *Phil. Mag.*, 1974, vol. 30, pp. 1353-1377.
135. K. Wakashima, M. Otsuka, and S. Umekawa: *J. of Comp. Mater.*, 1974, vol. 8, pp. 391-404.
136. S. Yoda, N. Kurihara, K. Wakashima, and S. Umekawa: *Metall. Trans.*, 1977, vol. 8A, pp. 2028-2030.
137. B.D. Cullity: *Elements of X-Ray Diffraction*, 2nd, Addison-Wesley Publishing Co., Reading, MA, 1978, pages.
138. C.D. Liu and M.N. Bassim: *Metall. Trans.*, 1992, vol. 24A, pp. 361-367.
139. E.A. Brandes: *Smithells Metals Reference Book*, 6th, Butterworths, London, 1983, pages.
140. L.E. Murr: *Interfacial Phenomena in Metals and Alloys*, Addison-Wesley, London, 1975, pp.142-163 pages.

141. S. Suresh: *Fatigue of Materials*, First paperback edition (with corrections and exercises), Cambridge University Press, Cambridge, GB, 1992, 617 pages.
142. P.R. Swann: in *Electron Microscopy and Strength of Crystals*, G. Thomas and J. Washburn, ed., Interscience Publishers, New York, NY, 1963, pp. 131-181.
143. P. Guyot and G.M. Raynaud: *Acta Metall. et Mater.*, 1991, vol. 39, pp. 217-322.
144. M. Sahoo and J.A. Lund: *Metall. Trans.*, 1973, vol. 4, pp. 39-45.
145. J.E. Bailey: *Phil. Mag.*, 1963, vol. 8, pp. 223-236.
146. J.A. Venables: *Phil. Mag.*, 1962, vol. 7, pp. 1969-1972.
147. H.M. Otte and J.J. Hren: *Exp. Mech.*, 1966, vol. 6, pp. 177-193.
148. G.V. Drunen and S. Saimoto: *Acta Metall.*, 1971, vol. 19, pp. 213-221.
149. S. Kajiwara: *Trans. of Nat. Res. Inst. Metals*, 1969, vol. 11, pp. 127-134.